3.5–cm Radar Investigation of Mars and Mercury: Planetological Implications

Thesis by
Bryan Jay Butler

In Partial Fulfillment of the Requirements
for the Degree of
Doctor of Philosophy

California Institute of Technology
Pasadena, California

1994

(Defended May 27, 1994)

Acknowledgements

To quote the Grateful Dead: "what a long, strange trip its been." My heartfelt thanks to: Dewey; Marty; Jodi; my family; Bob and Dave; the rest of the Steuben house gang; Brad, Eric and Nagy (long live the 4 musketeers!); and the many, many others (too numerable to name) who helped me not only survive this ordeal, but actually enjoy it at times.

ABSTRACT

Bistatic radar observations have been made using the combined VLA/Goldstone radar instrument at X–Band wavelength (near 8500 MHz). This thesis contains a description of the instrument, observations, data reduction, and implications of some of the measurements. While the instrument has been used to probe many objects, discussion will be restricted to the data sets for Mercury and Mars. This technique has provided the first *unambiguous* radar cross section maps of both planets, with surface resolutions as good as 150 km for Mercury, and 100 km for Mars. The analysis of the radar cross section maps has provided a rich harvest of new information about the surface and near–surface of both planets.

Mars was observed twice during the opposition of 1988, and 3 times during the opposition of 1992/93. During the 1988 observations, the subearth latitude was $\sim -24°$, providing a good view into the south polar regions. The Martian season at the time was mid southern summer ($L_s \sim 295°$), and thus the seasonal CO_2 ice cap had sublimated away, exposing the residual south polar ice cap (RSPIC). The RSPIC was the area with the highest cross section on the planet in 1988, with a peak normalized cross section of 0.716. This is incredibly high, especially considering that it was at an incidence angle of $\sim 66°$ at the time. The RSPIC also exhibited the odd characteristic that throughout much of its extent, more echo energy was received in the same sense circular (SS) polarization as that transmitted than in the opposite sense (OS), a so–called polarization inversion. This is a characteristic which has also been observed on the Galilean satellites, and on a portion of Greenland, and may be true for all cold, clear icy regions. This seems to be a result of the radar wave penetrating into a relatively lossless medium containing many volume scatterers. In the case of the RSPIC, the lossless medium is ice, whether CO_2 or H_2O, and the scattering centers are most probably cracks and

voids in the ice. Simulations indicate that the radar wave penetrates down to 10's of meters into the ice layer, implying that at the time the RSPIC was very clean, i.e., less than $\sim 1\%$ volume fraction of contaminating dust, to that depth.

During the 1992/93 observations, the subearth latitude was $\sim +6°$ to $\sim +9°$, providing a tolerable view into the north polar regions. The Martian season at the time was early northern spring ($L_s \sim 20°$), and thus much of the seasonal CO_2 cap was present, which covered the residual north polar ice cap (RNPIC). No regions with enhanced cross section were found in the north polar regions, in stark contrast to the south. Fits to a sensible backscatter function provide an indication of slight cross section enhancements near the Chasma Borealis, but the reliability of the fits remains in question due to the restricted incidence angle range of the data. There are at least 3 possible reasons for the fact that the north polar regions show no cross section enhancements: 1 - there is some fundamental difference in the structure and/or composition (amount of dust contaminant) of the two residual caps, 2 - the seasonal CO_2 cap which was present during the north polar experiments absorbed enough of the incoming radar energy to obscure the RNPIC, and 3 - the north polar regions were imaged with slightly poorer geometry. Some combination of the three is most likely.

Many other regions with anomalous cross sections were found on the surface of Mars. The large volcanic provinces of Tharsis and Elysium have very high cross sections associated with them. These are most probably a result of the extremely rough surfaces of the large volcanoes and their associated flows. One of the most intriguing features in the Mars data set is a region which extends west from Tharsis for over 2000 km, which displays no cross section distinguishable from the noise in either polarization, which we have termed "Stealth." The surface and near surface (to depths of meters) must be composed of very underdense material, with an absence of volume scatterers (rocks). The proximity of Stealth to Arsia and Pavonis Montes suggests that it may be comprised of pyroclastic materials which were blown westward after eruptions from these two large shield volcanoes.

Mercury was observed twice during the conjunction in August of 1991, once during the conjunction in November of 1992, and twice during the conjunction in February of 1994. The data in 1992 were compromised by transmitter problems and will thus only be very briefly discussed. The 1994 data will be only briefly mentioned, as well, since the data reduction has not been fully completed, and thus all results are very preliminary. During the 1991 observations, the subearth latitude was $\sim +10°$, providing nearly as good a view of the north polar regions of Mercury as is obtainable via earth based remote sensing. The feature with the highest SS cross section (.079) in either of the radar images was near the nominal polar position. This feature also exhibits a polarization inversion throughout much of its extent, similar to the RSPIC on Mars. This feature is probably the signature of water ice deposits in permanently shadowed regions near the pole, which explains the reduced cross section when compared to the Martian RSPIC. The ice may be covered by a thin layer of dust, which would protect the ice from erosion from energetic sources as well as contributing to the reduced cross section. Other regions with anomalous cross sections exist on the surface, most notably five large quasi–circular regions, which we refer to as "basins." It is clear from the 1992 data that the Caloris basin has no such cross section enhancement in its interior, and so our "basins" are different from Caloris in some manner. During the 1994 observations, the subearth latitude was $\sim -10°$, providing nearly as good a view of the south polar regions of Mercury as is obtainable from earth. Preliminary results indicate that there is a region of enhanced cross section near the south pole, similar to that near the north pole.

Contents

List of Tables

List of Figures

Chapter 1

Introduction

Radar experiments provide a unique method of probing the surfaces and subsurfaces of planetary bodies. Information on surface and subsurface structures and properties can be extracted from radar data. Since the radar reflection is sensitive to surface and subsurface structure on the order of the wavelength, radar experiments give a good idea of the surface texture of planetary bodies on easily understandable size scales, i.e., things you could pick up, walk over, etc. When used in combination with other information, radar data can be used to infer the physical and geological setting and history of regions of planetary surfaces. The development of radar as a tool in planetary astronomy began with studies of radar reflection from the surface of the Moon in the 1950's, and as more powerful radar instruments were constructed other solar system objects were probed. A detailed study of the history of planetary radar astronomy is beyond the scope of this thesis, but the interested reader can consult Evans and Hagfors (1968).

When a monochromatic radar wave is bounced off of the surface of a rotating planet, the resulting echo is dispersed in frequency and in time. The dispersion in frequency is a result of the different doppler shifts the reflected wave experiences for different portions of the planetary surface. The doppler shifts are determined by the line of sight velocity of the planetary surface elements, and are constant along lines parallel to the projected apparent pole (doppler strips). The dispersion

in time is a simple result of the different light time to different portions of the surface, i.e., that portion of the reflected wave which comes from the subearth point is received some time earlier than that portion which is reflected near the limb. For a spherical target, a contour of constant time delay (range ring) is a circle on the surface centered on the subearth point. In early radar experiments, these two effects were used to distinguish how portions of the surfaces of the planets reflected differently. An experiment which only uses the frequency dispersion is called a Continuous Wave (CW) experiment, and only has surface resolution in the direction perpendicular to the doppler strips. If both doppler strips and range rings are utilized, then "pixels" are created on the target surface, which correspond to the intersection of a strip and a ring. However, there remains an ambiguity, in that for a given doppler shift and time delay there are two points on the surface which give that shift and delay. This has traditionally been called the "North-South" ambiguity, since the two points are symmetric on the North and South sides of the doppler equator. Also, if the product of the total doppler spread and the total delay depth is greater than unity, then there are problems in the reconstruction of surface cross sections from delay–doppler data. Objects with this property are called "overspread." For Venus and Mercury this problem is not extreme, but Mars is such a rapid rotator that delay–doppler mapping is severely compromised. Recently, two techniques have been developed to try to resolve these problems. The first uses many CW observations of a single body at different geometries which are inverted to obtain a representation of the surface cross section as a function of location (Hudson and Ostro 1990; Harmon *et al.* 1992*b*). The second is the development of random long–code methods to overcome the problem of overspreading (Harmon *et al.* 1992*a*; Harmon and Slade 1992). Thompson and Moore (1989) developed an *ad hoc* technique where they continually adjusted the cross sections of surface regions to try to match CW observations at 12.6 cm. This is essentially similar to the first method, but certainly more inexact. All of these techniques still have characteristics which complicate the interpretation of data

obtained using them.

When the antennas of the Very Large Array[1] were fitted with X–Band receivers in 1988 in support of the Voyager mission, the possibility of a new technique in planetary radar astronomy became available. Used in conjunction with the 70–m DSN antenna in California, operated by the Jet Propulsion Laboratory (JPL), a powerful new radar instrument could be formed. The 70–m antenna could be used to transmit a monochromatic radar wave to the surface of a planet, and the reflected wave could then be received at the VLA. With the VLA as the receiving portion of the instrument, the received echoes could be imaged with the standard techniques of radio interferometry, and surface cross sections could then be *unambiguously* determined. While radar interferometry is certainly not a new concept, the number of antennas at the VLA make this instrument unique, and make it the most powerful radar instrument in the world. An initial test of the instrument to image the radar reflection from the rings of Saturn (Muhleman *et al.* 1987), proved the feasibility of the technique. Since that time, our group has used the instrument to map the surfaces of Mercury (Butler *et al.* 1993; Slade *et al.* 1992), Venus (Tryka *et al.* 1991; Tryka and Muhleman 1992), and Mars (Muhleman *et al.* 1991), and to obtain echoes from Saturn's largest moon, Titan (Muhleman *et al.* 1990; Muhleman *et al.* 1993). This thesis will present the results obtained so far from the observations of Mars and Mercury.

There is a well developed history of radar investigations of Mars, beginning in some sense with the first reports of variation of scattering properties as a function of Martian longitude (Goldstein and Gillmore 1963; Kotel'nikov 1963). As mentioned above, the traditional method of delay–doppler mapping has been restricted to relatively small portions of the surface, in equatorial regions (see e.g., Downs *et al.* 1975). However, many CW experiments have been done with Mars as the target (see e.g., Simpson *et al.* 1978*a*,*b*; Harmon and Ostro 1985; Harmon *et al.* 1992*b*).

[1]The VLA was built and is operated by the National Radio Astronomy Observatory, which is operated by Associated Universities, Inc., under cooperative agreement with the National Science Foundation.

Simpson *et al.* (1977) give a good review of measurements at several wavelengths done through the 1973 opposition. All of these experiments combined to show that Mars displays a great diversity in its radar cross section as a function of surface location, indeed, the most diversity of any probed solar system object to date (aside from Earth). Dual–polarization experiments also revealed that some regions of Mars depolarize relatively efficiently (Harmon and Ostro, 1985). By contrast, Mercury has received relatively little attention in past radar experiments. Some early measurements were taken to try to determine surface properties (Carpenter and Goldstein 1963; Muhleman 1965; Evans *et al.* 1965; Goldstein 1970 and 1971; Ingalls and Rainville 1972; and Zohar and Goldstein 1974), but only a very few recent observations to find such properties have been reported (Harmon *et al.* 1986; Clark *et al.* 1988). Some variation of cross section with surface location seemed to exist, but most of the surface seemed to have little contrast, unlike Mars.

In our experiments, the target planet is continuously illuminated with right circularly polarized (RCP) radiation, and power in both RCP and left circular polarization (LCP) is received and recorded at the VLA. We will use the convention of referring to the received RCP echoes as Same Sense (SS), and LCP echoes will be referred to as Opposite Sense (OS). The OS echoes are dominated by so called specular or quasi-specular phase-coherent, single facet reflections near the subearth point, in local first Fresnel zones. Most regions away from the subearth point in the OS data, and the entire planet in the SS data are essentially free of the echo energy from these reflections, and thus important information about surface and near surface structures of a size comparable to or larger than the resolution can be obtained by examination of these data. Structures here implies large regions of the planet's surface that exhibit similar radar reflection characteristics. The radar reflection itself is sensitive to much smaller scale structure (on the order of the wavelength, or centimeters for us). It is important to realize that echo energy which comes back to the VLA as the result of surface scattering events cannot be distinguished from that which comes from subsurface scattering events. Although

it seems sensible that a portion of the OS echo comes from single reflection events which occur at the actual surface, the rest of the OS echo, as well as most of the SS echo must come from multiple scattering events which can occur either at the surface or in the subsurface. Therefore, the inverse problem of determining the true nature of the surface and subsurface from data such as ours is incredibly difficult. The problem cannot be solved unambiguously, and possible solutions may only be found through modeling.

1.1 Organization

The bulk of this thesis is presented in two chapters, one each for Mercury and Mars. The overall organization is as follows.

Chapter 2 will cover the basics of the observations and data reduction. Only aspects of these subjects which are common to the observations of both Mercury and Mars will be discussed.

Chapter 3 discusses results to date for Mercury. Much of the material in this chapter comes from Butler *et al.* (1993), but there is some additional material, most notably results from 1992 and 1994 experiments. Also, the section on thermal emission results from Butler, *et al.* has been omitted here.

Chapter 4 discusses results to date for Mars. Most of the focus here is on the polar regions, and much of that material is soon to be submitted for publication (Butler *et al.* 1994). Other regions of interest (e.g. "Stealth") are also discussed, but their treatment is not nearly as complete as that of the polar regions.

Chapter 5 summarizes the results from chapters 3 and 4. In addition, measurements of future interest are discussed.

There are several appendices which discuss in gory detail some of the calculations performed in chapters 3 and 4. The thesis should read well without these, but they are included in the interest of completeness.

Chapter 2

Observations and Data Reduction

The purpose of this chapter is to explain those portions of the observations and data reduction which were common to both the Mars and Mercury experiments. Details specific to each object will be treated in the appropriate following chapters. The transmitting telescope is a 70–m parabolic dish, with an effective transmitting area, A_t of $\sim$ 2600 m^2, at an elevation angle of 45°. Transmission was at 8495 MHz (3.530 cm) with peak power of $\sim$ 350 kW for the 1988 Mars observations, and 8510 MHz (3.523 cm) with peak power of $\sim$ 460 kW for the 1992/93 Mars observations, and all Mercury observations. The VLA consists of 27 antennas of 25–m diameter, which are arranged in a Y shape on the plains of San Augustin, New Mexico. The antennas are cycled through 4 configurations: A, B, C and D, with different antenna positions for each configuration. The A configuration is that in which the antennas are furthest apart, with a maximum spacing of $\sim$ 36 km, while the D is the most compact, with a maximum spacing of $\sim$ 1 km. With the exception of the September, 1988 Mars observations, all of the Mars and Mercury experiments were conducted in the A configuration, which results in a fringe spacing of $\sim$ 0.2 arcseconds on the sky.

The basic measured quantity of an interferometer such as the VLA is a sampling

of the complex visibility function at the positions of the baselines between each of its antennas. Each of these samples can be referred to as a visibility. The visibility function is the 2 dimensional Fourier transform of the sky brightness function (see e.g., Thompson *et al.* 1991). Therefore, after proper calibration, an inverse discrete Fourier transform can be used to obtain an estimate of the sky brightness. Any of a number of deconvolution techniques may then be employed to try to back out the known effects of the discrete sampling, to obtain a better map of the sky brightness.

During each experiment, periodic observations of an unresolved quasi–stellar object were used to obtain the initial calibration of the phases and amplitudes of the observed complex visibilities. This object is generally referred to as the "phase calibrator," even though it is actually used to calibrate relative amplitudes as well. A single observation of a quasi–stellar object of well known absolute amplitude was used during each experiment to fix the absolute amplitude scale. This object is generally referred to as the "amplitude calibrator." Since the received radar echo energy is relatively narrow in frequency range, we used the VLA in its spectrometer mode. The spectral response of the VLA was calibrated by observing a strong source at the beginning and end of each experiment. This object is generally referred to as the "bandpass calibrator." The calibrators, with their known or derived source strengths in Jansky (1 Jy = 10^{-26} W/m^2/Hz), for all of the observations described here are listed in Tables 3.1 and 4.1.

After the initial calibrations, the fact that the spectral channels which contained radar echo flux also contained thermal emission flux from the planetary surface made it necessary to subtract the thermal emission signal from the data in those spectral channels. The thermal emission visibilities were formed by taking the average values of the visibilities from those channels which were not affected by the radar return, or by edge effects. These visibilities were subtracted directly from the visibilities of the central channel (van Langevelde and Cotton, 1991) to form the radar visibilities.

The next step was self–calibration (see, e.g., Cornwell and Fomalont, 1989, for a general discussion). Since the majority of the echo energy is in the OS polarization, in a nearly unresolved source region for our observed sources (the quasi–specular spike), the OS visibilities themselves are an excellent source for self–calibration. The resulting antenna complex gain corrections were then applied to the visibilities of all OS channels, and all of the SS channels, assuming that the phase errors in the received signals in all polarizations and spectral channels on each antenna of the VLA were the same. This is not entirely true, as the two polarizations actually come through different receivers, and thus have different thermal noise. However, this technique allows for correction of atmospheric, antenna reference system, and baseline (antenna position) errors, which were the same for both polarizations.

At this point, the visibilities were rotated to make the assumed rotation axis of the source coincide with "up" in the image plane. The position angle of the north pole, ψ, given in degrees East of North on the celestial sphere, is shown in Tables 3.1 and 4.1 for each experiment. The data were then ready to be mapped, and have the known antenna response (the "dirty beam") deconvolved out. After some experimentation, we settled on a modified CLEAN algorithm (see Högbom, 1974 for the first discussion of CLEAN) for the deconvolution. When using the CLEAN algorithm, the effective resolution is determined by what is called the "CLEAN beam." This is a 2–D gaussian kernel which is convolved with the final derived sky brightness, in order to smooth out unsampled high spatial frequencies. The size of the CLEAN beam is generally determined by the width of the central lobe of the synthesized beam, which is determined by the sampling of the visibilities, or the antenna positions during observation. The CLEAN beam sizes for each of the experiments are shown in Tables 3.1 and 4.2. The small size of some of the synthesized beams made it necessary to have a pixel size of 0.1 arcsec for all but the single D configuration experiment, in order to sample the central lobes well. The CLEAN algorithm can be aided greatly, especially in the case of very extended sources, by specifying an initial model of the sky brightness. The construction of

the initial model is different for Mercury and Mars, and thus will be covered in the appropriate chapter for each object.

In order to make comparisons between experiments with different geometries and resolutions, the final images were all reduced to common units. The measured flux at the VLA as a function of sky position (x, y) in Jy/beam is given in the case of our radar experiments by:

$$I(x,y) = \frac{P_t \; A_t \; \Omega_b}{4 \; \pi \; \lambda^2 \; D^2 \Delta f} \; \eta(x,y) \quad , \tag{2.1}$$

where P_t is the transmitted power, A_t is the effective transmitter area, which is a function of the elevation angle, Ω_b is the synthesized beam size (effectively the CLEAN beam size), λ is the transmission wavelength, D is the distance to Mars, Δf is the effective reception bandwidth, which is in our case the spectral channel width, and η is the surface cross section. The surface cross section, η, is the common unit all of the images were converted to, and is equivalent to the normalized radar cross section, i.e., it includes effects of the true Fresnel surface reflectivity and the radar backscatter phase function. Using the known quantities, the above can be reduced to:

$$\eta(x,y) = \kappa \; I(x,y) \quad . \tag{2.2}$$

Typical values of η for normal incidence vary from about 0.1 (SS echoes from the terrestrial planets) to 1.0 (OS echoes from the terrestrial planets and SS and OS echoes from icy surfaces).

Chapter 3

Mercury

3.1 Observations

We observed Mercury on five occasions: August 8 and 23 of 1991, November 23 of 1992, and February 21 and 26 of 1994. Physical and geometrical details of the observations are shown in Table 3.1, along with the phase calibrator used. The amplitude calibrator used for all of the Mercury observations was 3C286 whose flux at 8510 MHz (the center frequency for all Mercury observations) is 5.24 Jy. The bandpass calibrator for all of the Mercury observations was 3C84. Transmitter power was $\sim$ 450 kW for all 5 dates, however, other transmitter problems seriously compromised the quality of the 1992 data. The data for February 21, 1994 has not been reduced fully, and that from February 26, 1994 has not been reduced at all. Because of these considerations, most of the discussion in this chapter will concentrate on the 1991 data. The data from 1992 and 1994 will be mentioned only briefly.

The orientation of the planet on the sky at the central time of the observations on both days in 1991 is shown in Figure 3.1, where the disk has been rotated so that the north pole of Mercury points up on the page. Although the position of the rotational pole of Mercury is only known observationally to within a few degrees (Klaasen 1976; Harmon and Slade 1992), there are convincing theoretical

Table 3.1

Experimental Information for Mercury

date	8/8/91	8/23/91	11/23/92	2/21/94
subearth longitude, β_o	252.8	353.5	195.0	15.7
subearth latitude, ϕ_o	+10.7	+11.0	-2.3	-10.6
phase angle, α	129	195	195	167
sun–Mercury separation	21.0	5.0	4.7	4.7
position angle, ψ	23.6	20.7	20.0	338.2
geocentric distance, D (AU)	.67	.63	.69	.64
channel width, $\Delta\nu$ (Hz)	763	1526	763	763
phase calibrator flux (Jy)	1041+061 1.74	1041+061 1.74	1507-168 2.37	2229-085 0.902

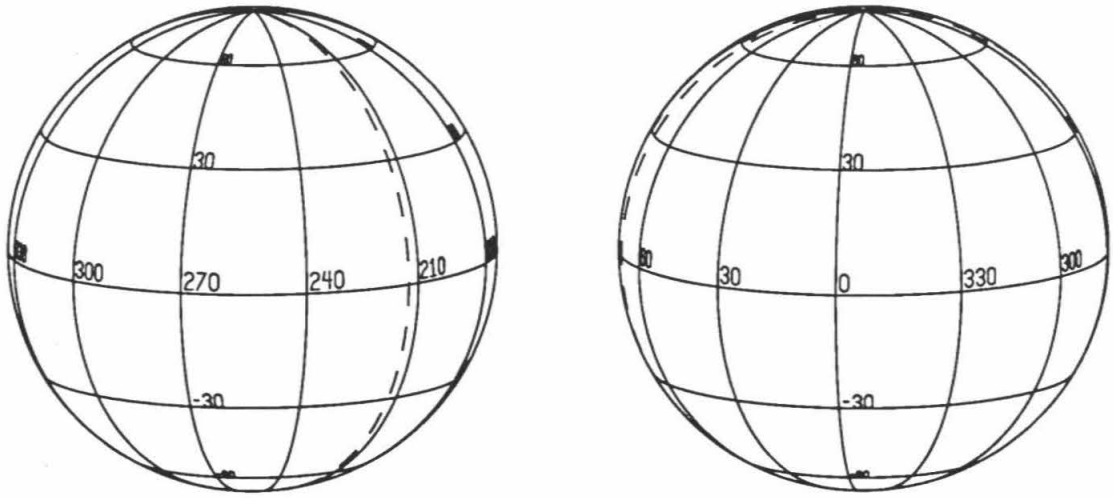

Figure 3.1: A schematic illustration showing the orientation of the visible disk of Mercury as projected on the sky for the two days of observation in 1991. The disk has been rotated so that north is up on the page. Planetary cartographic coordinates are shown; latitude and longitude lines are plotted at 30° intervals. The terminator is shown as a dashed line. In the figure on the left (for August 8), longitudes to the east (right) of the terminator are illuminated, while at right (August 23), longitudes to the west (left) of the terminator are illuminated.

arguments that the rotation axis should currently be very nearly normal to the orbital plane, and may have been there for as long as a billion years (Peale 1988). Throughout the remainder of this chapter it will be assumed that the rotation axis is normal to the orbit plane. Since the rotation rate of Mercury is slow enough that the planet only rotates through about 2 degrees of longitude during 8 hours of observation from earth, an entire evening's data can be combined into one map of the visible surface at the time without sacrificing much resolution.

The reflected radar echoes were only spread by about 400 Hz by this slow rotation. In order to maximize the signal to noise ratio (SNR) in a radar experiment, the bandwidth of the receiver should be matched to the bandwidth of the source. Due to data handling and hardware limitations at the VLA this was not possible, unfortunately. The narrowest possible receiver bandwidth is 763 Hz if observing in 2 polarizations (which correspond to the SS and OS polarizations), and 1526 Hz if observing in 4. On August 8, 1991, we observed in 2 polarizations, in 256 spectral channels. On August 23, 1991, we observed in 4 polarizations, in 128

spectral channels, in order to attempt to recover the entire polarization state of the reflected radar echoes. In the 1992 and 1994 experiments, we went back to 2 polarizations in 256 channels. All of the spectral channels contain thermal emission energy from the surface of Mercury, of course.

Calibration and data processing proceeded as described in Chapter 2, except for the following. Due to the mode in which the data were collected at the VLA, an unusual correction was required for the 1991 data. It was necessary to correct for on–line bandpass normalization, which is explained in more detail in Appendix D. Unfortunately, we did not realize this correction was necessary when Slade *et al.* (1992) was published. The correction (to first order) introduces a small linear scale factor into the final images. Because of this, the numbers in Slade *et al.* are slightly low, and the numbers presented in Butler *et al.* (1993) and here should be used instead.

As mentioned in Chapter 2, an initial model was used in the CLEANing process. For Mercury, this model was obtained from a fit of the visibilities for each polarization separately on each date (see Appendix A, section A.2). As shown in Table 3.2, the CLEAN beam sizes for the 1991 images were 0.35 and 0.30 arcseconds, which yielded unsmeared resolutions at the subearth point of Mercury of 170 and 140 km. The rotation of the planet lowered these resolutions to 180 and 150 km at the subearth point in the approximate direction of longitude on the surface. Using the known radar parameters, the value of κ from equation (2.2) were calculated, and are shown in Table 3.2. The observed pixel to pixel variations in the final radar cross section images are also shown in Table 3.2.

One of the problems in observing Mercury is its proximity to the Sun, which is a confusion source for most observations. Table 3.1 shows the angular separation of the Sun from Mercury for all of the experiments, calculated from their celestial positions at the time of observation. The individual antenna response at the VLA for such separations should be very small, but the brightness temperature of the Sun is $\sim 1.4 \times 10^4$ K at 3 cm (Allen 1964) and so an individual complex visibility

Table 3.2

Imaging Information for Mercury

date	8/8/91	8/23/91	11/23/92	2/21/94
CLEAN beam size (asec)	0.35	0.30	0.43	0.27
κ (eqn. 2.2)	0.3024	0.7367	0.2319	0.4684
ΔI_m (RMS noise, SS polarization	0.19	0.28	0.25	0.34
OS polarization	0.42	0.62	*	*
whole disk cross section (%)				
SS polarization	1.3 ± 0.065	1.6 ± 0.080	2.30 ± 0.12	2.23 ± 0.11
OS polarization	6.5 ± 0.33	8.7 ± 0.44	13.0 ± 0.65	11.5 ± 0.56
model fits:				
$A^a_{ss}(\%)$	2.12	2.43	3.80	3.32
n^a	1.25	1.25	1.1	1.2
$A^b_{os}(\%)$	59.0	95.8	*	*
α^b	.42	.38	*	*

[a] see equation (3.1)
[b] see equation (3.2)
* no value presently available

would have an appreciable solar component added to it. The difficulty is avoided by use of the rapid relative motion of the Sun and Mercury throughout the observations. Since the antennas and the phase reference system at the VLA were set to track the position of Mercury as it moved across the sky, the Sun moved in relation to the phase center of the array, thus causing it to move through the fringes of the interferometer response. The equivalent fringe width was ~ 0.20 (~ 8.7) arcseconds for the longest (shortest) baselines (result from maximum separation ~ 36 km in the A configuration of the VLA, minimum separation ~ 840 m), so the phase portion of the complex component due to the Sun moved through 2π radians each time it moved 0.20 (8.7) arcseconds relative to Mercury on the sky. In 1991, the true relative motion was ~ 2.4 arcseconds/minute on August 8, and ~ 2.2 arcseconds/minute on August 23. Since the CLEANed images can be thought of as using vector averages of the individual visibilities, and we made images from approximately 8 hours of data on each day, the phase of the component of the visibility from the Sun moved through 2π radians some 125 times on each day even for the shortest baselines, thus effectively averaging itself out. The result is similar for the 1992 and 1994 experiments.

3.2 Radar Data

Radar reflection images for the 1991 experiment in both SS and OS polarizations are shown in Figure 3.2. Also shown in Figure 3.2 are SS images for the 1992 and the first of the 1994 experiments. Residual radar reflection images for these days and polarizations are shown in Figure 3.3. These are termed residual because in order to enhance variations in cross section across the disk a model was subtracted from the actual measured response to remove the "average" radar response for all of these images. For the SS images, the model was a simple cosine law:

$$F_M(\mathrm{SS}) = A_{ss} \cos^n \theta_i \tag{3.1}$$

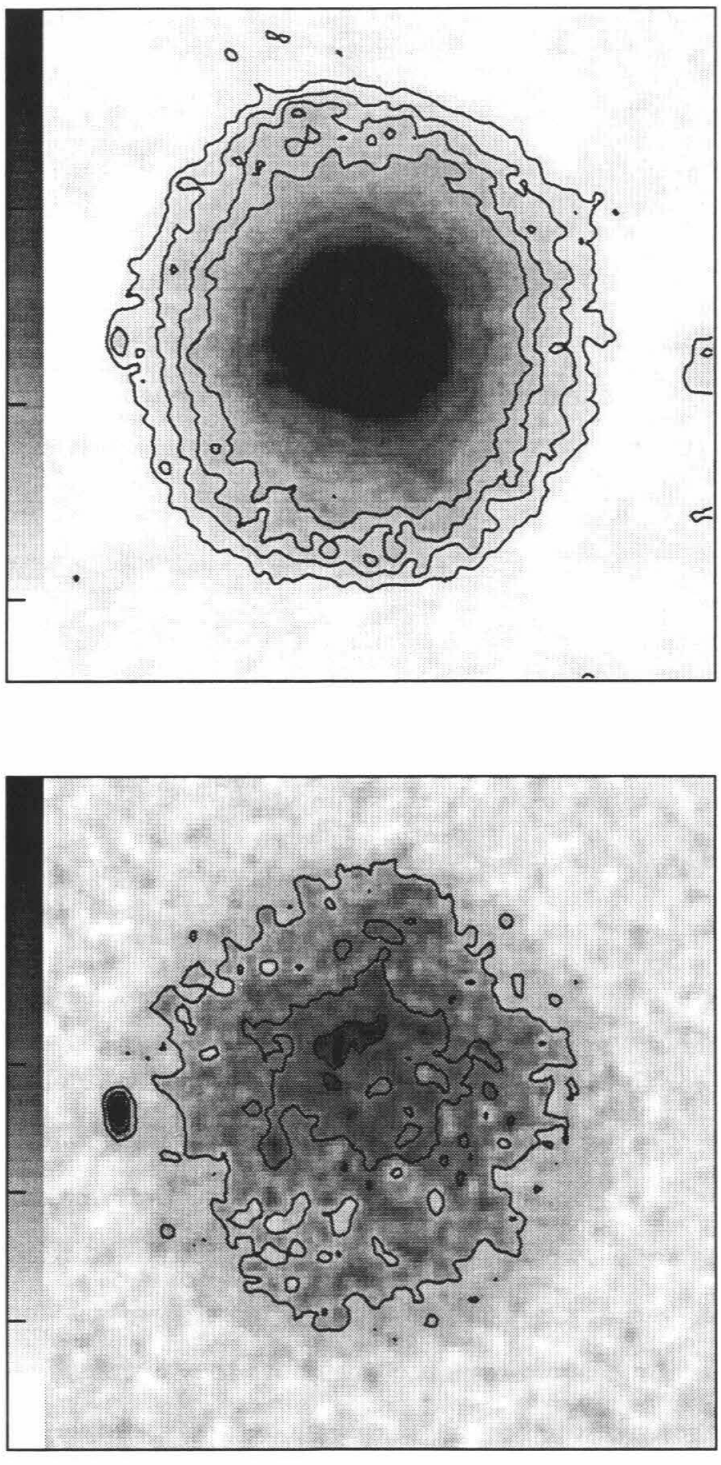

Figure 3.2 : True radar cross section images of Mercury. (a) Images for August 8, 1991, SS polarization on the left, OS on the right. Contours are at 1, 2, 3 and 4%.

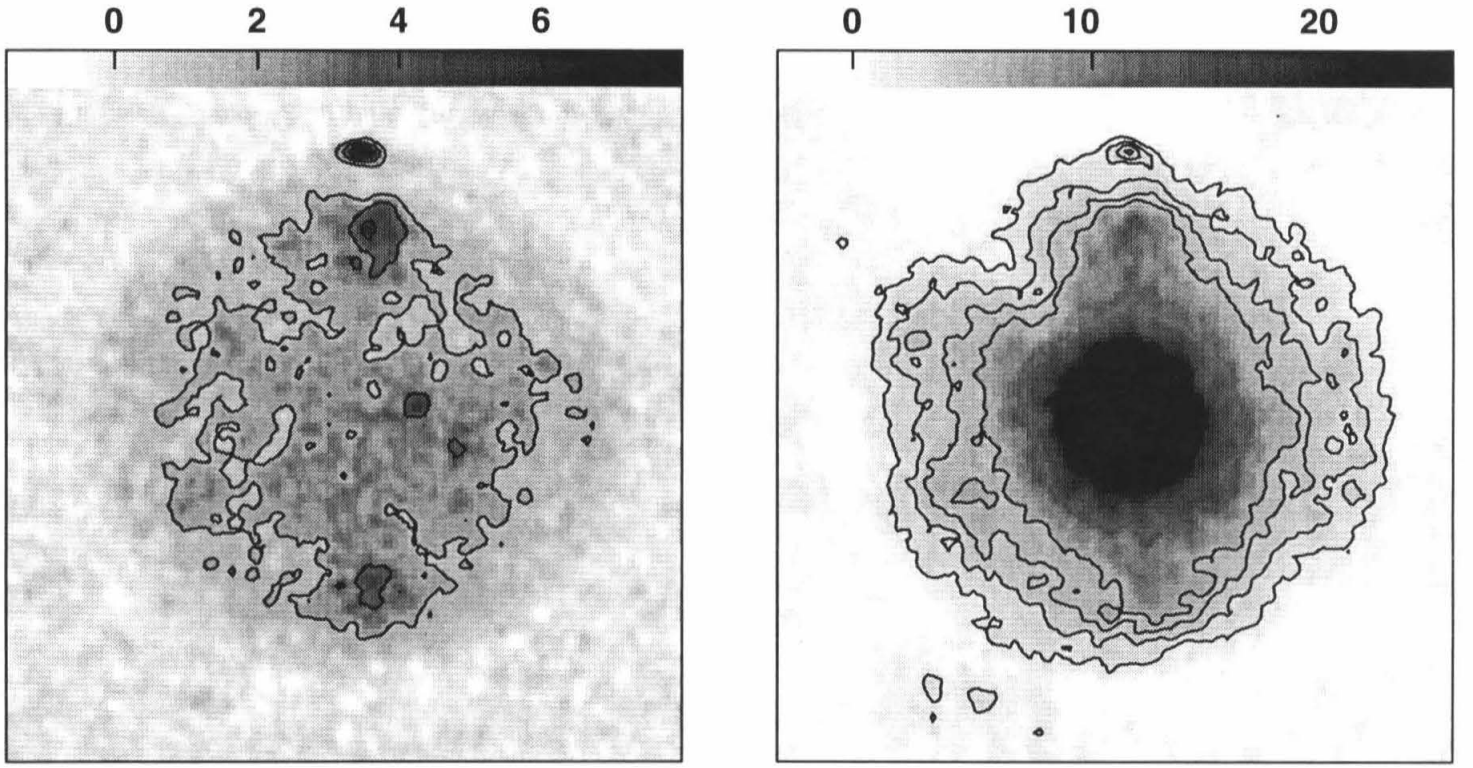

Figure 3.2 : (b) Images for August 23, 1991, SS polarization on the left, OS on the right. Contours are at 1.75, 3.5, 5.25 and 7%.

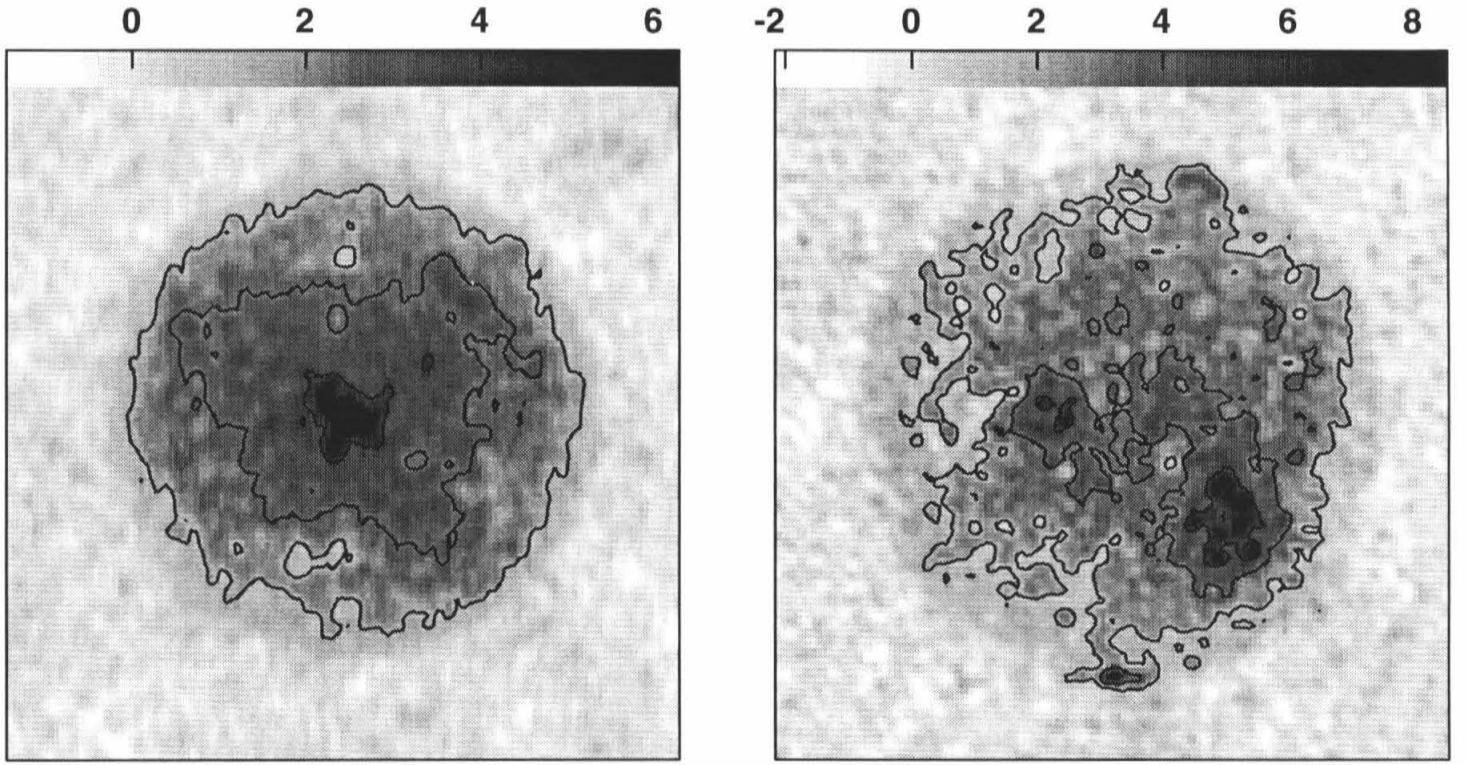

Figure 3.2 : (c) SS Images for November 23, 1992 (on the left, contours at 1.5, 3, 4.5 and 6%), and February 21, 1994 (on the right, contours at 2, 4, 6 and 8%).

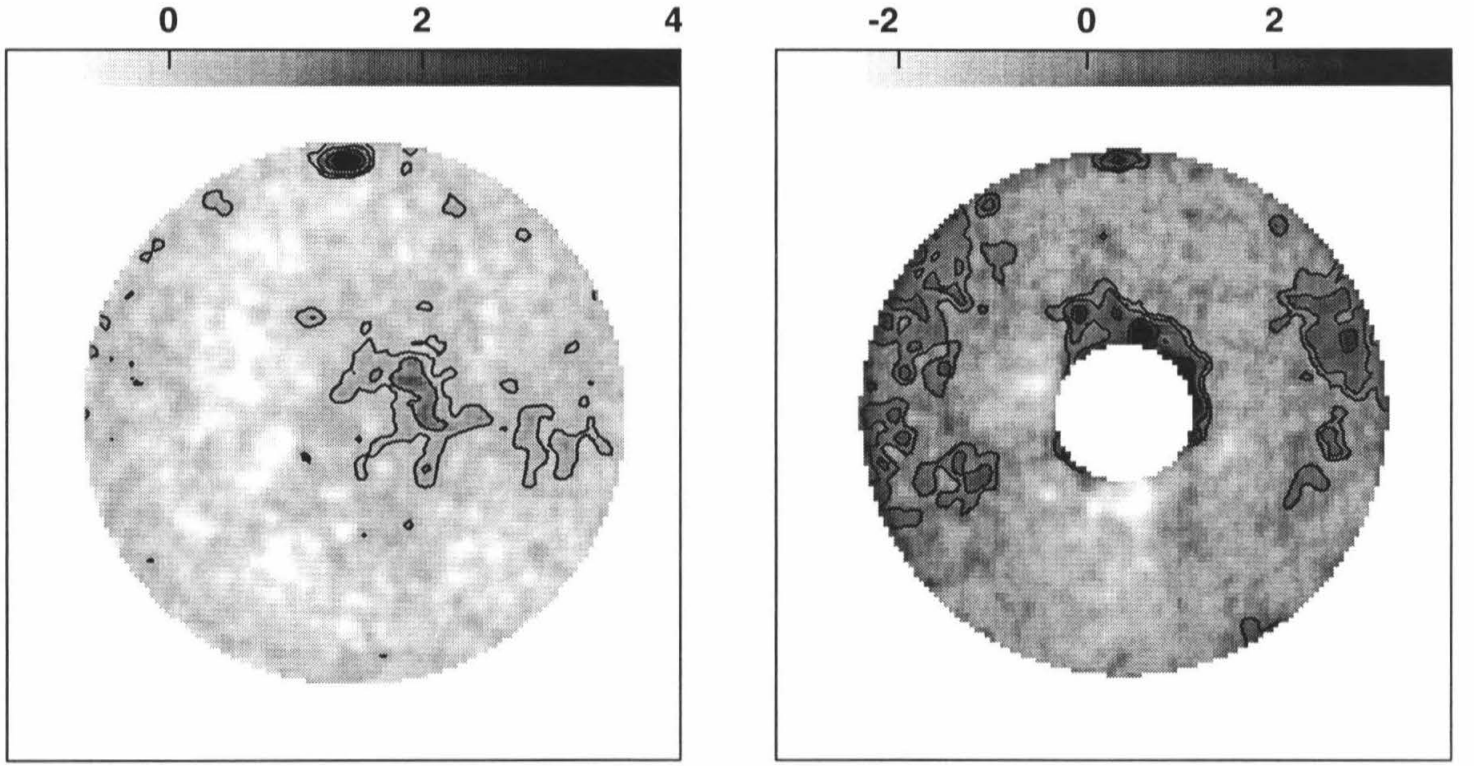

Figure 3.3 : Residual radar cross section images of Mercury. These images were obtained by subtracting a model from the actual measured cross sections in an attempt to enhance variations across the disk. (a) Images for August 8, 1991, SS polarization on the left, OS on the right. Contours are at .5, 1, 2, 3 and 4%. For the OS image, the interior has been blanked (incidence angles less than 15°) in order to see the more interesting variations at larger incidence angles.

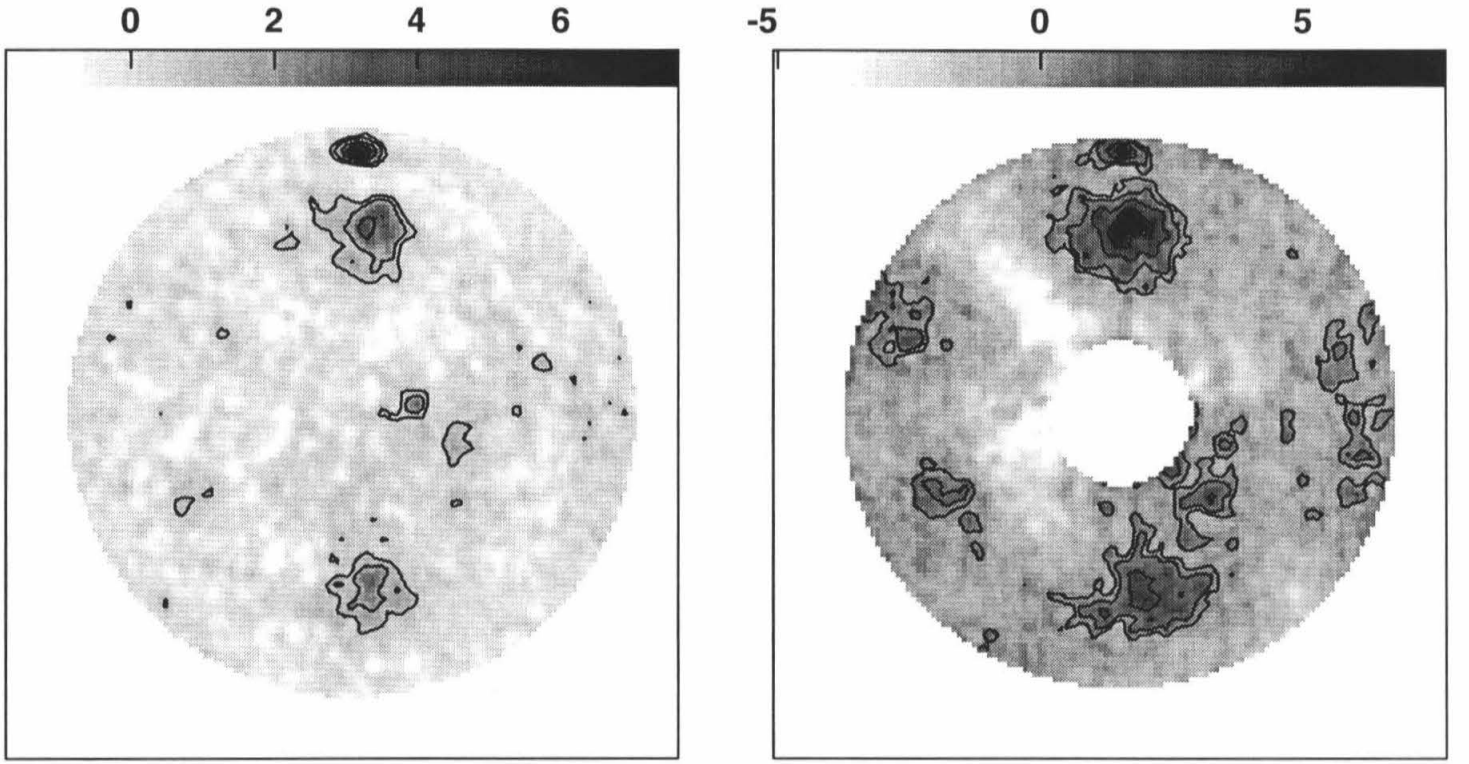

Figure 3.3 : (b) Images for August 23, 1991, SS polarization on the left, OS on the right. Contours are at .875, 1.75, 3.5, 5.25 and 7%. For the OS image, the interior has been blanked (incidence angles less than 15°) in order to see the more interesting variations at larger incidence angles.

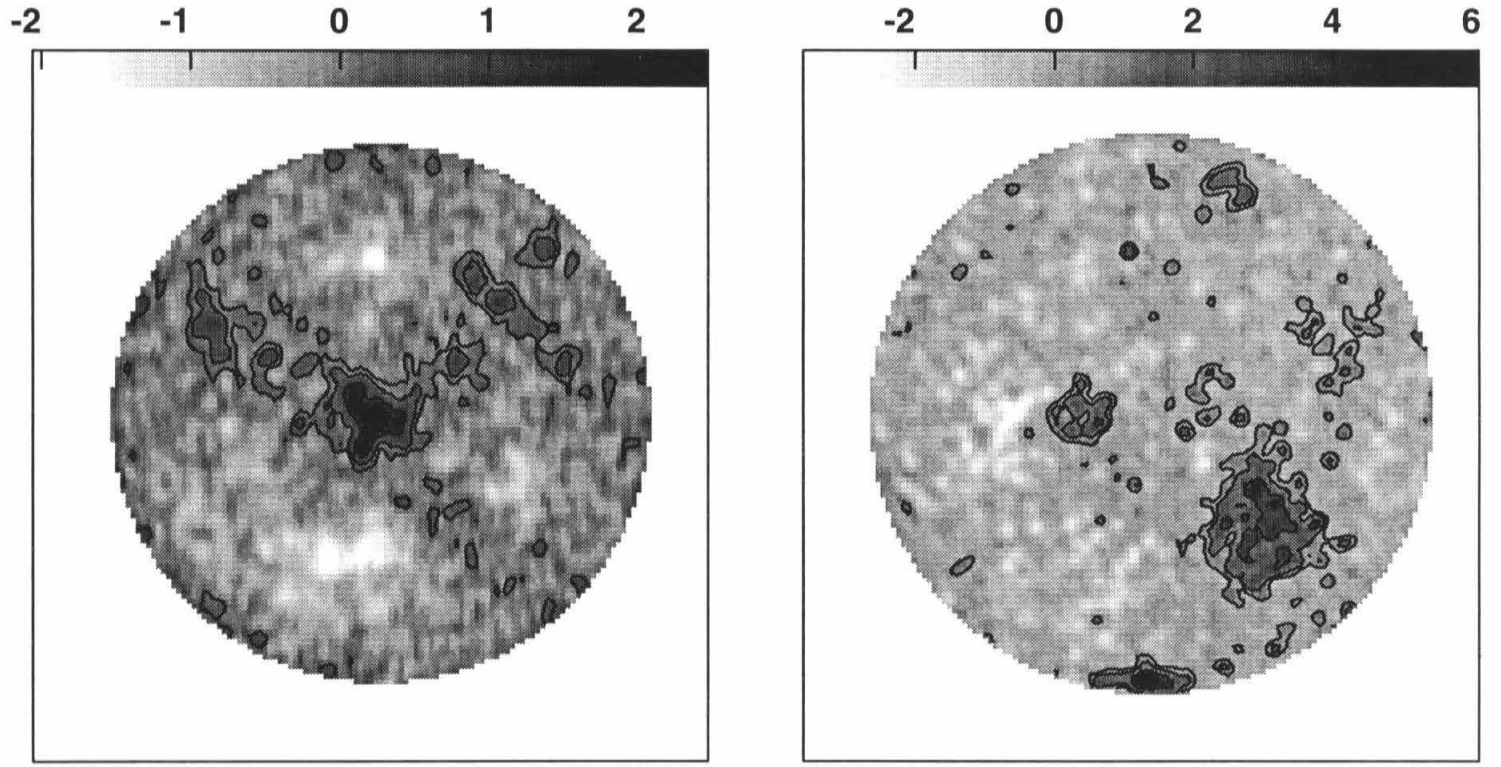

Figure 3.3 : (c) SS Images for November 23, 1992 (on the left, contours at .375, .75, 1.5 and 2.25%), and February 21, 1994 (on the right, contours at .75, 1.5, 3, 4.5 and 6%).

convolved with a gaussian of the proper size to account for the beam smearing. The best fit values of A_{ss} and n are shown in Table 3.2. For the OS images, a Muhleman model (Muhleman 1964) was used:

$$F_M(\mathrm{OS}) = A_{os}\left(\frac{\alpha}{\alpha\,\cos\theta_i + \sin\theta_i}\right)^3 \cos\theta_i \tag{3.2}$$

again convolved with the proper gaussian. Table 3.2 shows the best fit values of A_{os} and α. The SS and OS fits are performed as described in Appendix A, section A.1, with one difference. When making the data points to be fit (as annuli on the visible disk), pixels which are in "features" are excluded. The "features" include those listed in section 3.5 below, and the north and south polar features. In this manner, a better estimate of the average backscatter on the visible hemisphere is obtained. A comparison of the fit to our observed data for August 23, 1991 is shown in Figure 3.4. The data points with enhanced cross section near grazing incidence in the SS data in Figure 3.4 are due to the north polar feature, apparent in all of the images from 1991 shown in Figures 3.2 and 3.3, which will be discussed at length subsequently. In the residual OS images, small departures from the model in the area of the specular spike (at small incidence angles) will have much larger amplitude than even large departures outside of the spike. In order to better display the variations outside of the spike, the center portions (incidence angles less than 15°) of the OS images in Figure 3.3 have been blanked. For all of the images in Figures 3.2 and 3.3, the original data values were converted from units of Jy/beam to normalized cross section via equation (2.2), in order to facilitate direct comparison between the two days. Global values of cross section, or the ratio of total flux received from the entire illuminated hemisphere to total flux transmitted, are shown in Table 3.2. These are in the range of previously measured X-Band cross sections (Evans *et al.* 1966; Ingalls and Rainville 1972; Clark *et al.* 1986) and show that Mercury is a poorer radar reflector than Mars or Venus, and is similar to the Moon. Images showing circular polarization ratio, defined by $F_R(\mathrm{SS})/F_R(\mathrm{OS})$,

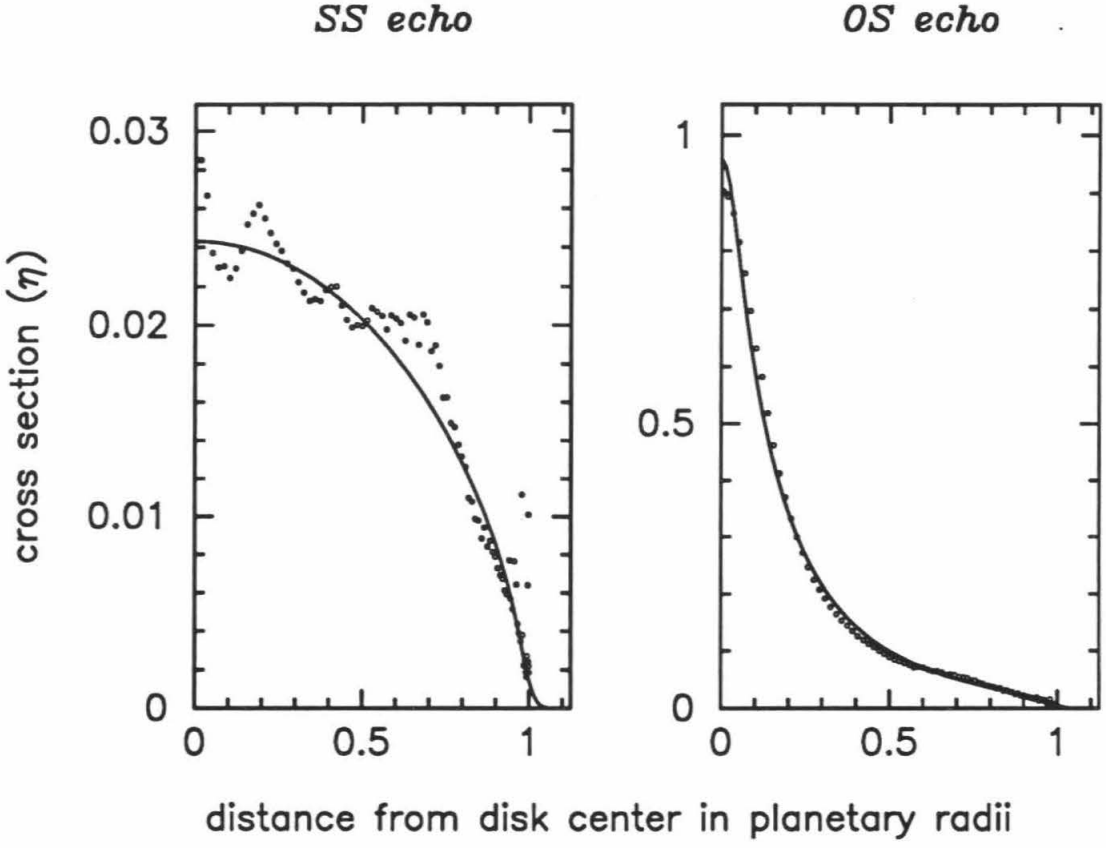

Figure 3.4: Plot of the model fits to our observed data of August 23, 1991. Our data was obtained by averaging pixels in one degree bins according to incidence angle over the entire imaged hemisphere. The fit to the SS data is shown on the left (see equation (3.1)). The fit to the OS data is shown on the right (see equation (3.2)).

are shown in Figure 3.5. In these images, the signature of the specular spike can be seen driving the ratios to near zero at small incidence angles. Also, the outer portions of these images are blank, as no ratio was taken if either the SS or OS signal was not statistically different from the noise for that polarization.

The images for both days show much small and large scale structure across the Mercurian surface. There is clearly a feature with enhanced cross section in both polarizations associated with the north pole. This feature also has the unusual property that its polarization ratio is > 1 throughout much of its extent (see Figures 3.5 and 3.6). There is also clearly a feature with enhanced SS cross section associated with the south pole. There are large (on the order of 500 km) quasi–circular structures in all of the images which also show enhanced cross section, but do not have the inverted polarization signature. There is also much small scale structure in all of the images. On the days where the radar cross sections can be compared to the photographs returned by Mariner 10, most of the small scale variation seems to be associated with craters and crater complexes. Each of these structures will be dealt with separately.

3.3 North Polar Feature

The area with the highest cross section in both of the 1991 experiments in the SS images is a large elliptic area near Mercury's north pole. After the model subtraction, this area also has the highest residual cross section in the 1991 OS images, outside of those in the specular spike. Figure 3.6 shows polar stereographic projections taken from the data shown in Figures 3.2 and 3.3, where the data from the two days has been averaged for the SS and OS polarizations separately. The SS and OS projections were formed using the residual data of Figure 3.3, while the ratio projection was formed using the raw data of Figure 3.2. Pixels in the ratio image are blanked if either the SS or OS data value is indistinguishable from the noise at that location. In the SS polarization data, the area with enhanced cross

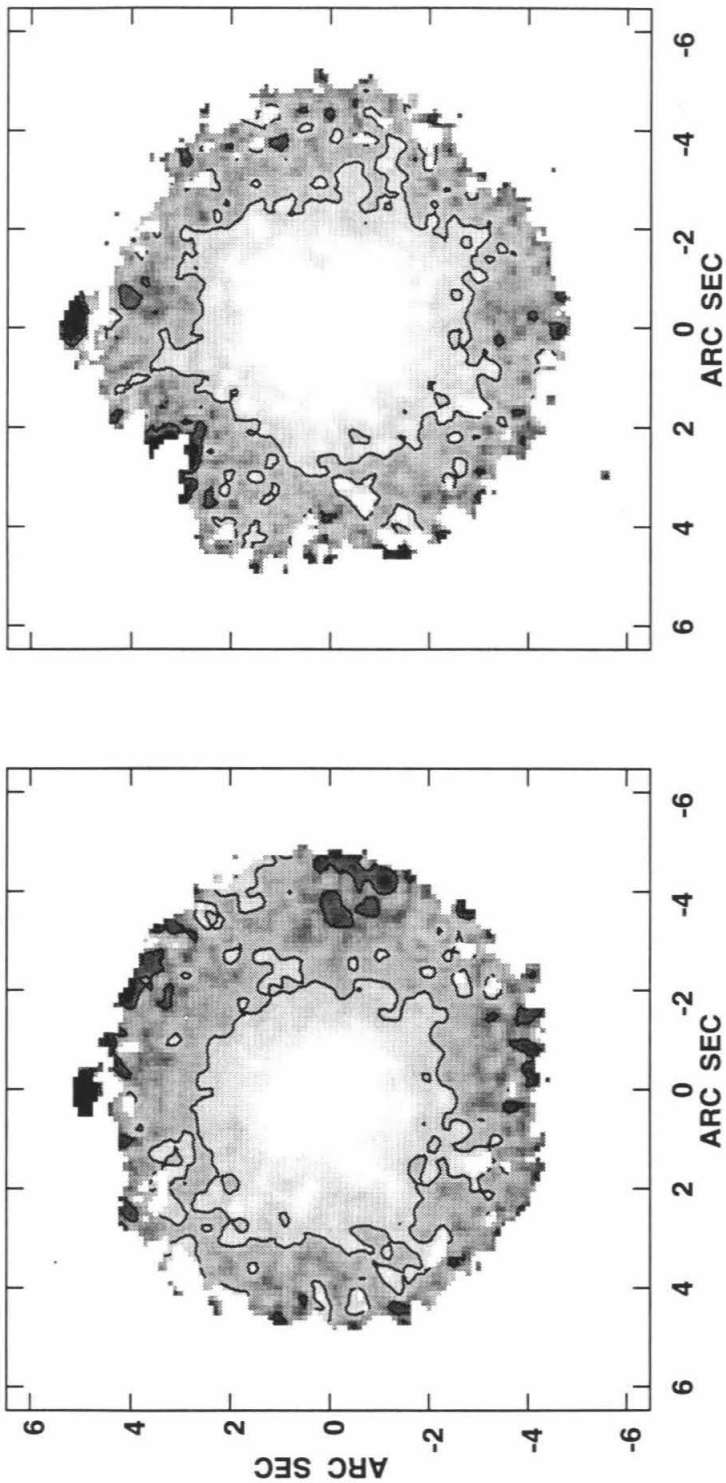

Figure 3.5 : Polarization ratio images of Mercury for 1991. These images are obtained by taking the ratio of the SS to the OS cross sections, pixel by pixel. The image on the left is for August 8, that on the right is for August 23. Contours from 0.0 to 2.0 in increments of 0.25. Darker shades are higher polarization ratios.

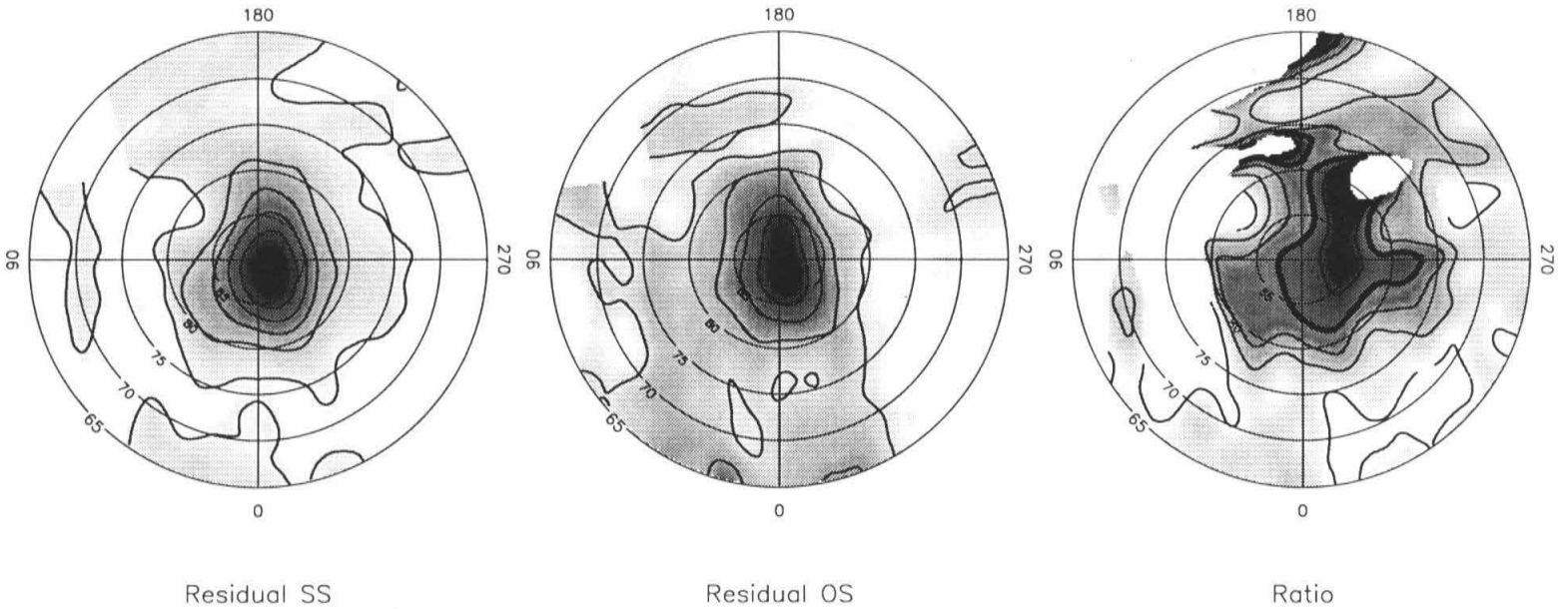

Figure 3.6 : Polar stereographic projections of the radar cross section in the vicinity of the north pole. For these projections, in areas which had coverage during both days of observations an average was taken of the two values. In other areas the value from the appropriate day was used. There is a small wedge in the upper left hand corner which was totally unobserved by us on either day. The projection on the left is for the SS polarization, that in the middle is for the OS, and that on the right is the polarization ratio (SS/OS). Contours for the OS and SS projections are from 0% to 5% in 1% increments, with darker shades corresponding to higher cross sections. Contours for the polarization ratio are from 0.25 to 2.0 in increments of 0.25, with darker shades corresponding to higher ratios. The contour at ratio = 1.0 is darkened.

section is centered at $\phi = 86°$, $\beta = 57°$ on day 1, $\phi = 88°, \beta = 315°$ on day 2, and $\phi = 88°, \beta = 315°$ after averaging. The size of the area on the surface is 350 X 1000 km on day 1, and 300 X 900 km on day 2, estimated from the half-power extent of the feature. The long axis of the ellipse is along the radar line of sight on both days, and is primarily a projection effect. We attribute the day to day differences to resolution problems, as a resolution element (synthesized beam) projected on the surface at the pole is 170 X 890 km on day 1, and 140 X 730 km on day 2, i.e., we are resolving the feature partially in one direction (perpendicular to the line of sight), and hardly at all in the other (along the line of sight). Since we see the feature in two views which are separated by about 100 degrees of rotation, and the size of the feature is less than 350 km perpendicular to the line of sight on both occasions, our best guess at the true size of the feature is that it is less than 350 km in diameter in any dimension. The positions and extents were all taken from the SS data, but OS values are similar, as can be seen in Figure 3.6. The peak SS cross section in the area is $4.2\% \pm 0.2\%$ for day 1, and $7.9\% \pm 0.3\%$ for day 2. The difference in the values for the 2 days probably indicates that we are probing into different physical portions of the material causing the enhancement, i.e., different shadowed terrain. These are remarkably high cross sections when compared to the global values, especially considering the fact that the incidence angle at the pole is $\sim 80°$. The highest polarization ratio (ratio of SS to OS echo) in a pixel in the region is ~ 2.0 for the first day, and ~ 1.7 for the second day, and the ratio throughout most of the extent of the feature is > 1 (see Figures 3.5 and 3.6). This region is the only extended region with a polarization ratio > 1 in all of our experiments. That fact, coupled with the high cross section, make the north polar region truly unique.

These polarization ratio values are similar to those obtained for the Galilean satellites (Campbell *et al.* 1978; Goldstein and Green 1980; Ostro 1982), Titan (Muhleman *et al.* 1990) and the Residual South Polar Ice Cap (RSPIC) on Mars (Chapter 4, and Muhleman *et al.* 1991), all of which are icy bodies or areas. Re-

cently, similar behavior has been measured on parts of the Greenland ice sheet (Rignot *et al.* 1993). There are many moderately successful explanations for this phenomenon (high cross section and high polarization ratio) (Hapke and Blewitt 1991; Hapke 1990; Ostro and Shoemaker 1990; Goldstein and Green 1980), most of which involve penetration of the coherent radar signal into relatively lossless volumes (cold ices), and multiple scattering therein, or so–called "coherent backscatter." We propose that since the north polar feature on Mercury is exhibiting this effect, there may be deposits of ices there. Although the cross section values of the north polar feature are lower than for these other bodies, we believe this is due to the fact that the ices do not fill an observational resolution cell (i.e., there is incomplete areal coverage) or are covered by a thin absorbing layer, or both. The cause of the slightly depressed cross section will be discussed in more detail subsequently. If ices are the cause of the enhancement, the deposits should be at least several meters thick (see Muhleman *et al.* 1991, and section 3.4.4 below). The measurement of a feature at the south pole provides evidence for this interpretation. This feature can be seen clearly in the SS image of the 1994 data shown in Figures 3.2 and 3.3. The peak SS cross section of this feature is $\sim$ 6.6%. It has been shown that there are similar north and south polar features in 13–cm radar images taken from the Arecibo instrument (Harmon *et al.* 1994). The measurement of features in both polar regions seems to indicate that the polar environment (especially temperature) is crucial. Collection of volatiles in polar regions and permanently shaded areas of Mercury is certainly not a new idea (see e.g., Kumar 1976; Gibson 1977; and Killen *et al.* 1990), and the existence of ices in permanently shaded polar regions has even been suggested (Thomas 1974). The immediate question which comes to mind is: why did the Mariner 10 images of the north polar regions show no ice cap or deposits? Even though the illumination angle at the pole was poor (it always will be since the obliquity is near 0), and the resolution of the images was not very good (see the images in Davies *et al.* 1978), any large ice deposits would show up clearly as very bright regions. We will subsequently argue that

the reason there were no such regions is that the ice deposits are most probably in permanently shaded regions, and/or covered by a shallow layer of dust or soil. Thus, they would never be seen by any passive visual imaging device.

It should be stated that this is not a unique interpretation, but is the only one which seems to hold up under scrutiny. An alternate explanation is that these features are simply caused by extremely reflective regions, which also depolarize very efficiently (attributable to large amounts of multiple scattering on the surface or in the subsurface), similar to Maxwell Mons on Venus and the Tharsis (Chapter 4, and Harmon *et al.* 1992*b*) and Elysium (Chapter 4, and Harmon *et al.* 1992a) flows on Mars. However, these other structures are relatively young in age, and seem implausible on the ancient surface of Mercury. It is also very hard to get a polarization ratio > 1 with surface reflections alone, although it is possible with a surface resembling an ensemble of corner reflectors. The strongest argument against this interpretation is the existence of such features in both polar regions. It seems that the probability of getting such regions at both poles, and only at the poles, would be incredibly low. As another possibility, it seems logical that the cold polar regions would be collecting areas for most of the volatiles on Mercury. Verification of this in the case of sodium is provided by a measurement of a north polar enhancement in atmospheric abundance (Killen *et al.* 1990). If this enhancement is a common event, some net deposition of sodium may occur in the polar regions. It is not clear what will happen to the sodium upon interaction with the surface, but it may form salts. If this is the case, these salts may provide an enhancement for backscatter. Other volatiles may react with surface minerals to make even more exotic materials. Again, the most important argument against these types of materials being the cause for our feature is that they could not provide the polarization ratio signature which we observe. These types of materials will probably be considerably more lossy than can be allowed for coherent backscatter to occur. However, until more is known about the optical properties of salts and other materials at very low temperatures, they cannot be excluded

entirely from consideration.

3.4 Polar Ices

There are several things which must occur to facilitate the deposition of ice at the poles of Mercury. First, there must be a net gain of volatiles at the planetary surface which are capable of forming ices. Then, these volatiles must undergo transport to the polar regions, which must be cold enough to condense the volatiles. Once at the poles, the volatiles must remain stable on the surface. Any scenario involving ices will certainly involve H_2O, since it is the most stable of the normal solar system ices (see e.g., Yamamoto 1985). Therefore, in the following discussion we will concentrate on H_2O ice. Using values of the polar temperatures shown in Butler *et al.* (1993) (obtained from the model of Paige *et al.* 1992) it appears that the polar regions are cold enough to condense water vapor throughout the Mercurian year, so that will be assumed throughout the following arguments (see also Mitchell 1993). Furthermore, any permanently shadowed regions are certainly sufficiently cold.

3.4.1 Sources and Sinks

To investigate whether there is some net gain of H_2O on Mercury, the source and sink mechanisms must be examined. First, we will consider sources and sinks which are relatively constant for long time intervals. In the simplest case, there are 2 sources: flux from impacting meteoritic material and outgassing from the planet itself. There are also 2 sinks: photodissociation in the tenuous Mercurian atmosphere, and loss to (or accumulation in) the polar regions. On the Moon, solar wind interactions may account for some gain or loss of H_2O (Arnold 1979) where the gain is from interaction with the surface materials, freeing H_2O molecules, and the loss is from sputtering of surface molecules with subsequent dissociation in the atmosphere. This sort of source mechanism has also been postulated for

Mercury (Gibson 1977), but uncertainties are large owing to incomplete knowledge of Mercury's magnetosphere. It is known that Mercury does have a fairly well developed magnetosphere, however, so most of the surface is shielded from direct interaction with the solar wind (Hood and Schubert 1979), although localized interaction still takes place (Goodstein *et al.* 1981), mainly at the polar cusps and where the plasma sheet in the magnetotail intersects the nightside surface. These sorts of uncertainties make it very hard to quantify the amount of source or loss due to solar wind processes. Because of this difficulty solar wind processes will not be considered here. Input from large comets may also be an important source (Arnold 1979), but is highly variable, and we are considering constant sources and sinks for now. The loss terms mentioned above will be discussed first.

Assuming that the ice has been accumulating into circular polar regions over solar system time scales (1 billion years), the loss to the pole can be written as:

$$L_{pole} = 2\pi R_{pole}^2 D_{pole} \quad \text{kg/yr} \quad , \tag{3.3}$$

where the factor of 2 comes from the fact that the deposits will be at both the north and south poles, R_{pole} is the radius of the circular polar region in km, and D_{pole} is its depth in m. It has been assumed that the density of the accumulated ice is 1 g cm^{-3}. Using a value of $R_{pole} = 300$ km (this is much larger than our best guess size, but would give approximately the same surface area as the observed elliptical feature for either day), $L_{pole} \sim 5 \times 10^5 \; D_{pole}$ kg/yr.

The photodissociation loss term is given by:

$$L_{diss} = \frac{M}{\tau} \quad , \tag{3.4}$$

where M is the total atmospheric mass of H_2O and τ is the photodissociation timescale. The photodissociation timescale has been estimated at $\tau = 2 \times 10^4$ s for H_2O vapor at Mercury aphelion, with a global average value twice as great (Kumar 1976; see also Allen *et al.* 1987; and Cochran and Schleicher 1993). Using

the upper limit from the Mariner 10 UV occultation experiment of 8×10^{14} cm^{-2} for the H_2O density (Broadfoot *et al.* 1976), $M \sim 2 \times 10^7$ kg and so $L_{diss} \lesssim 3 \times 10^{10}$ kg/yr. These loss terms will now be compared to the source terms mentioned above.

The meteoritic flux can be estimated from a knowledge of lunar fluxes and a scaling relation to obtain fluxes at Mercury from them. Present lunar fluxes are in the range 1.5 to 2×10^{-9} g cm^{-2} yr^{-1} (see e.g., Gault *et al.* 1972; Zook 1975), and primitive lunar fluxes have been estimated to be as high as 3.8×10^{-9} g cm^{-2} yr^{-1} (Laul *et al.* 1971). We will adopt the primitive value of 3.8 and a scaling relation for the total fluxes of : $F_{mercury} = 5.5\ F_{moon}$ (Cintala 1992). This yields a total meteoritic source at Mercury of $\sim 2 \times 10^7$ kg/yr, which falls in the range estimated by Morgan *et al.* (1987). The implied source term is then $S_{meteor} \sim 2 \times 10^6$ kg/yr with the assumption that 10% of the infalling meteoritic material is H_2O, which may be possible if all of the meteorites were carbonaceous chondrites. This may be a conservative estimate, however, as it has been recently proposed that the present meteoritic flux on the Earth is $\sim 1.7 \times 10^8$ kg/yr (Ceplecha 1992), which may imply higher rates at Mercury. Estimates of the outgassing source term are very uncertain. If Earth values are scaled to an equivalent Mercury mass, the outgassing source rate could be as high as 3.6×10^{12} kg/yr (Kumar 1976). A similar scaling for Mars values yield rates as high as 7.5×10^{10} kg/yr (Greeley 1987), although the best estimate given there is less by a factor of 20. While not as high as the Earth values, this is still higher than the photodissociation loss term if the upper value is used. This indicates that there may indeed be a net source of H_2O at Mercury (polar accumulation will occur for any value of $S_{outgas} > L_{diss}$). If the outgassing source is enough to exactly counteract the atmospheric loss ($S_{outgas} \equiv L_{diss}$), then the depth of the accumulated polar ice from meteoritic input alone could be on the order of 5 m on the observed radar–bright ellipse, if all of the meteoritic water made its way to the polar regions. We will now show that this is not the case.

3.4.2 Migration

In order to investigate the poleward migration of H_2O, assume that once a molecule is on the surface, if it is in a region which is hot enough to sublimate it, it undergoes a number of random hops until it reaches a region cold enough for it to condense. If each of the hops can be described by a ballistic trajectory, then the time for an average hop is: $t = \sqrt{2}v/g$, where v is the travel velocity and g is the surface gravity, and the average distance travelled on each hop is: $D = \frac{1}{2}vt$. The probability of capture into a polar region on a single hop is:

$$P = K\ \gamma\ (1 - \alpha) \quad , \tag{3.5}$$

where K is the fractional surface area covered by the polar regions, γ is the accomodation coefficient, i.e., the probability that if a molecule encounters a polar region it is captured (assumed to be 1 hereafter), and α is the probability of being lost on a single hop, i.e., $\alpha = 1 - e^{-t/\tau}$(τ is the dissociation time from above). The average number of hops needed to get to a polar region will be $n = 1/P$. The total traversal time is then:

$$t_t = n\ t = \frac{t}{P} = \frac{t}{K\ e^{-t/\tau}} \quad . \tag{3.6}$$

Using the rms velocity for a Maxwellian gas of $v = \sqrt{3kT/m}$, with a temperature of 500 K, $t \sim 317$ s for H_2O. Using $\tau = 2 \times 10^4$ s and $K \sim 7.5 \times 10^{-3}$ (circular polar regions with radius = 300 km), then yields $t_t \sim 4.3 \times 10^4$ s. So, a fraction $e^{-t_t/\tau}$ molecules will make it to the polar regions, which turns out to be about 12% using the values of t_t and τ from above.

To verify this, we have carried out a simulation of this polar transport in which molecules were randomly placed on a spherical surface and allowed to migrate. Starting at some time t_o (when the random placement occurs), at each time step, if a molecule finds itself in a sunlit area, it is allowed to hop. Each hop occurs in a random direction, but the distance of each hop is fixed (at $D = \frac{1}{2}vt$). During the hop, a probability for loss is assigned ($P_{loss} = 1 - e^{t/\tau}$), where t is the time spent

during the hop ($t = \sqrt{2}v/g$) and τ is the photodissociation timescale from above. A random number (ξ) uniformly distributed between 0 and 1 is generated, and if $\xi < P_{loss}$ the molecule is lost during the hop. If the molecule is not lost and the hop places the molecule in a "stable" area, defined to be a fractional portion of circular regions around the poles, then that molecule is considered to be trapped there and is not allowed to hop again. The simulation is allowed to continue until all molecules are either lost to photodissociation or trapped in the polar regions. This simulation is explained in more detail in Appendix E. Results from this simulation indicate that about 5% of the molecules make it to the polar regions, which is close to the derived 12% value.

3.4.3 Stability

Once the H_2O molecules condense at the polar regions, they must remain stable there. The stability is determined by whether enough of the ice evaporates to counter the net condensation of ice at the poles. The maximum mass evaporation rate is (Estermann 1955; see also Watson *et al.* 1961):

$$\dot{E} = P_v \sqrt{\frac{m}{2\pi kT}} \quad , \tag{3.7}$$

where $\dot{E}$ is the evaporation rate, P_v is the vapor pressure of the water ice at temperature T, and m is the mass of the water molecule. Figure 3.7 shows a plot of the evaporation rate for water ice as a function of temperature, using values of P_v obtained in the following manner.

Bryson *et al.* (1974) present data values for the vapor pressure of H_2O ice from 131.8 K to 187.02 K. They also present fits to an equation of the form: $lnP_v = -A/T + B$, in two distinct temperature regions: $T \geq 153$ K, and $T \leq 153$ K. They make the break at 153 K on the assumption that the ice deposited at temperatures below this was amorphous ice (which they call "vitreous ice"), and a transition to cubic ice occurs at $\sim$ 150 K. This assumption is suspect, however,

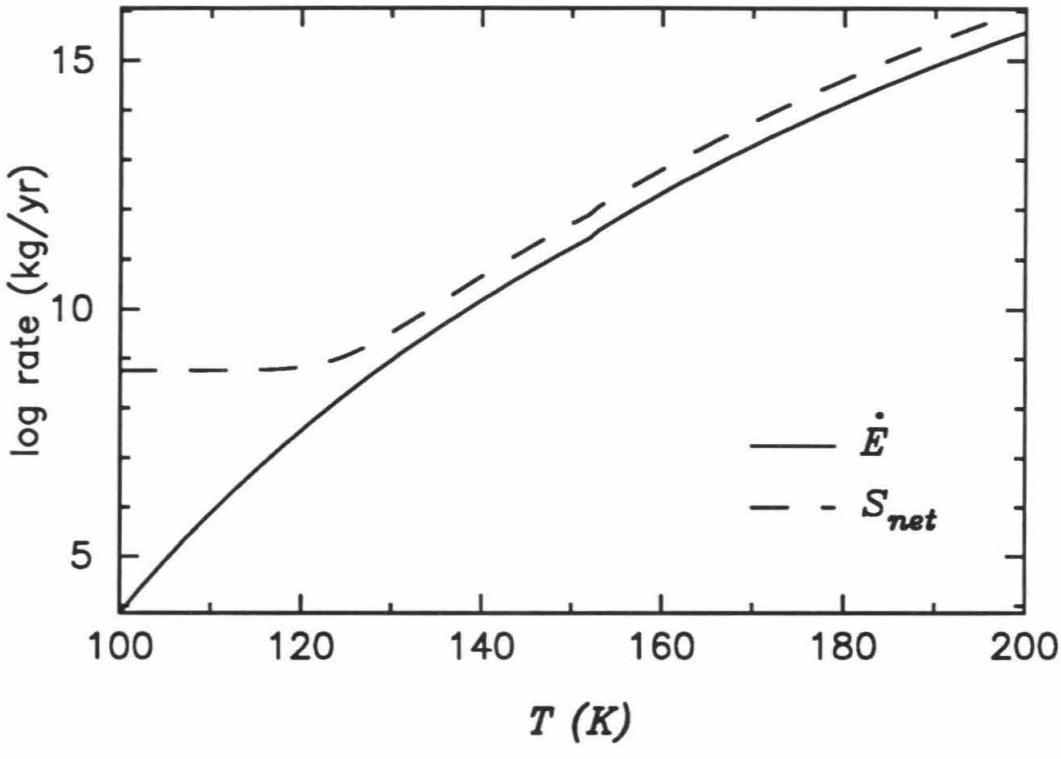

Figure 3.7: Plot showing the maximum evaporation rate ($\dot{E}$) as a function of temperature. Also shown is the net source rate needed to balance this evaporation rate in order to build polar deposits of 300 km radius and 50 m depth at both poles (see equation (3.8)).

Table 3.3

H_2O Vapor Pressure Fits

reference	Temp range (K)	A	B	χ^2
Bryson *et al.* (1974)	153–187	6143.0	24.0	0.4064
this work	153–187	6087.5	23.7	0.3416
Bryson *et al.* (1974)	132–153	5740.2	21.7	2.581
this work	132–153	5153.6	17.5	1.556
this work	132–187	5779.0	21.9	2.878

as the temperature of transition is strongly dependent upon rate of deposition and base temperature (Kouchi 1987; Hobbs 1974). Kouchi makes the statement that all of the ice deposited in the experiments of Bryson *et al.* was probably ice I_c. At any rate, using the tabulated values of pressure in Bryson *et al.* , we cannot duplicate the fits given in either range of temperatures by them. By using a fitting technique similar to that described in Appendix A, we have obtained our own set of fits to their data, shown in Table 3.3. Also shown in the table are the residuals of each of the fits, which are calculated via: $\chi^2 = \sum_i (ln(P_i) - (B - A/T_i))^2$ where the P_i are the tabulated vapor pressures at temperatures T_i in Bryson *et al.* . Unless there is some unequal weighting among the measurements which is not mentioned in Bryson, *et al.* , the discrepancy in the fits is significant. We tried fitting the entire temperature range, on the assumption that all of the ice was ice I_c in their experiments, and thus should have the same coefficients in the fit. That fit is also shown in Table 3.3, and it is clear that the fit is inferior to that with two distinct temperature ranges. We have thus chosen to use our new fit to the data in the two temperature ranges to calculate vapor pressures. The difference is significant for temperatures below about 120 K. At 120 K, the value of vapor

pressure from our fit is about a factor of 2 higher than the value from the Bryson *et al.* fit. This increases to a factor of 3 at 110 K, a factor of 5 at 100 K, and an order of magnitude at 90 K. The point here is that the vapor pressure of low temperature ice is very poorly known, and any attempt to make calculations based upon extrapolations of the measurements of Bryson *et al.* is compromised by this fact. We should also mention the recent work of Marti and Mauersberger (1993), who measured the vapor pressure of ice between temperatures of 170 K and 250 K. They mention there that the measurements of Bryson *et al.* are inapplicable, since they do not measure the vapor pressure directly. What they actually did was measure the sublimation rate, and then calculated the vapor pressure via equation (3.7). Although this may not be a true vapor pressure measurement, it is perfect for our calculations, since we are trying to get back to the maximum evaporation rate eventually anyway.

Note that the extrapolated pressures in Figure 3.7 (using equation (3.7) to get P_v from $\dot{E}$) are below the upper limit H_2O pressure from the Mariner 10 measurements ($P_{H_2O} \lesssim 10^{-13}$ bar (Broadfoot *et al.* 1976)) for values of temperature less than about 125 K. The plot in Figure 3.7 is appropriate for cubic ice, but some amount of the ice could be amorphous, since ice deposited ballistically on a surface colder than about 130 K has that form (Hobbs 1974; Kouchi 1987). The vapor pressure of amorphous ice can be as much as 2 orders of magnitude greater than that for cubic ice and varies greatly with the rate and temperature of deposition (Kouchi 1987). However, this form of ice is extremely fragile (Bar–Nun *et al.* 1987; Laufer *et al.* 1987), and forms in depths no more than on the order of microns to millimeters in the lab (see Kouchi *et al.* 1992 and references therein). As deposition continues beyond those depths, cubic ice forms above the amorphous ice. Also, the pressure under a meter of cubic ice on Mercury is about 3.7 kPa, certainly enough to destroy any fragile amorphous ice below. We therefore assert that the amorphous ice will be a very small fraction of the total volume.

The true net gain of H_2O at the pole can then be thought of as depending on

the relative rates of condensation and evaporation. The evaporation rate is given in equation (3.7). The condensation rate can be found by considering the total amount of volatile material available on the planet and how much of it gets to the pole. The amount is given by the addition of the sources above, along with an additional source due to any newly evaporated material since it is now available to be recondensed. Now, each of these sources must be multiplied by a factor which takes into account the amount of that available material which will make it to the pole. This in effect takes care of the loss (sink) from photodissociation. For the outgassing and meteoritic sources this factor (call it f_m) is exactly the fraction found in section 3.4.2, i.e., $f_m \sim 0.05$. For the evaporation source, this factor (call it f_e) should be close to 1, since most all material which is evaporated from the polar regions will recondense there after very few hops. To find this fraction, a migration simulation similar to that done above (explained in Appendix E) was carried out. In this simulation, however, instead of placing molecules at random on the planetary surface, they were all placed initially in the polar regions. After forcing each of the molecules to hop once, the simulation was allowed to continue as above. Results from this simulation indicate that about 85% of all molecules which are evaporated will find their way back to the polar region, i.e., $f_e \sim 0.85$. The net gain (or loss) at the pole is then:

$$L_{pole} = \dot{C} - \dot{E} = f_m S_{net} + f_e \dot{E} - \dot{E} = f_m S_{net} - (1 - f_e)\dot{E} \quad , \qquad (3.8)$$

where $\dot{C}$ is the condensation rate, and S_{net} represents the total net source of water. Equation (3.8) can now be used to solve for the required value of S_{net} for a given value of L_{pole}, assuming values for the factors f_m and f_e. This solution will obviously depend upon the evaporation rate, $\dot{E}$, and hence on temperature. Figure 3.7 shows a plot of S_{net}, using a value for the depth of the polar ice of 50 meters. Taking the value of $S_{net} = 3 \times 10^{10}$ kg/yr as the maximum possible source rate (to counter the maximum photodissociation loss rate) implies then that the

evaporation rate can be no more than about 10^{10} kg/yr for such polar deposits to be built. This in turn implies that the diurnal maximum temperature above which the ice will not collect quickly enough to build polar water ice deposits is slightly less than 140 K, even with this large net source. It was shown in Butler *et al.* (1993) (results from the model of Paige *et al.* 1992) that polar maximum temperatures may be as cold as 140 K only if the albedo of the surface is quite high, and even then only very near the pole. For an albedo of 0.85, the surface area with maximum temperatures less than 140 K is approximately equivalent to a circular cap of radius 30 km. This is much smaller than we think the true feature is. Also, the only reasonable way to get such high albedoes would be to have very smooth, clean, exposed ices directly on the surface. It will be argued subsequently that only one of these conditions is probably met, i.e., the ice is clean, but not exposed.

So, we have shown that ice deposits of many meters depth can be built up in the polar regions if the temperature is low enough and the net source rate is high enough. The scenario we have explored is probably significantly different from what is actually happening now, however. We have assumed that the outgassing and meteoritic sources and the photodissociation sink have been constant over the last billion years. While this may be true (or at least close) for the meteoritic source, it seems unrealistic for the outgassing source. Some volatiles may still be in the process of being degassed from the upper portion of the regolith, most notably sodium and potassium. However, outgassing which would provide the amount of water estimated above (e.g., volcanic) probably occurred and was shut off long ago on Mercury. With the knowledge that only about 5% of the molecules make it to the poles, our estimated meteoritic source could only make a deposit on the order of $\sim$ 5 cm in depth on each pole the size of our radar–bright ellipse. Even if our best guess size of 175 km is used as the size of the deposits, the deposits would only be on the order of 0.5 m. Thus it is probably the case that there is another source, or that the maximum diurnal temperature of the deposits must be colder

than 140 K.

Solar wind and cometary sources were mentioned briefly above, and these may be temporary sources of some amount of water which may be used to build the ice deposits. It has been estimated that the mass of water in a large comet may be as much as 10^{13} kg (Arnold 1979). However, it has been shown (Chyba 1987) that in the case of the Moon and Mars, nearly all of the volatile material from any cometary impact would be lost. The amount of volatile material retained on Mercury may be somewhat more (due to higher gravity) or less (due to higher average impact velocity). Ignoring the fact that most of the material may be lost, if somehow this entire amount could be deposited on one polar region the depth of the deposit would still be less than 10 cm. It would take 10 such events to build a 1 meter deposit! It has been estimated that only about 5 such events have happened on the Moon (Arnold 1979). With all of these considerations, it seems that normal cometary input would not supply the needed volume of H_2O. At any rate, with no resupply mechanism, any such deposit should soon be evaporated and eventually lost, even with temperatures as cold as our required 140 K. For cubic ice at 140 K, if all the evaporated ice were lost, then 1 meter of ice would be lost in about 40,000 years. We have shown above that most of the evaporated ice finds its way back to the cold traps, however (only $\sim$ 15% loss). With this aid, it would still take only about 250,000 years to evaporate a 1 meter deposit. Any ices built from solar wind source mechanisms would suffer this same fate. We are therefore led to the conclusion that it must be much colder than our derived temperature of 140 K in order to build ice deposits on the order of meters in depth.

Temperatures as cold as 100 K would have essentially negligible evaporation over solar system time scales (it would take about 100 billion years to evaporate 1 meter of material, even if all evaporated material were lost). If the water were condensing in such regions, then the source could be much less, as nearly all of it would be retained. This source rate will be estimated later. While regions on the nightside of the planet with temperatures as cold as 90 K have been measured

(Chase *et al.* 1976), they are quickly warmed as they are rotated into daylight. It seems that the only regions which will have maximum temperatures as low as 100 K are those which are permanently shadowed. Such regions will occur mostly in craters, and preferentially near the poles. It is not clear exactly how cold these areas would be on Mercury, but they may be as cold or colder than the measured coldest nightside temperatures (Paige *et al.* 1992; Ingersoll *et al.* 1992).

Estimates for the fractional surface area of the Moon which may be permanently shaded are as high as 5×10^{-3} (Watson *et al.* 1961), and this number may be higher on Mercury owing to the absence of any appreciable obliquity (assuming similar relief). Watson *et al.* also estimate that as much as 27.5% of all areas above 80° latitude are in permanent shadow on the Moon. Again, this number may be higher on Mercury. Much work has been done on the problem of lunar polar ices (see e.g., Watson *et al.* 1961; Arnold 1979; Lanzerotti and Brown 1981; Morgan and Shemansky 1991), where only the ices in permanently shaded areas are considered. There is still much controversy on the subject, but the most recent results seem to indicate that lunar polar ices would not be stable, due to the energy input from the H Lyα from the VLISM (Very Local Inter-Stellar Medium) which would vaporize any ices on the surface, even in permanently shaded areas (Morgan and Shemansky 1991). However, this assumes that the source is not strongly episodic, and that the H_2O ice on the surface is continually exposed to that radiation source. This problem is circumvented if even a tiny layer of absorbing material (dust or soil) is laid down on top of the ice deposit. This layer could be supplied by an impact event nearby, or by the gradual deposition of material from micrometeorite impacts nearby. Those ice deposits in the permanently shadowed regions of craters could also be covered up by material from the lip of the crater falling down. The covering layer would protect any underlying ice from impacting materials. If the layer is as thick as 10 cm, the probability that the underlying ice has been disturbed in the past billion years is very low (about 1%) if lunar values apply (Gault *et al.* 1974). The layer could present a problem for the radar

reflection, however, as it will absorb a fraction of the input energy.

3.4.4 Attenuation of the Radar Signal

Our data strongly indicate, and in light of the above arguments it seems reasonable, that ices could exist at the poles of Mercury. There is a problem with the absolute cross section values from the north polar region, however, which are in the range $\sim$ 4 to 8% at $\theta_i \sim 80°$. In comparison, the peak cross section of the RSPIC on Mars is $\sim$ 70% at $\theta_i \sim 67°$ (see Chapter 4). Since the RSPIC is known to have almost total coverage in its area and thought to be relatively pure ice, we will consider it to be the benchmark for comparison. Even though the upper portion of the RSPIC is thought to consist mainly of CO_2 ice, the optical constants are probably so similar for CO_2 ice and H_2O ice at centimeter wavelengths (see the discussion in Chapter 4, section 4.4.1.1 and references therein) that the difference in cross section should be negligible. So the polar region of Mercury has only about 5 to 10% of the cross section which it might have if it were entirely covered by exposed, relatively pure ice (neglecting incidence angle effects). This argues that the areal coverage is not complete, or the ice is contaminated, either by volume inclusions of absorbing materials or a covering layer of absorbing material, or some combination of these effects.

A covering layer may become a problem if it is too thick and too much energy is absorbed. In order to estimate this thickness, we have made a calculation for absorption in a dielectric layer above a perfect backscatterer. The resultant fraction of energy escaping in the direction of backscatter above the covering layer is:

$$f_{cl} = T_{12}\, T_{21}\, \frac{L}{1 - (R_{21}\, L)^2} \quad , \tag{3.9}$$

where T_{12} is the Fresnel transmittivity from space into the layer, T_{21} and R_{21} are the Fresnel transmittivity and reflectivity from the layer into space, and L is the 2-way loss in the layer. L is given by: $L = e^{-2\chi l}$, where χ is the absorption coefficient,

Table 3.4

Cover Layer Depths for 5% Cross Section

ρ (g cm^{-3})	ϵ_r	tan $\delta \times 10^3$	max depth (m)
0.1	1.077	0.587	4.09
0.5	1.429	2.75	1.13
1.0	2.000	5.34	0.551
1.5	2.088	8.24	0.320
2.0	4.000	12.0	0.192

ρ, density of the covering layer; ϵ_r real part of the complex dielectric constant for the material; and tan δ, loss tangent of the material, defined as the ratio of the imaginary part of the complex dielectric constant to the real part.

and l is the distance travelled in each direction in the layer. This distance is: $l = d \sec\theta_t$, where d is the depth of the layer, and θ_t is the transmission angle. This angle is found from Snell's Law: $\sin\theta_t = \frac{1}{n}\sin\theta_i$ where n is the index of refraction of the layer, and θ_i is the incidence angle. Table 3.4 shows depths for which 95% of the incoming energy is absorbed ($f_{cl} = 0.05$) for varying values of dielectric constant in the material, with $\theta_i = 80°$. For 90% absorption, ($f_{cl} = 0.1$), the depths in the last column should be multiplied by a factor of about 2/3. It is very hard to imagine what type of material may actually make up the layer, as the polar regions of Mercury undoubtedly collect many strange substances, but we have used a material with a dielectric constant of $\epsilon = 2.0 - i\,0.0107$ at a density of 1 g cm^{-3}, scaled to what we think may be representative densities. For materials with low absorption (loss tangent = $tan\,\delta = \epsilon_i/\epsilon_r < 0.003$, where ϵ_i and ϵ_r are the imaginary and real portions of the dielectric constant), maximum depths are on the order of a meter or more. For higher absorption materials (tan $\delta > 0.003$), the depths are less than 50 cm. It is not known what the general regolith depth

is on Mercury, but an estimate can be obtained by lunar analogy. Estimates for the regolith depth at the Apollo landing sites on the Moon range from 2 m to 15 m (Watkins and Kovach 1973). If the depth of the covering layer is as thick as 2 meters, then it must be very underdense in order for us to be probing beneath it.

During each subsurface scattering event, some amount of energy is absorbed by the scatterer. When many such events happen, too much energy may be absorbed by the scatterers. In order to evaluate when this may become a problem, assume that the ice deposits contain isotropic spherical scatterers of size on the order of our wavelength. The scatterers consist mainly of H_2O ice, but with some amount of absorbing materials included. Then the expected radar return is (Muhleman *et al.* 1991):

$$I = \frac{\varpi P_t A_t \Omega_b [H(\varpi, \mu)]^2}{16\pi\lambda^2 \Delta f D^2} \quad , \tag{3.10}$$

where parameters are as in equation (2.1), with the addition of ϖ, the single scattering albedo of the scatterers, and $H(\varpi, \mu)$ which are the H functions of Chandrasekhar (1960), with $\mu = cos\theta_i$. Setting this equal to equation (2.1) yields:

$$\varpi[H(\varpi, \mu)]^2 = 4\eta(\theta_i) \tag{3.11}$$

which can then be solved for ϖ, assuming a value of η. The range $0.05 < \eta < 0.1$, applicable to the north polar regions, yields values of the single scattering albedo of $0.19 < \varpi < 0.35$. If the absorbing material is described by a density of 3 g cm^{-3} with a complex dielectric constant of $7.0 - i\,0.42$ (a typical basaltic rock, see Campbell and Ulrichs 1969), then no corresponding limits can be placed on the volume fraction of the absorbing material in the scattering spheres, as even spheres consisting entirely of this type of material have a single scattering albedo of $\varpi \sim 0.63$, which is much higher than the calculated 0.35. This implies that the scatterers themselves will probably not absorb too much energy during scattering events. However, if the absorbing material is simply considered to exist mixed in with the surrounding matrix, absorption may still be significant during

propagation between scattering events. As in the consideration of the loss in any covering dielectric layer, the absorption is given by: $L = e^{-\chi s}$, where χ is again the absorption coefficient, and s is now the total distance travelled in the ice layer.

To estimate s, a Monte Carlo method similar to that used in Muhleman *et al.* (1991) was used, but with modifications. Photons were allowed to penetrate the upper surface of an ice layer at a given incidence angle. The photons were then scattered conservatively and isotropically a number of times until they left the upper surface. The total distance travelled by each photon was recorded, and after many photons were considered, an average of these distances was taken. This average value is then the best guess for the total travel length in the layer. If the propagation distance after the initial penetration is denoted by $d_{scat}^{(0)}$, and after the first scattering event is denoted by $d_{scat}^{(1)}$ and so on, then the propagation distance in step i can be found from (Kalos and Whitlock 1986):

$$d_{scat}^{(i)} = \frac{-ln(\xi^{(i)})}{\Sigma} \quad , \tag{3.12}$$

where the $\xi^{(i)}$ are independent pseudorandom numbers uniformly distributed on (0,1), and Σ is the probability per unit length for any interaction. This probability can be written:

$$\Sigma = \pi \; r_{scat}^2 \; N_{scat} \; \kappa_{ext} \tag{3.13}$$

for uniform sized spherical scatterers, where r_{scat} is the radius, N_{scat} is the number density and κ_{ext} is the extinction efficiency of the scatterers. The total length then travelled by the j^{th} photon is given by:

$$s^{(j)} = \sum_{i=0}^{M} d_{scat}^{(i)} \quad , \tag{3.14}$$

Table 3.5

Travel Length in an Ice Layer

$N_{scat}(\mathrm{m}^{-3})$	P	$\langle s \rangle$ (m)	d_{95} (m)	$\frac{\lambda}{2\pi<s>} ln(\frac{1}{\eta}) \times 10^2$
55	0.01	76	45	0.017
165	0.03	28	15	0.046
550	0.1	8.1	4.2	0.16
1650	0.3	2.8	1.4	0.46

N_{scat}, density of scatterers in the ice layer; P, packing fraction in the ice layer, or ratio of volume of scatterers in a unit cube to the volume of the cube; $\langle s \rangle$ average distance travelled in the ice layer; and d_{95}, depth beyond which 95% of the photons did not go in the ice layer.

where M was the total number of scattering events before the photon escaped from the upper boundary of the layer. Then the expected value of the length is:

$$\langle s \rangle \sim \frac{1}{J} \sum_{j=1}^{J} s^{(j)} \quad , \tag{3.15}$$

where J is the total number of photons used in the simulation. Table 3.5 shows values for $\langle s \rangle$ for varying values of N_{scat}, with $\theta_i = 80°, r_{scat} = 3.52$ cm and $\kappa_{ext} = 3.38$. Table 3.5 also shows the revised estimates of the minimum depth of an ice layer which would reflect at least 95% of the incoming energy, which can be compared to values in Table 3.4 of Muhleman *et al.* (1991). It is clear that large distances are travelled in the ice layer, making the possibility of appreciable absorption likely. In order to make sure that not too much energy is absorbed in the contaminated ice layer, the relation $e^{-\chi s} > \eta$ (the cross section) must hold. This implies that:

$$\frac{\epsilon_i}{\sqrt{\epsilon_r}} < \frac{\lambda}{2\pi s} ln\left(\frac{1}{\eta}\right) \quad , \tag{3.16}$$

where ϵ_r and ϵ_i are the real and imaginary portions of the complex ice layer dielectric. The dielectric constant of a layer composed of a mixture of ice and and absorbing material can be written (Kharadly and Jackson 1953):

$$\epsilon = \epsilon_1 + \frac{3V\epsilon_1\left(\frac{\epsilon_2-\epsilon_1}{\epsilon_2+2\epsilon_1}\right)}{1-V\left(\frac{\epsilon_2-\epsilon_1}{\epsilon_2+2\epsilon_1}\right)} \quad , \tag{3.17}$$

where ϵ_1 and ϵ_2 are the complex dielectric constants of the ice and the absorbing material, respectively and V is the volume fraction of the absorbing material. Table 3.6 shows values of ϵ, and $\epsilon_i/\sqrt{\epsilon_r}$ for various values of V, assuming an absorbing material dielectric constant as above $(7.0 - i0.42)$ and an ice dielectric constant of $3.2 - i3.2 \times 10^{-4}$ (Evans 1965). In order for the cross section, η, to be 5%, the number in the last column of Table 3.5 should be greater than the number in the last column of Table 3.6, for a given V and N_{scat}. In comparing the last columns of Tables 3.5 and 3.6, it is clear that even for small values of the volume fraction, too much energy will be absorbed for all reasonable values of N_{scat}. Therefore, the ice layer itself must be very pure, i.e., V is less than about 0.05 (5%). This probably indicates either that the ice was deposited in a relatively short period of time, or has some method of cleaning itself. It is not clear what sort of source mechanism could supply this much water in a short period. A very large comet could possibly do it, but the relative velocity between it and Mercury would have to be very low. It is also not clear how the ice could clear itself of the silicate inclusions. In the case of Mars this can occur through the repeated sublimation and condensation of the ice (leaving a dust lag). However, this mechanism would not work on Mercury, as once the ice deposit is formed in a permanently shadowed region, it never sublimates.

3.4.5 Conclusions Concerning Polar Ices

Our conclusion is that ices (at least H_2O) do exist at the poles of Mercury, but not in the form of totally exposed, uniform coverage ice caps. The ice deposits are

Table 3.6

Absorption by Mixed Ice and Silicates

V (%)	ϵ_r	$\epsilon_i \times 10^2$	$(\epsilon_i/\sqrt{\epsilon_r}) \times 10^2$
1	3.23	0.25	0.14
2	3.25	0.47	0.26
3	3.28	0.69	0.38
4	3.31	0.91	0.50
5	3.34	1.1	0.62
7	3.39	1.6	0.87
9	3.45	2.1	1.1
11	3.51	2.6	1.4
14	3.60	3.3	1.7
17	3.69	4.1	2.1
20	3.78	4.9	2.5
25	3.93	6.3	3.2

V, the volume fraction of the silicates in the mixture; ϵ_r, the real part of the complex dielectric constant; and ϵ_i, the imaginary part of the complex dielectric constant.

at least tens of meters in depth, probably formed relatively rapidly in permanently shaded regions, and were subsequently covered over by a shallow layer of dust or soil. Other ices may also collect in the same way, and contribute to our observed signal, depending on how cold it really is where the ices are being deposited. For example, using equation (3.7) with values of vapor pressure for CO_2 at 100 K (Brown and Ziegler 1980), 1 meter of CO_2 ice would be lost in about 5 years (with 15% of evaporated material lost). Even at 70 K, a meter would be lost in about 4 million years (again with 15% loss). Obviously, for solid CO_2 to be a part of the ice deposits, the temperature would have to be very cold.

The reduced cross section of the deposits can be explained by the combination of the patchiness of the ice coverage and absorption by the materials either within or on top of the ice deposits. The total cross section of a region containing such deposits can be written:

$$\eta = \eta_{ice}(1 - f)\ A_{ice} + \eta_0(1 - A_{ice}) \quad , \tag{3.18}$$

where f is the combined fraction of energy absorbed in the covering layer and the ice layer, A_{ice} is the fractional area covered by ices and η_0 is the background Mercurian cross section (at the incidence angle of the pole). Figure 3.8 shows a plot of the parameter space of A_{ice} and f which would allow a measurement of $\eta = 0.05$ or 0.1, assuming a background cross section of $\eta_0 = 3.0 \times 10^{-3}$, i.e. equation (3.1) with $A_{ss} = 2.4\%$ and $n = 1.25$. It was assumed that $\eta_{ice} = 1.0$. Examination of Figure 3.8 shows that even if as much as 80% of the incoming radiation is absorbed, the ice area coverage only needs to be on the order of 30%. The maximum depth from the d_{95} column of Table 3.5 can be used along with the coverage fraction to find an estimate for the upper limit on how much ice was really needed to build the polar ice deposits. The largest minimum depth from Table 3.5 is about 50 m, and using a value for A_{ice} of 0.275, the total volume of ice needed for the two ice caps of radius 300 km is $V_{ice} \sim 8 \times 10^3$ km^3, which implies a total mass loss to

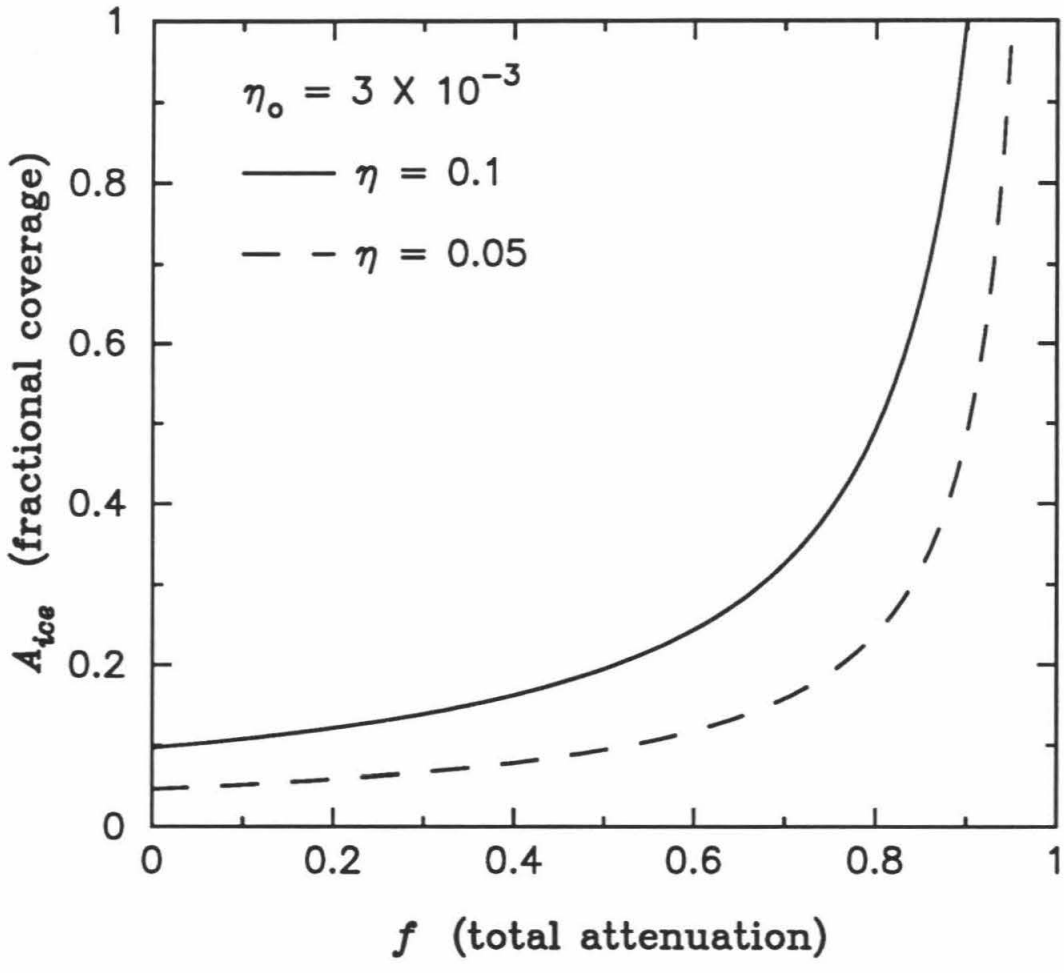

Figure 3.8: Plot showing the tradeoff between attenuation of the radar signal in the ice structures and the fractional areal coverage of such structures.

the poles of: $L_{pole} \sim 8 \times 10^{15}$ kg. This number is reduced by about a factor of 3 if our best guess size of the polar feature is used (radius $\sim$ 175 km). Note that this coverage fraction could be supplied by permanently shadowed regions alone if the estimate of 27.5% (Watson *et al.* 1961) is valid at Mercury. Note also that this supply rate ($\sim 3 \times 10^6$ kg/yr for a 175 km feature) is about equal to the estimated meteoritic source supply rate. Again, it does not seem unreasonable that we have probed polar ice deposits on Mercury.

3.5 "Basin" Features

There are several very large (> 500 km in at least one dimension) quasi–circular features seen in the SS images. We have chosen to call these features "basins," but only because of their large size, and somewhat circular appearance. We are not implying that the actual surface features must be basins in the geological or morphological sense, although that does remain a possibility for all but one of the features. The characteristics of these basin features are shown in Table 3.7. The sizes shown in that table are estimated from the half–power extent of each feature after model subtraction. The SS features can be seen clearly in Figures 3.2 and 3.3, and in Figures 3.9 and 3.10. Figure 3.9 is a Mercator projection of some of the data from Figure 3.3 into the planetary coordinate system, for latitudes between $-65°$ and $65°$ for each of the polarizations and each of the experiments separately. Figure 3.10 is a similar projection of an average of all of the SS images from Figure 3.3. The weights in the average were calculated as indicated in Appendix A, section A.1.4. Figure 3.9 shows that basins 2, 3 and 5 also have associated OS enhancements, with peak polarization ratios on the order of 0.5. It is not clear if the other two basins have associated OS enhancements, as they are very near the subearth point (in the specular spike).

The enhanced radar cross section of basins 2 and 3 was previously noted by Goldstein (1970, 1971) where he called them "spectral salients." The doppler data

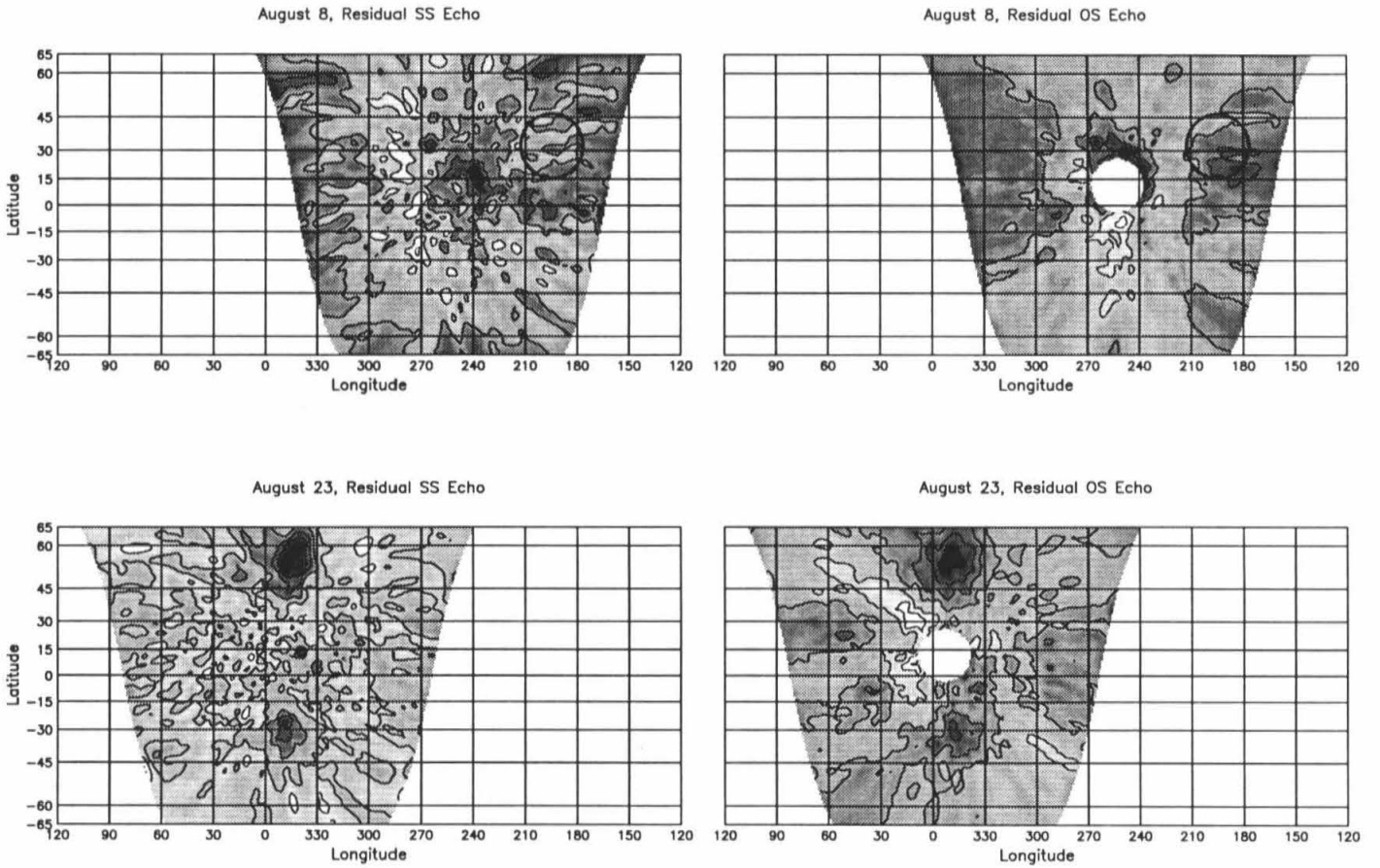

Figure 3.9 : Mercator projections of the residual radar cross section images for the 1991 experiments shown in Figure 3.3. Contours are at 3 σ levels for all of the projections, (negative contours are dashed). Darker shades are higher residual cross sections. The darkened circle on the August 8, 1991 projections shows the approximate location of the rim of the Caloris basin.

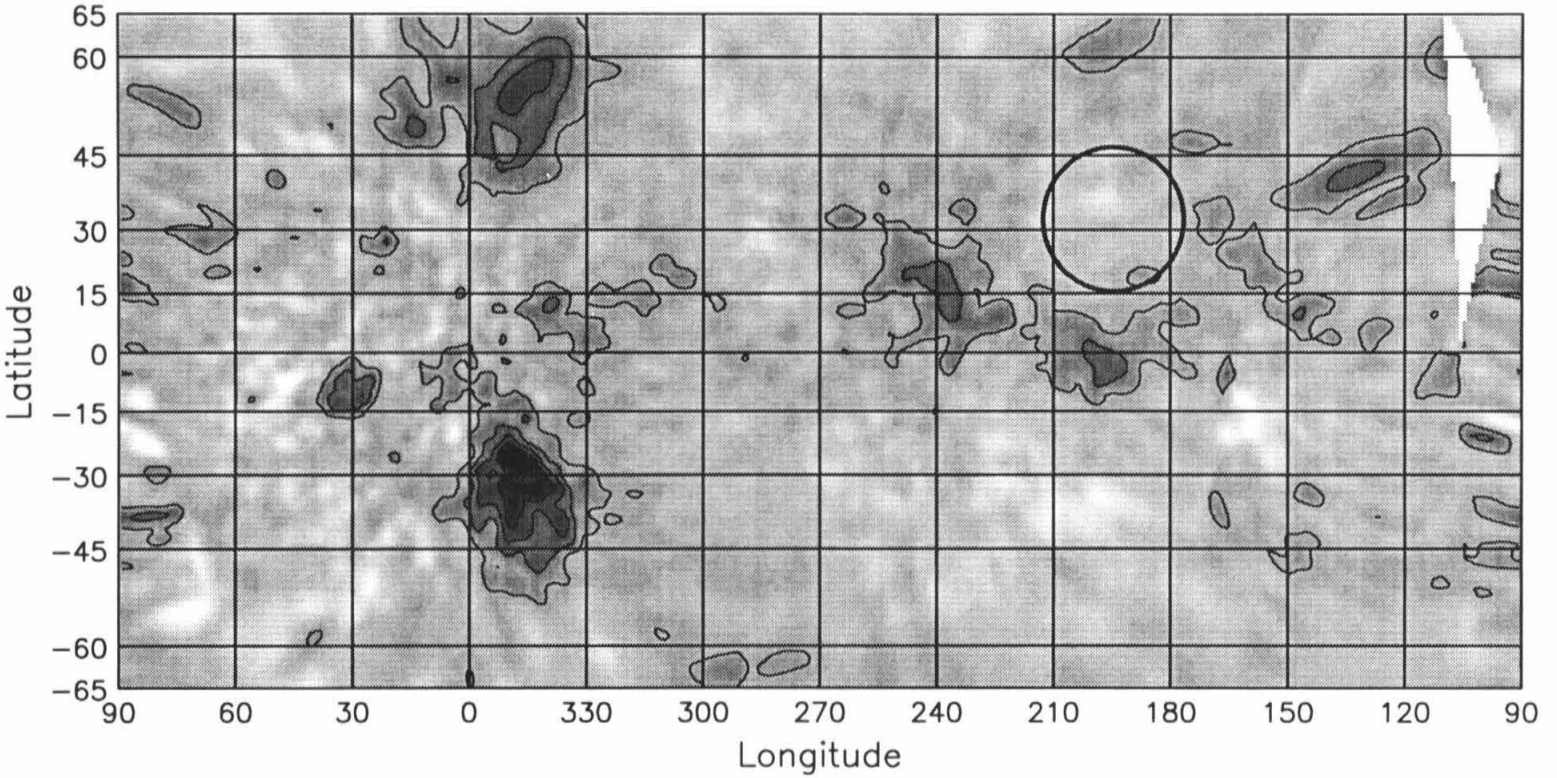

Figure 3.10 : Mercator projection of the average of the residual SS radar cross section images shown in Figure 3.3. Contours are at $1\sigma, 3\sigma, 5\sigma, 7\sigma$, and 9σ, where σ is estimated to be $\sim 0.3\%$. Darker shades are higher residual cross sections. The darkened circle shows the approximate location of the rim of the Caloris basin.

Table 3.7

Mercury "Basin" Features

basin number	date observed	peak cross section	central longitude	central latitude	incidence angle	size (km)
1	8/8/91	3.8% (1.8%)[a]	238.3°	+17.2°	15.5°	330 X 760
2	8/23/91	5.9% (4.2%)	347.9°	+55.0°	44.2°	410 X 590
3	8/23/91	4.7% (3.0%)	348.6°	−28.7°	40.0°	410 X 610
	2/21/94	7.4% (4.7%)	350.9°	−25.6°	27.9°	1040 X 1160
4	11/23/92	6.2% (2.5%)	197.3°	−3.5°	2.6°	610 X 710
5	8/23/91	2.8% (1.3%)	34.4°	−12.7°	47.0°	390 X 600
	2/21/94	6.6% (3.4%)	27.9°	−11.4°	12.1°	500 X 500

[a] numbers in parenthesis are peak cross section after model subtraction

collected in those experiments was north–south ambiguous, and thus the feature was thought to be one feature at $\beta \sim 353°$ and $\phi \sim \pm 52°$, where the $\pm 52°$ indicates that the feature could be north or south of the equator. It was impossible to know at that time that the feature was actually two features on either side of the equator! Goldstein noted the position of one other spectral salient located at $\beta \sim 245°, \phi \sim \pm 41°$. This corresponds closely to the longitude of basin 1, but the latitudes are significantly different. A smaller area of enhanced cross section (diameter $\sim$ 100 km) centered at $\beta \sim 246°, \phi \sim 11°$ was found in later, higher resolution delay–doppler experiments (Zohar and Goldstein 1974). This area must contribute to the cross section enhancement of basin 1.

The only one of the features which is in the hemisphere photographed by Mariner 10 is basin 5. This feature is very prominent in the Feb. 21, 1994 data (see Figure 3.9). The center of this feature is near the Kuiper crater (Kuiper is centered at $\phi \sim -11°, \beta \sim 32°$). The Kuiper crater and its environs were also visible in the Aug. 23, 1991 images. The feature is more subdued, as it is at significantly

higher incidence angle, but it is clearly there in both polarizations (see Figure 3.9). Kuiper is a very fresh, bright rayed crater, and the radar enhancement may be due to the fact that the rocks at size scales appropriate to scatter the radar wave (centimeters) have not had time to be pounded into powder (regolith), and can multiply scatter the incoming waves effectively. This effect has been proposed to explain the radar backscatter enhancements from some of the bright rayed craters on the Moon, most notably the Tycho crater (Thompson 1974; Zisk *et al.* 1974).

While the possibility remains that all of the other basins are in terrain similar to the Kuiper basin area, there are indications that this is not the case. There are many other bright rayed craters in the photographed hemisphere, none of which have a significant radar backscatter enhancement. Also, if basins 2, 3 or 4 were caused by a bright rayed crater, some of the rays should be visible in the Mariner 10 images. This is not the case, indicating that these basins are probably not caused by this mechanism.

An alternative is that these enhancements are indeed the signatures of large impact basins similar to the Caloris basin. It has been proposed that a possible mechanism of getting Mercury into its current 3:2 spin orbit coupled state is through many large impacts (Boyce and Stevenson 1991). If this is the case, the basins resulting from such impacts must be either completely obliterated, or on the unphotographed hemisphere, as there is a relative lack of large impact basins on the photographed hemisphere of Mercury when compared to the Moon (Murray *et al.* 1974). We may be seeing the indications of several such large impact basins. In order to test this hypothesis, the backscatter characteristics of the Caloris basin must be examined.

The Caloris basin and its immediate environs were visible during two of our five experiments. On August 8, 1991, it was on the eastern limb, providing only a nominal look at the region. However, on November 23, 1992, we had an excellent view of the entire region, and indeed this date was chosen for that fact. Figures 3.9 and 3.10 show the approximate location of the rim of the basin on the appropriate

projections. It can be seen from these figures that there seem to be cross section enhancements encircling the basin in the residual SS images, with no enhancements in the interior. Indeed, basins 1 and 4 are part of this ring of enhanced backscatter surrounding Caloris, both nearly within 1 Caloris diameter of the rim. However, in the residual OS image for August 8, 1991 (see Figure 3.9) the enhancement encompasses a portion of the interior of the basin, and extends outward mainly to the southeast. It is not surprising that there might be an enhancement of OS cross section from the eastern rim of Caloris during this experiment, as it would have had many more facets facing the radar (from the basin walls) than expected for a surface with no relief, i.e., we were seeing the signature of the back wall of the Caloris basin.

The OS enhancement from the adjacent material is more puzzling. The enhancement occurs mainly in the Odin Planitia and Tir Planitia geologic units (McCauley *et al.* 1981). This material is what has been termed "smooth plains" material, and whether it is of volcanic or impact origin is unknown (Kieffer and Murray 1987). In the impact case, the enhancement may be due to the large numbers of subsurface scatterers which would be laid down along with the covering material. In this case, the materials should encircle the Caloris basin, and should have basically the same radar signature at all locations. This may be what we are seeing in the residual SS images. Local concentrations of scatterers (rocks, blocks, etc...) could then be the cause of the cross section enhancements of basins 1 and 4. In the volcanic case, the enhancement may be due to enhanced surface roughness, similar to the Tharsis and Elysium volcanic deposits on Mars. In the impact case, one would expect to see OS enhancements encircling the entire basin. This signature is not seen, making a weak argument in favor of the volcanic origin of the smooth plains material. In this case, the volcanic material could have flowed out of only the eastern portion of the basin, forming the smooth plains there. It is not clear why there should be an OS enhancement in the interior of the basin, but no SS enhancement. The ground there should be incredibly broken up, providing

many scattering sites for the incident radar wave. Enhancements would then be seen in both polarizations. The lack of such enhancements in the SS data from 1991 may simply be a look angle effect, since the basin was so near the limb, but the 1992 data cannot be explained by this effect.

All of this evidence indicates that none of our basins are really similar to the Caloris basin. Basin 5 is clearly not a large impact basin, and is probably related to the Kuiper crater. Basins 1 and 4 are probably related to Caloris, whether through ejecta material, or subsequent volcanic activity. The interior of Caloris has no backscatter enhancement, indicating that basins 2 and 3 are not similar to it. The question then remains, what could basins 2 and 3 be? The locations of basins 2 and 3 correspond closely to positions of two of the "emission patches" reported in Potter and Morgan (1990), where enhanced atmospheric sodium was measured. They attribute the enhanced atmospheric sodium abundance to magnetospheric effects, since the emission patches usually occurred in north–south pairs. An alternative explanation for atmospheric enhancements of sodium and potassium has been proposed by Sprague *et al.* (1990) after measurement of a potassium enhancement over the Caloris basin. They claimed that their atmospheric enhancement was due to increased diffusion and degassing in the surface and subsurface of the Caloris basin due to its cracked and fractured nature. There is still considerable disagreement over the cause of the atmospheric enhancements (see e.g., Sprague 1992; Killen and Morgan 1993). After the 1991 experiments, we proposed that basins 2 and 3 may be similar to the Caloris basin, since they were all tenuously related through the atmospheric enhancements, and if the Sprague *et al.* explanation was the correct one, then the highly cracked and fractured ground could provide an enhancement in backscatter. However, as shown above, the 1992 data clearly show that there is no enhancement in the interior of the Caloris basin, making similarity with basins 2 and 3 improbable. Because of this, our data cannot be used in support of either of the hypotheses for the atmospheric enhancements. However, basins 2 and 3 may still be in some way related to the

enhancements, as it is not clear what the effect of net deposition of significant amounts of sodium and potassium in such areas would be on our radar data. If either reacts with surface rocks to make salts, increased backscatter could result.

The most likely explanation for basin 3 is that it is related to the Caloris impact, but not in the same way as basins 1 and 4. The location of the basin is near the antipode of the Caloris basin, which is located at $\phi \sim -30°, \beta \sim 15°$. It is believed that seismic focusing from the impact which created the Caloris basin caused ground movements of up to 1 km, highly fracturing the surface there (Hughes *et al.* 1977; see also Watts *et al.* 1991). If this is the case, the incredibly fractured surface which would result could provide the backscatter enhancement we see. The explanation for basin 2 still remains somewhat of a mystery.

3.6 Other Features

There are many other interesting structures which can be seen in both the SS and OS residual projections of Figure 3.9. Only the features in the 1991 data will be discussed here, as there was insufficient time to study the others. The features from August 8, 1991 will be discussed first. There seems to be a feature near to but distinct from basin feature 1. This feature appears in both the SS and OS images, and is centered at $\phi \sim 33°, \beta \sim 265°$. It is the only feature which appears in both polarizations on that day, with the possible exception of the basin feature. There is a feature extending from approximately longitude 320° to longitude 360° in the SS image which is undoubtedly the signature of basin feature 2, which was just barely visible on the western limb. The only other significant features in the SS image are the ones mentioned in the above section which somewhat encircle the Caloris basin. Their centers are at: $\phi \sim 7°, \beta \sim 209°; \phi \sim -2°, \beta \sim 196°; \phi \sim -4°, \beta \sim 175°; \phi \sim 48°, \beta \sim 173°$; and $\phi \sim 62°, \beta \sim 199°$. The two westernmost of these features may be compared with Mariner 10 photographic images, which show that they both lie in areas consisting

of smooth plains material.

There are many features in the images from August 23, 1991. Enhancements in the SS image which are in the mapped hemisphere include one which is north and west of the Monet crater (Monet is centered at $\phi \sim 44°, \beta \sim 10°$), which may be associated in some way with basin feature 2, and one which encompasses the interior and rim of the Ts'ai Wen–Chi crater, and extends to the north and northwest of it (Ts'ai Wen–Chi is centered at $\phi \sim 24°, \beta \sim 23°$). The only enhancement other than the basin features in the OS image in the mapped hemisphere is just north and west of Lermontov crater (Lermontov is centered at $\phi \sim 16°, \beta \sim 49°$). In the unmapped hemisphere, there is a collection of enhancements in a region between basins 2 and 3, and extending to the east. Those in the SS image are centered at: $\phi \sim -13°, \beta \sim 340°$; $\phi \sim 3°, \beta \sim 331°$; and $\phi \sim 19°, \beta \sim 306°$. In the OS image, the enhancement is centered at $\phi \sim -7°, \beta \sim 333°$.

3.7 Conclusions

It seems clear from these measurements that Mercury has a very diverse surface and subsurface. Our radar measurements show structure on scales from a little more than 100 kilometers to more than 1000 kilometers. The small scale structure seems mostly to be associated with craters and crater complexes where it can be compared directly to photographic results from Mariner 10 and the associated geologic maps. Unfortunately, all but one of the larger structures are in unphotographed areas, and thus cannot be linked with any sort of ground truth. The one basin in a region photographed by Mariner 10 is centered near the Kuiper crater, and is probably related to its ejecta. The explanations for the other large structures remain speculative, but there is some basis for an explanation for all but one of them. Two of the structures are near enough to the rim of the Caloris basin that they are probably related either to its ejecta, or subsequent volcanism. The other structure is probably related to the Caloris impact through the seismic

focusing at the antipode. Future imaging of the surface of Mercury is the only way to answer the questions about what these large structures actually represent.

The most interesting structures probed by us were features near and including the north and south poles. The polarization characteristics and signal strength of these features indicate that ices exist in some quantity in the polar regions of Mercury. The most likely explanation is that these ices exist in permanently shaded areas at these high latitudes, where it can be very cold, and the ices can be stable over solar system time scales. The ices must be relatively clean, implying that deposition probably occurred relatively rapidly. Because of the relatively low absolute cross section when compared to radar returns from other icy bodies, the ices are also probably covered by a shallow layer of dust or soil, or areal coverage is incomplete, or both. More measurements with these features visible will help to better constrain their size and cross section characteristics. These measurements should also revive some interest in searching for ices in the lunar polar regions.

Chapter 4

Mars

4.1 Observations

We observed Mars twice in the fall of 1988, and twice in the winter of 1992/93. The physical and geometric parameters for all of the experiments are shown in Table 4.1, along with the calibrators used. All of these experiments were conducted when the VLA was in its A configuration, or when the antennas are most spread out, with the exception of the first 1988 experiment. In the A configuration, the maximum antenna separation is $\sim$ 36 km, producing a fringe spacing of $\sim$ 0".2 on the sky. The first experiment in 1988 was conducted with the VLA in its D configuration, which is the most compact, i.e., yielding the lowest resolution, but the highest signal to noise ratio. The subearth longitude range from $\sim$ 196° to $\sim$ 337° was to be covered by an experiment on Dec. 9, 1992, but serious transmitter problems made the data from that experiment unusable.

Calibrations and data processing proceeded as described in Chapter 2, except for the following. Due to the relatively rapid rotation of Mars, the radar echo energy was spread over several spectral channels in the center of our observed bandwidth. The frequency spread of Mars at our center frequency was $\sim$ 28 kHz, yielding $\sim$ 9 channels of 3052 Hz width, or $\sim$ 5 channels of 6104 Hz width. This rapid rotation made it necessary to split each data set into a number of "snapshots"

Table 4.1

Experimental Information for Mars

date	9/13/88	10/22/88	12/29/92	1/12/93
VLA configuration	D	A	A	A
subearth longitude, β_o	79.7 – 196.4	39.2 – 159.4	81.6 – 193.6	337.3 – 65.1
subearth latitude, ϕ_o	-20.4	-23.7	+9.0	+6.5
phase angle, α	13.7	20.0	8.6	4.4
position angle, ψ	329.0	332.9	345.7	342.4
geocentric distance, D (AU)	.40	.46	.63	.63
solar longitude, L_s	271.1	295.1	18.2	24.8
center frequency, ν_o (MHz)	8495	8495	8510	8510
channel width, $\Delta\nu$ (kHz)	1.526	3.052	3.052/6.104	3.052
transmit power, P_t (MW)	350	230/350	440	440
phase calibrator flux (Jy)	P0106 2.27	0006–063 1.61	0748+240 1.05	0748+240 1.05
amplitude calibrator flux (Jy)	3C48 3.28	3C48 3.28	3C286 5.24	3C286 5.24
bandpass calibrator	P0106	0006–063	3C84	3C84
CLEAN beam diameter (asec)	na	0.3 – 0.91	0.3 – 0.41	0.3 – 0.5

before the self–calibration step in the calibration, to reduce longitudinal smear. The duration of the snapshots was chosen such that a surface point would not rotate through a distance more than the width of the synthesized beam, which is the effective resolution cell size. This duration turned out to be between 10 and 15 minutes. This also effectively determined the desired channel width for the observations, as it was not desirable to have a location on the surface rotate through an entire spectral channel in a snapshot. Each of the individual snapshots had to be processed separately from the self–calibration on.

The procedure of CLEANing the images was more complicated for Mars than for Mercury. In these experiments, the CLEAN beam width varied from $\sim 0".25$ to $\sim 0".91$, with the smaller widths on each date occurring when Mars was near zenith and the larger occuring when it was near the horizon. Rather than map all of the snapshots at the same resolution, which would have necessarily been the worst resolution, we decided to map each of them with a resolution given by either $0".3$, or the intrinsic synthesized beam width, whichever was larger. The small size of some of the synthesized beams made it necessary to have a pixel size of $0".1$, in order to sample the central lobes well. Now, we had already CLEANed the data from the second 1988 experiment, but at a pixel size of $0".2$, and a resolution of $0".5$ (see Muhleman *et al.* (1991), which discusses the SS data). In order to get the highest resolution possible, we decided to reduce these data again.

The initial CLEAN model was obtained by using a combination of a best–fit model from the old, lower resolution 1988 SS data, with a default model for sky positions which corresponded to Martian latitudes, ϕ, and longitudes, β, not viewed in 1988. To obtain the best–fit model, we formed a set of measurements as a function of surface position, given information on viewing geometry from the very accurate JPL ephemeris. This set was then fit in a least squares sense to a sensible backscatter model (see Appendix A, sections A.1.1 and A.1.2). In the SS polarization, the model was a simple cosine model. In the OS polarization, we found that a fit to a singular backscatter model produced unacceptably large

deviations at large incidence angles ($\theta_i \gtrsim 20°$). For this reason, we adopted a hybrid backscatter model, with Muhleman model (Muhleman 1964) form for $\theta_i \leq 20°$, and cosine model form for $\theta_i > 20°$ (similar to the SS polarization). The cosine portion of the OS echo has been referred to as the "diffuse" echo, while the Muhleman portion has been referred to as the "quasi–specular" echo. For the default SS model, we used $\eta = 0.06 \cos \theta_i$, where η is defined by equation (2.1). The model for the cosine portion of the OS polarization was $\eta = 0.1 \cos \theta_i$. A fit was done to the visibilities of the central channel for each snapshot to find the appropriate parameters for the Muhleman model portion (see Appendix A, section A.2.2). In practice, the final CLEANed image was only affected very slightly by the choice of the default backscatter model, as expected.

The construction of the initial CLEAN model had to also take into account the frequency response of the individual channels with which we had resolved the disk. The initial CLEAN model for polarization p, as a function of position on the sky (x, y), and frequency channel (f) was then calculated via:

$$M_{pf}(x, y) = F_f(x) \cdot S_p(\phi, \beta, \theta_i) \quad , \tag{4.1}$$

where F_f is the frequency response function for channel f, x and y are the two orthogonal image plane coordinates, and S_p is the backscatter model described above. F_f is a function of the sky coordinate in the direction perpendicular to the apparent rotational pole of the planet projected on the sky plane, x (see Appendix B). ϕ, β, and θ_i were determined from x, y and the viewing geometry.

For each of the snapshots and polarizations, the model was constructed separately for each of the $2n + 1$ channels containing echo energy, then each channel was CLEANed in a somewhat standard fashion. The final image for each snapshot was then constructed by:

$$I(x, y) = \sum_{f=-n}^{n} T_f(x) \cdot I_f(x, y) \quad , \tag{4.2}$$

where I_f were the individual CLEANed channel images, and T_f is a taper function intended to make adjacent channels merge together smoothly (see Appendix C).

Since there are so many snapshot images, they have been included as Appendix F, rather than shown here. Each image in the appendix is referenced by the date and the snapshot number, which is shown on each of the panels. As is clearly seen, the amount of data contained in this data set is nearly overwhelming. Relevant physical data is shown in Table 4.2 for each of the snapshots.

Several features are immediately noticeable in the images in Appendix F. There is a clear cross section enhancement in both polarizations associated with the south pole. The north pole, however, shows no such enhancement. There is a large region extending West of the Tharsis volcanoes which is a very poor reflector in both polarizations. We have termed this region "Stealth," for obvious reasons. All of the young volcanic regions show echo enhancements in both polarizations (most notably the Tharsis and Elysium regions). There are many other small scale features, as well. Each of these features will be dealt with separately in the following. But, first, the large scale (global) cross sections and global backscatter fits will be discussed.

4.2 Global Cross Sections

Figure 4.1 shows the global cross section measured in all of the experiments. This cross section is the projected area of a perfectly reflecting sphere which would return the same flux to the VLA if placed in the same position as Mars, normalized by the geometric cross section of Mars. All of these values except those for the Sept. 13, 1988 experiment were obtained by summing the flux in the final CLEANed images to a radial distance equal to the limb of Mars plus 1 CLEAN beam width. The Sept. 13, 1988 data were collected in the D configuration of the VLA, and thus contain many samples of the inner portion of UV space. Because of this, more accurate estimates of the total flux in the map are obtained from fits to the UV

Table 4.2

Imaging Information for Mars

date	snapshot	CLEAN beam size (asec)	κ (eqn. 2.2)	ΔI_m (RMS noise, %)	
				SS	OS
10/22/88	1	0.70	0.297	0.231	0.181 (0.236)
10/22/88	2	0.40	0.905	0.621	0.540 (0.766)
10/22/88	3	0.70	0.293	0.218	0.182 (0.472)
10/22/88	4	0.50	0.573	0.375	0.336 (0.546)
10/22/88	5	0.50	0.571	0.367	0.309 (0.635)
10/22/88	6	0.45	0.704	0.455	0.406 (1.945)
10/22/88	7	0.38	0.986	0.629	0.547 (1.276)
10/22/88	8	0.50	0.569	0.320	0.266 (0.855)
10/22/88	9	0.40	0.889	0.519	0.503 (1.397)
10/22/88	10	0.35	1.162	0.660	0.614 (1.245)
10/22/88	11	0.43	0.770	0.371	0.344 (1.352)
10/22/88	12	0.35	0.765	0.406	0.376 (1.226)
10/22/88	13	0.33	0.861	0.441	0.434 (1.291)
10/22/88	14	0.32	0.916	0.476	0.491 (1.822)
10/22/88	15	0.31	0.976	0.514	0.498 (1.414)
10/22/88	16	0.35	0.766	0.443	0.457 (1.355)
10/22/88	17	0.40	0.587	0.425	0.513 (1.630)
10/22/88	18	0.30	1.043	0.563	0.792 (2.157)
10/22/88	19	0.33	0.862	0.491	0.482 (2.660)
10/22/88	20	0.30	1.042	0.556	0.620 (2.520)
10/22/88	21	0.30	1.042	0.551	0.709 (1.675)
10/22/88	22	0.34	0.811	0.446	0.486 (1.405)
10/22/88	23	0.35	0.765	0.447	0.495 (1.098)
10/22/88	24	0.35	0.765	0.455	0.498 (1.038)
10/22/88	25	0.37	0.685	0.422	0.460 (0.749)
10/22/88	26	0.38	0.650	0.412	0.408 (0.689)
10/22/88	27	0.41	0.560	0.365	0.355 (0.881)
10/22/88	28	0.43	0.510	0.338	0.322 (0.892)
10/22/88	29	0.44	0.488	0.343	0.307 (0.733)
10/22/88	30	0.45	0.468	0.348	0.319 (0.539)
10/22/88	31	0.48	0.414	0.309	0.337 (0.807)
10/22/88	32	0.52	0.354	0.278	0.247 (0.413)
10/22/88	33	0.60	0.268	0.239	0.227 (0.473)
10/22/88	34	0.58	0.288	0.259	0.261 (0.468)
10/22/88	35	0.64	0.238	0.222	0.303 (0.868)
10/22/88	36	0.73	0.184	0.179	0.200 (0.340)
10/22/88	37	0.81	0.151	0.151	0.162 (0.248)
10/22/88	38	0.91	0.121	0.136	0.186 (0.289)

Table 4.2, *cont.*

date	snapshot	CLEAN beam size (asec)	κ (eqn. 2.2)	ΔI_m (RMS noise, %)	
				SS	OS
12/29/92*	1	0.41	1.777	1.190	1.063 (2.276)
12/29/92*	2	0.38	2.053	1.435	1.275 (2.912)
12/29/92*	3	0.34	2.540	1.855	1.586 (2.652)
12/29/92*	4	0.34	2.528	1.885	1.685 (2.262)
12/29/92*	5	0.34	2.512	1.856	1.651 (2.193)
12/29/92*	6	0.30	3.216	2.490	2.124 (2.833)
12/29/92*	7	0.30	3.205	2.437	2.098 (3.053)
12/29/92*	8	0.30	3.190	2.557	2.066 (2.998)
12/29/92	9	0.30	1.607	1.812	1.597 (2.126)
12/29/92	10	0.30	1.617	1.878	1.699 (2.042)
12/29/92	11	0.30	1.627	1.921	1.714 (2.190)
12/29/92	12	0.30	1.639	1.968	1.819 (2.204)
12/29/92	13	0.30	1.658	2.334	2.151 (2.828)
12/29/92	14	0.30	1.669	2.484	2.280 (2.465)
12/29/92	15	0.30	1.685	2.731	2.469 (2.620)
12/29/92	16	0.30	1.692	2.663	2.466 (2.646)
12/29/92	17	0.30	1.691	2.605	2.343 (2.502)
12/29/92	18	0.30	1.687	2.618	2.405 (2.548)
12/29/92	19	0.30	1.667	2.473	2.278 (2.597)
12/29/92	20	0.30	1.656	2.239	2.061 (2.895)
12/29/92	21	0.30	1.637	2.067	1.942 (2.313)
12/29/92	22	0.30	1.626	1.978	1.857 (2.152)
12/29/92	23	0.30	1.571	1.792	1.654 (2.050)
12/29/92	24	0.30	1.562	1.785	1.654 (1.910)
12/29/92	25	0.30	1.550	1.697	1.600 (2.007)
12/29/92	26	0.30	1.564	1.743	1.594 (2.101)
12/29/92	27	0.30	1.559	1.659	1.553 (2.079)
12/29/92	28	0.31	1.458	1.539	1.473 (2.015)
12/29/92	29	0.35	1.143	1.149	1.096 (1.434)
12/29/92	30	0.37	1.024	0.967	0.949 (1.366)

* measurements taken with 6104 Hz channel width.

Table 4.2, *cont.*

date	snapshot	CLEAN beam size (asec)	κ (eqn. 2.2)	ΔI_m (RMS noise)	
				SS	OS
1/12/93	1	0.30	1.656	0.733	0.715 (1.188)
1/12/93	2	0.30	1.685	0.755	0.764 (1.341)
1/12/93	3	0.30	1.665	0.735	0.727 (1.160)
1/12/93	4	0.30	1.693	0.758	0.745 (1.324)
1/12/93	5	0.30	1.713	0.761	0.767 (1.298)
1/12/93	6	0.30	1.732	0.844	0.904 (2.683)
1/12/93	7	0.30	1.690	0.759	0.771 (2.004)
1/12/93	8	0.30	1.674	0.751	0.807 (1.654)
1/12/93	9	0.30	1.664	0.780	0.851 (1.473)
1/12/93	10	0.30	1.644	0.779	0.848 (1.597)
1/12/93	11	0.30	1.632	0.767	0.840 (1.415)
1/12/93	12	0.30	1.613	0.758	0.924 (1.547)
1/12/93	13	0.30	1.602	0.766	0.950 (1.608)
1/12/93	14	0.30	1.587	0.796	0.961 (2.034)
1/12/93	15	0.30	1.580	0.804	0.889 (1.542)
1/12/93	16	0.30	1.573	0.832	0.853 (1.506)
1/12/93	17	0.30	1.570	0.869	0.898 (1.753)
1/12/93	18	0.33	1.335	∞^*	0.809 (1.096)
1/12/93	19	0.34	1.219	∞^*	0.705 (0.889)
1/12/93	20	0.39	0.929	0.547	0.560 (0.786)
1/12/93	21	0.41	0.843	0.505	0.509 (0.677)
1/12/93	22	0.45	0.704	0.433	0.452 (0.784)
1/12/93	23	0.50	0.573	0.359	0.364 (0.970)

* these shapshots had no usable SS data.

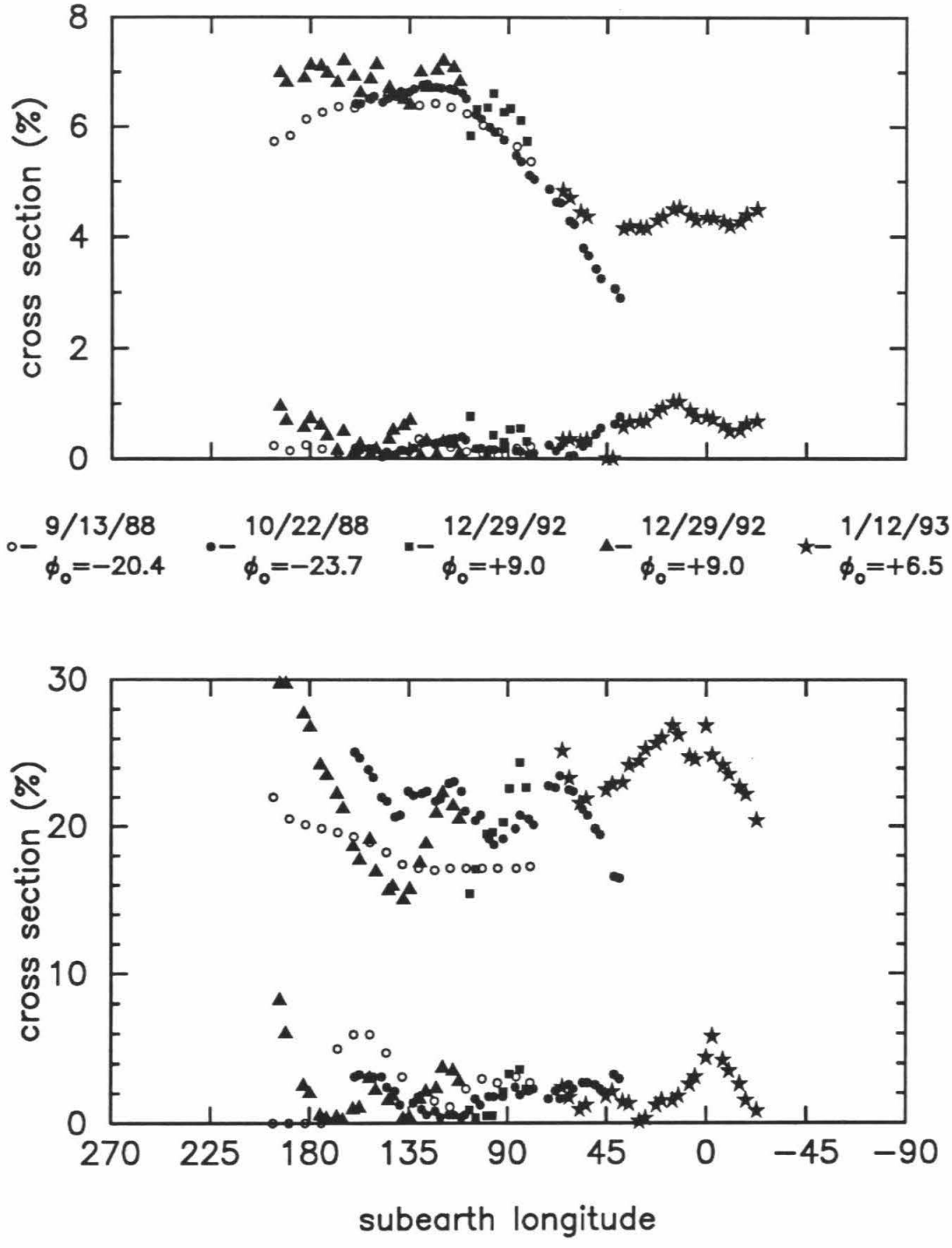

Figure 4.1: Normalized global cross section for all of the Mars experiments. SS polarization is in the upper panel, OS in the lower. Also shown are the residuals (as absolute error) of the global cross sections derived from the global backscatter fits.

data, as explained in Appendix A, sections A.2.1 and A.2.2. The data from 1988 had two problems which must be mentioned. During the first 11 snapshots of the October 22 experiment, the subreflector on the Goldstone antenna was incorrectly pointed, thus yielding a reduced value of total transmitted power. There was no way to find out exactly what this reduction was, but we obtained a good estimate by trying to make the total flux in the SS polarization vary smoothly across the transition. The resultant estimate of the transmitted power was 230 kW for those 11 snapshots (as opposed to 350 kW for the rest of the experiment). The second problem was one which we discovered while doing our Mercury experiments. This involves the particular mode of data collection at the VLA, and is described in Appendix D. In the case of the Mercury observations, the problem was correctable, since the necessary data had been recorded on tape. Unfortunately, in 1988, the VLA tape archives did not contain the necessary data, and so there was no reliable way to correct for this problem. The method we chose to correct these cross sections was to find a multiplicative factor for each polarization from our experience with the Mercury data. This correction factor was ~ 1.35 for the OS data, and ~ 1.15 for the SS data.

As expected from inspection of the SS images, there is a significant enhancement in the global cross section encompassing the longitudes of the Tharsis and Elysium volcanic provinces. This is not the case for the OS cross sections, however. This is due to the fact that the quasi–specular return is reduced for rougher surfaces. Since much of the total OS echo is in the quasi–specular spike, the global cross section is reduced. It seems logical that the surface roughness in the young volcanic provinces of Tharsis and Elysium would be greater than elsewhere, due to the numerous lava flows. This explains both the SS global cross section enhancements and the slight depression in the OS global cross sections.

4.3 Global Backscatter Fits

In order to obtain an idea of what the backscatter response of each surface location was, fits to a sensible backscatter model were calculated from the CLEANed image data for each polarization (see Appendix A, section A.1 for a description of the fits and the functional form of the backscatter models used in them). The fits were calculated for surface points in a sinusoidal projection with 1° increments on the equator. Because the true resolution is less than 1°, the solutions have been filtered to several resolutions for presentation. Transformations from the original sinusoidal to other projections were obtained by reprojecting the data with the correct transformation (a good discussion of mapping transfomations can be found in: Snyder 1987) via some interpolation technique. For the interpolation, we decided on a variant of the Shepard method (Renka 1988). For the fits to the diffuse portion of both polarizations (the cosine model), the beam convolution was ignored (see Appendix A, section A.1.3). In practice, we found that including the beam convolution in these fits changed the solutions only very slightly for many test locations, and there is a significant savings computationally if the convolution is not included. However, for the fits to the quasi–specular portion of the OS data (with either Muhleman's or Hagfors' model) this was not the case, and the beam convolution was included. This is due to the sharply peaked nature of these models near normal incidence, i.e., the slope of the model causes the change in response to be significant across one beam width.

As explained in the previous section, in the OS fits we found that a fit to a singular backscatter model produced unacceptably large residuals at incidence angles $\gtrsim 20°$ for most regions of Mars (see Figure 4.5). Because of this, a hybrid model was used, with the form of a Muhleman model at incidence angles near normal, and the form of a cosine model for larger incidence angles. It has been previously noted that the Hagfors model (Hagfors 1964) fits the backscatter data for Mars at small incidence angles better than the Muhleman model (Downs *et al.* 1975), and

it has thus been used for most of the analysis of OS echoes from Mars (see e.g., Harmon *et al.* 1982; Harmon and Ostro 1985). In order to test this, we performed fits to a Hagfors model with the same data used for the Muhleman model fits. In order to check if one model fit the data better than the other, residuals were calculated for each of the fits. This residual calculation only included surface locations which were within 5° of the subearth point for any of the snapshots, because the fits are not well constrained when there is no data very near normal incidence. From the calculated residuals, we cannot state that either of the fits is better, i.e., the residuals were essentially the same for the two types of fits. A plot of the fit parameters, averaged over the regions just described for each type of fit, is shown in Figure 4.2. Note that the anticorrelation of the roughness parameters (C and α) plotted in the upper panel of Figure 4.2 is expected, as rougher surfaces have lower values of C, and higher values of α. Also shown in the figure is the global cross section, calculated for a planet whose entire surface has backscatter parameters as shown. For the Muhleman model, the global cross section is:

$$\begin{aligned} \eta &= 2A_{os}\int_0^1 r\sqrt{1-r^2}\left(\frac{\alpha}{r+\alpha\sqrt{1-r^2}}\right)^3 dr \\ &= 2A_{os}\alpha^3\left(\frac{1+\pi\alpha(3\alpha^2-1)-2\alpha^2(1+3\ln\alpha)+\alpha^4(2\ln\alpha-3)}{2\alpha(1+\alpha^2)^3}\right) \quad . \end{aligned} \tag{4.3}$$

For the Hagfors model, the global cross section is:

$$\begin{aligned} \eta &= \rho_o C\int_0^1 r\left(\frac{1}{(1-r^2)^2+Cr^2}\right)^{\frac{3}{2}} dr \\ &= \frac{\rho_o C}{C-4}\left(\frac{C-2}{C}-\frac{1}{\sqrt{C}}\right) \quad . \end{aligned} \tag{4.4}$$

In practice, since C is generally $\gg 1$, $C-2 \sim C$, so $(C-2)/C \sim 1$, and $1/\sqrt{C} \ll 1$, so $\eta \sim \rho_o$, or, the global cross section is nearly equal to the Fresnel reflectivity at normal incidence for the surface near the subearth point for the Hagfors model. The other value plotted in Figure 4.2 is an estimate of the mean tilt angle, $\overline{\phi}$. This

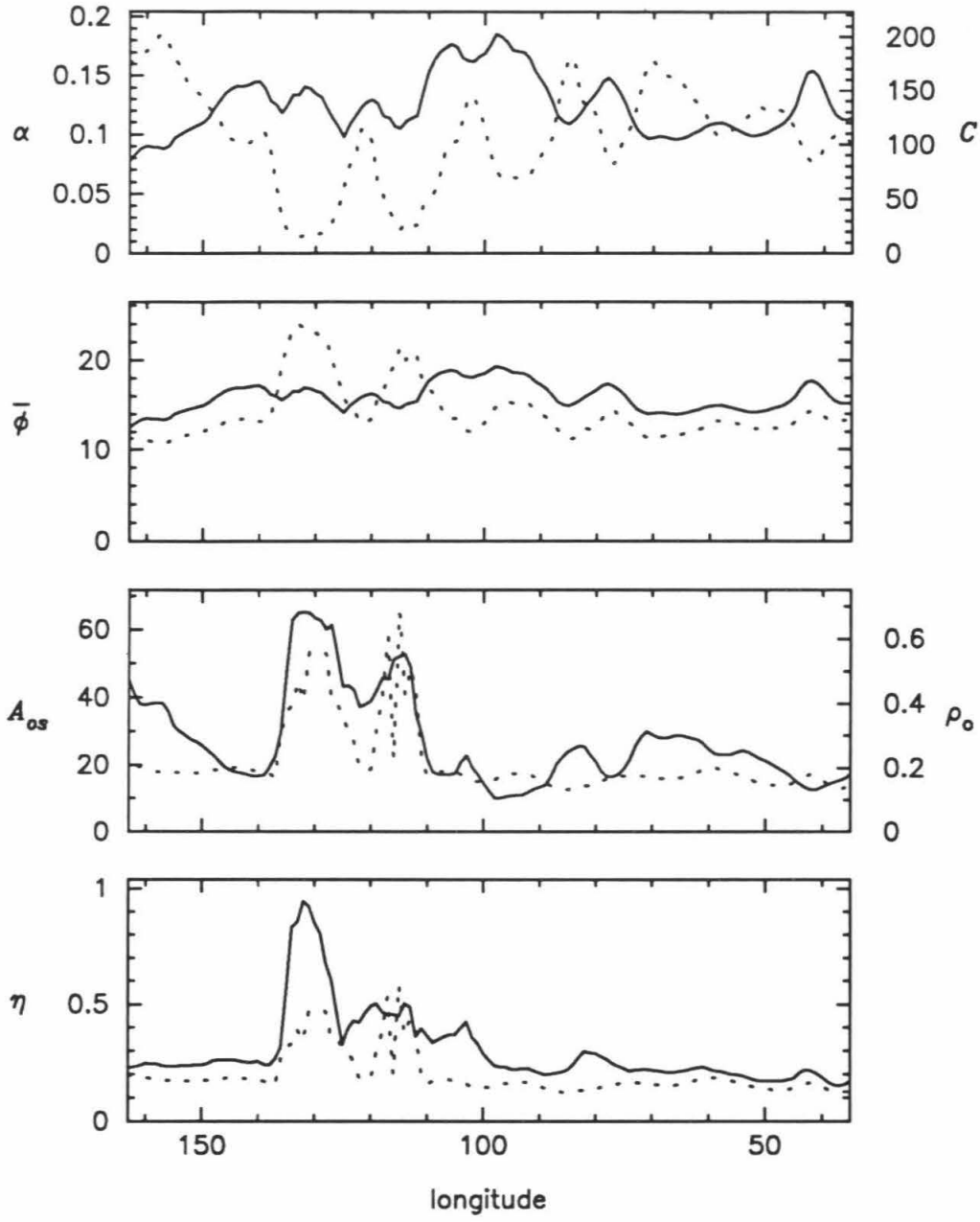

Figure 4.2: Backscatter fit parameters for the Muhleman and Hagfors model fits in 10° swaths around the subearth point for each of the experiments. Solid lines are the Muhleman parameters, dashed the Hagfors. Upper panels show "roughness" parameters α (for Muhleman model) and C (for Hagfors model). Upper middle panels show the value of the mean tilt angle ($\overline{\phi}$), in degrees (see equation 4.5). Lower middle panels show scaling coefficients A_{os} (for Muhleman model) and ρ_o (for Hagfors model, this is the Fresnel reflectivity at normal incidence). Lower panels show the global cross section given the parameters in the upper panels (see equations 4.3 and 4.4). (a) Fit parameters for the 10/22/1988 data.

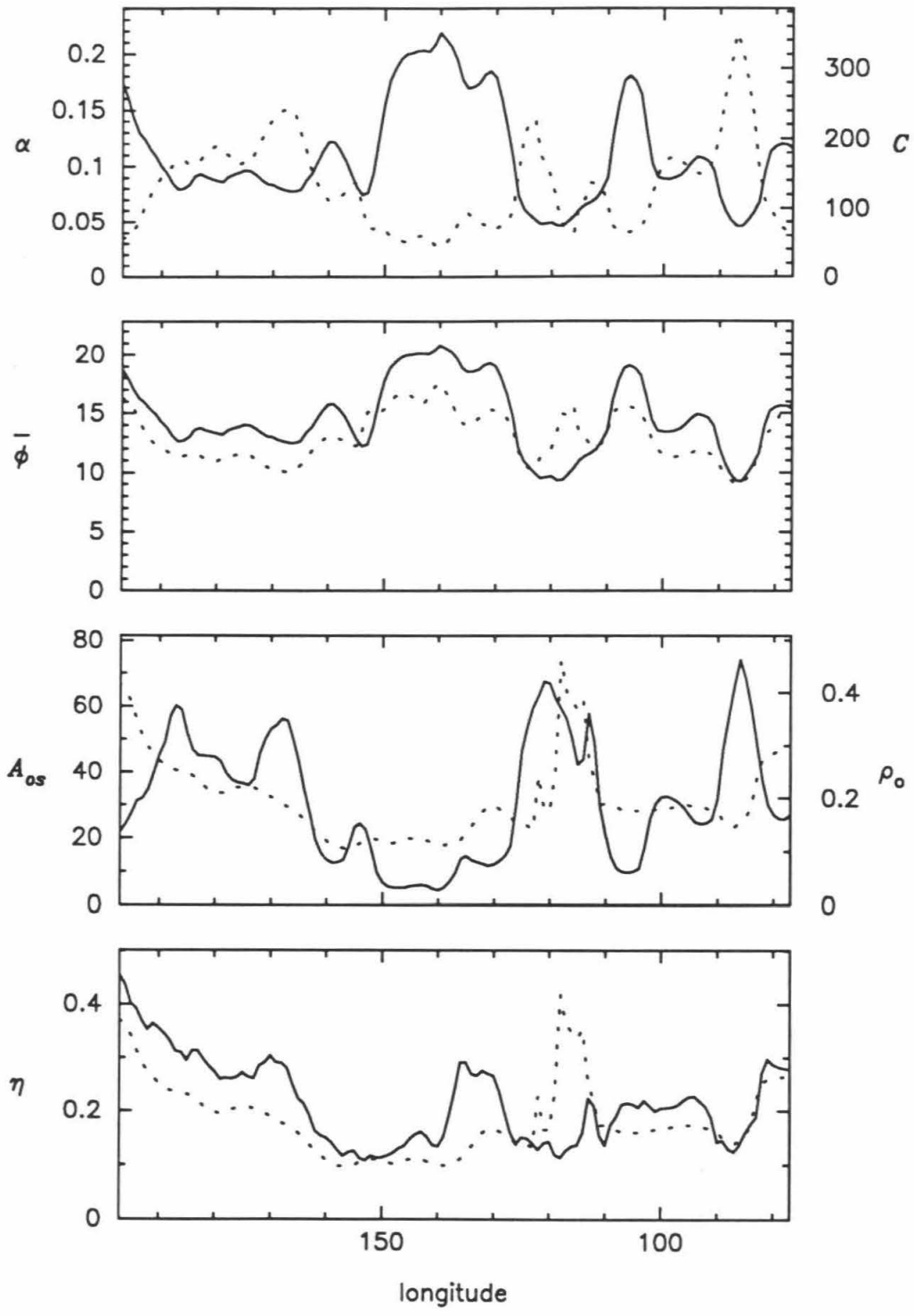

Figure 4.2: (b) OS Fit parameters for the 12/29/1992 data.

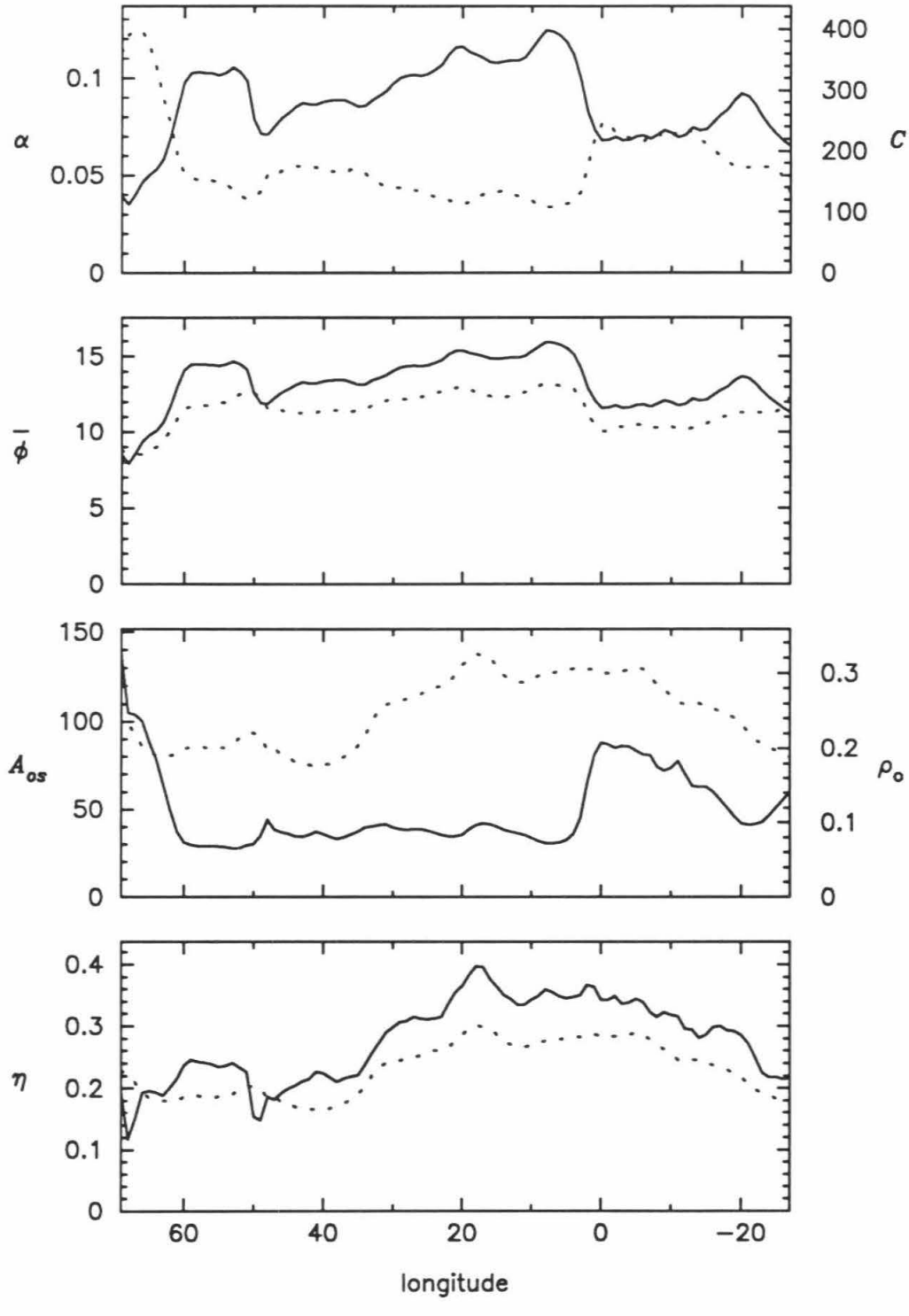

Figure 4.2: (c) OS Fit parameters for the 1/12/1993 data.

was plotted in order to compare the "roughness" parameters of the two models, α for the Muhleman model, and C for the Hagfors. The mean tilt angle is calculated via (Muhleman 1966; Evans and Hagfors 1968):

$$\overline{\phi} = \frac{\int_\phi \phi\, S(\phi)\, \cos\phi\, \sin\phi\, d\phi}{\int_\phi S(\phi)\, \cos\phi\, \sin\phi\, d\phi} \quad , \tag{4.5}$$

where $S(\phi)$ is the backscatter model of interest. The integration was carried out over the full range $0 \leq \phi \leq 90°$. A similar value of interest is the mean slope, given for the Hagfors model by (Evans and Hagfors 1968):

$$\overline{\tan\phi} \sim \frac{1}{2\sqrt{C}} \cdot \frac{C-4}{C-\sqrt{C}-2} \cdot \ln(4C) \tag{4.6}$$

for large values of $C\,(> 100)$. For the Muhleman model, the mean slope is given by (Muhleman 1966):

$$\overline{\tan\phi} \sim \sqrt{\alpha} \quad . \tag{4.7}$$

This number could also be shown, but seems to be somewhat less generally used. A more commonly quoted "roughness" parameter is θ_{rms}, or the so–called rms roughness. For the Hagfors model, this quantity is given by: $\theta_{rms} \sim 1/\sqrt{C}$. However, we feel that this particular measure of the surface roughness gives no more information that the mean tilt, and thus have not used it. It should be stressed that using a single number to characterize the roughness of a surface can be misleading. We have simply shown the number to make comparisons between the two models, and to give a general feeling for the relative roughness of areas on the surface of Mars. Too much should not be read into the actual values of any of these "roughness" parameters, as it is not clear if they really have any physical meaning. Recent measurements of slope statistics on various Earth terrains have indicated a substantial deviation from a simple exponential or gaussian distribution of slopes, and the derived roughness parameters were significantly different than those derived from planetary radar experiments of the past (McCollom and Jakosky

1993). This difference may be real, and due to the different environments, but it may also be an indication of the weakness of the models in representing real surfaces. It is clear that the models are not giving values which make sense for the longitudes of the Tharsis volcanoes, and this is not particularly surprising, considering the extreme roughness which may be present there. However, for other regions, the numbers seem to make some sense, and the agreement between the two scattering models is surprisingly good.

Maps showing the best fit parameters for the cosine backscatter models in both polarizations using all of the A configuration data are shown in Figures 4.3 and 4.4.

All of the major features mentioned briefly at the end of the previous section can be seen in these maps, in addition to some others. Note that most of the major features are present in both SS and OS polarizations. This is to be expected, as any surface which depolarizes very efficiently should return nearly equal amounts of echo energy in the two polarizations. This is because multiple reflections are most certainly occurring, and so the returned polarization is essentially random. Some exceptions exist, most notably features in the OS map at Valles Marineris, and near Utopia Planitia. Along with the fit parameters shown in Figures 4.3 and 4.4 are plots of global cross section for the fits. This value is similar to the global cross sections calculated above for the quasi–specular fit parameters, i.e., where the cross section is calculated as if the entire planet had the same backscatter properties as the location of interest. In the case of the cosine model, this is calculated by:

$$\begin{aligned} \eta &= 2\,A_{ss} \int_0^1 (1-r^2)^{\frac{n}{2}}\, r\, dr \\ &= \frac{2\,A_{ss}}{n+2} \quad . \end{aligned} \tag{4.8}$$

The average backscatter parameters for the entire globe are shown in Table 4.3. This is our best estimate of what the "average Mars" backscatter parameters are for the diffuse echo in both polarizations at 3.5 cm.

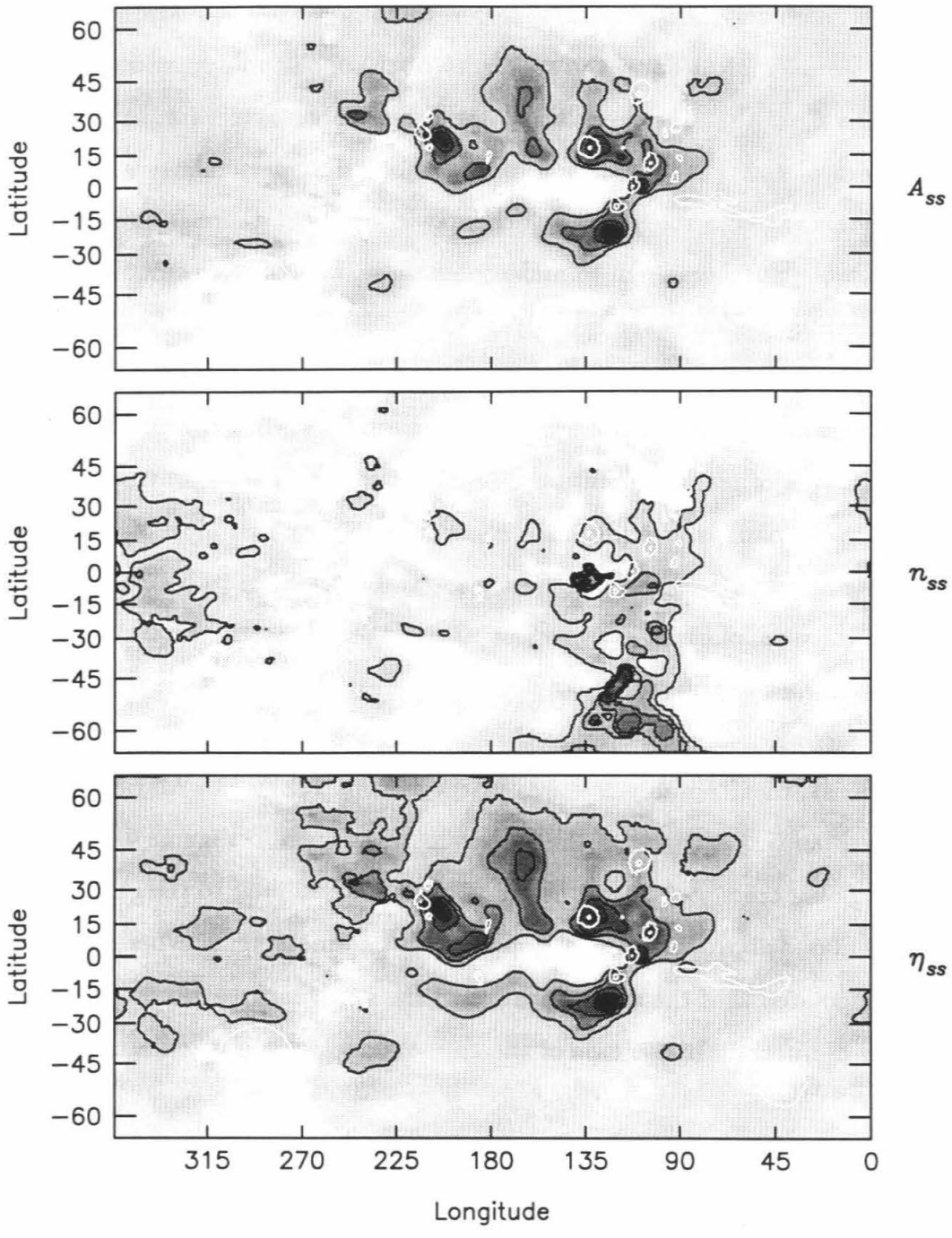

Figure 4.3: Images showing the backscatter fit parameters for the SS polarization. The three parameters shown are the scaling coefficient, A_{ss}, the cosine exponent, n_{ss}, and the global cross section, η_{ss}, given A_{ss} and n_{ss} (see equation 4.8). (a) Mercator projection from latitude -65 to +65. Contours levels are at .1, .2, .3, and .4 in the upper panel (A_{ss}), 1, 2, 3, 4, 5, 6, and 7 in the middle panel (n), and .05, .1, .15, .2, and .25 in the lower panel (η). The white outlines are locations of prominent geological/topographical features.

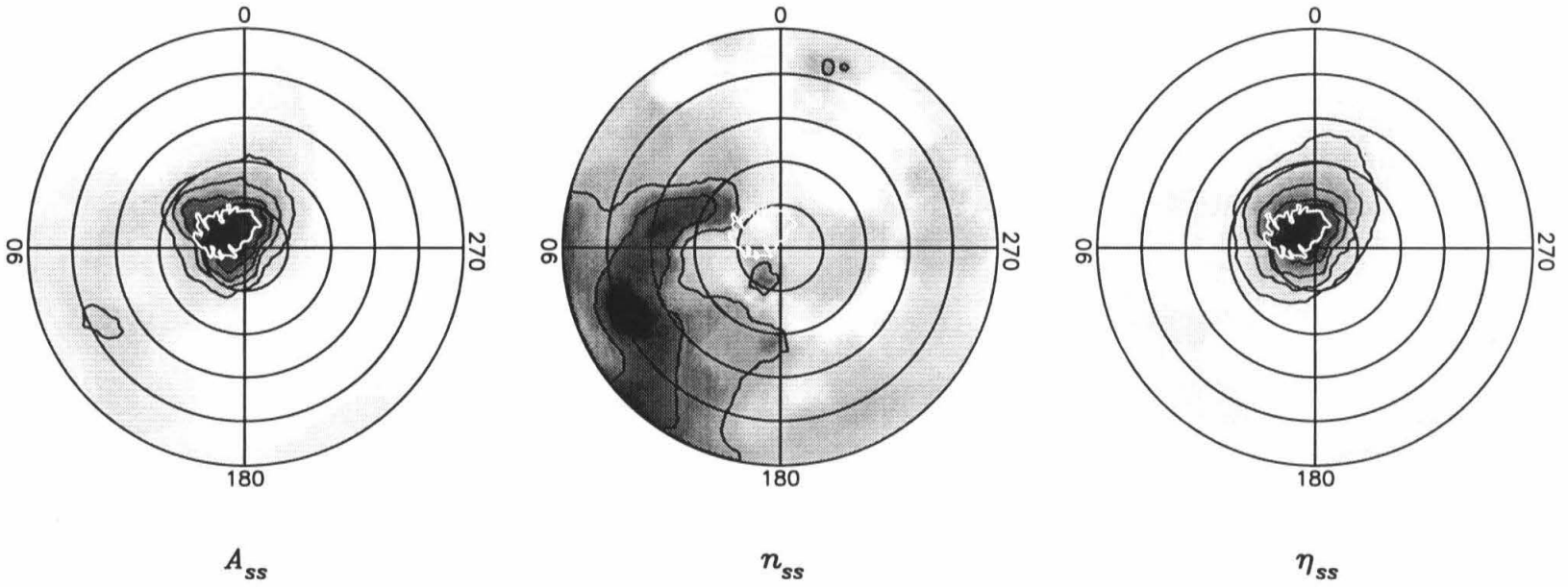

Figure 4.3 : (b) Polar stereographic projection for the south polar region. Latitude circles are at 5° increments. Contours levels are at .1, .2, .3, .4, .5, and .6 in the left panel (A_{ss}), 1, 2, and 3 in the middle panel (n_{ss}), and .05, .1, .2, .3, .4, and .5 in the right panel (η_{ss}). The white outline shows the approximate extent of the residual south polar ice cap (RSPIC).

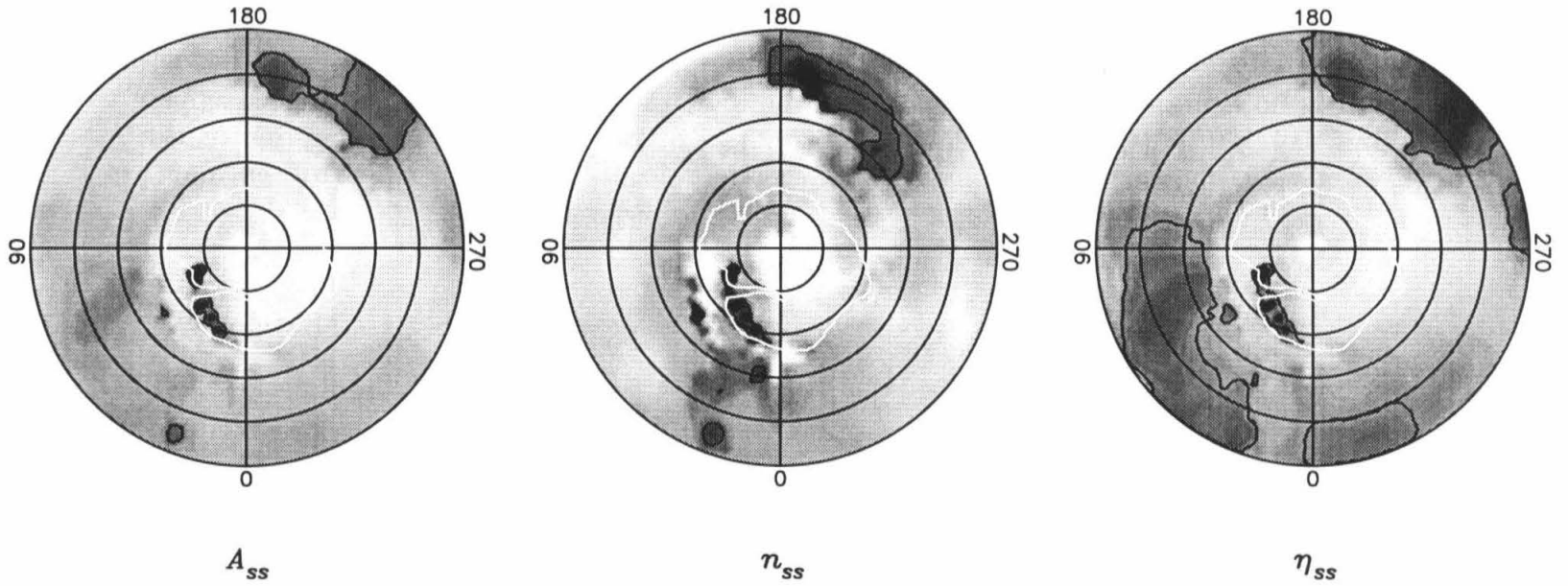

Figure 4.3 : (c) Polar stereographic projection for the north polar region. Latitude circles are at 5° increments. Contours are at .1 and .2 in the left panel (A_{ss}), 1 and 1.5 in the middle panel (n_{ss}), and .05 and .1 in the right panel (η_{ss}). The white outline shows the approximate extent of the residual north polar ice cap (RNPIC).

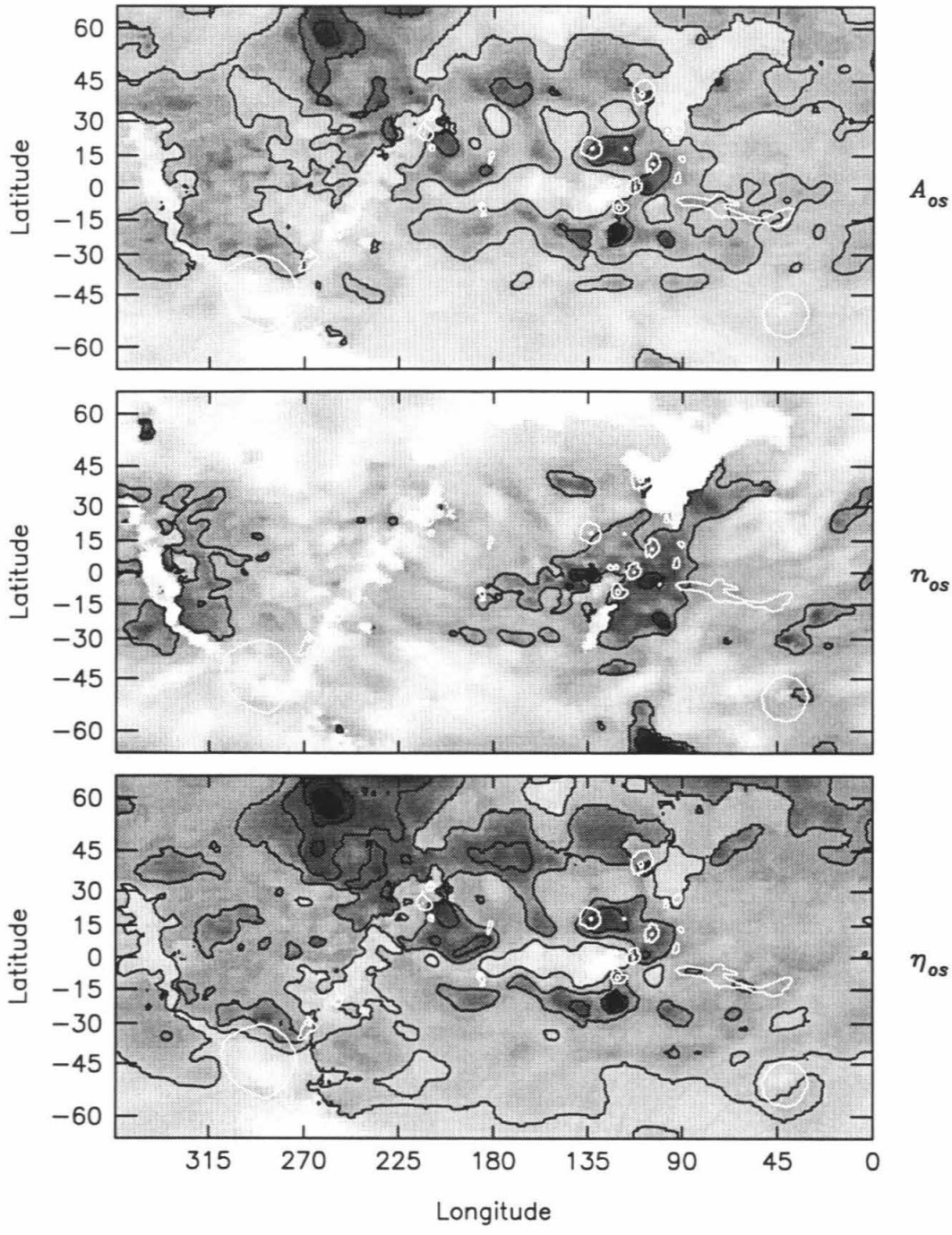

Figure 4.4: As Figure 4.3, but for the cosine portion of the OS backscatter fits. (a) Mercator projection from latitude -65 to +65. Contour levels are at .1, .2, .3, and .4 in the upper panel (A_{os}), 1 and 2 in the middle panel (n_{os}), and .05, .1, .15, .2, and .25 in the lower panel (η_{os}).

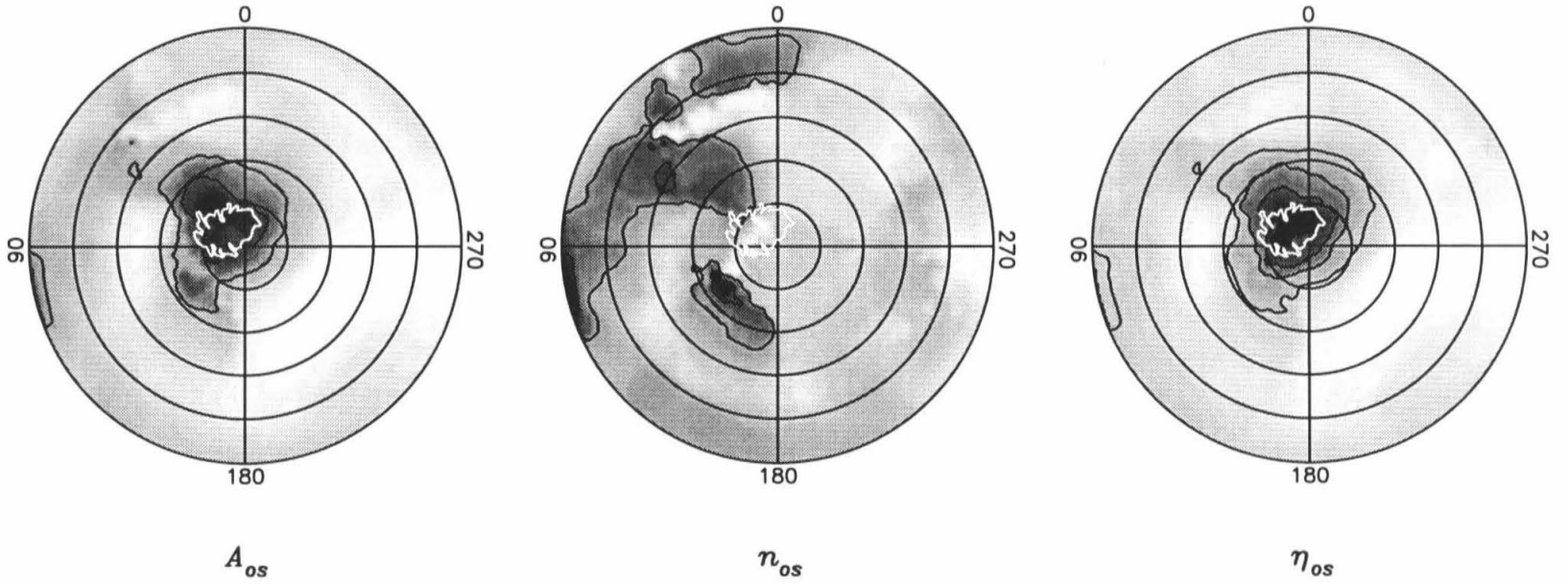

Figure 4.4 : (b) Polar stereographic projection for the south polar region. Latitude circles are at 5° increments. Contour levels are at .1, .2, and .3, in the left panel (A_{os}), 1 and 2 in the middle panel (n_{os}), and .05, .1, and .2, in the right panel (η_{os}). The white outline shows the approximate extent of the residual south polar ice cap (RSPIC).

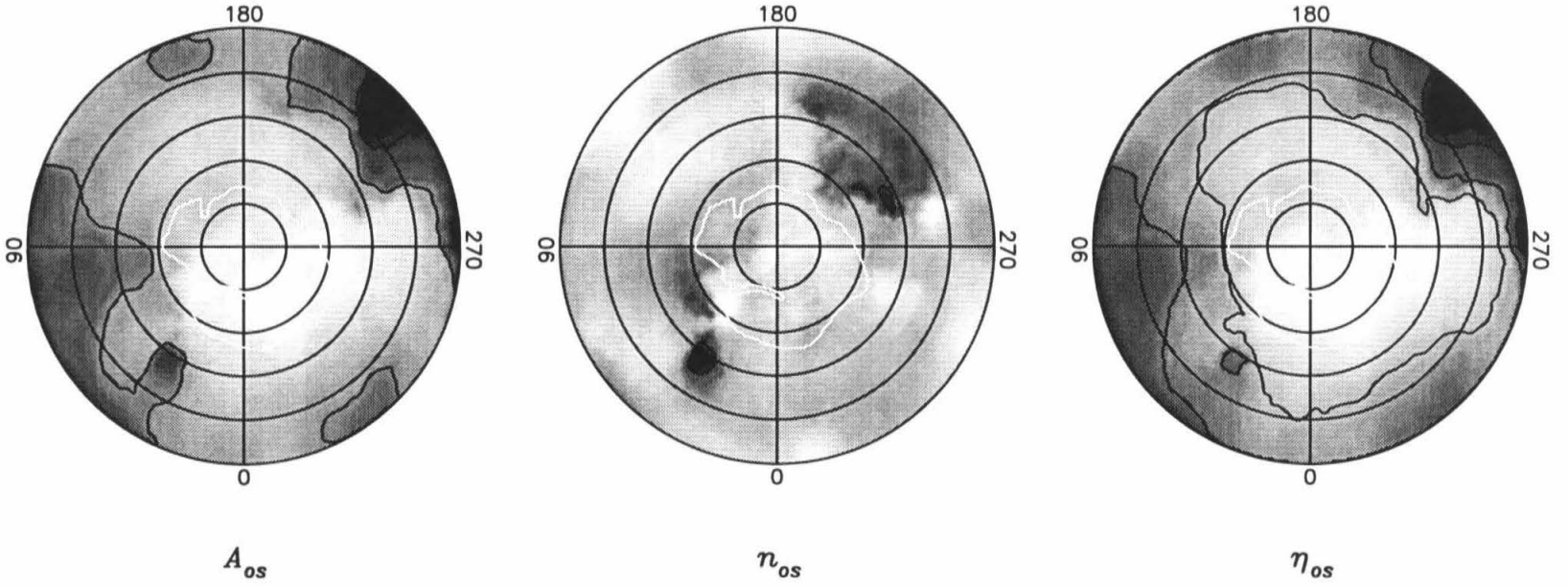

Figure 4.4 : (c) Polar stereographic projection for the north polar region. Latitude circles are at 5° increments. Contour levels are at .1 and .2 in the left panel (A_{ss}), 1 in the middle panel (n_{os}), and .05, .1, and .15 in the right panel (η_{os}). The white outline shows the approximate extent of the residual north polar ice cap (RNPIC).

Table 4.3

Global Average Diffuse Backscatter Parameters

	SS	OS
A (%)	6.5	10.3
n	0.71	0.61
η^a (%)	4.6	7.7

[a] η is the global cross section for a planet with a backscatter law: $A \cos^n \theta_i$.

4.3.1 Testing the Fits

As a test of all of the fits, model global cross sections were calculated for our observed geometries, given the fit parameters for all locations visible on the disk. The residuals of the fits, calculated as the absolute value of the measured cross section minus the model cross section, are shown in Figure 4.1. Most of the matches are quite good, especially in the SS polarization. However, some snapshots have significant residuals in the OS polarization, indicating the possibility of improvement of the OS fits. It should be noted that deviations from the true data are obviously expected, as the fits are minimizing the global response of each surface location. Therefore, if in a particular geometry, that location displays some deviant backscatter behavior, this will not be reflected in the fits. Because of this, the fits should only be used to obtain a general idea of the reflectivity of large regions of the planet. For inspection of small regions, the data from each snapshot which contains that region should be inspected individually for the best results.

Figure 4.5 shows an example of the OS fit to a surface location at $\phi = 8°, \beta = 40°$, which has typical fit parameters. It can clearly be seen here that the quasi–specular backscatter models (Muhleman and Hagfors) do a very poor job of fitting the data at large incidence angle. However, using the hybrid model, with cosine

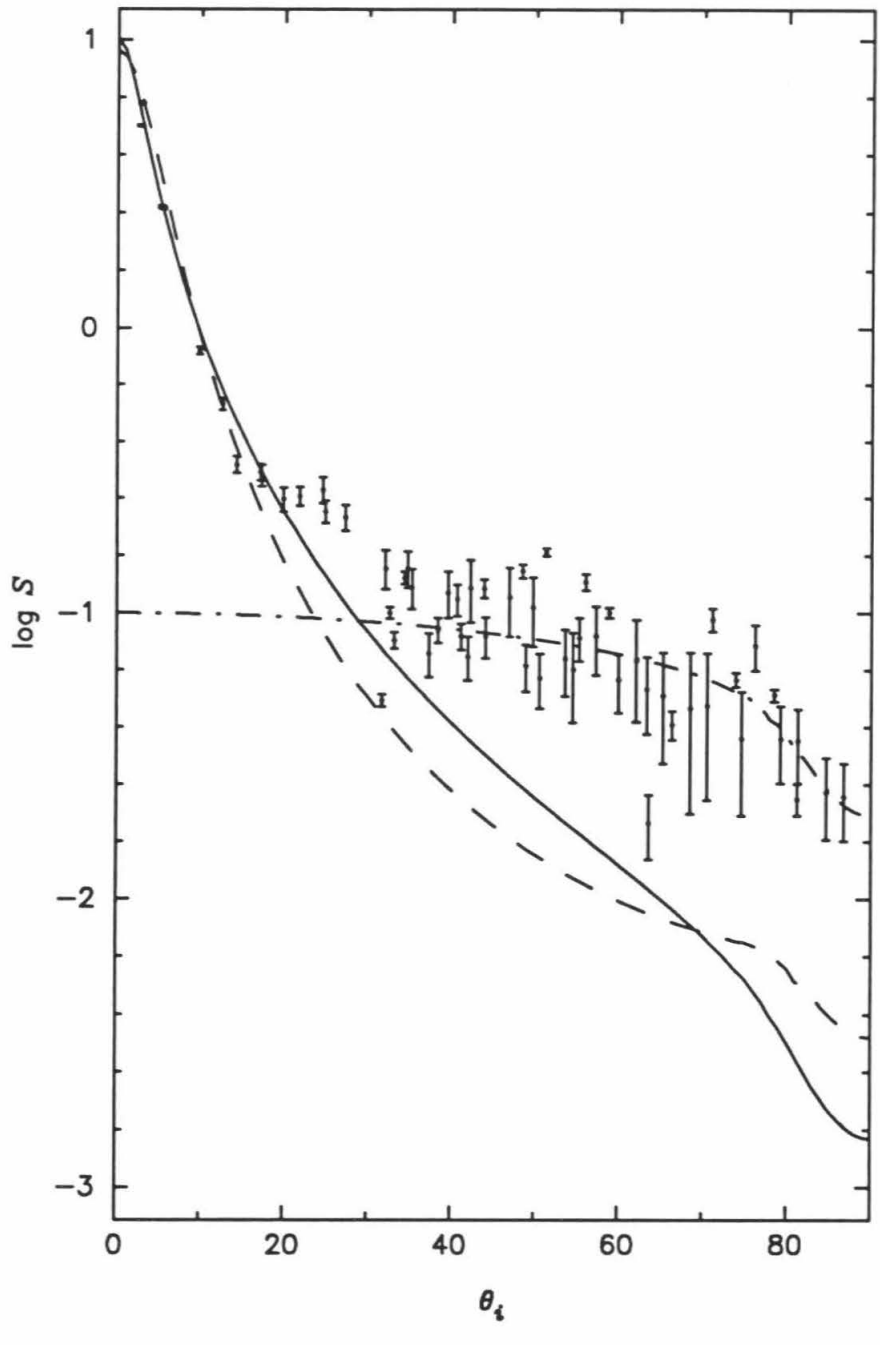

Figure 4.5: OS backscatter data and fits for $\phi = +8°, \beta = 40°$. OS fits to data at angles less than 20° are shown as the solid line (Muhleman) and the dashed line (Hagfors). Fit to cosine model at angles greater than 30° is shown as the dash–dot line.

model form at large incidence angle, does a much better job of fitting the entire range. Figure 4.6 shows examples of SS fits to several locations, one with very high cross section (near Pavonis Mons), one with average cross section (the same as for Figure 4.5), and one with very low cross section (in "Stealth," see discussion below). This figure shows that although the fits do a good job of fitting the data in a general sense, there are substantial deviations. Because of this, normal "goodness–of–fit" criteria have less meaning than usual. The standard test of the believability of a fit to noisy data is given by:

$$Q\left(\frac{\nu}{2}, \frac{\chi^2}{2}\right) \quad , \tag{4.9}$$

where Q is the complement of the incomplete Gamma function, ν is the number of degrees of freedom ($N-2$ for us, where N is the number of measurements used in the fit), and χ^2 is given by:

$$\chi^2 = \sum_{i=1}^{N} \frac{(P_i - S(\theta_i))^2}{\sigma_i^2} \quad , \tag{4.10}$$

where P_i is the i^{th} data value, $S(\theta_i)$ is the model value, and σ_i^2 is the variance of the measurement. The fact that we use a modified weight (see Appendix A, section A.1.3) in our fits also gives this test less meaning. Values of Q calculated for our fits are consistently low, indicating that in a strict sense, the models do not fit the data. Again, however, the models are not meant to fit the data in this sense, as real deviations from the model are expected. Each of the most important features in the images and maps will now be discussed, beginning with the polar regions.

4.4 Polar Reflectivities

During the course of a Martian year, the polar caps grow and recede according to season, but never entirely disappear. The ice which persists throughout the

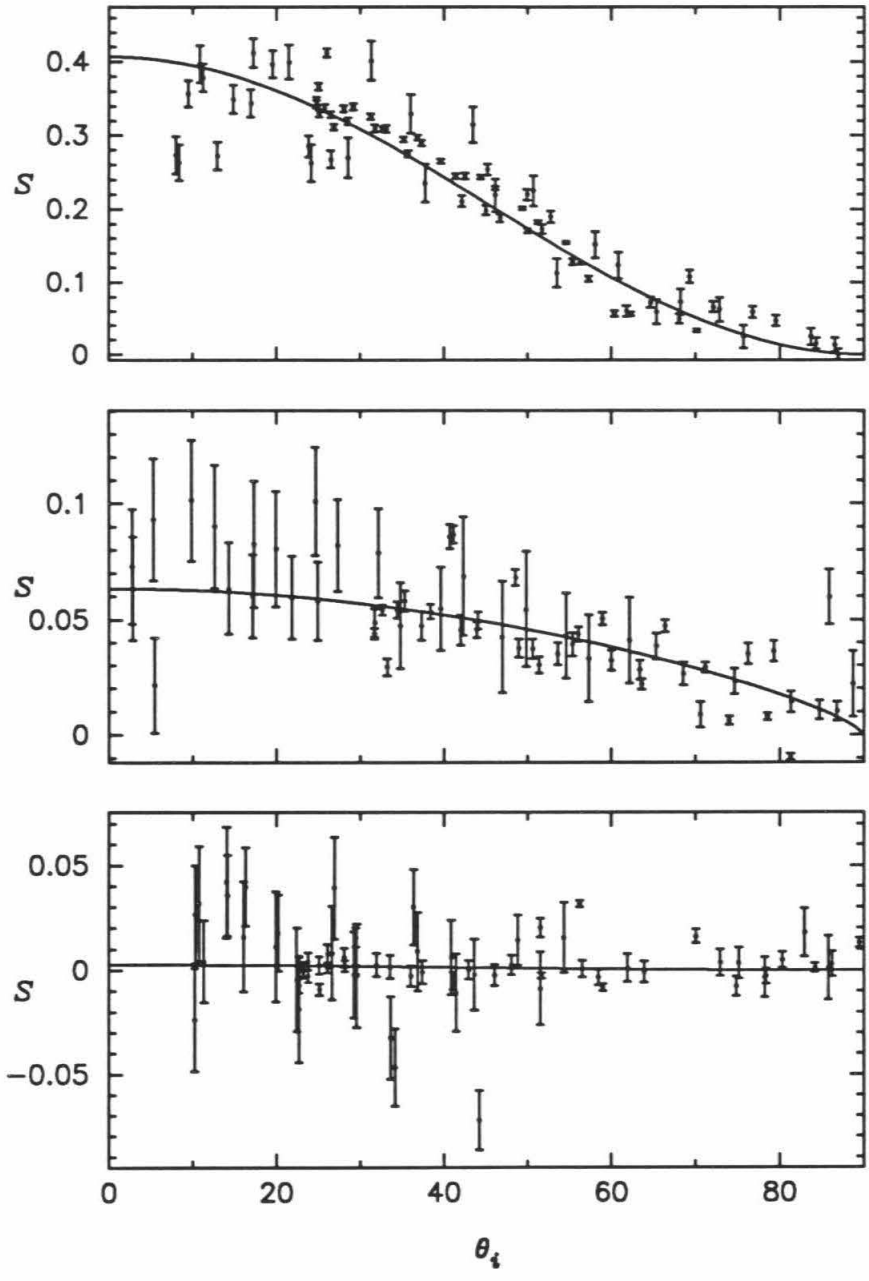

Figure 4.6: SS backscatter data and fits for three locations. Top panel is a location near Pavonis Mons, at $\phi = 1°, \beta = 107°$. Middle panel is an "average" location, at $\phi = 8°, \beta = 40°$. Lower panel is a location in "Stealth," at $\phi = -1°, \beta = 140°$.

entire year at each pole is generally referred to as the residual ice cap, while the fluctuating portion is generally referred to as the seasonal cap. The seasonal cap accumulates throughout the winter at each pole, then sublimates away during the summer. The north and south residual caps display some common characteristics, yet there exist substantial differences between the two. The south cap (RSPIC) is offset slightly from the pole, and is much smaller than the north cap (RNPIC). Viking data indicated that the RNPIC was comprised of H_2O ice (Kieffer *et al.* 1976; Farmer *et al.* 1976; Jakosky and Haberle 1992). The story for the RSPIC is not as clear, as in at least 2 years the temperatures measured by the Viking and Mariner spacecraft stayed at the vapor pressure equilibrium point for CO_2, indicating that it was the ice present (Kieffer 1979; Paige *et al.* 1990), but H_2O ice would also be retained there.

Figure 4.7 shows polar stereographic images of the 3.5–cm radar cross section of the polar regions of Mars. These images were constructed by projecting the proper polar region (south for the 1988 data, north for the 1992/93 data) for each snapshot into an individual stereographic image, then averaging these individual images with weights chosen similarly to those described in Appendix A, section A.1.4. Ephemeris information necessary for the projections was obtained from the very accurate JPL ephemeris.

4.4.1 South Pole

The south polar images show a feature with a very high cross section in both polarizations. The bright feature corresponds very closely to the location of the RSPIC, which we resolve. In a single snapshot, the RSPIC is only resolved in the direction perpendicular to the line of sight. However, averaging all of the snapshots allows us to resolve it in all dimensions. The size of the equivalent resolution element is shown in Figure 4.7, where it can be seen that the RSPIC is clearly well–resolved. The peak cross section is $\eta \sim 71.6\% \pm 0.9\%$, centered at $\phi \sim -87°.3, \beta \sim 33°.7$ for the SS polarization, and $\eta \sim 31.2\% \pm 1.4\%$, centered at

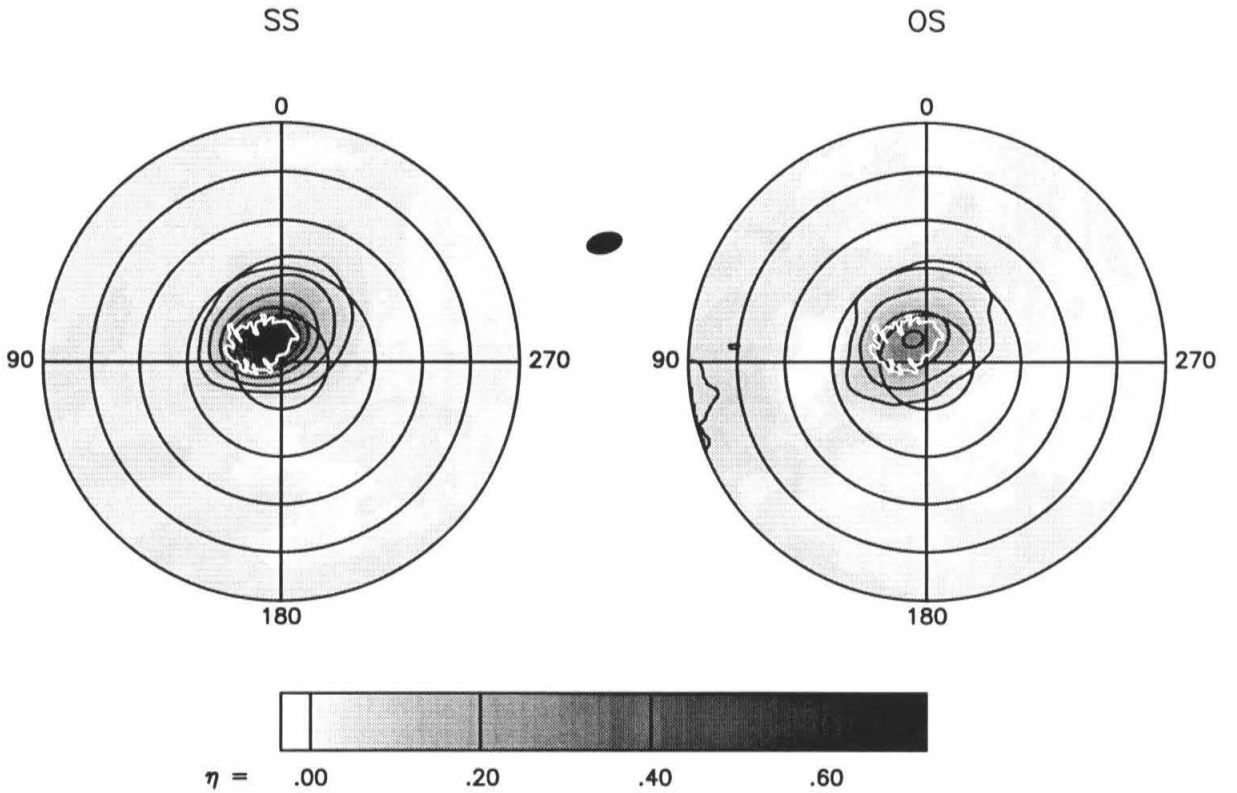

Figure 4.7 : Polar stereographic radar cross section images, created by projecting the appropriate region for each snapshot, then summing the projections. Equivalent resolution exactly at the pole is shown as a darkened ellipse. SS images are on the left, OS on the right. (a) south pole projection, from 1988 data, during mid southern summer ($L_s \sim 295°$). Contours levels at $\eta = 0.05, 0.1, 0.2, \ldots, 0.7$. The white line shows the approximate extent of the residual south polar ice cap (RSPIC).

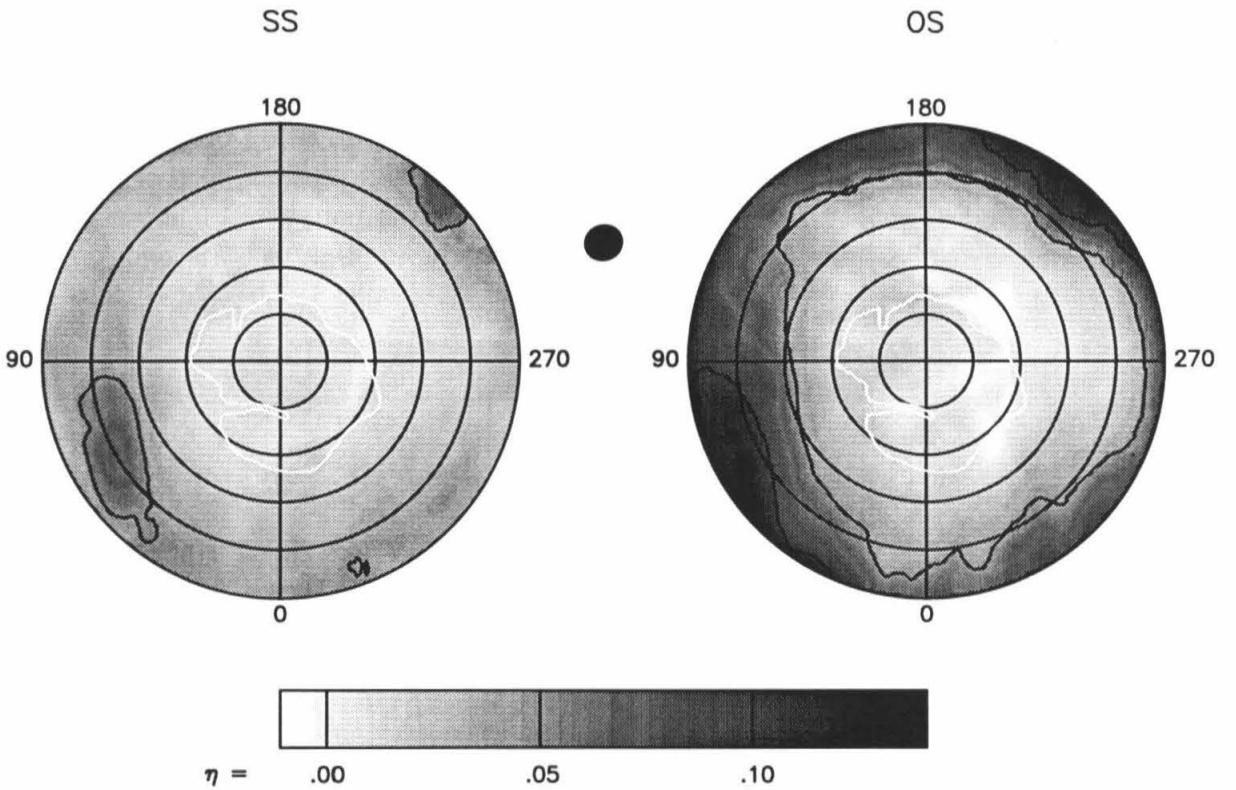

Figure 4.7 : (b) north pole projection, from 1992/93 data, during early northern spring ($L_s \sim 20°$). Contour levels at $\eta = 0.05$ and 0.1. The white line shows the approximate extent of the residual north polar ice cap (RNPIC).

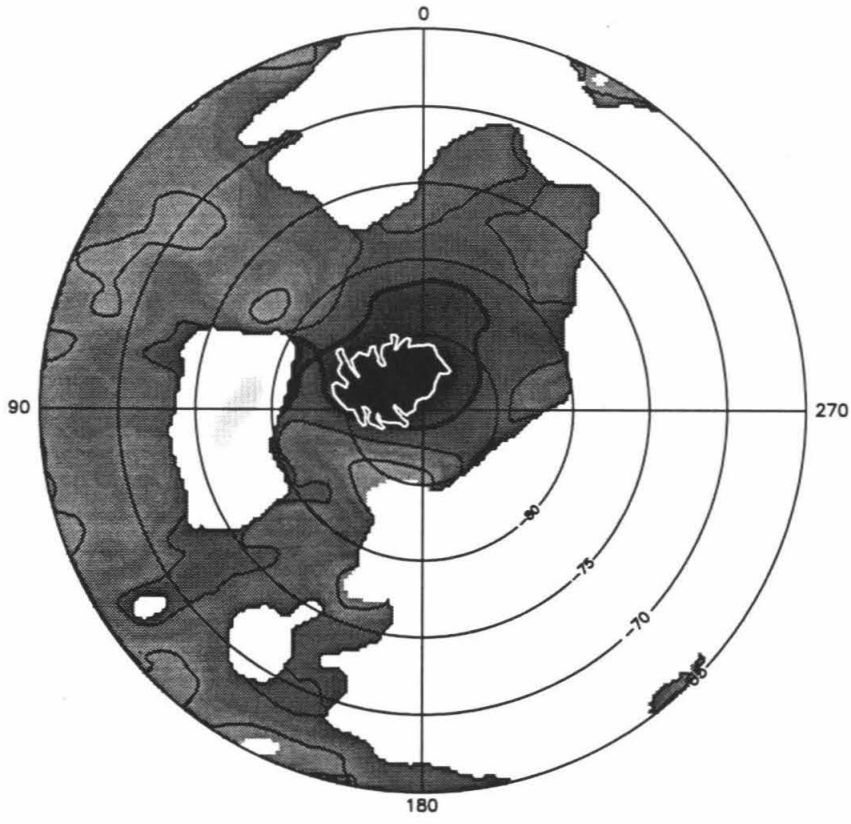

Figure 4.8: Polar stereographic image of polarization ratio (ratio of SS cross section to OS cross section) for the south polar regions. Blank regions are regions where the signal in either the SS image or the OS image was indistinguishable from the noise. Contour levels are at: 0.5, 1.0, 1.5, 2.0, and 2.5, with the contour at 1.5 darkened. The white line shows the approximate extent of the residual ice cap (RSPIC).

$\phi \sim -87°.0, \beta \sim 31°.0$ for the OS polarization. If only the highest resolution data are used in the averaging process, the peak cross sections become $\sim 83.5\% \pm 1.4\%$, and $\sim 35.4\% \pm 2.3\%$ for the SS and OS polarizations, respectively, at nearly the same locations. This is an indication that although we are resolving the RSPIC, we are not fully resolving the highest cross section feature or features. These cross sections are very high, particularly considering that they occur at an incidence angle of $\sim 66°$. Figure 4.8 shows a polar stereographic image of the polarization ratio, or the ratio of SS to OS echo power, for the south polar region. The blank portions of the image are pixels which were not significantly different from an

estimate of what the noise is in the final summed SS and OS polar images. The peak ratio is $\sim$ 2.3, and the ratio throughout the extent of the highly reflective region is > 1. The occurrence of high cross sections and polarization ratios > 1 is an uncommon one in radar studies, but has been found for other icy bodies in the solar system (Campbell *et al.* 1978; Goldstein and Green 1980; Ostro *et al.* 1992; Butler *et al.* 1993). Recently, similar behavior has been measured on parts of the Greenland ice sheet (Rignot *et al.* 1993). The mechanism is poorly understood, but the effect is probably due to the penetration of the radar wave into a relatively lossless medium which contains many scatterers (so–called "coherent backscatter") (Goldstein and Green 1980; Hapke 1990; Ostro and Shoemaker 1990; Hapke and Blewitt 1991). At the time of our 1988 observations, the season was southern mid–summer ($L_s = 295°.1$), so most of the southern seasonal cap should have been sublimated away, and indeed, measurements showed that this was the case (Iwasaki *et al.* 1990). So, at the time of our 1988 observations we were probing into the upper layers of the RSPIC, which must at the time have met the two criteria for coherent backscatter; transparency, and many scatterers.

4.4.1.1 RSPIC Transparency and Contamination

If the RSPIC were composed of pure H_2O ice, it would indeed be very transparent at 3.5–cm, as it has a very low absorption coefficient (Evans 1965; Warren 1984). Unfortunately, no accurate measurements exist of the absorption coefficient of pure CO_2 ice at microwave frequencies (Simpson *et al.* 1980; Warren 1986). Simpson *et al.* give an upper limit of $\tan\delta < 0.005$, where the loss tangent, $\tan\delta = \epsilon_i/\epsilon_r$ for a material with dielectric constant $\epsilon = \epsilon_r - i\,\epsilon_i$. It seems unlikely that the loss tangent for pure CO_2 ice would be nearly this large, as that for pure H_2O ice is about a factor of 50 less. In the following, we will assume that the microwave loss tangent for CO_2 ice is the same as that for H_2O ice, i.e., $\tan\delta = 10^{-4}$. If future measurements show the loss tangent of pure CO_2 ice is substantially higher, then our measurements strongly indicate that the upper layers of

the RSPIC were composed of H_2O ice during southern mid–summer in 1988. The real portions of the dielectric constants for H_2O and CO_2 ice at 3.5–cm are ~ 3.2 and ~ 2.25, respectively. At any rate, as contaminants are mixed in, the absorption can increase to the point where too much energy is absorbed during travel between scattering events. If we assume that the RSPIC is a smooth ice layer with buried subsurface scatterers, then a constraint on the amount of contaminant material can be deduced from the relation:

$$T^2 e^{-\chi s} > \frac{\eta}{4\pi} \quad , \tag{4.11}$$

where T is the Fresnel power transmittivity from vacuum into the ice medium, χ is the absorption coefficient of the material comprising the portion of the RSPIC probed, s is the total distance travelled, and η is the measured cross section. This can be rewritten:

$$\frac{\epsilon_i}{\sqrt{\epsilon_r}} < \frac{\lambda}{2\pi s} ln\left(\frac{4\pi T^2}{\eta}\right) = \xi \quad . \tag{4.12}$$

The amount of contaminant material will mainly affect the quantity on the lefthand side, while the density of scatterers affects that on the right (for given geometry and cross section). Table 4.4 shows values of ξ, for a wide range of values of packing fraction (ratio of volume of scatterers to unit volume) of subsurface isotropic scatterers. The values for s listed in Table 4.4 were obtained from a Monte Carlo simulation in which photons were allowed to penetrate into a non–absorbing infinite half–space. The photons were then scattered conservatively and isotropically a number of times until they left the upper surface. The simulation is described in Chapter 3, with one difference. Instead of using only one size of scattering particles, a power law distribution was allowed for. This changes the probability for any interaction per unit length, Σ, to the following:

$$\Sigma = \pi N_o \left(\frac{\lambda}{2\pi}\right)^{3-q} \int_{x_1}^{x_2} x^{2-q} \kappa_{ext}(x)\, dx \quad , \tag{4.13}$$

Table 4.4

Scattering Simulation

P	s	d_{95}	$\xi \times 10^4$
0.01	116.0[a] (173.3)[b]	61.6 (92.3)	1.238 (0.8289)
0.03	38.7 (56.1)	20.5 (30.3)	3.711 (2.560)
0.1	11.5 (17.1)	6.0 (9.2)	12.49 (8.400)
0.3	3.9 (5.7)	2.1 (3.1)	36.83 (25.20)

[a] $q = 3$ for power law size distribution of scatterers
[b] $q = 2$ for distribution

P, scatterer packing fraction; s, average total photon travel distance; d_{95}, depth beyond which 95% of the photons did not go; ξ, see equation (4.10).

where λ is the wavelength, $x = 2\,\pi\,a/\lambda$ is the size parameter for particles of radius a, κ_{ext} is the extinction cross section, and we adopt a power law expression for the number of particles of size a:

$$N(a) = N_o\, a^{-q} \quad . \tag{4.14}$$

If the packing fraction is held constant for all distributions, we have:

$$\Sigma = \frac{3\,\pi\,P\,\int_{x_1}^{x_2} x^{2-q}\,\kappa_{ext}(x)\,dx}{2\,\lambda\,\int_{x_1}^{x_2} x^{3-q}\,dx} \tag{4.15}$$

for packing fraction P. The integral in the numerator was evaluated numerically, using a Romberg integration scheme, with extinction cross sections calculated from the classical Mie scattering theory (see e.g., Wang and van de Hulst 1991). The values in the last column of Table 4.4 were calculated using a value of $\eta = 0.75$, at an incidence angle of $\theta_i = 65° \Rightarrow T = 0.88$, for CO_2 ice. The values for H_2O ice were

slightly higher, but were always within 10% of the CO_2 values. For the scatterer distribution, we used $q = 2$, and $q = 3$, with size cutoffs at $a_1 = \lambda/3, a_2 = 3\lambda$, i.e., scatterers from about 1 cm to about 10 cm. The numbers for $q = 2$ are in parenthesis in Table 4.4. Also shown in Table 4.4 is the value d_{95}, which is the depth beyond which 95% of the photons in the simulation did not penetrate. We take this as an indicator of the minimum depth of the portion of the RSPIC which we are probing, which is on the order of 10 m. Table 4.5 shows values of $\epsilon_i/\sqrt{\epsilon_r}$, to be compared with ξ, for both CO_2 and H_2O ices (H_2O values in parenthesis), with a range of volume fraction of silicate inclusions having dielectric: $\epsilon = 7.0 - i\,0.42$, which is typical of terrestrial basalts (Campbell and Ulrichs 1969). The dielectric constant of the ice–silicate mixture was calculated from (Kharadly and Jackson 1953):

$$\epsilon = \epsilon_1 + \frac{3V\epsilon_1\left(\frac{\epsilon_2-\epsilon_1}{\epsilon_2+2\epsilon_1}\right)}{1 - V\left(\frac{\epsilon_2-\epsilon_1}{\epsilon_2+2\epsilon_1}\right)} \quad , \tag{4.16}$$

where ϵ_1 and ϵ_2 are the complex dielectric constants of the ice and the silicate, respectively and V is the volume fraction of the silicate material. Comparison of the two quantities shows that for all but the extreme combination of very high scatterer packing fraction and very low contaminant inclusion fraction, the constraint is violated, i.e., too much energy is absorbed. So, the upper 10 meters or so of the RSPIC must have been very clean at the time, with less than 1% volume fraction of contaminating Martian dust.

4.4.1.2 RSPIC Scattering Centers

The other requirement is that the RSPIC contain many scattering centers. We will now investigate what these scattering centers could be. If we assume that the RSPIC is a layer of conservative, isotropic scatterers, then the expected radar return is given by (Muhleman *et al.* 1991):

$$I_c = \frac{\varpi P_t A_t(E)\Omega_b[H(\varpi,\mu)]^2}{16\pi\lambda^2\Delta f D^2} \quad , \tag{4.17}$$

Table 4.5

Dielectric of Ice with Silicate Contamination

V^a	ϵ_r	$\epsilon_i \times 10^2$	$\tan\delta \times 10^3$	$(\epsilon_i/\sqrt{\epsilon_r}) \times 10^4$	ϖ^b
0	2.25[c] (3.20)[d]	0.023 (0.032)	0.100 (0.100)	1.50 (1.79)	.999 (.998)
1	2.28 (3.23)	0.17 (0.25)	0.739 (0.770)	11.15 (13.83)	.989 (.982)
2	2.31 (3.25)	0.32 (0.47)	1.37 (1.44)	20.84 (25.91)	.985 (.972)
3	2.33 (3.28)	0.47 (0.69)	2.00 (2.10)	30.57 (38.03)	.978 (.959)
4	2.36 (3.31)	0.62 (0.91)	2.62 (2.76)	40.35 (50.18)	.972 (.956)
5	2.39 (3.34)	0.78 (1.1)	3.24 (3.41)	50.17 (62.37)	.965 (.950)
6	2.42 (3.37)	0.93 (1.4)	3.86 (4.07)	60.04 (74.60)	.959 (.943)
7	2.45 (3.39)	1.1 (1.6)	4.47 (4.72)	69.97 (86.87)	.950 (.936)
8	2.48 (3.42)	1.3 (1.8)	5.08 (5.36)	79.95 (99.19)	.946 (.928)
9	2.51 (3.45)	1.4 (2.1)	5.68 (6.00)	89.98 (111.54)	.940 (.920)
10	2.54 (3.48)	1.6 (2.3)	6.28 (6.64)	100.07 (123.94)	.932 (.911)

[a] volume fraction of silicate contaminant

[b] single scattering albedo for a power law distribution of spheres with the given dielectric

[c] numbers for CO_2 ice

[d] numbers for H_2O ice

where parameters are as in equation (2.1), with the addition of ϖ, the single scattering albedo of the scatterers, and $H(\varpi, \mu)$ which are the H functions of Chandrasekhar (1960), with $\mu = cos\theta_i$. Setting this equal to equation 2.1 yields:

$$\varpi[H(\varpi, \mu)]^2 = 4\eta(\theta_i) \quad , \tag{4.18}$$

which can then be solved for ϖ, assuming a value of η. A value of $\eta = 0.75$ at an incidence angle of 65° implies a single scattering albedo of: $\varpi \sim 0.987$. So, the scattering elements themselves must have a very high single scattering albedo, implying that they cannot have significant amounts of included contaminants, i.e., Martian dust. Table 4.5 shows values of average single scattering albedo for a distribution of ice spheres with the given amount of contaminant. The distribution had the same size cutoffs as for the simulation above, with a value of 3 for q. A value of 2 for q reduces the single scattering albedo by a few percent. The table shows that only if the spheres contain less than 1% by volume of dust do they have a high enough single scattering albedo. Therefore, the scatterers cannot be Martian rocks, or dust pockets or layers buried in the RSPIC. The alternative is that the scatterers are simply cracks or voids in the ice layer, which may or may not be filled with frost.

4.4.2 North Pole

Examination of the north polar images tells a significantly different story. In the north, there seems to be no region located northward of $\sim +75°$ which has the sort of effect measured in the south, i.e., high cross section OR polarization ratio > 1. There are two regions at lower latitudes which show marginally enhanced cross sections (peak OS cross sections ~ 0.14) but no polarization inversion (ratio of ~ 0.5). The fact that there was no highly reflective region associated with the north cap was of considerable surprise to us. It is not clear to us why the north polar cap displayed backscattering that was not in any manner similar to the south

cap, but we will examine three possible explanations.

4.4.2.1 Geometry

It is possible that the difference was due entirely to the different viewing geometry. During our 1988 measurements, the subearth latitude was $\sim -24°$, giving us a relatively good view of the pole and the RSPIC. During our 1992/93 measurements, the furthest north the subearth latitude got was $\sim +9°$, so the pole was considerably closer to grazing incidence. It is unfortunate that our experiment scheduled for December 9, 1992 was compromised by transmitter problems, as the subearth latitude was $\sim +12°$ at the time. At any rate, the difference may be simply due to the higher incidence angle, but there are several indications that this is not the case. First, the radar features seen by us on the north and south poles of Mercury (see Chapter 3), which were similar to the Martian RSPIC feature, were seen at an incidence angle of about 79°, similar to the 81° on December 29 on Mars. So, it seems that materials with these properties can be probed at such high incidence angles. It may be true that there is something fundamentally different about the structure of the material causing the effect on Mercury, but there is no compelling evidence that this is the case. Also, the large extent of the northern cap implies that there were icy regions which were at much lower incidence angles during the experiments, indeed comparable to the 66° of the south polar observations. However, to assess whether the geometry was indeed a factor, we examined the fits to a sensible backscatter function for the polar regions (see section 4.2 and Figures 4.3 and 4.4). The south polar feature still shows up in the fits for both polarizations, as expected. In the north, there are some features in the SS fit, near the southeastern edge of the residual cap, although the peak cross section of these features is down by about a factor of 6 from the RSPIC feature. Also, this feature does not show up at all in the OS fit. This seems to indicate that the geometry is a factor, but the reliability of the fits remains in question, since the excursion in incidence angle for most of the polar fits is less than 15°, and at high incidence

angles. This makes the extrapolation to normal incidence somewhat suspect.

4.4.2.2 Seasonal Cap

As a second possibility, the seasonal cap which was covering the RNPIC may have obscured the underlying icy material. At the time of the north polar observations, the Martian season was early northern spring ($L_s \sim 20°$), so a significant portion of the entire extent of the seasonal cap would be expected to still be present. This time of year is when the recession of the seasonal cap seems to halt each year, with the edge of the cap at a latitude of about 66° (James *et al.* 1992). Hubble Space Telescope images taken at about the same time as our observations confirm this (James *et al.* 1994). So, what exactly is the seasonal cap, and how could it have affected our measurements?

Leighton and Murray (1966) were the first to describe in a quantitative way the condensation and sublimation of CO_2 at the Martian poles. The condensation and sublimation arise as a consequence of the imbalance between absorbed solar insolation and reradiated thermal energy. The energy balance in polar regions is maintained by condensation in the winter, and sublimation in the summer. In the winter, temperatures drop until they reach the vapor–pressure equilibrium point of CO_2, which is about 150 K in Martian conditions. At that point, CO_2 begins to condense on the surface and in the atmosphere. The relative amount which condenses on the surface vs. that in the atmosphere seems to be controlled by the amount of dust in the polar atmosphere (Pollack *et al.* 1990). During clear conditions, the majority of the condensation occurs directly on the surface, while the opposite is true during very dusty conditions. At a dust opacity of ~ 1, approximately equal amounts condense on the surface and in the atmosphere. Observations indicate that the atmosphere was relatively dust free at the time of our observations, and for some time previously (Clancy *et al.* 1993), so most of the condensation must have occurred at the surface. The surface frost created by such condensation would have low intrinsic porosity, and would quickly go through

a process of densification to a polycrystalline layer. Even if the majority of the condensation occurs in the atmosphere, creating grains on the order of a few tens of microns or less in size (Pollack *et al.* 1977; Kieffer 1990), which then fall to the surface, the same process of densification into a low porosity polycrystalline layer should occur (Eluszkiewicz 1993). The total amount of CO_2 deposited in one winter varies with location, but a good estimate for the region of the RNPIC is 75 g cm^{-2} (Paige 1985). If this amount of CO_2 reaches its fully dense state ($\rho \sim 1.6$ g cm^{-3}), this would imply a layer with a thickness of about 50 cm. Both H_2O and dust are co–deposited along with the CO_2, but the amounts in a given year are very small. An estimate of the amount of co–deposited dust is about 10 mg cm^{-2}, which is between the estimates of Kieffer (1990), and Pollack *et al.* (1979), and implies a CO_2 to dust ratio of greater than 1000.

Assuming that the seasonal cap contains nothing which scatters efficiently at our wavelength, its effect on our measurements would be to introduce a loss term due to the absorption as the radar wave travels through the cap. The cross section, η (as defined in equation (2.1)), of a perfectly backscattering half–space ($\eta = 1$) which is covered by a layer of CO_2 ice would be:

$$\eta = \frac{T^2 L}{1 - \left(\frac{RL}{4\pi}\right)^2} \quad , \tag{4.19}$$

where T is the Fresnel power transmittivity from vacuum into the upper CO_2 layer, R is the Fresnel reflectivity $(1 - T)$, and L is a two–way loss term: $L = e^{-2\chi l}$, where χ is the absorption coefficient for the CO_2 layer, and l is the distance travelled in each direction in the layer. The term $2\chi l$ can be rewritten as: $4\pi d\epsilon_i/(\lambda\sqrt{\epsilon_r - \sin^2\theta_i})$ where θ_i is the incidence angle, λ is the wavelength, d is the depth of the CO_2 layer, which has dielectric $\epsilon = \epsilon_r - i\,\epsilon_i$. Table 4.6 shows values of the cross section for different depths of the covering CO_2 layer and incidence angles. These values were calculated with a CO_2 dielectric of $\epsilon = 2.25 - i\,2.25 \times 10^{-4}$, as discussed above. The Fresnel transmittivities were calculated by allowing the

Table 4.6

Effect of Seasonal Cap on Cross Section

	$\theta_i = 65°$	70°	75°	80°	85°
$d = 0.5$ m	.761	.683	.561	.373	.0990
1 m	.736	.660	.542	.360	.0953
2 m	.688	.616	.505	.336	.0890
4 m	.601	.537	.439	.291	.0768

d, the depth of the seasonal cap; θ_i, the incidence angle.

surface to have facets with an exponential distribution of tilts, with a roughness parameter of $\alpha = 0.1$ (Muhleman 1964). Table 4.6 clearly shows that while the effect of the seasonal cap is not negligible, it would not reduce the energy enough to mask the lower surface entirely. Thus, we conclude that the reason the RNPIC had no feature similar to that from the RSPIC can be due only partially to the presence of the seasonal cap. The features between 65° and 70° latitude in Figure 4.7 which have slightly enhanced cross section but no polarization inversion may, however, be due to the seasonal cap. If some regions of the cap were somewhat thicker than others at the time of observation, and contained many scatterers, then they might have enhanced cross section. The reason that they have no polarization inversion can be attributed to the fact that the layer was not thick enough to shield the underlying dust/rock surface, and thus there was a combination of regular surface scattering from the underlying dust/rock surface and coherent backscatter type scattering from the icy layer.

4.4.2.3 Physical and Compositional

If the lack of a highly reflective feature is not due to the different geometry or the effects of the seasonal cap, it must imply a fundamental difference between the

residual caps in the north and south. The difference must be caused by either of two things: either the ice of the RNPIC is not transparent, or there is a lack of scatterers therein. If the ice is not transparent, it implies the inclusion of some significant amount of contaminant, most probably Martian dust. There has been some indication that the north polar cap is "dirtier" than the south (Paige 1985), and we may be seeing the signature of this in our radar data. However, Kieffer (1990), has shown that the albedo of the RNPIC most probably implies that the ice is either old, coarse and very clean, or young, fine, and with a dust fraction similar to the current atmosphere. The thermal inertias derived by Paige (1985) indicate that the RNPIC is a coarse grained or nearly solid admixture of water ice, rock and dust. These two results taken together seem to imply that the RNPIC has very little dust, less than about 0.1% by volume (Kieffer 1990).

If there is a lack of scatterers, then there must either be a different source mechanism for the scatterers, or the RNPIC must destroy the scatterers at a higher rate than the RSPIC. We have shown above that the scatterers in the RSPIC are probably cracks or voids in the ice. Any crack or void which has a conduit to the atmosphere would be closed very rapidly (on a seasonal time scale) by condensation during the winter, and thus these types of discontinuities are probably not the ones of interest for us. Other discontinuities are probably removed through viscous relaxation over time, due to the burden of any overhead ice. Because the RNPIC is H_2O ice, it reaches higher temperatures in the summer than the RSPIC, which stays at the CO_2 frost point (Paige 1985). This may make the RNPIC much more efficient at the closing of cracks through viscous relaxation, i.e., annealing. To calculate a relaxation timescale, we used a simplified model where the ice is in adjacent blocks of length D, separated by cracks of width δ. We used an ice flow law of the form (Glen 1955):

$$\dot{e} = A\tau^n \quad , \tag{4.20}$$

where $\dot{e}$ is the sheer strain rate (or creep rate), τ is the sheer stress, and A is the inverse of the dynamic viscosity. If we take the sheer stress at any point as the

hydrostatic pressure of the column of ice above that point, then it can be written as $\tau = \rho g z$ for material with density ρ, at gravity g and depth z. The time required for the cracks to be reduced in width by a factor of 2 can then be written:

$$\Delta t = \frac{\delta}{2 D A (\rho g z)^n} \quad . \tag{4.21}$$

Now, the parameter A has a dependence on temperature, T and hydrostatic pressure, P, given by:

$$A = A_o \exp(-Q/RT) \exp(-PV/RT) \quad , \tag{4.22}$$

where R is the gas constant, Q is the activation energy and V is the activation volume. The measured value of V is small (Weertman 1973), and therefore $Q \gg PV$ for the low hydrostatic pressures in the upper meters of the residual ice caps, so we have ignored the volume term in the above expression. Assuming that we know the temperature as a function of depth, this leaves the following parameters: δ, D, A_o, Q, and n. In order for the cracks to be efficient scatterers, they should have widths of the order of the wavelength, which gives us some constraint on δ. The value for D can be estimated from the scattering simulation above, and is given by $D = 1/\Sigma$, so we can constrain it's value as well. Unfortunately, the ice rheology parameters are far less constrained. For H_2O ice, the problem is not that these parameters are not known at all, but that they haven't been measured under the proper conditions. Generally all laboratory tests and field measurements designed to observe the values for these parameters are done at Earth Artic/Antartic conditions, i.e., temperatures above about 220 K. This is not only not cold enough for Mars, but indeed the ice may have different structure. At any rate, if we use the best values found at low temperatures, we have $Q = 60$ kJ/mol (Weertman 1983), and $A_o = 5.3 \times 10^{-3} \mathrm{Pa}^{-1}\,\mathrm{s}^{-1}$ for $n = 1$ (Doake and Wolff 1985), or $A_o = 4.3 \times 10^{-13} (\mathrm{Pa}^{-1})^3\,\mathrm{s}^{-1}$ for $n = 3$ (Paterson 1981; Weertman 1983). With a given temperature profile, a relaxation timescale profile could then be calculated.

We chose a very simple temperature profile with a surface temperature of 190 K, a linear decrease to a temperature of 155 K at 0.5 m depth, and a constant 155 K to 100 m depth. The calculated minimum relaxation times were then $\sim 10^7$ years for diffusion creep ($n = 1$) and $\sim 10^6$ years for power law creep ($n = 3$). This was for a crack width of $\delta = 1$ cm, and a block width of $D = 0.5$ m. Thus, even at the higher temperatures of the RNPIC, ice with rheology typical of that on Earth would retain cracks of even 1 cm width for very long times. If the ice is not hexagonal (ice I_h, as on Earth), but rather cubic (ice I_c), which it may well be at the lower Martian temperatures, then it may even be harder and able to retain cracks for longer periods (Poirier 1982). H_2O ice at the temperatures of the RSPIC ($\sim$ 142 K) would also be even harder. Unfortunately, we have found no measurements of the rheological properties of CO_2 ice, under any conditions. Even though it seems likely that it is much softer, we hesitate to say much about it until the measurements have been made. If it turns out that CO_2 ice is so soft that centimeter size cracks should close on short timescales, then it would probably indicate that the RSPIC was either wholly H_2O ice at the time we observed it, or that it was H_2O ice overlain by a relatively thin (10's of meters at most), and scatterer free CO_2 ice layer.

The most likely mechanisms for crack and void production in the ice of the residual caps are through either motion or thermal processes. Since the RSPIC most likely stays at near constant temperature throughout the year, production of discontinuities through thermal processes would be practically nonexistent there. On the other hand, when the RNPIC changes from sublimating the seasonal CO_2 ice to sublimating the residual H_2O ice, the temperature rises as much as 2.5 K/day (Paige 1985), which is probably enough to cause thermal cracking to significant depths (Mackay 1993). Production of discontinuities through motion can either be due to the motion of the ice itself (glaciation), or through ground motion (tectonics). Since Mars has been relatively quiescent in its recent history (excluding the Tharsis environs) the majority of production through motion is most likely

through glacial type processes. If it is the crack production which is different for the two residual caps, then this may indicate that the south polar regions have significantly more relief than the north polar regions, and hence more ice motion. Alternatively, the increased amount of ice motion may be caused by the fact that the upper portions of the RSPIC are CO_2 ice, and the CO_2 ice is much "softer" than H_2O ice, thus allowing it to flow much faster. There is then the problem of needing the ice to flow so fast that it has no time to anneal, even though it is relatively soft.

4.4.3 Conclusions Regarding Polar Regions

We have measured the backscattering characteristics of the north and south polar regions of Mars. There is a highly reflective feature in the south, with polarization ratio > 1. The location of this feature corresponds very well with the position of the RSPIC, and is certainly caused by it. There is no such feature in the north polar regions, however. We feel that there are 3 possible explanations for this. First, the viewing geometry was different enough when we observed the two polar regions that part of the difference may be attributable to an incidence angle effect. Fits of the data in the north to a sensible backscatter function to correct for viewing geometry seem to indicate the presence of features with slightly enhanced reflectivities, but the reliability of the fits remains in question at the large incidence angles near the pole. It is clear, however, that a simple correction for viewing geometry does not explain the absence of a feature in the north, as a feature as bright as that at the RSPIC taken to the incidence angles of the RNPIC would have shown up clearly in the raw data itself. Second, the north polar measurements were taken in early northern spring, so the bulk of the northern seasonal cap was still lying on top of the residual cap. While the attenuation in the seasonal cap by itself cannot explain the absence of high reflectivities, it may be a contributing factor. Third, there may be some fundamental difference between the north and south residual caps, aside from the possibility that the south is CO_2, and

the north is H_2O. This difference may be that the north residual cap has enough contaminants (dust) mixed in to a depth of 10's of meters that the penetrating radar wave is absorbed. Alternatively, there may be some difference in either the production or destruction of cracks and voids in the two residual caps. This would imply that the RSPIC was either more efficient at creating such discontinuities, or the RNPIC was more efficient at destroying them. Until we have better rheological data for both H_2O and CO_2 ices under the proper conditions, and a measurement of the loss tangent of CO_2 ice at 3.5 cm, pinning down such differences remains speculative.

Determining which of these 3 factors is the most important for the difference between the two residual caps requires more measurements. We have an opportunity to observe the RNPIC at much better viewing geometries (subearth latitudes as high as $\sim +20°$), and in the absence of the seasonal cap (L_s from about 85° to 130°) in the spring of 1995, when the VLA will again be in it's A configuration. This will provide some of the answers, and the rest can be addressed by measurements of the rheology of both CO_2 and H_2O ice, and measurement of the loss tangent of CO_2 ice.

4.5 "Stealth(s)"

Inspection of the images of Appendix F shows a dark region extending west from the region of the Tharsis volcanoes in both polarizations. This region also shows up clearly in the fits described above, shown in Figures 4.3 and 4.4. Pixels in the region show radar cross sections which are indistinguishable from the noise in most snapshots, hence we have termed the region "Stealth" (Muhleman *et al.* 1991). In that paper, we determined that a region was contained in Stealth if in three consecutive snapshots, its pixels had signal at or below the noise in the SS images. Here, we modify the criterion for containment in Stealth to be if the global fit to the SS polarization produces a value of A_{ss} (cross section at normal

incidence) which is less than 1.25%. The value of 1.25% is a rough estimate of the noise level in the fits. Figure 4.9 shows a portion of the map showing A_{ss} taken from the global backscatter fits described above, smoothed to 3° resolution, with the outline of our best estimate of the boundary of the Stealth region. Also shown on that figure is the boundary presented in Muhleman *et al.* (1991) for comparison. Any such determination of the exact boundary of the region must necessarily be somewhat arbitrary, so we are not implying that the outline shown in Figure 4.9 is that exact boundary, it should only be used to obtain a general idea of where the region is. Estimating the extent from the OS fits would provide a similar boundary. There are certainly regions within the boundary which have measureable signal in some snapshots, and a detailed examination of all locations for all geometries is pending.

So, what do the very low cross sections of this region really mean? There are two possible physical end–member models which could explain the cross sections: (1) the region is an infinite half–space with impedance matched to free space, i.e., there is no reflection at the boundary of the surface, or (2) the region is perfectly conducting, but smooth, and tilted away from the radar in the particular geometries which we observed in, i.e., there is reflection at the boundary, but none of the energy is reflected back in the direction of the observer. There are strong arguments that the first explanation is the correct one. The fact that we observed in many different geometries, including two different subearth latitudes, with the region visible makes it less likely that the surface was simply tilted away from us at all times. Also, the measurements in 1992 had subearth latitude very near the northern boundary of Stealth, and while the OS cross sections in the region are reduced, they do not go away entirely (or reduce to near the equivalent SS cross sections), which would happen if the region were very smooth, and tilted away from us on that occassion. Measurements have been made with the Goldstone antenna when the subearth latitude crossed near the center of Stealth, and again, while the OS echo energy from the region was reduced significantly, it did not vanish entirely

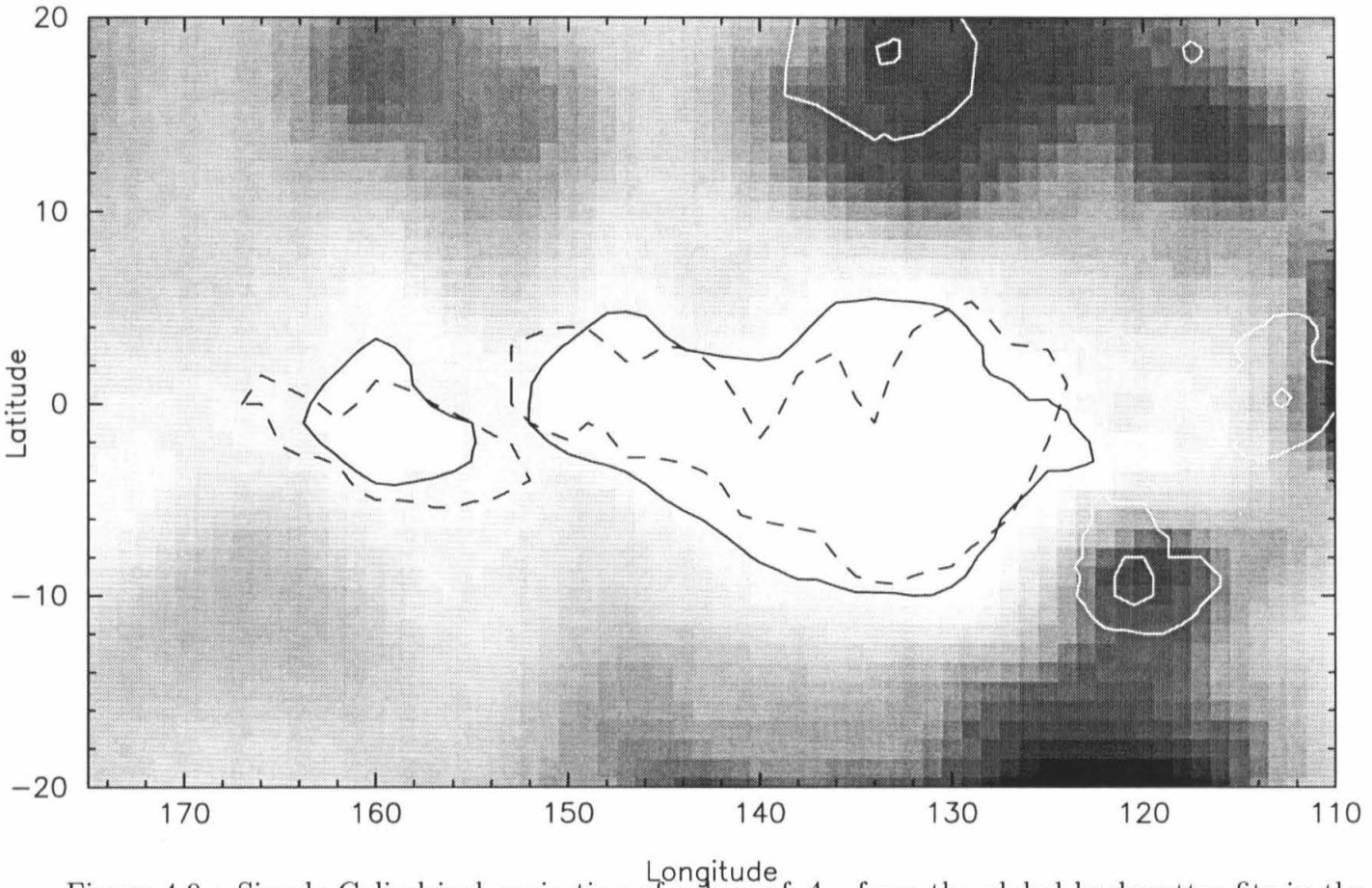

Figure 4.9 : Simple Cylindrical projection of values of A_{ss} from the global backscatter fits in the region of "Stealth." The solid black line is the 1.25% contour for A_{ss}, which gives our best estimate of the boundary of Stealth. The estimate of Muhleman *et al.* (1991) is shown as the broken black line. White outlines denote the approximate geological boundaries of the calderas and shields of the Tharsis volcanoes (from Scott and Tanaka (1986), and Greeley and Guest (1987)). Gray scale range is from -.8% to 48.4%.

(Thompson *et al.* 1992). The fact that the OS cross sections in the region are so low also supports the first explanation. Thermal inertias measured for the region are very low (Christensen 1986; Palluconi and Kieffer 1981), also indicating that the surface is comprised of fine grained, low density material, supporting the first explanation. Passive radio measurements of the surface at 2 and 6 cm suggest that the density of the region is very low (Rudy 1987), although those measurements are globally averaged over longitude, and thus are not resolving the region in that dimension. Other passive radio measurements (at 1.3 cm) which truly resolve the area suggest that the microwave emissivity of the region is very near unity (D. O. Muhleman, private communication), supporting the idea of near zero reflectivity. The second explanation is also less physically appealing, as regions with such super–smoothness are rarely encountered on real surfaces. Thus, we have pursued modifications of the first explanation, i.e., Stealth is a very underdense region with a lack of scatterers to significant depth. Such a region would have very low cross section because there would be little reflection from the actual surface, and the energy of the radar wave would be absorbed by ohmic losses in the subsurface before encountering anything which could scatter it back.

In order to estimate the depth of the Stealth deposit, we perform a calculation similar to that leading to equation 4.19. We take a layer of depth d, and dielectric constant $\epsilon = \epsilon_r - i\,\epsilon_i$ over an infinite half space with backscatter properties of the average Martian surface, i.e., with backscatter cross section η_s. Since minimum depths are desired, the calculation is performed at normal incidence. The observed cross section of such a surface is:

$$\eta = 4\,\pi \left(R + (1 + R\,L') \frac{T^2\,L'}{1 - (R\,L')^2} \right) \quad , \tag{4.23}$$

where R is the Fresnel power reflectivity at normal incidence, T is the Fresnel power transmittivity, and L' is a loss measure given by:

$$L' = \frac{\eta_s}{4\pi} e^{\frac{-4\pi d \epsilon_i}{\lambda \sqrt{\epsilon_r}}} \quad , \tag{4.24}$$

where λ is the wavelength. We adopt the average SS backscatter value at normal incidence (from averaging all of the solutions to the global backscatter fits, see Table 4.3) of 0.06 for η_s. Now, if equation 4.23 is taken as shown, it is incredibly hard to get a measurement of cross section as low as 0.015, our definition of Stealth. This is due to the reflection at the very surface (the $4\pi R$ term). Even a surface with ϵ_r as low as 1.15 has a cross section higher than 0.015. There are indications, however, that the surface of Stealth is very rough, both from our OS measurements and those of others (see e.g., Simpson *et al.* 1978a; Thompson *et al.* 1992). In light of this, it is probably appropriate to drop the surface reflection term, since multiple reflections will probably occur at the surface, and the first R in the expression will be replaced by R^m (for m bounces), which goes to 0 rapidly. With this modification, we get the depths presented in Table 4.7 for the Stealth deposit. The dielectrics shown were calculated by scaling a typical basalt dielectric at 1 g cm^3 to the desired density using the Rayleigh mixing formula (Campbell and Ulrichs 1969). It is not clear that these dielectrics are appropriate, as the deposit may have high porosity (i.e., be pumice or a tuff, see below), and thus it may have a lower dielectric. It has also been shown that the Rayleigh scaling formula does not work for rocks with high porosity (Campbell and Ulrichs 1969). In order to try to account for this, we performed some of the calculations with reduced values of ϵ_i, as shown in Table 4.7. There is an indication that the depth is at least somewhat deeper than those shown in Table 4.7 in the measurements of very low cross sections for this region at 13–cm (Harmon *et al.* 1992*b*). We therefore estimate that the Stealth region is probably at least as deep as 5 meters. It can of course be much deeper, and a good measurement of the OS cross section of the

Table 4.7

Minimum Depth of the Stealth Deposit

ρ	ϵ	D (m)
0.1	1.077 - i .00086	4.69
0.1	1.077 - i .00043	9.38
0.2	1.16 - i .0019	2.20
0.4	1.33 - i .0043	1.04
0.4	1.33 - i .00215	2.07
0.6	1.53 - i .0073	0.65
0.8	1.75 - i .0112	0.45
1.0	2.00 - i .0160	0.33

region when it is directly under the radar may give the true depth of the region. For this determination, a longer wavelength would be desirable. Now that we have an idea of the physical state of the Stealth region, we can investigate what it means geologically.

The Stealth region is between the provinces of Amazonis and Memnonia, in the eastern part of what has been called Mesogaea. It has portions in what have been mapped geologically as the Memnonia, Amazonis, Tharsis and Phoenicis Lacus quadrangles. The western half of the southern boundary of Stealth coincides very well with the boundary between the northern lowlands and the southern highlands. The break between the east and west sections of Stealth is caused by the Mangala Valles region, a proposed large outflow channel caused by catastrophic flooding (Tanaka and Chapman 1988). The geology of the region where Stealth is has been studied by many investigators (see e.g., Scott and Tanaka 1982; Carr 1984; Schultz and Lutz 1988). The region appears to contain a very thick deposit of

loosely consolidated (very friable) material which has undergone extensive wind erosion (see Cutts and Smith 1973, McCauley 1973, and Ward 1979, in addition to the just mentioned references). There is no distinct geologic, topographic, or albedo region which corresponds with Stealth. In fact, it seems to contain portions of very different geological terrains, and covers a topographic range of $\sim$ 7 km above the datum in the east, to near the datum level in the west (slopes in the region are generally less than 1°, in a northwest direction). From the geologic map of Scott and Tanaka (1986), much of the eastern and northern portion of Stealth lies in their upper and middle Medusae Fossae units (Amu and Amm). They interpret the upper portion of this formation to be a nonwelded ash–fall or ash–flow tuff (ignimbrite) or thick accumulation of eolian debris. There is some argument against this (Francis and Wood 1982; Shultz and Lutz 1988), but we agree in principle with this interpretation, since this would be a good candidate for the material comprising Stealth. It has been shown that a terrestrial ignimbrite is relatively radar bright (Fielding *et al.* 1986), indicating that the material is more likely an ash fall or tephra. Radar sounding of ash fields on Kilauea (Gaddis *et al.* 1989) and the Galapagos (recent X–SAR results) have indicated that they have very low cross sections, which provides confirmation of this interpretation. Scott and Tanaka (1982) further suggest that the source of the material (ash) was probably a series of fissures and vents now covered up by the material itself. We suggest that while this may be the case, it may also be that the source of at least part of the materials is the Tharsis shield volcanoes Pavonis and Arsia Montes. We make this suggestion based upon the eastern extent of Stealth, which almost abuts the Arsia Mons caldera, and the smaller volcanoes of Biblis and Ulysses Paterae. In fact, the entire southeastern portion of Stealth lies directly on top of what has been mapped as undivided Tharsis lava flows (Scott and Tanaka 1986). It is hard to understand how lava flows could have such low cross sections, particularly considering that much of the rest of the Tharsis (and Elysium) flows have very high cross sections. It must be that these flows are covered by at least a thin

layer of material similar to that described above, which has not been recognized previously, probably due to resolution constraints. Indications are that the current wind direction is east to west in this region (Ward 1979; Thomas and Veverka 1979; Lee *et al.* 1982). The development of yardangs in the region also indicate that that has been the primary direction of wind for some time (Ward 1979). Wind streaks also indicate significant downslope winds from all of the Tharsis volcanoes, but especially Arsia Mons (Veverka *et al.* 1977; Lee *et al.* 1982). Thus, any material ejected from Pavonis and Arsia Montes would make its way into Stealth. A less likely explanation is that the material comprising Stealth is a very low porosity volcanic material other than ash, e.g., reticulite. The problem with this is that the material must have sufficient strength to support several meters of overlying material for long periods of time.

While Stealth is the most noticeable large region of low cross section on the planet, there are other regions which have low cross sections. It should be stressed at the beginning of this section that there are no other locations of low cross section which have been imaged by us in near as good a geometry as Stealth, and none which have cross sections as low as Stealth. In order to try to account for the poorer imaging geometry of the other regions of low cross section, we adopt the additional criteria that in order to be considered "stealthy," a region must have been imaged with a look angle at least as good as 35°. There is one other large region on the planet which satisfies these requirements, which is shown in Figure 4.10. Note that the region is much smaller in extent than Stealth ($\sim 2 \times 10^5\,km^2$, as opposed to Stealth, which is $\sim 10^6\,km^2$). The region is contained mostly in the northwest portion of the Argyre basin, in Argyre Planitia. On the map of Scott and Tanaka (1986), the stealthy area lies almost exclusively in the etched unit of Argyre Planitia (Nple). This is a unit which, similar to the Medusae Fossae units discussed above, has been heavily degraded by wind erosion, indicating a very loosely consolidated surface (Scott and Tanaka 1986; Carr 1984). In this respect, it is similar to the region of Stealth. This may be an indication that all surfaces

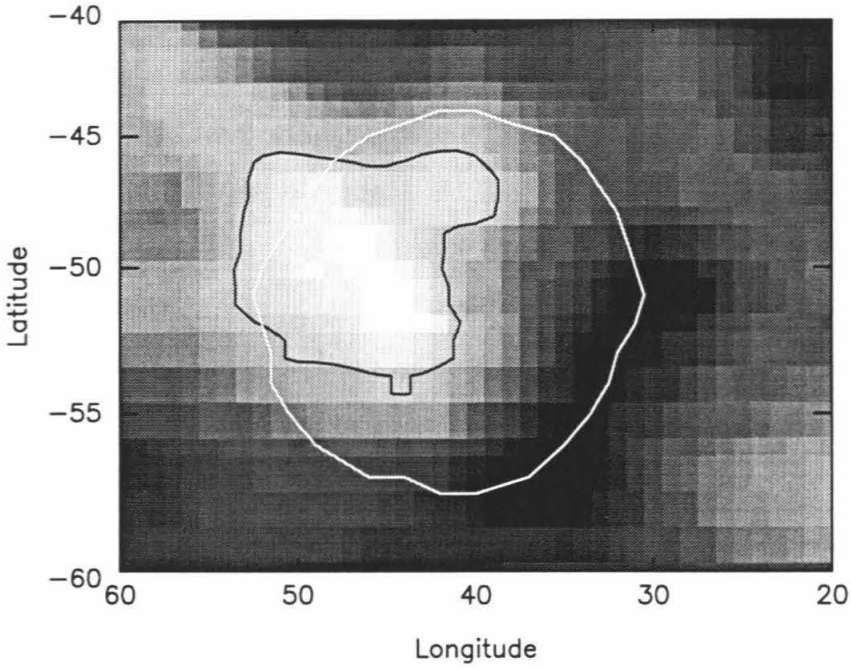

Figure 4.10: Mercator projection of values of A_{ss} for the global backscatter fits for the other "stealthy" region of Mars. The solid black line is the 1.25% contour for A_{ss}. The white outline is a very rough approximation of the Argyre basin rim. Gray scales are from .82% to 3.6%.

which are heavily eroded by wind on Mars are stealthy.

It is unfortunate that the Hellas basin was imaged with such poor geometry. Since it is the other major region of highly eroded southern plains (Carr 1984), we expect that it will be stealthy, similar to the Argyre region. The preliminary result is that the region of Hellas indeed has low cross section, but the best incidence angles for most of the region are $\gtrsim 60°$. Because of this, we cannot make any definitive statement about it. If future measurements allow us to make a statement about the materials in the Hellas basin, it will help in the geologic interpretation of that region. It has been proposed lately (Moore and Edgett 1993) that the Hellas basin is an area of net dust erosion, and that there should be very few rocks and boulders there. Again, this seems like the perfect setting for another stealthy region. The other region of heavy wind erosion on Mars is in the high latitude plains. Without a drastic increase in transmitter power, we can never hope to determine whether that region has similar backscatter characteristics from ground based radar experiments (because of the poorer geometry).

4.6 Volcanic Provinces

Since Mariner 9, it has been recognized that volcanism is one of the most important and wide spread geologic processes on the surface of Mars. Most aspects of Martian volcanism have been extensively studied, and there is a correspondingly abundant literature (see e.g., Carr 1973; Scott and Carr 1978; Greeley and Spudis 1981; Mouginis–Mark *et al.* 1992). In brief, there are several types of volcanic landforms on Mars, including: large shields, similar to the Hawaiian islands, but much larger; smaller steep sided domes; highland paterae; Alba Patera, which is a unique volcanic structure; and many types of volcanic plains. Several of these structures show up clearly in our data, and will now be discussed.

Aside from the RSPIC, and excluding regions under the quasi–specular spike, the young volcanic provinces of Tharsis and Elysium have the highest cross sections

on Mars. SS cross sections in the lava flows south of Arsia Mons (in the Daedalia Planum) are as high as 0.5 near normal incidence, and just south and east of Elysium are as high as 0.4. Figure 4.9 shows a portion of the map showing A_{ss} taken from the global backscatter fits described above, smoothed to 3° resolution, to emphasize the Tharsis and Elysium regions. All of the following maps will be shown at this resolution. Figure 4.9 shows that each of the large shield volcanoes has a backscatter enhancement associated with it, although the details of the feature vary from volcano to volcano. Table 4.8 shows the characteristics of the major features shown in Figure 4.9, most of which are related to one of the shield volcanoes or its flows. The exceptions are the feature just south of Orcus Patera, the two features in Amazonis Planitia, and the feature we call "South Spot," which will be discussed later. Also shown in Table 4.8 are values for two "average" regions for comparison, one of which has parameters very close to the global values, and the other of which has parameters very close to the global value when the high cross section volcanic regions are excluded. Aside from the high cross sections in both polarizations, it is immediately clear that the young volcanic regions depolarize very efficiently. In fact, they are almost like perfect diffuse reflectors, i.e., polarization ratios are ~ 1, and the exponent in the cosine law is between 1 and 2. This is an indication that these regions are incredibly rough in the size range from about 1 cm to about 10 cm.

Much work has been done lately on trying to classify volcanic flow types from radar backscatter data (Campbell *et al.* 1993; Gaddis 1992; Gaddis *et al.* 1989; Blom *et al.* 1987). The two major lava flow types are pahoehoe, which has a generally smooth, billowy surface structure, and 'a'a, which has a very jagged, clinkery surface on nearly all size scales. Terrestrial 'a'a flows seem to have an approximate lower limit on L–Band (24 cm) polarization ratio of 0.20 at $\theta_i = 10°$, increasing to 0.40 at 60° (Campbell and Campbell 1992). These numbers increase to about 0.30 and 0.50 at C–Band (Bruce Campbell, unpublished data). It appears harder to discriminate between pahoehoe and 'a'a using shorter wavelengths, due

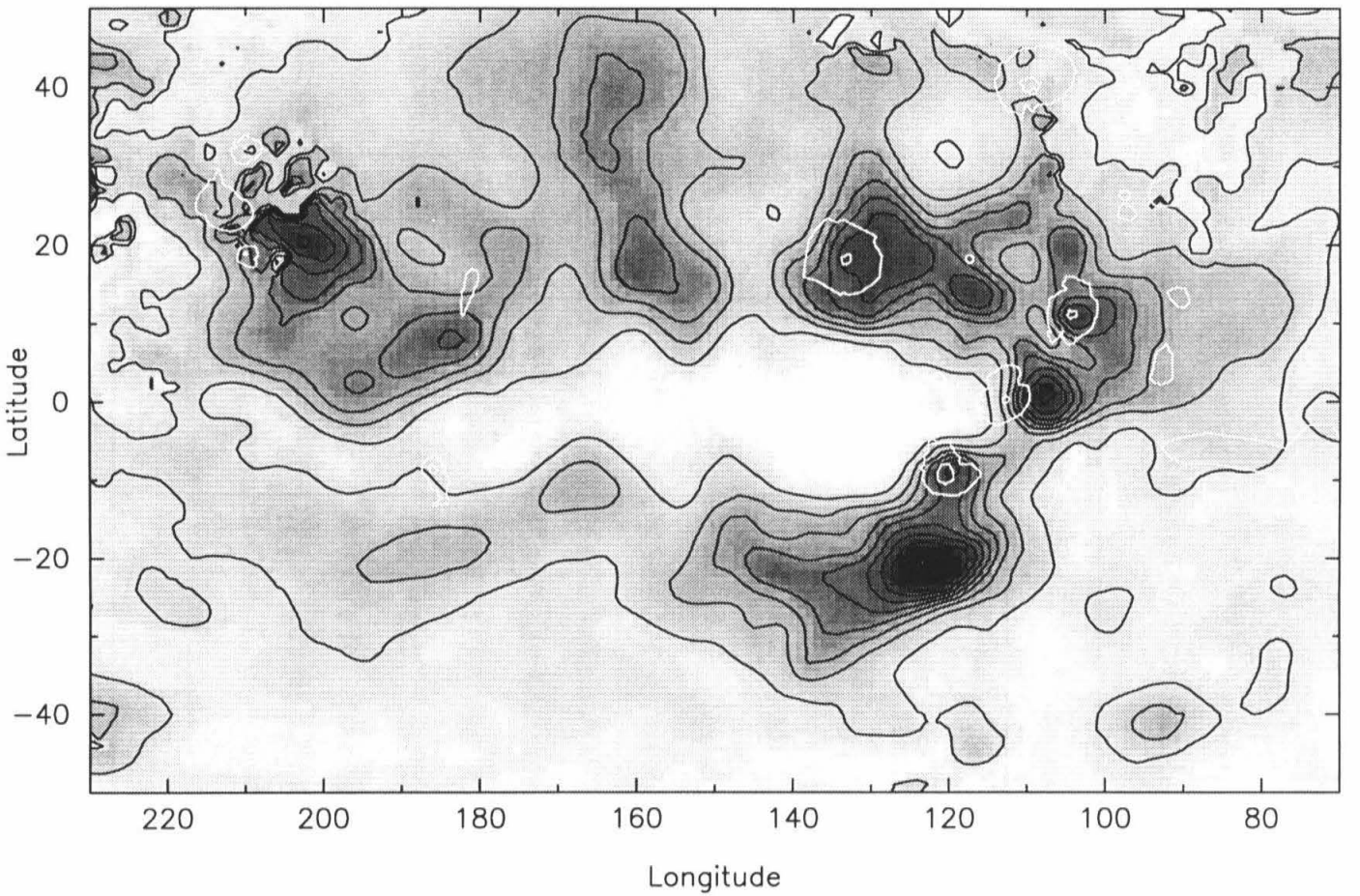

Figure 4.11 : Simple Cylindrical projection of A_{ss} from the global backscatter fits showing the regions of Tharsis and Elysium. Contours are at 5% increments. White outlines denote the approximate geological boundaries of the volcanic constructs (from Scott and Tanaka (1986) and Greeley and Guest (1987)). Gray scale range is from -.8% to 49.3%.

Table 4.8

Volcanic and Other Features

name	location	A_{ss} (%)	n_{ss}	A_{os} (%)	n_{os}	$\overline{\mu}^a$
Arsia	-9, 120	31.7	1.68	26.1	1.59	$1.18 \pm .03$
Daedalia	-21, 122	49.3	1.57	45.4	1.51	$1.10 \pm .02$
Pavonis	1, 107	40.7	1.93	28.4	1.56	$1.15 \pm .02$
Ascraeus	11, 104	33.7	1.71	22.7	1.27	$1.28 \pm .03$
Olympus	19, 133	31.6	1.25	22.7	0.87	$1.12 \pm .02$
East Olympus 1	18, 125	34.5	1.26	28.7	1.13	$1.09 \pm .02$
East Olympus 2	14, 117	34.9	1.56	27.5	1.37	$1.15 \pm .02$
Orcus	8, 184	25.4	0.74	22.5	0.62	$1.03 \pm .02$
Elysium	20, 203	40.7	1.22	25.4	0.73	$1.10 \pm .03$
South Amazonis	17, 160	23.6	1.11	18.4	0.78	$1.03 \pm .02$
North Amazonis	39, 163	21.9	0.55	20.4	0.63	$0.92 \pm .02$
South Spot	-41, 93	12.7	1.41	17.4	1.03	$0.62 \pm .03$
"average" 1	8, 40	6.4	0.74	10.1	0.59	$0.54 \pm .03$
"average" 2	0, 5	3.0	0.47	8.1	0.96	$0.41 \pm .07$

[a] $\overline{\mu}$ is the "average" polarization ratio for the feature, obtained by averaging the ratio of SS to OS polarization for each snapshot having the location visible with $30° < \theta_i < 70°$.

to the compression of the dynamic range of the signal (i.e., most things appear slightly rough at 3.5 cm). However, it seems clear that any flow surface with a polarization ratio approaching unity at 3.5 cm has a structure resembling 'a'a. We therefore suggest that the young lava flows on Mars have surface structures which resemble terrestrial 'a'a flows much more than terrestrial pahoehoes. Each of the major volcanic features listed in Table 4.8 will now be discussed briefly.

4.6.1 Arsia Mons

The region on Mars with the highest SS cross section, aside from the RSPIC, is just south of Arsia Mons, in the Daedalia Planum. SS cross sections there reach as high as 0.5 at normal incidence, which is quite high. Figure 4.10 shows a map of the parameter A_{ss} in the region around Arsia Mons, including the portion of Daedalia Planum that has the backscatter enhancement. It appears that the enhancement runs from the caldera of Arsia Mons, south across the flank of the shield into the volcanic plains of the Daedalia Planum, and then westward. This follows the trend of the regional topography. The enhancement is bounded on the east by the topographic high of the Claritas Fossae, just as the lava flows emanating from the southwestern flank of Arsia Mons are (Plescia *et al.* 1980). The flows in the part of the Daedalia Planum with the cross section enhancement probably came from the summit and flanks of Arsia Mons itself and are quite young (Scott *et al.* 1981). They are, however, not the youngest of the flows to come from Arsia Mons, which are confined to a region much closer to the shield. It does not appear that the backscatter cross section allows for discrimination between flows that are very young, and those that are slightly older.

4.6.2 Pavonis Mons

Just north of Arsia Mons is Pavonis Mons, another of the giant Tharsis shield volcanoes. Figure 4.13 shows a map of the parameter A_{ss} in the region around

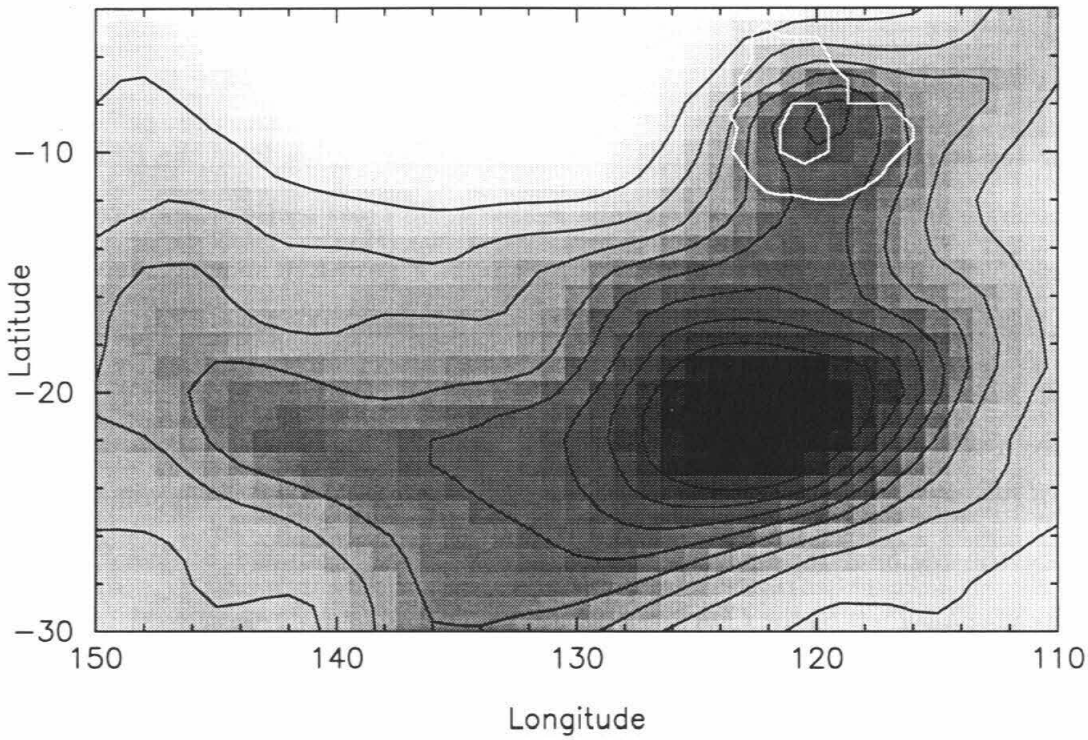

Figure 4.12: Simple Cylindrical projection of A_{ss} from the global backscatter fits showing the region of Arsia Mons. Contours are at 5% increments. The white outlines denote the approximate geological boundaries of the caldera and flanks of the shield (from Scott and Tanaka (1986)). Gray scale range is from -.8% to 49.3%.

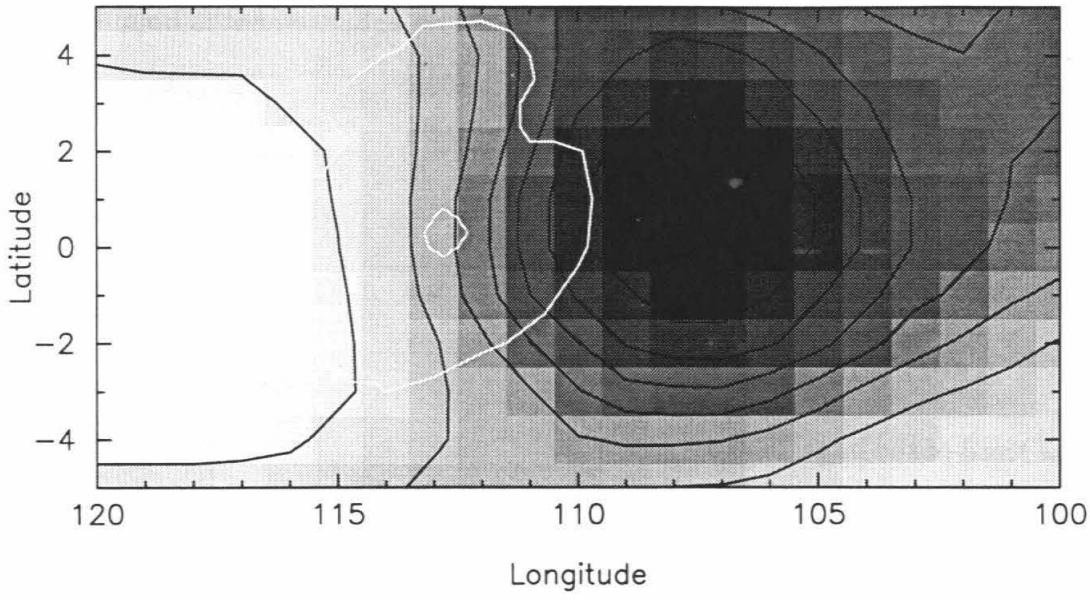

Figure 4.13: Simple Cylindrical projection of A_{ss} from the global backscatter fits showing the region of Pavonis Mons. Contours are at 5% increments. The white outlines denote the approximate geological boundaries of the caldera and flanks of the shield (from Scott and Tanaka (1986)). Gray scale range is from 1.8% to 40.7%.

Pavonis Mons. Pavonis Mons is unique among the large Tharsis shield volcanoes in that there is clearly no cross section enhancement associated with the caldera. In fact, the enhancement is clearly to the east of the volcano and barely extends onto the flanks of the shield itself. It is not clear why this is the case for Pavonis Mons alone of the Tharsis shield volcanoes. It would seem that for some reason the flows on the flanks of the shield are not as rough as those on the other shields. It has been noted that Pavonis Mons is unique among the three large shield volcanoes in that it alone appears to have a shield surface that postdates the formation of grabens and troughs (Zimbelman and Edgett 1992). If these flows were relatively smooth, the lack of an enhancement could be due to them. The cross section enhancement to the east of the shield is centered in a very young lava flow which actually extends from the southern tip of Ascraeus Mons (Scott *et al.* 1981). However, the northern portion of this flow (immediately south of Ascraeus Mons) has a significantly lower cross section, perhaps suggesting a transition from smoother lava near the source

vents, grading to rougher flows near at the end. The enhancement is bounded on the south by the northern portion of the Syria Planum, another volcanic province which is older than Tharsis. There is no clear geologic or topographic boundary to the east of the enhancement, but it may be the indication of a flow boundary which has been previously unnoticed.

4.6.3 Ascraeus Mons

The third of the large Tharsis shield volcanoes, Ascraeus Mons, is the northernmost of them. Figure 4.14 shows a map of the parameter A_{ss} in the region around Ascraeus Mons. The major enhancement seems to be restricted to the caldera and flanks of the shield itself. There is a slight enhancement which extends to the north, in the young lava flows there, which is itself bounded to the north by the Ceraunius Fossae. The slight depression in cross section just to the west of the shield is common to the three large shield volcanoes. These locations are in what have been called the "lobe–shaped deposits" (Carr *et al.* 1977), and contain odd deposits which have been interpreted to be landslides or debris flows (Carr *et al.* 1977; Scott *et al.* 1981), or ice/debris glaciers (Lucchitta 1981). Zimbelman and Edgett (1992) also argue that at least a portion of these deposits is pyroclastic in origin. Our data supports any of these interpretations, since these landforms would probably have lower cross section than the surrounding young lava flows.

4.6.4 Olympus Mons

Olympus Mons is the largest known volcano in the solar system, rising to ~ 25 km above the datum, and having basal dimensions of $\sim 600 \times 800$ km. The shield is bounded by a 2 to 8 km high scarp, whose origins are unknown. Figure 4.15 shows a map of the parameter A_{ss} in the region of Olympus Mons. The major enhancement seems to start in the caldera, proceed down the eastern flank of the shield into the very young lava flows to the east of the shield (some of the youngest

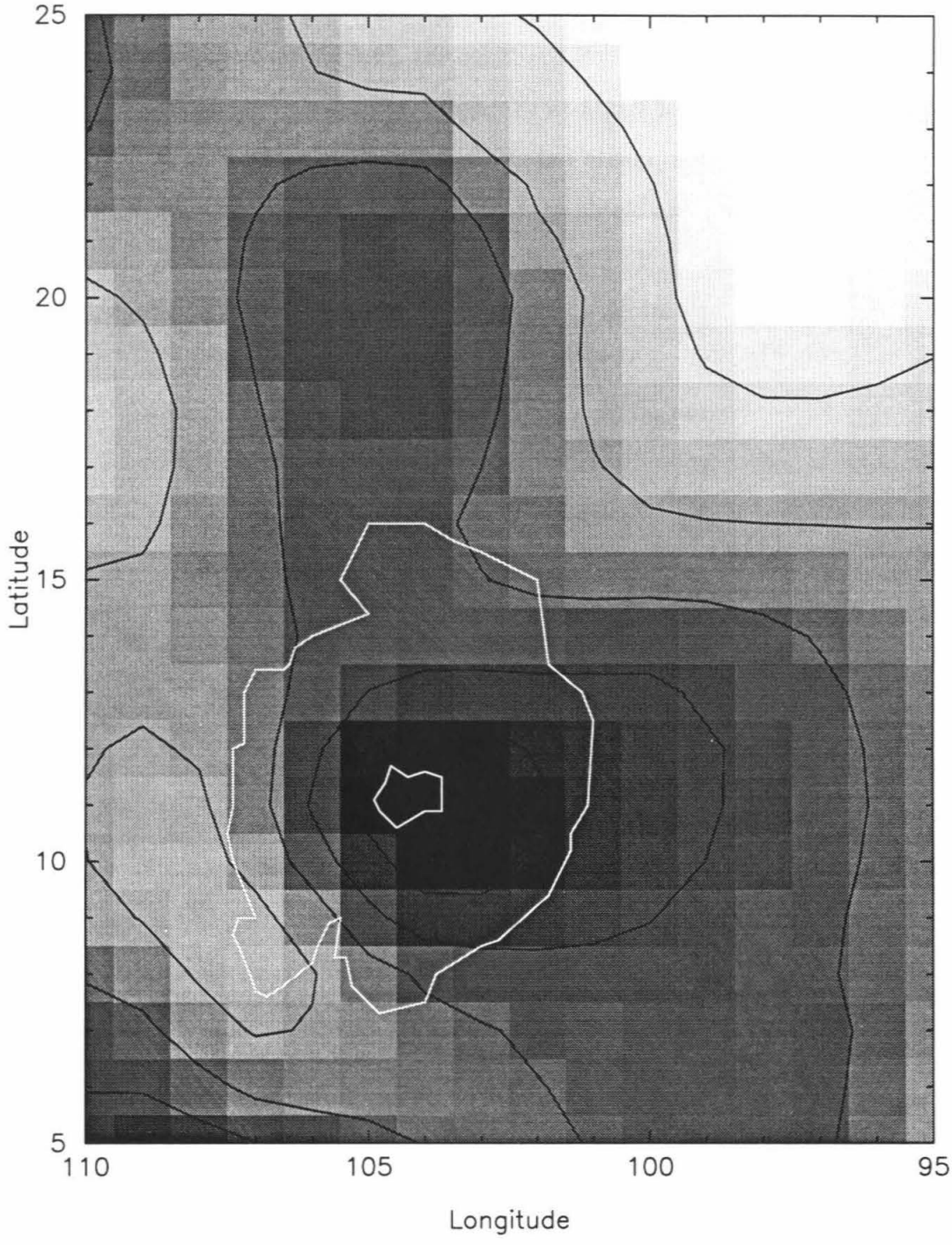

Figure 4.14: Simple Cylindrical projection of A_{ss} from the global backscatter fits showing the region of Ascraeus Mons. Contours are at 5% increments. The white outlines denote the approximate geological boundaries of the caldera and flanks of the shield and of the smaller volcano Uranius Patera to the north (from Scott and Tanaka (1986)). Gray scale range is from 7.1% to 33.7%.

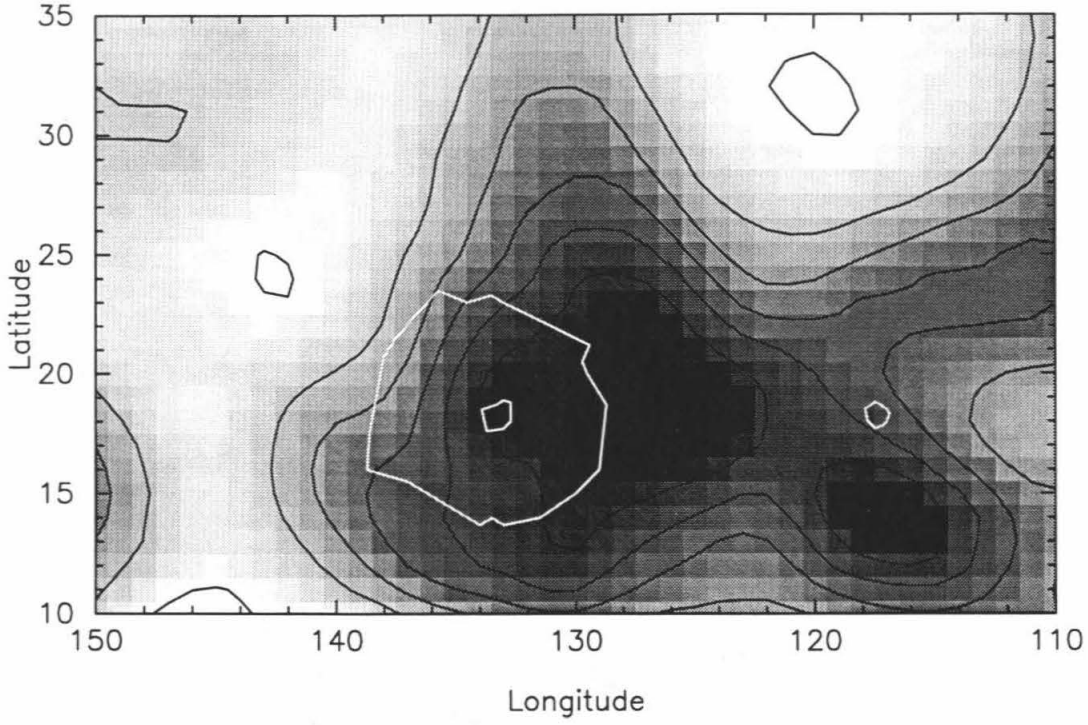

Figure 4.15: Simple Cylindrical projection of A_{ss} from the global backscatter fits showing the region of Olympus Mons. Contours are at 5% increments. The white outlines denote the approximate geological boundaries of the caldera and flanks of the shield and of the smaller volcano Jovis Tholus to the east (from Scott and Tanaka (1986)). Gray scale range is from 4.5% to 34.9%.

terrain on Mars (Scott *et al.* 1981)), continuing east and south into some of the young lava flows emanating from the northern flank of Pavonis Mons. The bend in the enhancement in its southern boundary at about longitude 123° is coincident with a deposit of Terra material (older exposed crust), and is probably caused by it. The flows immediately west and north of the shield are older (Scott *et al.* 1981), and have no associated cross section enhancement. This may be due to weathering of the lava surface there, or mantling by dust. Note also that the aureole has no related enhancement, except for the possibility of a slight enhancement on the eastern edge of the northern lobe. The origin of the aureole of Olympus Mons is still unknown, but many possibilities have been proposed, including that it is one of: eroded remains of an older volcano (Carr *et al.* 1973); eroded lava flows from Olympus Mons (Morris and Dwornik 1978); an eroded ash flow tuff (King and Riehle 1974); thrust sheets caused by the weight of Olympus Mons on bedded deposits (Harris 1877); the result of subglacial eruption of lavas (Hodges and Moore 1979); a deposit caused by gravity sliding of the outer flanks of Olympus Mons (Lopes *et al.* 1982); or, a series of pyroclastic deposits (Morris 1982). We cannot definitively discriminate between these models of formation from our data. It is clear that if both this region and the region comprising Stealth (see above) are ash flows or pyroclastic deposits, there is something different about the two areas. This is because although there is no cross section enhancement in the region of the aureole, it is nowhere near as poor a reflector as Stealth. In fact the aureole region has cross sections slightly higher than the average Mars, but less than the rest of the Tharsis region.

4.6.5 Alba Patera

Alba Patera is a unique volcanic feature on the surface of Mars, and has no analog on the surfaces of the earth, moon, or Mercury. It is very large (as large as 10^6 km^2 (Greeley and Spudis 1981)), and has a huge central caldera. It is a rather old volcanic feature that has been degraded and tectonically modified. Inspection

of Figure 4.11 (where the white outline is the approximate extent of the caldera only) shows that we see no cross section enhancement in the area of Alba Patera. This could be due to the fact that the flows around the volcano are older and thus more eroded than the younger flows of the Tharsis region, or that the flows are simply much smoother. There is some evidence that the flows are indeed smoother, as there are many tube–fed flows (which tend to be pahoehoe), and sheet flows (which tend to have very smooth upper surfaces) emanating from Alba (Greeley and Spudis 1981). It is probably a combination of the two effects that causes no cross section enhancement to exist for the region.

4.6.6 Smaller Tharsis Volcanoes

There are several smaller volcanic constructs in the Tharsis region, most of which are thought to be older shield volcanoes or domes which have been covered up to near their summits by the flows from the younger shield volcanoes (Greeley and Spudis 1981; Robinson and Garbeil 1994). These include Ulysses Patera, Biblis Patera, Jovis Tholus, Uranius Patera, Ceraunius Tholus, and Tharsis Tholus. Although these volcanic structures are generally too small for us to resolve, it seems clear that none of them have a related cross section enhancement (see Figure 4.11). This is probably due to the fact that these constructs are older, and more highly eroded than the younger Tharsis volcanoes and their flows.

4.6.7 The Elysium Region

The Elysium volcanic region is similar to the Tharsis region in that it sits atop a broad topographic high, and has several large central volcanic shields. It is late Hesperian to early Amazonian in age, making it much older than the youngest Tharsis regions, although the older Tharsis flows were probably being extruded at about the same time as those in Elysium (Scott and Tanaka 1986, and Greeley and Guest 1987). The largest of the three central shields is Elysium Mons, which

rivals the large Tharsis shield volcanoes in size. The other two central shields (Albor Tholus and Hecates Tholus) are much smaller, and seem to be older than Elysium Mons. Figure 4.15 shows a map of the parameter A_{ss} in the Elysium region, extending east through what has been called the Elysium Basin, which is just south of Orcus Patera (Scott and Chapman 1991). None of the three shield volcanoes has a cross section enhancement on its shield, with the possible exception of the very easternmost portion of the flank of Elysium Mons. The major enhancement extends east from near the base of Elysium Mons, in what has been mapped simply as Elysium lava flows (Greeley and Guest 1987). Greeley and Guest make no special distinction between the area of the enhancement and the rest of the Elysium flows. We suggest that this enhancement may mark a distinct flow from Elysium Mons. The distinction must reflect something about the texture of this flow, but whether the enhanced roughness is caused by the flow being younger than surrounding flows, or some other factor, is unanswerable with our data alone. There is another enhancement just south and west of Orcus Patera, in what has been called the Elysium Basin (Scott and Chapman 1991), and the Cerberus Formation (Plescia 1990). It is generally agreed that this entire region is the location of a large paleolake, and that there are extensive volcanic deposits there. However, Plescia (1990) argues that the coverage by volcanics is nearly complete, and that the volcanic activity postdates the fluvial activity. Scott and Chapman (1991), on the other hand, argue that substantial portions of the basin floor are sedimentary, and that the volcanics there predate the fluvial activity. Our data seems to favor the model of Plescia, since older, eroded volcanics, especially if weathered by standing water, would not have near the cross section enhancement that relatively young volcanic material would. This region is one of the few that has published results from the new 12.6 cm long–code technique at Arecibo (Harmon *et al.* 1992a). Their maps are very similar to ours, including the confinement of a backscatter enhancement to the eastern flank of Elysium Mons, an enhancement extending southeast toward Elysium Basin (our major enhancement), and the

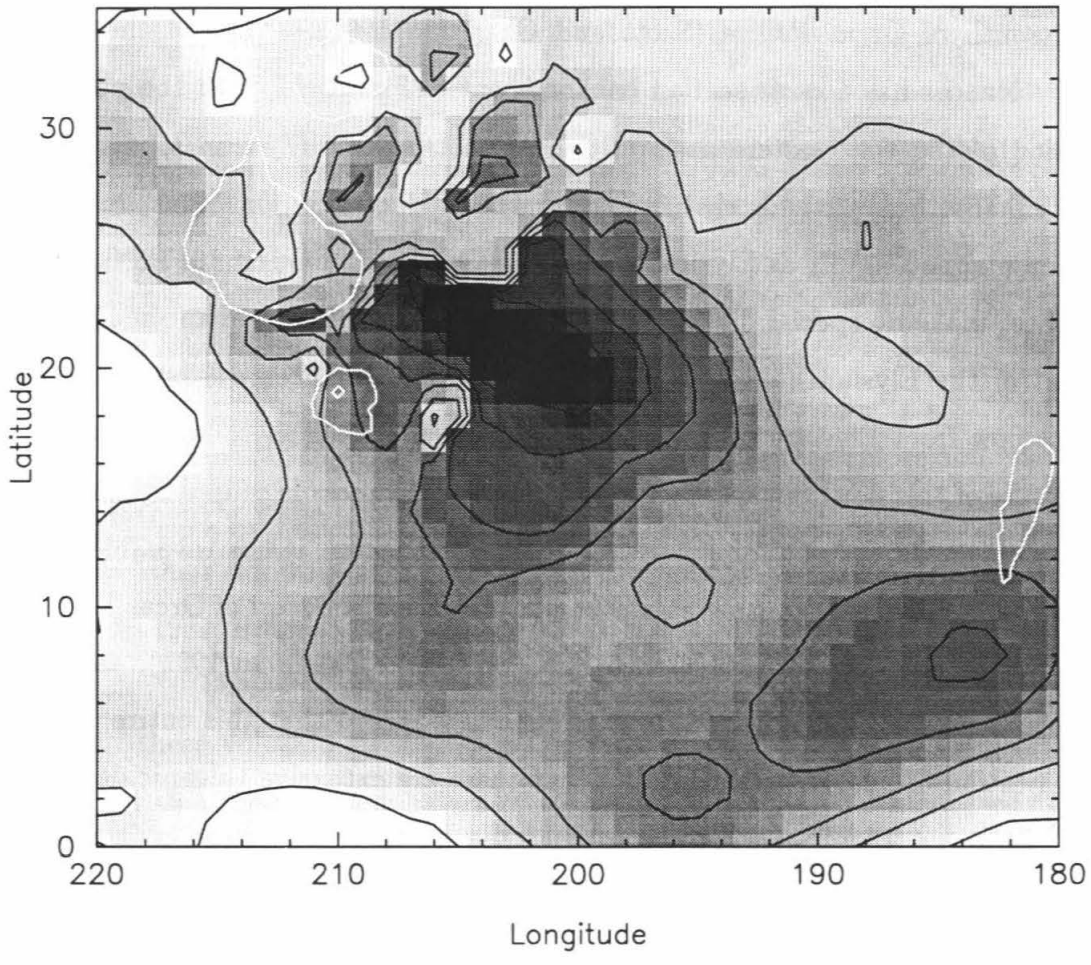

Figure 4.16: Simple Cylindrical projection of A_{ss} from the global backscatter fits showing the Elysium region. Contours are at 5% increments. The white outlines denote the approximate geological boundaries of the calderas and flanks of the three Elysium shield volcanoes (Hecates Tholus to the north, Elysium Mons in the center, Albor Tholus to the south), and Orcus Patera to the east (from Greeley and Guest (1987)). Gray scale range is from 3.0% to 40.7%.

enhancement just south of Orcus Patera, in the Elysium Basin.

4.6.8 Apollinaris Patera

Apollinaris Patera is the only large shield volcano outside of the Tharsis and Elysium regions (Greeley and Spudis 1981). It is located near the boundary between the southern highlands and northern lowlands. Its age is not well known, but estimates place it between the older Elysium and younger Tharsis provinces. Its outline is shown on Figure 4.11, at $\phi \sim -9°, \beta \sim 186°$ (from Greeley and Guest 1987). It can be seen from that figure that there is no enhancement associated with the volcano. This is consistent with the geologic analysis of the volcano given by Robinson *et al.* (1993), who contend that the main edifice of the volcano is composed mostly of air–fall deposits or pyroclastic flows, similar to the highland paterae (see next section). They also propose that the flows comprising what they call the "fan" are pahoehoe flows. Both of these types of volcanic materials would have no cross section enhancement, and thus we agree with this interpretation.

4.6.9 Highland Paterae

The highland paterae are older volcanic constructs in the southern highlands. They include Tyrrhena Patera, Hadriaca Patera, Peneus Patera, and Amphitrites Patera, all near the rim of the Hellas basin. The highland paterae were initially interpreted as shield volcanoes which erupted large volumes of fluid lava. However, more detailed analysis led to the interpretation that they are pyroclastic in origin, i.e., ash shields (Greeley and Spudis 1981). Even more recent studies have indicated that at least Hadriaca Patera and Tyrrhena Patera are consistent with an origin by the emplacement of gravity–driven pyroclastic flows (Greeley and Crown 1990; Crown *et al.* 1992; Crown and Greeley 1993). However, it is still not clear whether the pyroclastic materials need to be welded (as in an ash–flow tuff), or not (as in an ash fall). Examination of Figures 4.3 and 4.4 show that there seem to be

no cross section enhancements near these paterae (Hadriaca and Tyrrhena paterae are shown on those figures). However, results for these areas are compromised by the particularly horrible viewing geometry we have had for the Hellas basin region in general. We have no data at incidence angle less than $\sim 70°$ for the east rim of Hellas. Good data for the highland paterae may be able to answer the question of whether the material composing the volcanoes is welded or not, since welded materials (ignimbrites) should have a cross section enhancement (Fielding *et al.* 1986), while non–welded ash falls would not be expected to have such an enhancement (Gaddis *et al.* 1989).

4.7 Other Features

There are many other features in both the SS and OS cross section images (and in the fits) shown in Appendix F. This section will briefly discuss some of them.

In our initial analysis of data from the 1988 experiment, we only identified one location which had an SS cross section enhancement and was clearly not associated with the Tharsis region. We called this region the "south spot," since it was the furthest south feature we saw at the time (aside from the RSPIC feature). This feature shows up clearly in the SS images from 1988 (see Appendix F). Figure 4.17 shows a map of the parameter A_{ss} for this region. This region is centered at $\phi \sim -41°, \beta \sim 93°$, which is in a region between the Thaumasia Fossae (to the south) and Solis Planum (to the north). This is an exposed area of Noachian basement material (Scott and Tanaka 1986) which has been heavily cratered. Inspection of the highest resolution Viking images of the region show a very complex intersecting valley network (see e.g., Viking frame 532A16). However, this is certainly not a unique region in that respect, and it is not clear to us what is really causing the cross section enhancement there.

Near the region of the South Spot, there is an extensive region that in the backscatter fits has consistently high values of the SS cosine exponent n_{ss}. Ex-

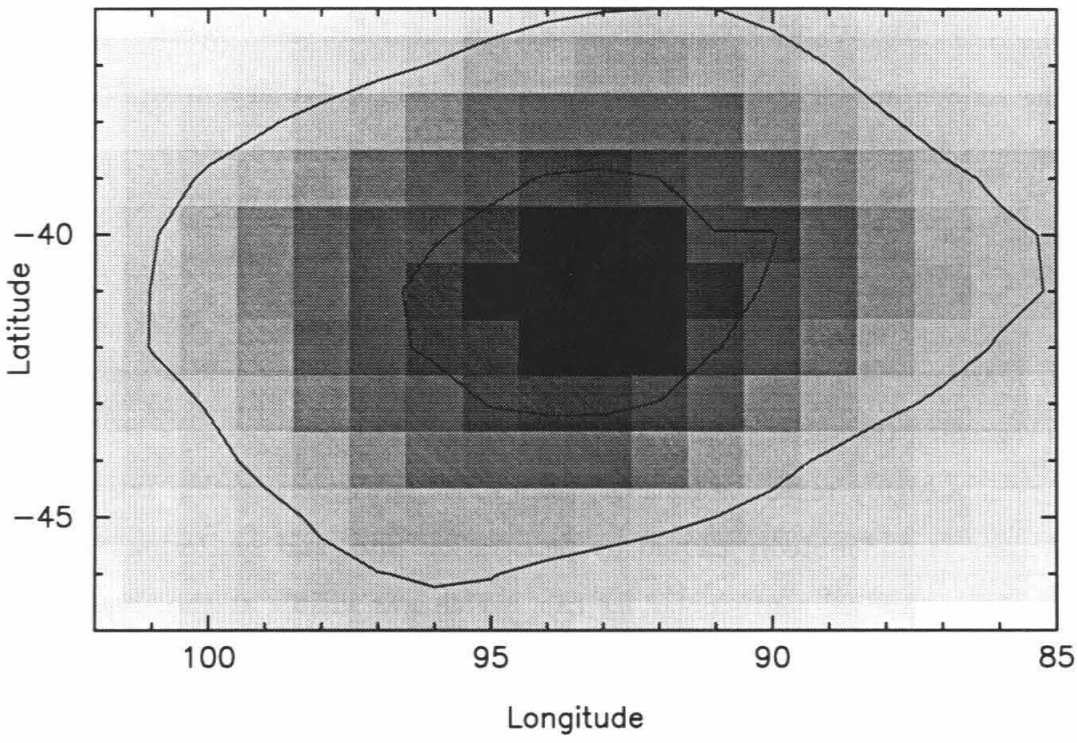

Figure 4.17: Simple Cylindrical projection of A_{ss} from the global backscatter fits showing the region of the South Spot. Contours are at 5% increments. Gray scale range is from 2.4% to 12.7%.

ponents in this region reach values as high as 9. The high values ($\gtrsim 4$) start at $\phi \sim -41°, \beta \sim 114°$, and trend southwest to $\phi \sim -58°, \beta \sim 132°$. This is the region of the Icaria Fossae, a series of deep grooves and troughs cut into the surface (Scott and Tanaka 1986). The sharp rise of the backscatter near normal incidence is thus probably due to the exposure of the groove bottoms in that geometry. However, it is curious that the OS exponents show no similar enhancement. Indeed, it seems that this sort of behavior explains the sharp rise of the OS reflectivities from the floor of the Valles Marineris near normal incidence (see Appendix F, and note the sudden appearance of the Valles Marineris in the images from 1/12/93 starting near snapshot 15). Why this is not the case remains a mystery.

4.8 Conclusions

Our Martian radar reflection experiments have yielded many new and exciting results regarding the surface and subsurface of the red planet.

There is a highly reflective feature in the south, with polarization ratio > 1. This feature is undoubtedly caused by penetration into, and scattering within, the ice of the residual south polar ice cap, which was visible at the time. We found no such feature in the north polar regions. We feel that there are 3 possible explanations for the difference: 1 - there is a fundamental difference in the structure and/or composition (amount of dust contaminant) of the two residual caps; 2 - the seasonal CO_2 cap which was present during the north polar experiments absorbed enough of the incoming radar energy to obscure the residual cap; or 3 - the north polar regions were imaged with slightly poorer geometry. Some combination of the three is most likely.

We have identified a very large ($\sim 10^6\,\mathrm{km}^2$), poorly reflecting area which we call "Stealth." This region displays cross sections which are indistinguishable from the noise in most geometries. It is most likely an ash fall deposit at least several meters in depth resulting from pyroclastic eruptions of Arsia and Pavonis Montes.

The Argyre Planitia exhibits similarly low cross sections, but is clearly a different type of deposit.

The volcanic provinces of Tharsis and Elysium have regions of very high cross section. Most of these regions are contained in fairly young lava flows. The regions have polarization ratios on the order of unity, indicating that they have a very rough surface morphology on size scales from 1 to 10 cm, similar to terrestrial 'a'a flows. The very high cross sections also indicate this, by terrestrial analogy. The large shields tend to have high cross sections on their eastern flanks, maybe indicating something about the direction of the wind in these locations.

Chapter 5

Summary and Conclusions

We have used the combined VLA/Goldstone radar instrument to probe the surfaces and subsurfaces of Mercury and Mars. This technique provides the first unambiguous cross section images of these surfaces at any radar wavelength, with surface resolutions as good as 150 km for Mercury, and 100 km for Mars. The analysis of the radar cross section images has provided a rich harvest of new information about the surface and near–surface of both planets.

Our Mercury experiments were the first to probe and identify an unusual feature at the north pole, which we have subsequently shown is probably due to the presence of water ice in permanently shadowed regions near the poles. A similar region exists near the south pole. This is an exciting discovery, and may have implications regarding similar deposits on the lunar surface. There are several large, quasi–circular regions on the surface of Mercury which have anomalously high radar cross sections. Only one of these "basins" is on the hemisphere photographed by Mariner 10, near the young, bright rayed crater Kuiper. The others are all in unphotographed terrain. The Caloris basin shows no such anomaly, indicating that these large structures are probably not large impact basins. Unambiguous identification must await photo reconnaissance.

Our Mars experiments were the first to probe and identify an unusually high cross section feature at the south pole, which is undoubtedly due to the ice of the

residual cap there. There is no such feature at the north pole, which we think could be caused by some combination of the following three effects: 1 - a fundamental difference in the structure and/or composition (amount of dust contaminant) of the two residual caps, 2 - the seasonal CO_2 cap which was present during the north polar experiments absorbed enough of the incoming radar energy to obscure the north residual cap, and 3 - the north polar regions were imaged with slightly poorer geometry. Many other regions with anomalous cross sections were found on the surface of Mars. The large volcanic provinces of Tharsis and Elysium have very high cross sections associated with them. These are most probably a result of the extremely rough surfaces of the large volcanoes and their associated flows. One of the most intriguing features in the Mars data set is a region which extends west from near Arsia and Pavonis Montes for over 2000 km, and has an areal extent of $\sim 10^6\,\mathrm{km}^2$. This region displays no cross section distinguishable from the noise, prompting us to name it "Stealth." The surface and near surface (to a depth of at least 5 meters) must be composed of very underdense material, with an absence of volume scatterers (rocks). The proximity of Stealth to Arsia and Pavonis Montes suggests that it may be comprised in part of pyroclastic materials which were blown westward after eruptions from these two large shield volcanoes.

5.1 Future Measurements

We plan to continue our radar probing of the surfaces of Mars and Mercury in the future, since there remain interesting questions which may be answered by such experiments. Measurements of Mercury will be carried out to try to complete the longitudinal coverage of the surface. While most surface locations have been imaged, many of them have only been imaged at poor geometries (i.e., large incidence angles). There are at least two outstanding questions which our previous experiments on Mars have raised. First is the curious difference in the scattering behavior of the two polar caps. We have an opportunity to address this

problem during the opposition in the winter of 1994/95. The subearth latitude will be at $\sim +20°$, and the season will be mid northern summer, so the north seasonal cap should be sublimated away. Unfortunately, the VLA does not move to its A configuration until the second term of 1995, so we will not get the best resolution. However, the relative importance of the three contributing factors to the difference in the polar cross sections can still be addressed. The second question is whether the Hellas basin is a "stealthy" region, similar to Stealth, and the Argyre Planitia. Unfortunately, there are no good opportunities to observe the Hellas basin in this decade, so this question must go unanswered for some time. There are still some longitudes of Mars which have relatively poor coverage, which we would like to observe, as well. The final planned observation in this vein is one which will probe the polar areas of the Moon, to see if there are deposits there similar to those in the polar regions of Mercury. There are many problems with such an experiment, however. Probably the most important is that the Moon is in the near–field of the VLA, thus making invalid one of the basic assumptions going into the relationship between sky brightness and the sampled visibility function (Thompson *et al.* 1991). Basically, the spherical nature of the received radiation is not accounted for. A correction for this effect, which is exactly accurate for a point source, can be applied to the received signal, and we hope that this will be adequate for a distributed source as well. Another problem is that the area illuminated on the surface of the moon by the 70 meter Goldstone antenna is very small. We may get around this by using the 34 meter antenna for illumination.

Appendix A

Radar Backscatter Fits

This appendix presents the technique and specific methods used to do fits to the types of sky brightness functions expected in planetary radar experiments. The general method can be applied to fits both in UV and image space, which are related by a 2D Fourier transform. In general, we have a set of measurements, $\{P_i\}_{i=1}^{N}$, which we would like to fit in a least squares sense to a sensible backscatter model. In all cases, the backscatter model is of the form: $S(a) = A\ f(a,\zeta)$, where A is some scaling coefficient, and $f(a,\zeta)$ gives the form of the backscatter function, for a given ζ. In order to do a least squares fit, first construct a χ^2 variable via:

$$\chi^2 = \sum_{i=1}^{N} w_i \left(P_i - S(a_i)\right)^2 = \sum_{i=1}^{N} w_i \left(P_i - A\ f(a_i,\zeta)\right)^2 \quad ,$$

where the w_i are the weights of the respective measurements. From this point on in this appendix, all summations are assumed to range from 1 to N, unless explicitly noted otherwise. χ^2 is then minimized by:

$$\frac{\partial \chi^2}{\partial A} = -2 \sum w_i \left(P_i - A\, f(a_i,\zeta)\right) f(a_i,\zeta) = 0$$

and,

$$\frac{\partial \chi^2}{\partial \zeta} = -2\, A \sum w_i \left(P_i - A\, f(a_i,\zeta)\right) \frac{\partial f(a_i,\zeta)}{\partial \zeta} = 0$$

from which (using $f_i = f(a_i, \zeta)$, and $f_i' = \partial f(a_i, \zeta)/\partial\zeta$):

$$A = \frac{\sum w_i P_i f_i}{\sum w_i f_i^2} = F(\zeta)$$

and,

$$A = \frac{\sum w_i P_i f_i'}{\sum w_i f_i f_i'} = G(\zeta) \quad .$$

So, the minimization of χ^2 has been reduced to solving the equation $F(\zeta) - G(\zeta) = 0$ for ζ, which may be done with some root finding method. In all cases we would also like to have the constraint $\zeta \geq 0$, knowing *a priori* that values of $\zeta < 0$ are physically unrealistic. This can be achieved by introducing the change of variable $m^2 = \zeta$. Now, $\partial\chi^2/\partial m = (\partial\chi^2/\partial\zeta) \cdot (\partial\zeta/\partial m)$, and since $\partial\zeta/\partial m = 2m$, the above equations for $F(\zeta)$ and $G(\zeta)$ are not changed, except for the replacement of ζ by m^2. After finding m^2, and hence ζ, via some root finding method, it is simple to calculate $A = F(\zeta)$. This is the general technique, which will now be expanded upon for fits in UV and image space for each of the SS and OS polarizations.

A.1 Image Space Fits

In this type of fit, we have a directly observed sky brightness function, and the data points are taken from one or more CLEANed images. The two polarizations will be treated separately in the following.

A.1.1 SS Case

In this case, a sensible backscatter model has the form:

$$S_{ss}(\theta) = A_{ss} \cos^n \theta$$

So, using the terminology of the above section (and using $c_i = \cos\,\theta_i$):

$$f_i = c_i^n \qquad ; \qquad f_i' = ln\,(c_i)\,c_i^n \quad .$$

A.1.2 OS Case

For this case, there are several theories regarding the scattering from rough surfaces. We will derive solutions for the two most commonly used models, the Muhleman model and the Hagfors model, which were developed independently at about the same time.

Muhleman, (1964), derived the radar response from a rough surface by estimating the probability of a given surface element being perpendicular to the radar line of sight. For the model of choice, he defined the surface as a series of connected facets, with an exponential distribution of heights and a Poisson distribution of lengths. The resulting expression is:

$$S_{os}(\theta) = A_{os}\,\cos\,\theta\,\left(\frac{\alpha}{\sin\,\theta + \alpha\,\cos\,\theta}\right)^3 \quad ,$$

where α is a measure of surface roughness (the mean slope is: $\overline{\tan\,\phi} \sim \sqrt{\alpha}$ (Muhleman, 1966)). Larger values of α imply rougher surfaces. So, (using $c_i = \cos\,\theta_i$, and $s_i = \sin\,\theta_i$):

$$f_i = c_i\left(\frac{\alpha}{s_i + \alpha\,c_i}\right)^3 \qquad ; \qquad f_i' = \frac{3\,s_i\,c_i}{\alpha^2}\left(\frac{\alpha}{s_i + \alpha\,c_i}\right)^4 \quad .$$

Hagfors, (1964), rigorously solved for the scattering by evaluating the Kirchoff–Huygens solution of the scalar wave equation (with many assumptions). For the model of choice, he defined a surface with gaussian height variations and an exponential autocorrelation function for the horizontal variations. The resulting

expression is:

$$S_{os}(\theta) = \frac{\rho_o C}{2}\left(\frac{1}{\cos^4\theta + C\sin^2\theta}\right)^{\frac{3}{2}} \quad ,$$

where ρ_o is the Fresnel reflectivity at normal incidence, and C is a roughness parameter (the mean slope is: $\overline{\tan\phi} = (C-4)\ln(4C)/(2\sqrt{C}(C-\sqrt{C}-2))$, (Evans and Hagfors, 1968)). Smaller values of C imply rougher surfaces. So, (again using $c_i = \cos\theta_i$, and $s_i = \sin\theta_i$):

$$f_i = \frac{C}{2}\left(\frac{1}{c_i^4 + C\,s_i^2}\right)^{\frac{3}{2}} \quad ; \quad f_i' = \frac{1}{2}\left[\left(\frac{1}{c_i^4 + C\,s_i^2}\right)^{\frac{3}{2}} - \frac{3\,C\,s_i^2}{2}\left(\frac{1}{c_i^4 + C\,s_i^2}\right)^{\frac{5}{2}}\right] \quad .$$

A.1.3 Beam Convolution

The above has ignored the fact that the actual data is a convolution of the backscatter function with a Gaussian beam on the sky. If this is taken into account, then in both cases f_i is given by:

$$f_i = f(r_i) = 2\,ln(2)\int_0^1 \frac{1}{\rho_{o_i}^2}\,S(r)\;e^{-ln(2)\frac{r^2+r_i^2}{\rho_{o_i}^2}}\;I_o\left(\frac{2\,r_i\,r\,ln(2)}{\rho_{o_i}^2}\right)\,r\;dr \quad ,$$

where $r_i = \sin\theta_i$, ρ_o is the Gaussian beam half-width (in units of apparent planetary radii), and I_o is the modified Bessel function of order 0. f_i' is the same as f_i, with $S(r)$ replaced by $S'(r) = \partial S/\partial n$ for the SS case, and $S'(r) = \partial S/\partial\alpha$, or $S'(r) = \partial S/\partial C$ for the OS case. In all cases, $S(r)$ and $S'(r)$ are exactly as in the unconvolved definitions of f_i and f_i' with the substitutions: $\sin\theta = r; \cos\theta = \sqrt{1-r^2}$. These integrals for f_i and f_i' must be solved numerically, which makes the least squares solution considerably slower.

A.1.4 Weights

The only remaining problem is the choice of the weights. In a standard weighted least squares fit, the weights would be determined by the variances of the individual

measurements, σ_i^2, i.e., the normalized weights would be found from:

$$w_i = \frac{\hat{w}_i}{\sum \hat{w}_k} \quad ,$$

where the individual weights are given by:

$$\hat{w}_i = \frac{1}{\sigma_i^2} \quad .$$

But, we modify the weights in the following ways, depending on which of the two types of image space fits we are performing. In the first type of fit, the data points are taken from a single image, as averages of the pixels in annuli on the disk. This is the case for the Mercury observations. In this case, the weights are determined solely by the number of individual data points in the each annulus, since the true measurement variances of all the pixels in the map are the same. So, the individual weight for the i^{th} annulus is given simply by $\hat{w}_i = n_i$, the number of pixels in that annulus, since the variance is inversely proportional to the number in the annulus. In the second type, the measurements are for a particular point on the surface, which come from different images. This is the case for the Mars observations. Each of these images has different variance for the individual pixels. Also, in this case, we would like the weights to contain some measure of the surface resolution of the measurement. We decided on:

$$\hat{w}_i = \frac{1}{\sigma_i^2} \frac{1}{B_i D_i}$$

where σ_i^2 is the pixel variance, B_i is the resolution cell size (beam size), and D_i is the distance to the planet for the i^{th} measurement. In this manner, the higher resolution images receive more weight in the fits.

A.2 UV Space Fits

In this type of fit, we have the actual measured visibilities, and would like to fit them. So, we must first derive the visibility function $V(u,v)$ for the sky brightness functions produced in planetary radar, and introduced in sections A.1.1 and A.1.2. The visibility function is obtained from the sky brightness by:

$$V(u,v) = \int_{-\infty}^{+\infty}\int_{-\infty}^{+\infty} S(x,y)\; e^{i2\pi(ux+vy)}\,dx\,dy \quad .$$

Since both of the radar sky brightness distributions are azimuthally symmetric, it is convenient to make a change to polar coordinates:

$$\begin{aligned} V(u,v) &= \int_0^{2\pi}\int_0^{R} S(r,\theta)\; e^{i2\pi(ur\cos\psi+vr\sin\psi)} r\,dr\,d\psi \\ &= \int_0^{R} S(r)\,r\,dr \int_0^{2\pi} e^{i2\pi r(u\cos\psi+v\sin\psi)}\,d\psi \quad . \end{aligned}$$

The evaluation of the integral over ψ is the same in both cases, and proceeds as follows. First, calculate the value of $u\cos\psi + v\sin\psi$,

$$\begin{aligned} u\cos\psi + v\sin\psi &= \sqrt{u^2+v^2}\left(\frac{u}{\sqrt{u^2+v^2}}\cos\psi + \frac{v}{\sqrt{u^2+v^2}}\sin\psi\right) \\ &= \sqrt{u^2+v^2}\left(\frac{u/v}{\sqrt{(u^2/v^2)+1}}\cos\psi + \frac{v/u}{\sqrt{(v^2/u^2)+1}}\sin\psi\right) \\ &= \sqrt{u^2+v^2}\left(\sin(\tan^{-1}(u/v))\cos\psi + \sin(\tan^{-1}(v/u))\sin\psi\right) \\ &= \sqrt{u^2+v^2}\left(\sin(\pi/2-\tan^{-1}(v/u))\cos\psi + \sin(\tan^{-1}(v/u))\sin\psi\right) \\ &= \sqrt{u^2+v^2}\left(\cos(\tan^{-1}(v/u))\cos\psi + \sin(\tan^{-1}(v/u))\sin\psi\right) \\ &= \sqrt{u^2+v^2}\cos(\psi-\tan^{-1}(v/u)) \end{aligned}$$

then, using $\xi = 2\pi r\sqrt{u^2+v^2}$:

$$\int_0^{2\pi} e^{i2\pi r(u\cos\psi+v\sin\psi)}d\psi \;=\; \int_0^{2\pi} e^{i\xi\cos(\psi-\tan^{-1}(v/u))}d\psi$$

$$
\begin{aligned}
&= \int_0^{2\pi} e^{i\xi\cos\psi} d\psi \\
&= \int_0^{\pi} e^{i\xi\cos\psi} d\psi + \int_{\pi}^{2\pi} e^{i\xi\cos\psi} d\psi \quad .
\end{aligned}
$$

To evaluate the second integral, make the substitution $\phi = \psi + \pi$:

$$
\int_{\pi}^{2\pi} e^{i\xi\cos\psi} d\psi = \int_0^{\pi} e^{i\xi\cos(\phi+\pi)} d\phi = \int_0^{\pi} e^{-i\xi\cos\phi} d\phi
$$

substituting this back in:

$$
\begin{aligned}
\int_0^{2\pi} e^{i2\pi r(u\cos\psi + v\sin\psi)} d\psi &= \int_0^{\pi} e^{i\xi\cos\psi} d\psi + \int_0^{\pi} e^{-i\xi\cos\phi} d\phi \\
&= \int_0^{\pi} e^{i\xi\cos\psi} d\psi + \int_0^{\pi} e^{-i\xi\cos\psi} d\psi \\
&= \int_0^{\pi} \left(e^{i\xi\cos\psi} + e^{-i\xi\cos\psi} \right) d\psi \\
&= 2\int_0^{\pi} \cos(\xi\cos\psi) d\psi \quad .
\end{aligned}
$$

Now, this integral is related to the well known Bessel function integral:

$$
J_o(\xi) = \frac{1}{\pi}\int_0^{\pi} \cos(\xi\cos\psi) d\psi \quad ,
$$

where J_o is the Bessel function of order zero. So,

$$
\int_0^{2\pi} e^{i2\pi r(u\cos\psi + v\sin\psi)} d\psi = 2\int_0^{\pi} \cos(\xi\cos\psi) d\psi = 2\pi J_o(2\pi r\sqrt{u^2+v^2}) \quad .
$$

Substituting this into the equation for the visibility function yields:

$$
V(u,v) = 2\pi \int_0^{R} S(r)\, r\, J_o(2\pi r\sqrt{u^2+v^2})\, dr \quad .
$$

It is convenient to make a change of variable to $\rho = r/R$ here, and define the quantity $\beta = R\sqrt{u^2+v^2}$ yielding:

$$
V(\beta) = 2\pi R^2 \int_0^{1} S(\rho)\, \rho\, J_o(2\pi\beta\rho)\, d\rho \quad .
$$

We can now use the sky brightness functions presented earlier in this appendix to derive the visibility function for the SS and OS cases.

A.2.1 SS Case

Assume again that the sky brightness in the case of the SS echo is:

$$S_{ss}(\rho) = A_{ss}\cos^n\theta = A_{ss}(1-\rho^2)^{n/2} \quad .$$

So the visibility function is:

$$V_{ss}(\beta) = 2\pi R^2 A_{ss}\int_0^1 \rho\,(1-\rho^2)^{n/2} J_o(2\pi\beta\rho)\,d\rho \quad ,$$

which can be solved using the following integral relation:

$$\int_0^1 x^{\nu+1}(1-x^2)^{\mu} J_\nu(bx)\,dx = 2^\mu\Gamma(\mu+1)b^{-(\mu+1)}J_{\nu+\mu+1} \quad ,$$

where Γ is the standard Gamma function. So,

$$V_{ss}(\beta) = 2\pi R^2 A_{ss} 2^{\frac{n}{2}}\Gamma(\frac{n}{2}+1)(2\pi\beta)^{-(\frac{n}{2}+1)}J_{\frac{n}{2}+1}(2\pi\beta)$$

let $\nu = n/2+1$, and use the fact that $\Lambda_\nu(z) = \Gamma(\nu+1)\left(\frac{1}{2}z\right)^{-\nu}J_\nu(z)$, then

$$\begin{aligned} V_{ss}(\beta) &= \pi R^2 A_{ss}\Gamma(\nu)(\pi\beta)^{-\nu}J_\nu(2\pi\beta) \\ &= \frac{\pi R^2 A_{ss}}{\nu}\Lambda_\nu(2\pi\beta) \quad , \end{aligned}$$

which reduces to the well-known result: $V_{ss}(\beta) = A_{ss}\pi R^2\Lambda_1(2\pi\beta)$ for $n=0$, i.e., a uniform disk. For the purpose of the least squares fit, the πR^2 term can be absorbed into the scaling coefficient, A_{ss}, leaving (using $a_i = 2\pi\beta_i$):

$$f_i = \frac{\Lambda_\nu(a_i)}{\nu} \qquad ; \qquad f_i' = \frac{\partial}{\partial\nu}\left(\frac{\Lambda_\nu(a_i)}{\nu}\right) = \frac{\partial}{\partial\nu}\left(\Gamma(\nu)\left(\frac{2}{a_i}\right)^\nu J_\nu(a_i)\right) \quad .$$

Now,

$$f_i' = \frac{\partial\Gamma(\nu)}{\partial\nu}\left(\frac{2}{a_i}\right)^\nu J_\nu(a_i) \qquad \text{(term 1)}$$

$$-\Gamma(\nu)\left(\frac{2}{a_i}\right)^\nu ln\left(\frac{a_i}{2}\right) J_\nu(a_i) \qquad \text{(term 2)}$$

$$+\Gamma(\nu+1)\left(\frac{2}{a_i}\right)^\nu \frac{\partial J_\nu(a_i)}{\partial\nu} \qquad \text{(term 3)} \quad .$$

For term 1, use the fact that $\partial\Gamma(\nu)/\partial\nu = \Gamma(\nu)\psi(\nu)$, where $\psi(\nu)$ is the Digamma function, or logarithmic derivative of the Gamma function, so that term 1 $= (\psi(\nu)/\nu)\Lambda_\nu(a)$. Term 2 is simply: $-(ln(a_i/2)/\nu)\Lambda_\nu(a_i)$. For term 3, use the following definition of the Bessel function derivative with respect to order:

$$\frac{\partial J_\nu(a_i)}{\partial\nu} = J_\nu(a_i)ln(\frac{a_i}{2}) - (\frac{a_i}{2})^\nu \sum_{k=0}^{\infty}(-1)^k \frac{\psi(\nu+k+1)}{\Gamma(\nu+k+1)}\frac{(\frac{a_i^2}{2})^k}{k!} \quad .$$

So adding all of the terms and simplifying yields:

$$f_i' = \Lambda_\nu(a_i)\left(\frac{\psi(\nu)}{\nu}\right) - \Gamma(\nu)\sum_{k=0}^{\infty}(-1)^k \frac{\psi(\nu+k+1)}{\Gamma(\nu+k+1)}\frac{(\frac{a_i^2}{2})^k}{k!} \quad .$$

A.2.2 OS Case

We have only derived the visibility function for the case of the Muhleman model sky brightness response. This is mainly due to the fact that the Hagfors model blows up at large incidence angles, thus making it necessary to make an ad hoc assumption about where to cut off the integral (at what angle). So, the sky brightness in this case is:

$$S_{os}(\rho) = A_{os}\cos\theta\left(\frac{\alpha}{\sin\theta+\alpha\cos\theta}\right)^3 = A_{os}\sqrt{1-\rho^2}\left(\frac{\alpha}{\rho+\alpha\sqrt{1-\rho^2}}\right)^3$$

and the visibility function is:

$$V_{os}(\beta) = 2\pi R^2 A_{os}\int_0^1 \rho\sqrt{1-\rho^2}\left(\frac{\alpha}{\rho+\alpha\sqrt{1-\rho^2}}\right)^3 J_o(2\pi\beta\rho)\,d\rho \quad .$$

Again, the constant $2\pi R^2$ can be absorbed into the value of the scaling coefficient, A_{os} for the purpose of the least squares fit. So, again using $a_i = 2\pi\beta_i$,

$$f_i = \alpha^3 \int_0^1 \rho\sqrt{1-\rho^2}\left(\frac{1}{\rho+\alpha\sqrt{1-\rho^2}}\right)^3 J_o(a_i\rho)\,d\rho \quad .$$

Now, the value for f_i' can be found by:

$$\begin{aligned}
f_i' &= \frac{\partial}{\partial\alpha}\left(\alpha^3 \int_o^1 \rho\sqrt{1-\rho^2}\left(\frac{1}{\rho+\alpha\sqrt{1-\rho^2}}\right)^3 J_o(a_i\rho)\,d\rho\right) \\
&= 3\alpha^2 f_i \\
&\quad +\alpha^3\frac{\partial}{\partial\alpha}\left(\int_o^1 \rho\sqrt{1-\rho^2}\left(\frac{1}{\rho+\alpha\sqrt{1-\rho^2}}\right)^3 J_o(a_i\rho)\,d\rho\right) \\
&= 3\alpha^2 f_i \\
&\quad +\alpha^3 \int_o^1 \rho\sqrt{1-\rho^2}\frac{\partial}{\partial\alpha}\left(\left(\frac{1}{\rho+\alpha\sqrt{1-\rho^2}}\right)^3\right) J_o(a_i\rho)\,d\rho \\
&= 3\alpha^2\left(f_i + \alpha\int_o^1 \rho(1-\rho^2)\left(\frac{1}{\rho+\alpha\sqrt{1-\rho^2}}\right)^4 J_o(a_i\rho)\,d\rho\right) \quad .
\end{aligned}$$

A.2.3 Weights

When doing the UV space fits, in order to save computational intensity, the visibilities were averaged in bins according to their value of β. So, the weight for a given bin point is simply proportional to the number of visibilities which went into the average for that bin, since the individual measured visibilities should all have the same variance.

Appendix B

Frequency Response

The frequency response across an individual untapered frequency channel at the VLA is the well known sinc function (Rots, 1990) (see Figure B.2):

$$F(\nu) = \frac{\sin\left(\frac{2\pi\Delta\nu}{\Delta\nu_\circ}\right)}{\frac{2\pi\Delta\nu}{\Delta\nu_\circ}}$$

where $\Delta\nu = \nu - \nu_\circ$, with $\nu_\circ$ the channel center frequency, and $\Delta\nu_\circ$ the frequency separation between the first nulls of the function, i.e., twice the nominal channel width. Now, in order to utilize this in the construction of the initial CLEAN models for Mars, we need instead $F(x)$, where x is the spatial sky coordinate perpendicular to the projected apparent rotational pole of Mars. This geometry is chosen because frequency shift is due only to the line of sight velocity of the planetary surface elements, which is constant along lines parallel to the projected apparent pole (doppler strips). In order to find the functions $F(x)$, we must first find a relation between frequency, ν, and sky position, x (which can be directly related to position on the planetary surface).

The total bandwidth of a planet as viewed on the sky from the earth can be found from (Goldstein, 1964, and Shapiro, 1967):

$$B^2 = |\mathbf{w}_t|^2 - \frac{(\mathbf{R}\cdot\mathbf{w}_t)^2}{|\mathbf{R}|^2} \quad ,$$

where B is the bandwidth, $\mathbf{w}_t$ is the total rotation vector and $\mathbf{R}$ is the vector joining the centers of the earth and the planet. The total rotation is given by:

$$\mathbf{w}_t = \mathbf{w}_o + \mathbf{w}_s \quad ,$$

where $\mathbf{w}_o$ is caused by relative motion between the planet and the earth, and $\mathbf{w}_s$ is the true spin vector. The orbital part may be calculated by:

$$\mathbf{w}_o = \frac{\dot{\mathbf{R}} \times \mathbf{R}}{|\mathbf{R}|^2} \quad ,$$

where $\dot{\mathbf{R}}$ is the time derivative of $\mathbf{R}$. Now, at this point, given access to a full ephemeris, one could find B. However, we'd like to reduce the expression for B to one containing only parameters which are easily accessed, e.g., in the Astronomical Almanac. So, substituting the definition of $\mathbf{w}_t$ into the original equation yields:

$$B^2 = |\mathbf{w}_o + \mathbf{w}_s|^2 - \frac{(\mathbf{R} \cdot (\mathbf{w}_o + \mathbf{w}_s))^2}{|\mathbf{R}|^2} \quad .$$

Using the fact that $|\mathbf{w}_o + \mathbf{w}_s|^2 = |\mathbf{w}_o|^2 + |\mathbf{w}_s|^2 + 2\ \mathbf{w}_o \cdot \mathbf{w}_s$,

$$B^2 = |\mathbf{w}_o|^2 + |\mathbf{w}_s|^2 + 2\ \mathbf{w}_o \cdot \mathbf{w}_s - \frac{(\mathbf{R} \cdot \mathbf{w}_o + \mathbf{R} \cdot \mathbf{w}_s)^2}{|\mathbf{R}|^2} \quad .$$

Since $\mathbf{R} \cdot \mathbf{w}_o = \frac{\mathbf{R} \cdot (\dot{\mathbf{R}} \times \mathbf{R})}{|\mathbf{R}|^2} = 0$,

$$B^2 = |\mathbf{w}_o|^2 + |\mathbf{w}_s|^2 + 2\ \mathbf{w}_o \cdot \mathbf{w}_s - \frac{(\mathbf{R} \cdot \mathbf{w}_s)^2}{|\mathbf{R}|^2} \quad .$$

Substitute $|\mathbf{R}|^2\ |\mathbf{w}_s|^2\ \cos^2\theta_{Rs}$ for $(\mathbf{R} \cdot \mathbf{w}_s)^2$, where θ_{Rs} is the angle between $\mathbf{R}$ and $\mathbf{w}_s$, and $|\mathbf{w}_o|\ |\mathbf{w}_s|\ \cos\theta_{os}$ for $\mathbf{w}_o \cdot \mathbf{w}_s$, where θ_{os} is the angle between $\mathbf{w}_o$ and $\mathbf{w}_s$ to get

$$B^2 \ = \ |\mathbf{w}_o|^2 + |\mathbf{w}_s|^2 + 2\ |\mathbf{w}_o|\ |\mathbf{w}_s|\ \cos\theta_{os} - |\mathbf{w}_s|^2 \cos^2\theta_{Rs}$$

$$= |\mathbf{w}_s|^2(1 - \cos^2 \theta_{Rs}) + |\mathbf{w}_o|^2 + 2\ |\mathbf{w}_o|\ |\mathbf{w}_s|\ \cos \theta_{os}$$
$$= |\mathbf{w}_s|^2 \sin^2 \theta_{Rs} + |\mathbf{w}_o|^2 + 2\ |\mathbf{w}_o|\ |\mathbf{w}_s|\ \cos \theta_{os} \quad .$$

In order to continue, some geometry must be introduced. First, a distinction must be made between the direction of the spin vectors of possible observed planets. If the spin vector of the observed planet points North of the ecliptic of the solar system, I will refer to it as a "direct" spin vector, otherwise, I will refer to it as a "retrograde" spin vector. Venus, Uranus and Pluto are the planets with retrograde spin vectors. Now, for direct spin vectors, $\theta_{Rs} = 90° + \phi_o$, and for retrograde spin vectors, $\theta_{Rs} = 90° - \phi_o$, where ϕ_o is the subearth latitude on the planet. So, $\sin \theta_{Rs} = \cos \phi_o$ for both cases. The geometry for θ_{os} is more complicated, and for this, a distinction between positions in orbit of the planets must be made. I will refer to inferior planets which are between greatest elongations on the inferior conjunction side as "near." I will also use this adjective to describe superior planets which are between quadratures on the opposition side. I will use the term "far" for all other configurations (see Figure B.1). Now, the expression for θ_{os} involves both the orientation of the spin vector, and the position in the orbit of the planet. If the spin vector is direct and the planet is near, or if the spin vector is retrograde and the planet is far, then $\cos \theta_{os} = \cos \phi_o\ \cos \psi$, otherwise, $\cos \theta_{os} = -\cos \phi_o\ \cos \psi$, where ψ is the angle between the north pole of the planet and north on the celestial sphere. So,

$$B^2 = |\mathbf{w}_s|^2 \cos^2 \phi_o + |\mathbf{w}_o|^2 \pm 2\ |\mathbf{w}_o|\ |\mathbf{w}_s|\ \cos \phi_o\ \cos \psi \quad .$$

Now,

$$|\mathbf{w}_o| = \left|\frac{\dot{\mathbf{R}} \times \mathbf{R}}{|\mathbf{R}|^2}\right| = \frac{|\dot{\mathbf{R}} \times \mathbf{R}|}{|\mathbf{R}|^2} = \frac{|\dot{\mathbf{R}}|\ |\mathbf{R}|\ \sin \theta_{R\dot{R}}}{|\mathbf{R}|^2} = \frac{|\dot{\mathbf{R}}|}{|\mathbf{R}|}\ \sin \theta_{R\dot{R}} \quad ,$$

where $\theta_{R\dot{R}}$ is the angle between $\mathbf{R}$ and $\dot{\mathbf{R}}$. We can find $\sin \theta_{R\dot{R}}$ from knowledge of the relative positions of the earth and the planet. For inferior plan-

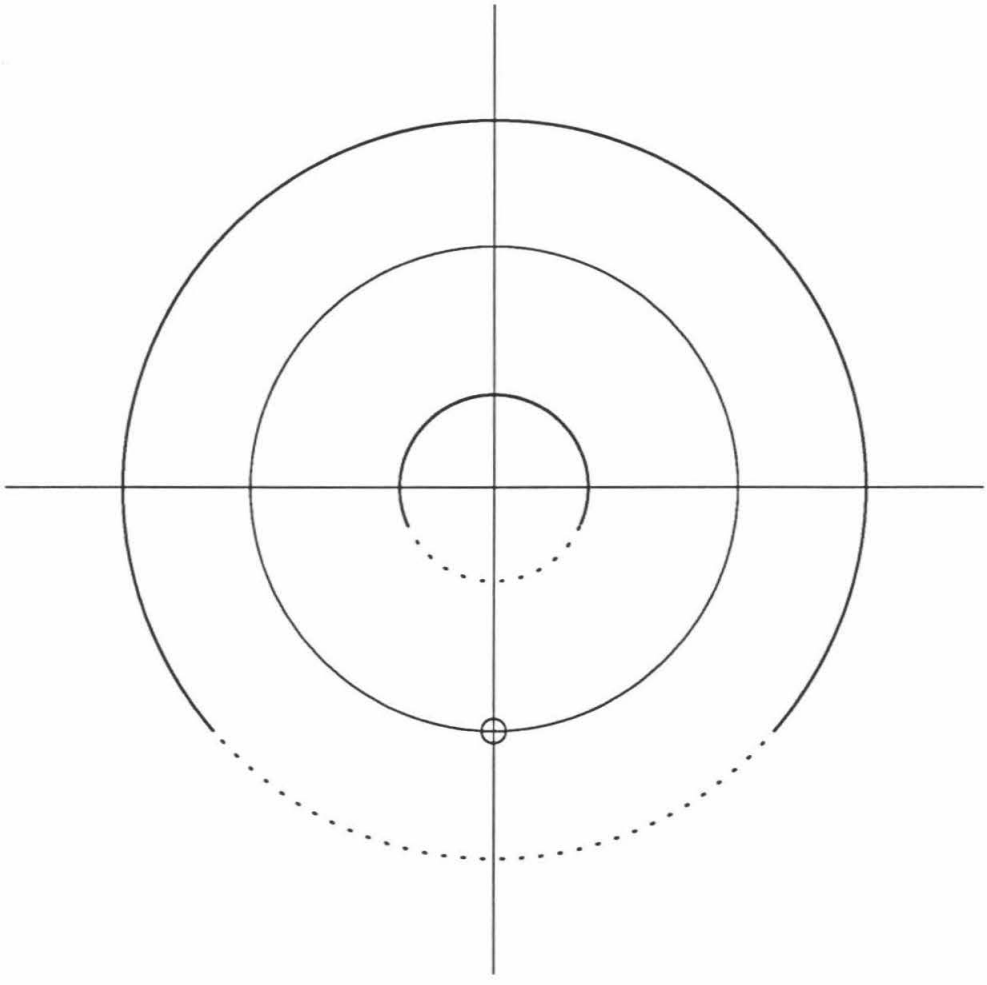

Figure B.1: Geometry for doppler shift calculations. The open circle is the observer position (Earth), "near" orbital positions are dashed, "far" are solid.

ets, $\sin\theta_{R\dot{R}} = \cos\alpha$, where α is the phase angle at the time of observation (planetocentric elongation of the earth from the sun). For superior planets, $\sin\theta_{R\dot{R}} = \sqrt{1 - |\mathbf{R}_s|^2 \sin^2\alpha}$,where $\mathbf{R}_s$ is the vector connecting the sun to the observed planet. The value of $|\dot{\mathbf{R}}|$ is found similarly, and is given by $\dot{D}/\sin\alpha$ for inferior planets, and $\dot{D}/(|\mathbf{R}_s|\sin\alpha)$ for superior planets. $\dot{D}$ is the rate of change of geocentric distance to the observed planet. This is the only parameter in the final expression for B which is not readily available, and we obtain it from the JPL ephemeris, though it could be found by interpolating values for the geocentric distance in the Astronomical Almanac and estimating the derivative. Now, to convert to a true total doppler spread, $\Delta\nu_t$,

$$\Delta\nu_t = \frac{4\,R_p}{\lambda}\,B \quad ,$$

where R_p is the planetary radius, and λ is the wavelength of interest. Since doppler shifts are linear in x, the doppler shift of a given point can be written:

$$\Delta\nu = \frac{\Delta\nu_t}{2}\,\frac{\Delta x}{R_p} \quad .$$

This equation relates the doppler shift $\Delta\nu$ to the position shift Δx. So, we have:

$$F(x) = \frac{\sin\left(\frac{2\pi\Delta x}{\Delta x_\circ}\right)}{\frac{2\pi\Delta x}{\Delta x_\circ}} \quad ,$$

where $\Delta x_\circ$ can be found from the above relation, noting that it is for an equivalent frequency separation equal to twice the intrinsic channel width (the width between the first nulls, or $\Delta\nu_\circ$), and $\Delta x = x - x_\circ$, with $x_\circ$ the position corresponding to the center of the channel. Figure B.2 shows an example of the calculated frequency response across the sky for one of the images of the October 22, 1988 Mars experiment. This figure shows what the frequency response would be for a Sinc filter of width 3052 Hz. In the actual experiment, we used Hanning smoothed Sinc filters, so the intrinsic width of the Sinc functions during that experiment was 1526 Hz

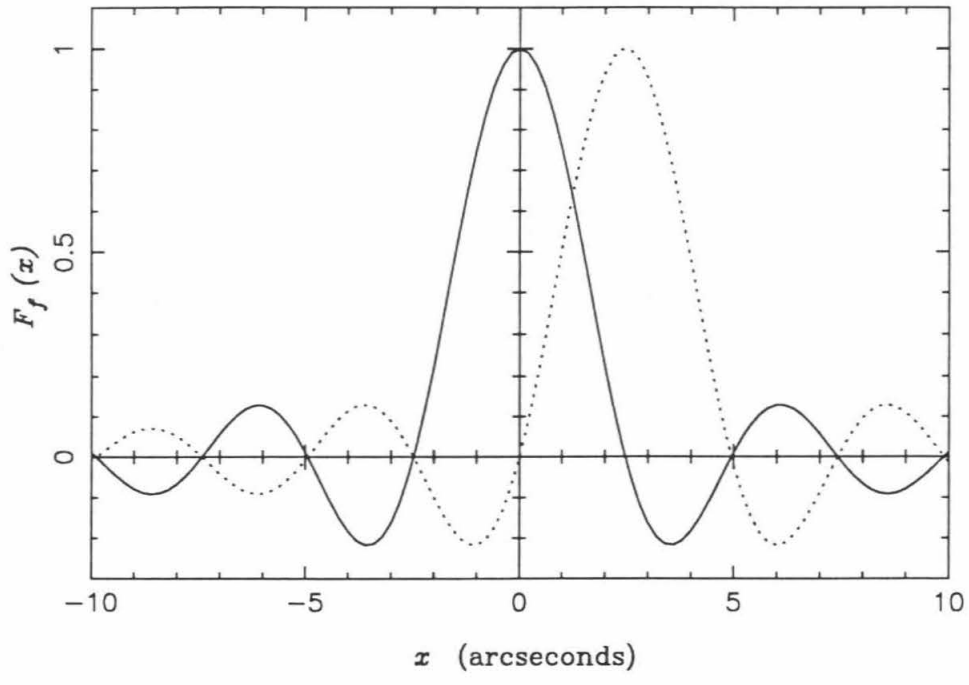

Figure B.2: Frequency response vs. sky position for Sinc filters. The solid line is for the central channel ($F_o(x)$), the dashed is for the adjacent channel ($F_1(x)$). This response is for an untapered channel width of 3052 Hz, with appropriate parameters for the October, 1988 Mars observations. Δx_o is ~ 5 arcsec for this example. Note that for the actual experiment, 3052 Hz Hanning tapered filters were used, so the Sinc functions were half this wide.

(see explanation below).

There is a complication which must be explained at this point. The x coordinate introduced above is the coordinate which is perpendicular to the projected apparent rotational pole. This is different from the nominal x coordinate in the images of Mars, which is perpendicular to the spin vector, $\mathbf{w}_s$. The images have this x coordinate so that planetographic north is "up" in the images. This is accomplished by rotating the images by the position angle of the planet in the sky plane at the time of observation. However, the error introduced in the images from this difference in coordinates is very small, as $|\mathbf{w}_s| \gg |\mathbf{w}_o|$. As an example, in the October 1988 observations of Mars, $|\mathbf{R}_s| \sim 1.42$ AU, $\dot{D} \sim .00435$ AU/day, and $\alpha \sim 20°$, so, $\sin \theta_{R\dot{R}} \sim 0.874, |\dot{\mathbf{R}}| \sim .009$ AU/day, and $|\mathbf{R}| \sim 0.46$ AU, implying

an orbital portion of the rotation of: $|\mathbf{w}_o| \sim 0.017$ rad/day. Now, the spin vector of Mars is: $\mathbf{w}_s \sim 6.45$ rad/day, so the contribution of the orbital portion of the apparent rotation is indeed very small.

Since the sinc function has such large sidelobes, the VLA data collection architecture allows observers to perform Hanning smoothing on any collected data, in order to suppress the sidelobe level. The frequency response of Hanning smoothed frequency channels is related to the original unsmoothed response derived above in the following way (Rots, 1990):

$$H_f(x) = \frac{1}{4}\,(F_{f-1}(x) + F_{f+1}(x)) + \frac{1}{2}\,F_f(x) \quad ,$$

where f indicates the relative channel number. We took advantage of this Hanning smoothing in all of our measurements of Mars.

Appendix C

Taper Function

Since we have resolved the disk of Mars in frequency channels, we need some method to combine those channels into a final image. First, assume that the channels have all sampled the sky brightness function exactly within some distance of their center, where the center is at $x = 0$. Outside of this "exact" region on both sides, they have noisy samples of the sky brightness. In order to combine these channels, we construct a filter function for each channel which has a value of 1 in the exact region, and which tapers off smoothly to 0 at some distance beyond that on both sides (see Figure C.1). In order to maximize the smoothness of the taper at its edges, we enforce the following constraints:

$$T(x) = \frac{\partial T(x)}{\partial x} = \frac{\partial^2 T(x)}{\partial x^2} = 0 \quad , \quad |x| = x_1 + x_2 \quad .$$

So, $x_1 - x_2$ is half the total width of the exact region, the function tapers to 0 at $|x| = x_1 + x_2$, and $2\,x_2$ is the total width of the taper region on each side of the channel center. We would like the function to have even symmetry about the channel center, i.e., $T(x) = T(-x)$. We would also like the sum of taper functions for adjacent frequency channels to be 1 in the region $x_1 - x_2 \leq |x| \leq x_1 + x_2$, i.e., there is an odd symmetry about $x = x_1$ and $T(x) = 0.5$. The function which we

decided on is:

$$T(x) = \begin{cases} 1, & |x| \leq x_1 - x_2; \\ \frac{|(|x|-x_1-x_2)^3|}{2x_2^3}, & x_1 \leq |x| \leq x_1 + x_2; \\ 1 - \frac{|(|x|-x_1-x_2)^3|}{2x_2^3}, & x_1 \geq |x| \geq x_1 - x_2; \\ 0, & |x| > x_1 + x_2. \end{cases}$$

The logical choice for x_1 is half the intrinsic channel width. After experimentation, we found that a value of $x_2 = 2\,x_1/3$ gave the most satisfactory results for the Mars images. Now, in the true images, we do not have an exact sampling of the sky brightness function anywhere except exactly at the channel center. This is due to the fact that there is some frequency response across the channel (see Appendix B). If this frequency filter is denoted by $F(x)$, then the best estimation of the true sky brightness is given by the image value divided by $F(x)$. Therefore, in forming our final taper function we divide by this frequency response:

$$T_{final}(x) = \frac{T(x)}{F(x)}$$

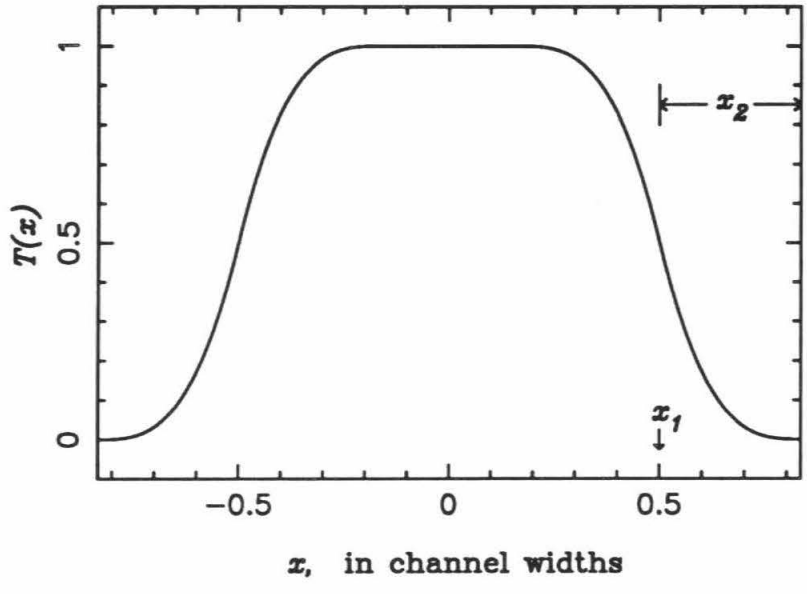

Figure C.1: Taper function, $x_1 = 0.5, x_2 = 1/3$

Appendix D

Correction for on–line Bandpass Normalization

When these observations were made, we used a method known in the language of the VLA as "on–line bandpass normalization." This makes a normalized spectrum by dividing the individual visibilities by the geometric mean of the autocorrelations of the two antennas involved, channel by channel. The normal method (if on–line bandpass normalization is not used) is to divide all of the channels by the average of the "lag–zero" terms of the autocorrelations of the two antennas involved. A good explanation of this is contained in Clark and van Gorkom, (1981). The advantage of on–line bandpass normalization is that it does a rough calibration of the bandpass response function of the receivers. Unfortunately, in our case, we had so much radar echo energy in the central radar channel that the autocorrelation values of the individual antennas were affected in that channel. Thus, on–line bandpass normalization effectively reduced the flux in the central channel. We did not realize that this was the case until recently. Fortunately, however, all of the autocorrelation values are stored in the original data archive, and can be retrieved. Therefore, we could reverse the process and undo what was done in the on–line bandpass normalization. If we desired, for each time step, we could have read off the autocorrelation values for each antenna, each channel, and each source (Mer-

cury and all of the calibrators), multiplied each visibility value by the geometric mean of the autocorrelation values for the two antennas involved, and started the calibration from scratch (choosing some other type of spectrum normalization). Since the initial calibration was still valid, however (the bandpass calibration is essentially separate from the initial phase and amplitude calibration), we chose to simply apply a correction to the initially calibrated visibilities of the form:

$$V'_{ijk} = V_{ijk} * C \quad ,$$

where V'_{ijk} is the new (corrected for on–line bandpass normalization) visibility for baseline i–j, and spectral channel k, V_{ijk} is the associated original calibrated visibility, and C is the correction factor. C is found by:

$$C = \frac{\sqrt{V_{iik}\ V_{jjk}}}{\frac{1}{N}\sqrt{\sum_l V_{iil} \sum_l V_{jjl}}} \quad ,$$

where the summations are performed over the channels which are in the inner 75% of the spectrum (in order to avoid edge effects), but whose autocorrelations are not affected by radar echo energy, and N is the number of such channels. This preserves the initial calibration, while correcting for the on–line bandpass normalization. After this correction was performed, a true bandpass calibration was applied using data taken on the source 3C84. This procedure was performed on the data from both August 8 and August 23. The whole–disk reflectivities in both the OS and SS polarizations were increased from what they were previously, as expected. However, in the SS data the effect was small in the CLEANed maps, i.e., there were no pixels in the new images which were different than the original images by more than 3σ. In the OS data, the effect was only to increase the total amount of energy in the quasi–specular spike, while the "features" (including the north polar feature) remained essentially unchanged.

Appendix E

Molecule Migration Simulation

This appendix describes in detail the simulation of migration of molecules mentioned in sections 3.4.2 and 3.4.3. The concept is fairly simple: place molecules on a planetary surface, and allow them to migrate on the surface according to where they are until they are lost to the system. Migration is through a number of hops from place to place. The loss can occur in either of two ways: by destruction of the molecule, or by capture of the molecule by a cold trap, i.e., where the molecule is stable for an infinite time period. This process is done for a number of molecules, and those that are terminated due to the second loss mechanism are counted. The only destruction mechanism currently considered is photodissociation during each hop. The only locations where molecules are forever stable are portions of circular regions at the poles of the planet. Much of the material here is derived from the excellent discussion of Hunten *et al.* , (1988). Before describing the simulation, the geometry must be explained. The planetary surface is assumed spherical, with radius R_{planet}, centered at the origin of a right–handed coordinate system (see Figure E.1). Positions are noted by: $\mathbf{r} = (\phi, \beta)$, i.e., the simulation uses spherical geometry. The two angle coordinates are shown in Figure E.1. The conversion from these angle coordinates to Cartesian coordinates is: $x = r \sin\phi \sin\beta; y = r \cos\phi; z = r \sin\phi \cos\beta$, where $r = R_{planet}$ for points on the surface of the sphere. The position of the sun in the system is: $\mathbf{r}_{sun} = (\pi/2, 0)$, at

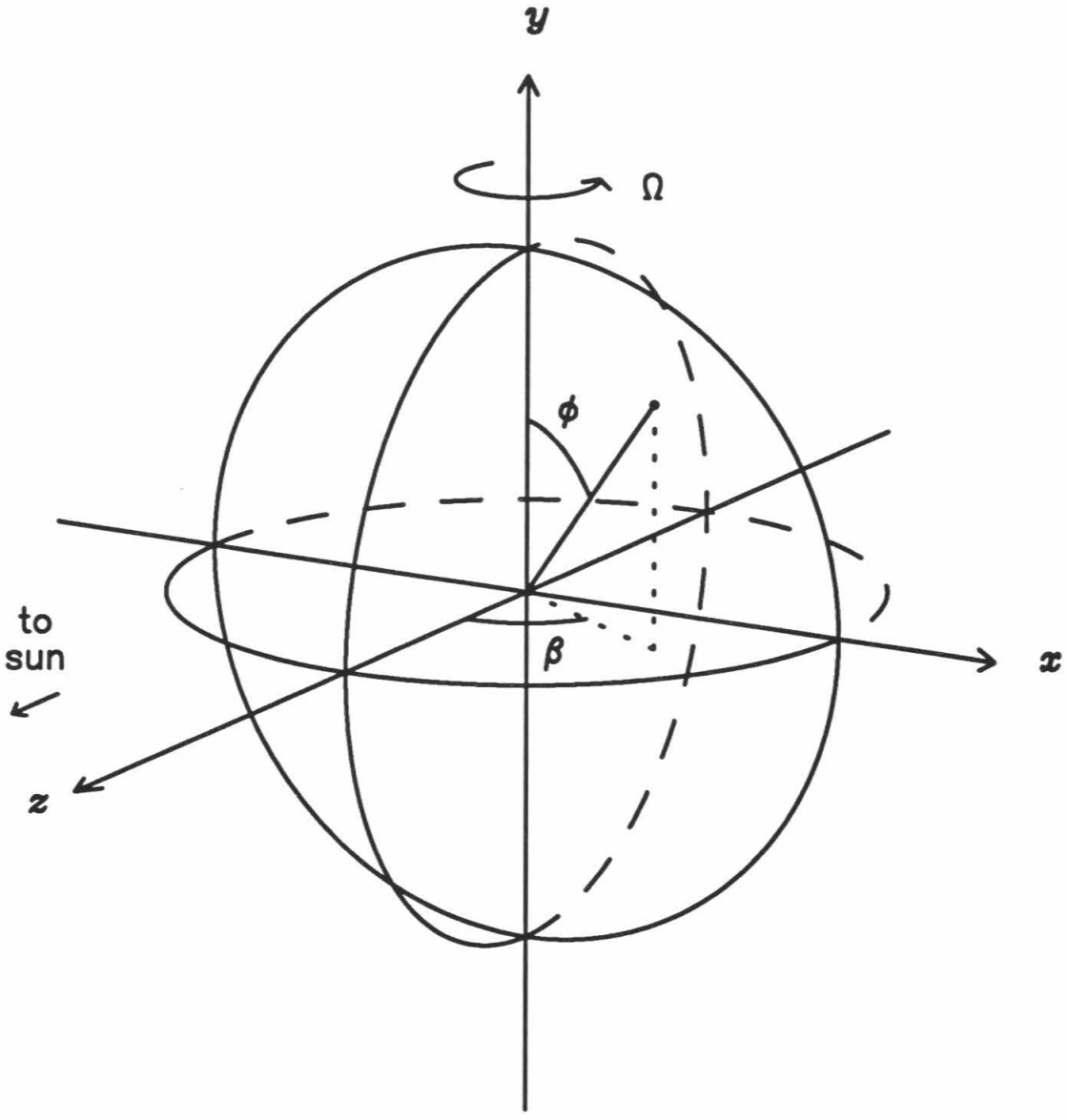

Figure E.1: The geometry for the migration simulation.

infinite distance ($r_{sun} = \infty$).

E.1 Algorithm and Math

The algorithm is as follows:

I. place molecules on the surface

II. initialize times, $t_{sim} \leftarrow 0, t_{rot} \leftarrow \Delta t_{rot}$

III. repeat

A. allow any remaining molecule in a sunlit area to hop

B. check for destruction or infinite stability

C. if destroyed, remove the molecule from further consideration

D. if infinitely stable, count the molecule and remove it

E. $t_{sim} \leftarrow t_{sim} + t$

F. if $t_{sim} > t_{rot}$ then

$t_{rot} \leftarrow t_{rot} + \Delta t_{rot}$

rotate all molecular surface positions by an angle $\Omega \Delta t_{rot}$

IV. until no more molecules to consider

Each of these steps will now be described in full detail.

E.1.1 Molecule Placement

The initial distribution of the molecules is to be random, except in the case of polar placement, which will be covered later. Assume there is access to a pseudorandom number generator which generates numbers evenly distributed on (0,1). Random placement of each molecule then follows from use of two such numbers. Since areas must be equally probable, and since the differential area element on the surface of

the planet is given by: $dA = \sin\phi\, d\phi\, d\beta$, we want β evenly distributed on $(0, 2\pi)$, i.e., $\beta = 2\pi\,\xi_1$ where ξ_1 is the first pseudorandom number. Finding ϕ is not quite so simple. The probability distribution function (pdf) for ϕ is: $f(\phi) = \sin\phi$. This has the associated cumulative distribution function (cdf):

$$F(\phi) = \int_0^{\phi} f(\theta)d\theta = \int_0^{\phi} \sin\theta d\theta = 1 - \cos\phi.$$

Normalization requires that this cdf be equal to 1 at $\phi = \pi$, so the final cdf is: $F(\phi) = (1 - \cos\phi)/2$. The accessible pseudorandom numbers have the cdf: $F(\xi) = \xi$, i.e., they are uniformly distributed. To transform one to the other, set the two cdf's equal, so: $\cos\phi = 1 - 2\xi$. So, to find the initial location of randomly placed molecule i, simply generate two pseudorandom numbers, then $\beta_i = 2\pi\,\xi_1, \phi_i = \cos^{-1}(1 - 2\xi_2)$.

The other desired type of initial placement is one in which all of the molecules start out within the circular regions which define the infinitely stable areas. Assume that each stable region is a flat circular disk, centered on the pole (i.e., ignore the surface curvature in the stable region). Then, a differential area element on this disk is: $dA = r_p\, dr_p\, d\beta$, where r_p is the distance from the pole. So, the initial value of β is obtained in the same manner as in the random placement case: $\beta = 2\pi\xi_1$. To solve for the value of ϕ, first solve for the value of r_p, using the same technique of transformation of random variables as used above (setting the cdf's equal), to obtain: $r_p = R_{pole}\sqrt{\xi_2}$. Then, calculate ϕ from r_p: $\phi = \sin^{-1}(r_p/R_{planet}) = \sin^{-1}\left(\sqrt{\xi_2}\, R_{pole}/R_{planet}\right)$. Here, R_{pole} is the radius of the circular polar stable region. Since the computer will always return values in the range $0 < \sin^{-1} x < \pi/2$ for all $x > 0$, some method must be employed to place molecules in the stable area near π (the south pole). I simply place every other molecule in the south. So, to find the initial location of randomly placed molecule i, simply generate two pseudorandom numbers, then $\beta_i = 2\pi\,\xi_1, \phi_i = \sin^{-1}\left(\sqrt{\xi_2}\, R_{pole}/R_{planet}\right)$, then if i is even, $\phi_i = \pi - \phi_i$. In the polar placement case, Step I in the algorithm must be

changed to: place molecules on the surface, and force them to hop once.

E.1.2 Hopping

Any molecule i which satisfies the criteria $z_i > 0$ (or, equivalently, $\beta_i < \pi/2$ or $\beta_i > 3\pi/2$) is in a sunlit area and should be allowed to hop. All hopping molecules are assumed to travel a distance D, having time of flight t, in a random direction. The time of flight is the ballistic, or free–fall time, which is: $t = \sqrt{2}v/g$ for projection at 45° from the horizontal at velocity v (g is the surface gravity of the planet). I will use the rms speed of a Maxwellian gas for the velocity: $v = \sqrt{3\,k\,T/m}$ where T is the ambient temperature and m is the molecular mass. I will assume that T is constant on the sunlit side. With these assumptions, the hop distance is given by:

$$D = \frac{v\,t}{2} = \frac{3\sqrt{2}}{2}\frac{k\,T}{m\,g} \quad .$$

So, given an old position, $\mathbf{r}_o$, I want a new position, $\mathbf{r}$, that is a distance D away, in a random direction. Let the direction be ψ, so $\psi \in (0, 2\,\pi)$, which can be calculated via: $\psi = 2\,\pi\,\xi$, with ξ a pseudorandom number as above. Let ψ be measured West from true North. The geometry is then shown in Figure E.2. δ is known, because $\mathbf{r}$ is a fixed distance from $\mathbf{r}_o$, i.e., $\delta = D/R_{planet}$. The new angle ϕ can be found from the following spherical trigonometric identity:

$$\cos\phi = \cos\phi_o\,\cos\delta + \sin\phi_o\,\sin\delta\,\cos\psi$$

the new angle β is given by: $\beta = \beta_o \pm \epsilon$, where the sign of the $\pm$ term is decided by the direction of ψ: $+$ for $\psi > \pi$, $-$ for $\psi < \pi$. ϵ can be found from the same identity as was used to find ϕ:

$$\cos\delta = \cos\phi\,\cos\phi_o + \sin\phi\,\sin\phi_o\,\cos\epsilon$$

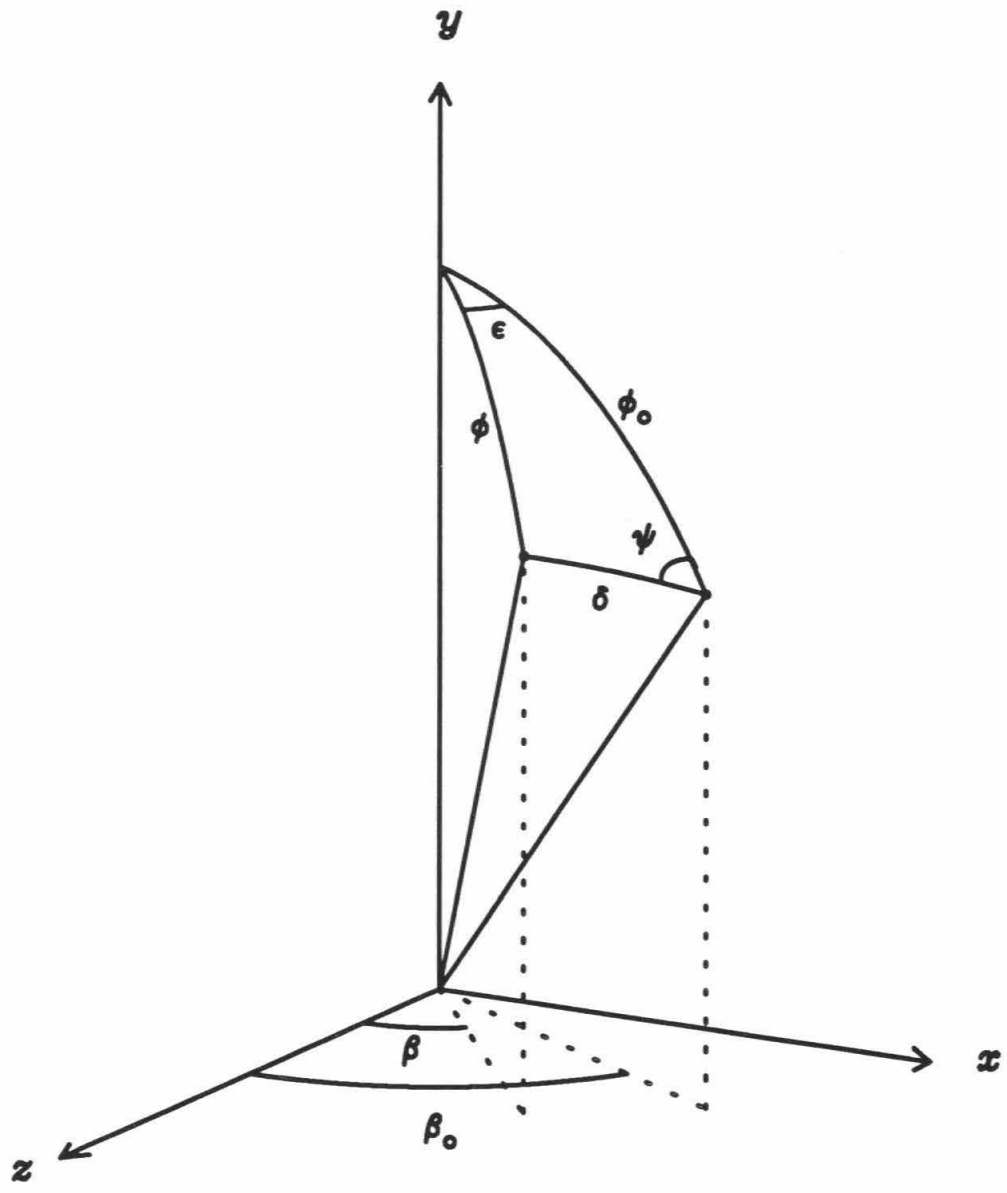

Figure E.2: Geometry for a hop of a molecule on the surface of the planet.

E.1.3 Destruction and Stability

As mentioned previously, the only loss mechanism being considered is photodissociation. The probability that a molecule is lost to photodissociation on a single hop is: $P = 1 - e^{-t/\tau}$, where τ is the photodissociation loss timescale. So, to check for loss to photodissociation, generate a pseudorandom number, ξ, then if $\xi < P$, the molecule is lost. A statistically equivalent method is to let $P = e^{-t/\tau}$, then if $\xi > P$, the molecule is lost.

The only regions where molecules are stable forever are in areas contained in circular polar regions. In this manner, a particular amount of permanently shadowed regions can be specified, above a certain latitude. Any molecule i is thus "lost" (captured by the polar regions) to the simulation if two conditions are met. First, a hop (or initial placement, in the random initial placement case) must place the molecule in the circular polar region, i.e., $|y_i| > y_{pole}$, where $y_{pole} = \sqrt{1 - (R_{pole}/R_{planet})^2}$. In the spherical geometry, this means: $\phi_i < \phi_{pole}$ or $\phi_i > \pi - \phi_{pole}$, where $\phi_{pole} = \sin^{-1}(R_{pole}/R_{planet})$. Second, the molecule must actually hit one of the shadowed regions. This is accomplished by generating a pseudorandom number ξ, and checking it against the proscribed fractional area of the shadowed regions, f_{shad}, i.e., if $\xi < f_{shad}$, then the molecule has indeed made it to a region which is cold enough to retain it forever.

E.1.4 Planetary Rotation

Given the planetary rotation rate, Ω, and the desired time interval between rotations, Δt_{rot}, the amount of planetary rotation is: $\theta = \Omega \Delta t$. The rotation axis is normal to the orbit plane, and is thus parallel to the y–axis (see Figure E.1). So, each time a rotation is to take place, each of the molecules remaining in the simulation must have their positions modified. This is simply an increment in the β coordinate by θ for each molecule. With the computing power currently available, it is possible to set the desired rotation interval equal to the time of flight for each

hop, i.e., $\Delta t_{rot} = t$ (defined in Hopping section above).

E.2 Discussion of Assumptions

The following is a non–exhaustive list and discussion of important assumptions.

1. The initial positions of the molecules are random.

   This is probably valid for meteoritic and outgassing sources, which are the only ones being considered at this point. It is probably not valid for a cometary source, but might suffice if long time averaging is considered. It is probably not valid for solar wind sources, as they would preferentially deposit on the night side (especially where the plasma sheet intersects the surface) and at the poles.

2. The sunlit side is only $z > 0$.

   This is not strictly true for Mercury, since the sun is so large in the sky. The total fractional area which is sunlit and has $z < 0$ must be very small, however, so it seems this is valid.

3. Only sunlit molecules can hop.

   This is also not strictly true, as part of the surface which has just been rotated out of sunlight will undoubtedly be hot enough to vaporize H_2O molecules. Again, however, it seems that the total fractional area of such regions must be small, so the assumption is valid.

4. Hops all occur with the same initial angle from horizontal, and with the same velocity.

   This is equivalent to assuming the distances, D, and times of flight, t, are the same for all hopping molecules. One implication of this is that the surface temperature is assumed constant on the sunlit side (and that it is hot enough to vaporize H_2O), and constant on the night side (and cold enough to condense H_2O). This is not strictly true, but using a true temperature

distribution would make things necessarily much more complicated. Given the intended simplicity of the model, at this point the added complexity is not warranted. The assumption is probably valid for the night side, in any case, and the effect of the day side gradient may average out over many hops (i.e., longer hops in hot regions, near the subsolar point, and shorter hops in less hot regions), as long as a sensible average temperature is chosen. Using a value of 45° for the angle of projection above horizontal is similar to assuming that many hops will happen for any given molecule, with angles above horizontal distributed between 0° and 90°, which average to 45°. Again, this is not exactly correct, but the added complexity seems to be unwarranted. Using the rms value for velocity of the Maxwellian gas is also not strictly correct for Mercury. The gases in the tenuous atmosphere tend to have velocity distributions which deviate from a classical Maxwell–Boltzmann distribution. Again, to do it right (even assuming a Maxwellian velocity distribution, and drawing the velocities randomly from it) would greatly increase the complexity of the simulation. This also is not warranted at this time, but in fact may need to be done eventually. This entire section (4) is the weakest part of the simulation, but a vast amount of work would have to be done to get it exactly right, and the benefit may not be that great.

5. The only destruction is by photodissociation.

This is really just assuming that photodissociation is the fastest destruction mechanism. The maximum photodissociation rate for any product of H_2O at 0.9 AU is $9.37 \times 10^{-6}\text{sec}^{-1}$, while the maximum photoionization rate is $4.35 \times 10^{-7}\text{sec}^{-1}$ (Allen *et al.* , 1987). It is clear that of photodestruction processes, photodissociation dominates. Since the atmosphere is so tenuous, molecular interactions in the atmosphere are negligible, so no H_2O is lost to atmospheric chemistry. Since the H_2O molecule is relatively heavy, thermal (Jeans) escape is very small (the time scale for thermal escape of atomic oxygen approaches the age of the solar system). While radiation pressure is

important for Na and K due to the deep Fraunhofer lines of the sun, it is relatively unimportant for H_2O. The interaction of the molecules with the surface could provide for some loss, if the H_2O becomes chemically bound to the surface. This rate should be very small, however, as most of the incoming molecules are simply scattered (hop again), or adsorbed, in which case they are promptly evaporated. So, it seems that the assumption of photodissociation as the only loss is valid.

6. The only regions where a molecule can be stable forever are areas in circular polar regions.

   As shown in Chapter 3, temperatures must stay very cold for a H_2O molecule to be stable against evaporation for long time–scales. These temperatures are probably only obtained in permanently shadowed regions. The fractional area of permanently shadowed regions away from the polar regions is very small and may be neglected.

E.3 Results

For each of the tests about to be shown, the model was run 200 times, using 1000 molecules on each run. The numbers which come out of each run are: the percent of molecules which start in the infinitely stable polar regions (n_{start}), the percent of molecules which end up in these regions (n_{stable}), the average number of hops for stable molecules (n_{hop_1}), and the average number of hops for photodissociated molecules (n_{hop_2}). Random initial placement tests will be discussed first. The parameters used in the first run were:

$T = 500$ K

$m = 18$ amu (H_2O molecules)

$g = 3.70\text{m/s}^2$

$\tau = 2.0 \times 10^4$ s

$R_{planet} = 2439$ km

$R_{pole} = 425$ km

$f_{shad} = 0.275$.

As a check of whether the random initial placement was truly random, the percent of molecules initially in the stable regions should be:

$$P_p = \frac{2\int_{\phi=0}^{\phi_{pole}}\int_{\beta=0}^{2\pi}\sin\phi d\phi d\beta}{4\pi} \times f_{shad} \times 100\% = (1-\cos\phi_{pole}) \times f_{shad} \times 100\% \quad .$$

With the above parameters, this comes out to: $P_p \sim 0.42\%$. The numbers from the run yielded: $n_{start} = 0.419 \pm 0.189\%$, which is consistent. Second, to check that the assumption of each molecule undergoing many hops (see above), the average numbers of hops were: $n_{hops_1} = 43.80 \pm 6.99$, and $n_{hops_2} = 60.57 \pm 1.97$. So, it seems that indeed, this assumption is valid. Now, to show what percent of molecules became stable forever, a histogram was constructed, and is shown in Figure E.3. The histogram shows that the resultant distribution is approximately gaussian. The formal statistical result after all 200 runs was: $n_{stable} = 5.169 \pm 0.664\%$. Table E.1 shows the results for a number of other runs, for which the parameters were as above, except as tabulated. It seems that reasonable choices in the parameters result in $\sim 5\%$ of H_2O molecules making it to the stable regions. Table E.1 also shows results for tests run with the same parameters, but with initial placement in the stable polar regions. For these runs, reasonable choices in the parameters result in $\sim 85\%$ of H_2O molecules making it back to the stable regions.

Table E.1

Migration Simulation Results

T (K)	R_{pole} (km)	f_{shad}	initial placement	n_{stable} (%)
500	425	.275	random	5.18 ± 0.71
500	425	1.0	random	6.44 ± 0.74
500	300	1.0	random	4.59 ± 0.65
500	175	1.0	random	2.94 ± 0.51
350	425	.275	random	4.30 ± 0.56
500	600	.275	random	7.86 ± 0.79
500	425	.275	polar	80.7 ± 1.4
500	425	1.0	polar	93.5 ± 0.76
500	300	1.0	polar	90.6 ± 0.94
500	175	1.0	polar	82.3 ± 1.2
350	425	.275	polar	86.5 ± 0.97
500	600	.275	polar	85.3 ± 1.0

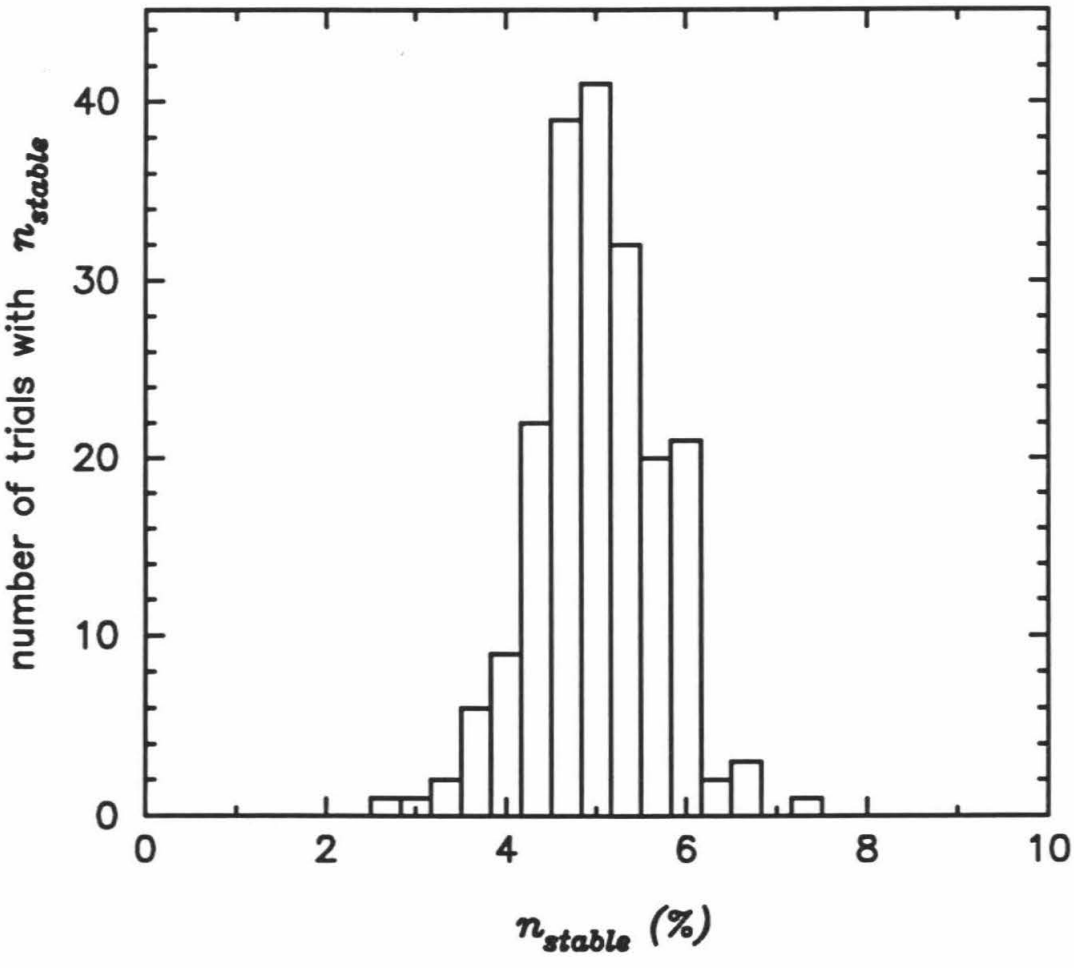

Figure E.3: A histogram of the number of stable molecules in a migration simulation. The histogram is a compilation of the results of 200 separate runs, each tracking 1000 molecules.

Appendix F

Mars Cross Section Images

This appendix contains all of the images of Mars obtained by us in the high resolution experiments. Each page contains images of both SS (on the left) and OS (on the right) polarizations, and is identified by the date of observation, the snapshot number for that date, and the subearth longitude (β_o). Also contained on each page is a cartoon showing the planetary coordinates, and locations of major geologic and topographic features (taken from Scott and Tanaka, (1986), Greeley and Guest, (1987), and the USGS Mars topographic maps (I-2160)). Sky coordinates are indicated by the tick marks at the edge of each image, which are 1 arcsec apart. The OS images are blanked interior to an incidence angles of 25°, in order to show the more interesting variations outside the quasi–specular spike. On all of the gray scale plots, darker shades represent higher cross sections. Note that each snapshot has its own gray scale stretch, in order to show the detail in each image better. Note also that snapshots 18 and 19 of the 12/29 data have no real usable SS polarization data.

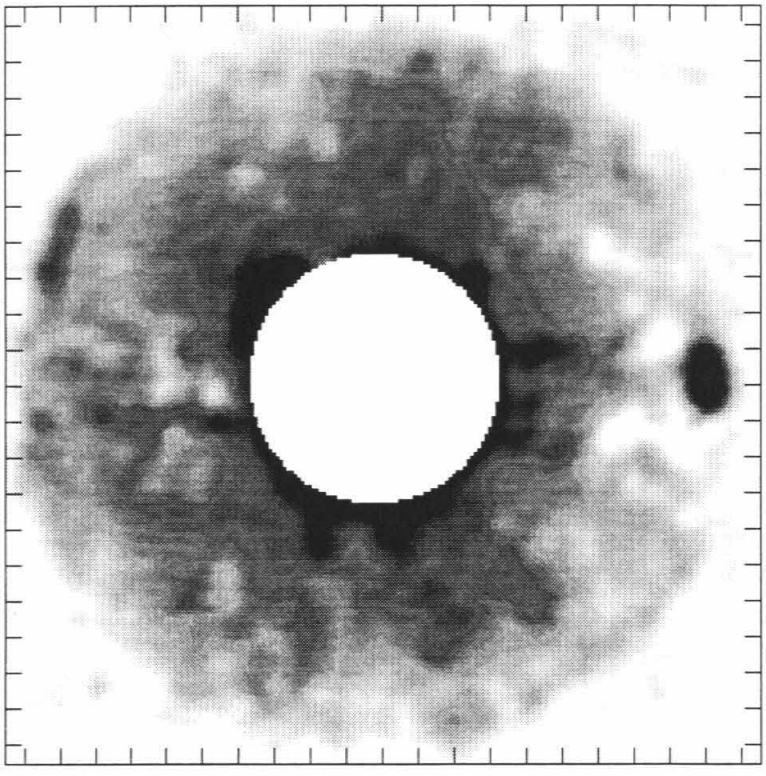

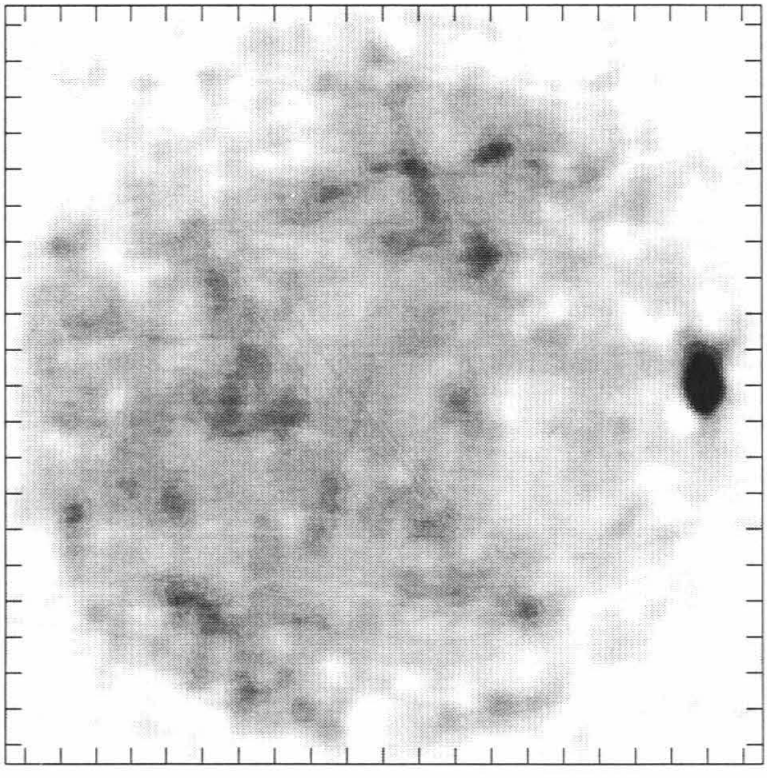

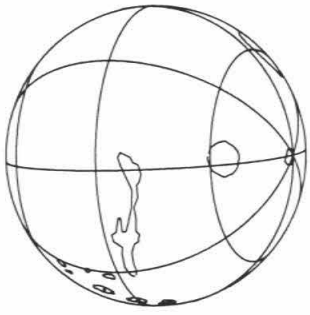

Date: 10/22/88

Snapshot: 1

β_o = 39.2

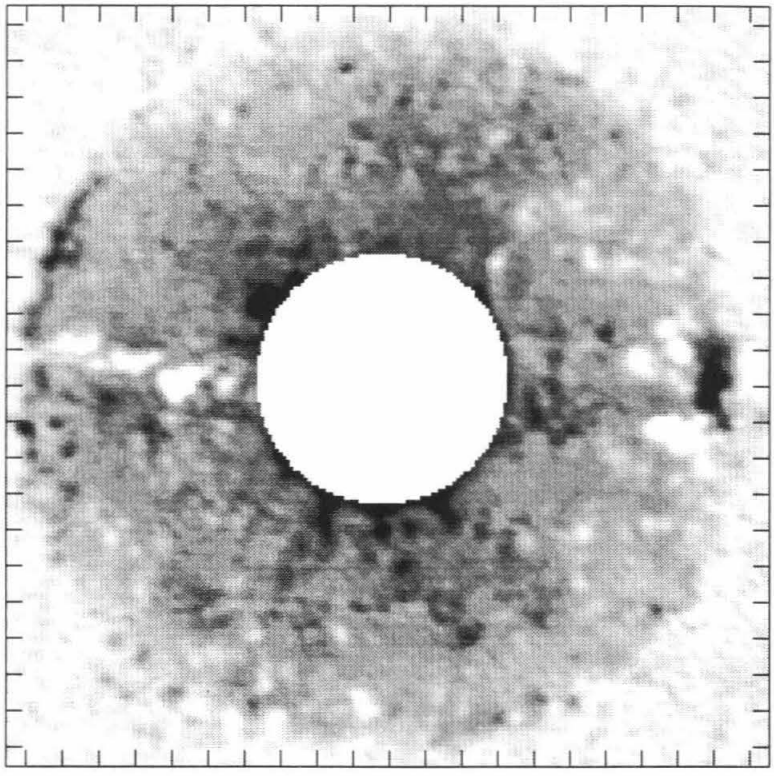

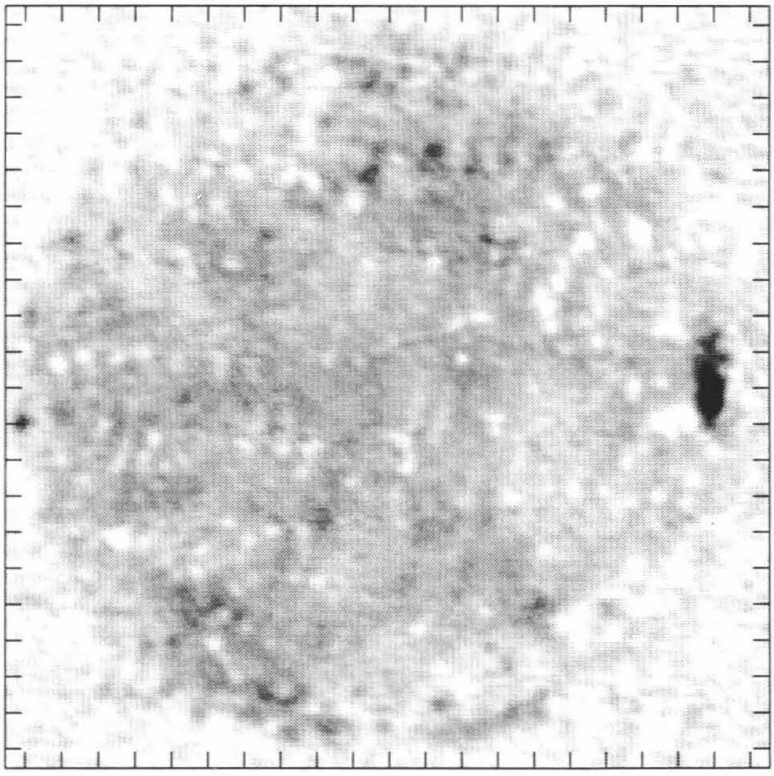

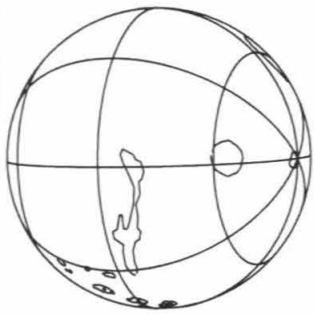

Date: 10/22/88

Snapshot: 2

β_o = 41.5

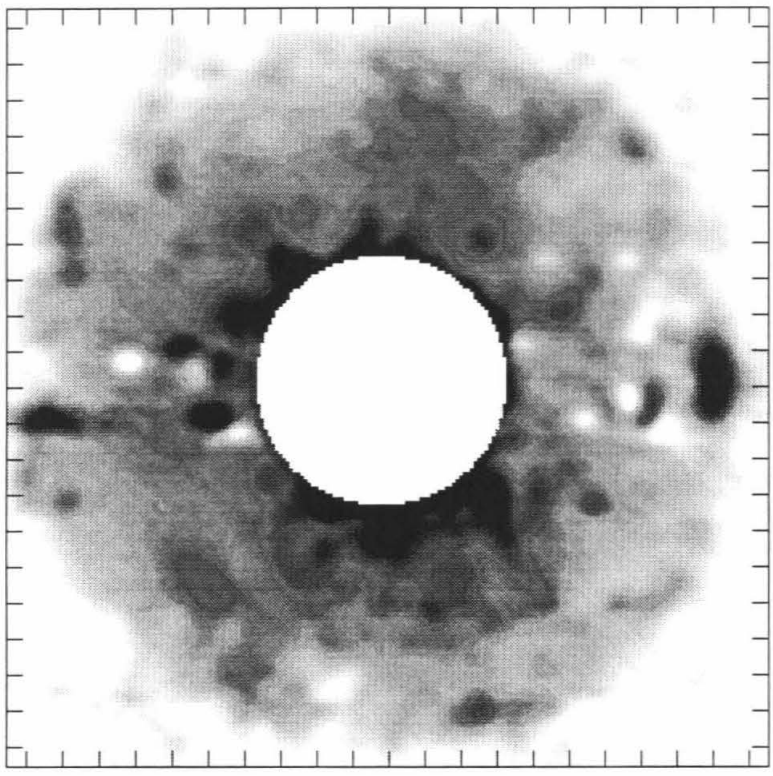

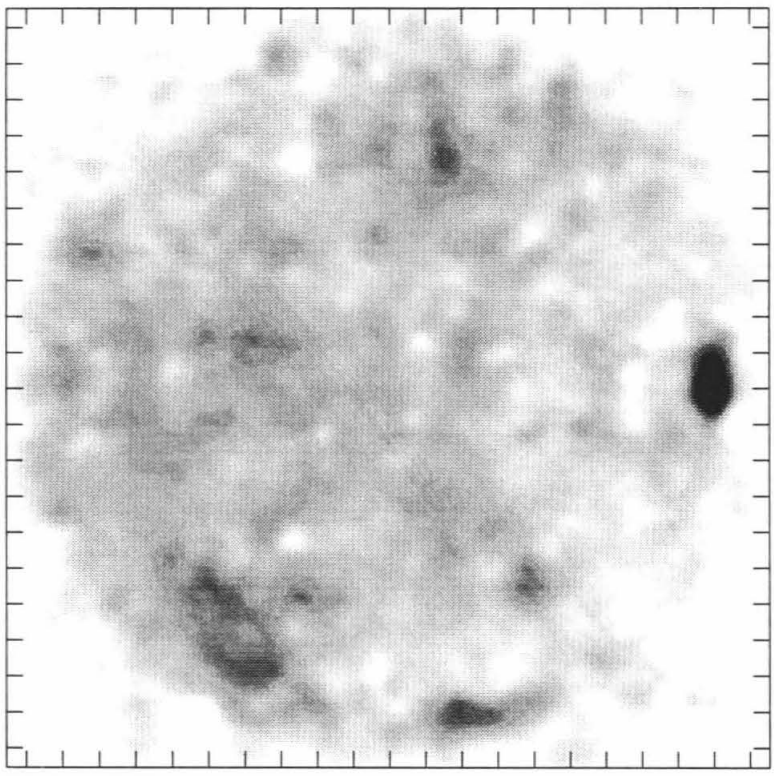

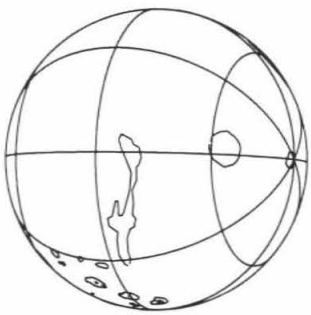

Date: 10/22/88

Snapshot: 3

β_o = 48.0

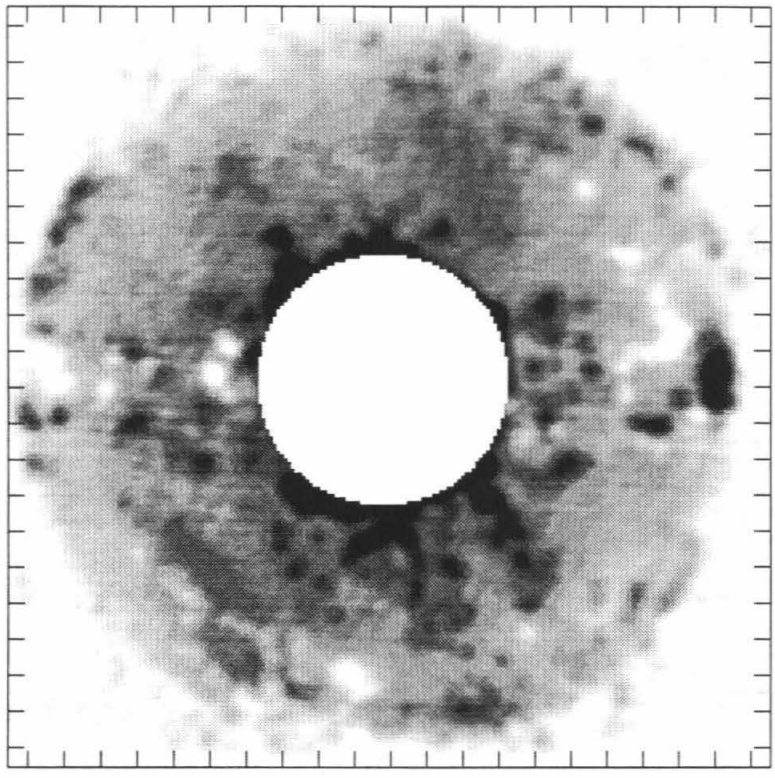

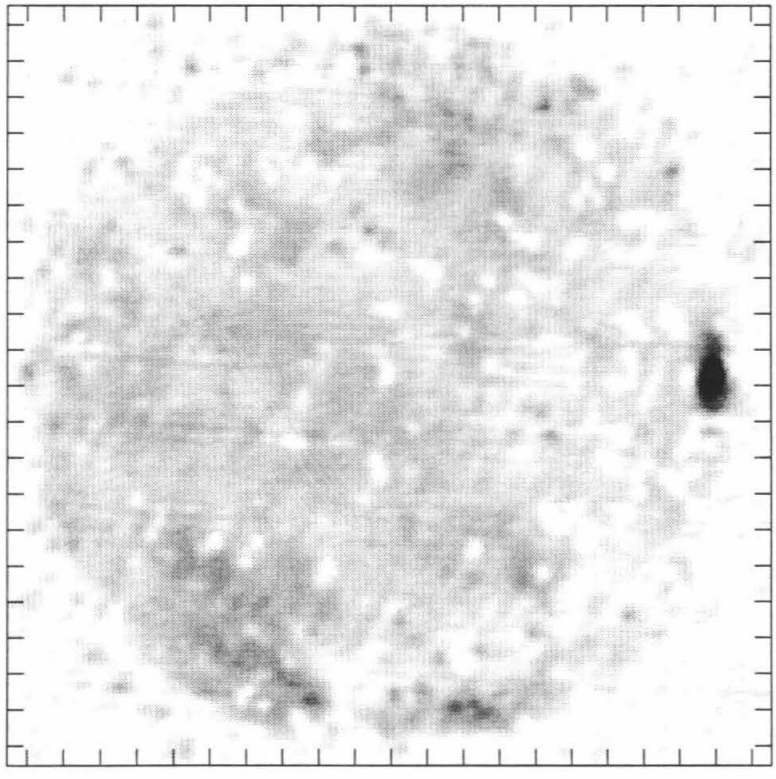

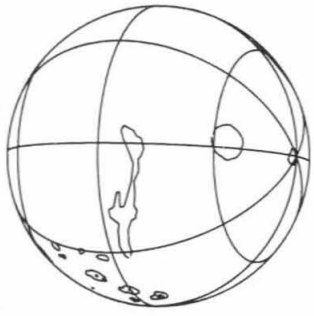

Date: 10/22/88

Snapshot: 4

β_o = 50.2

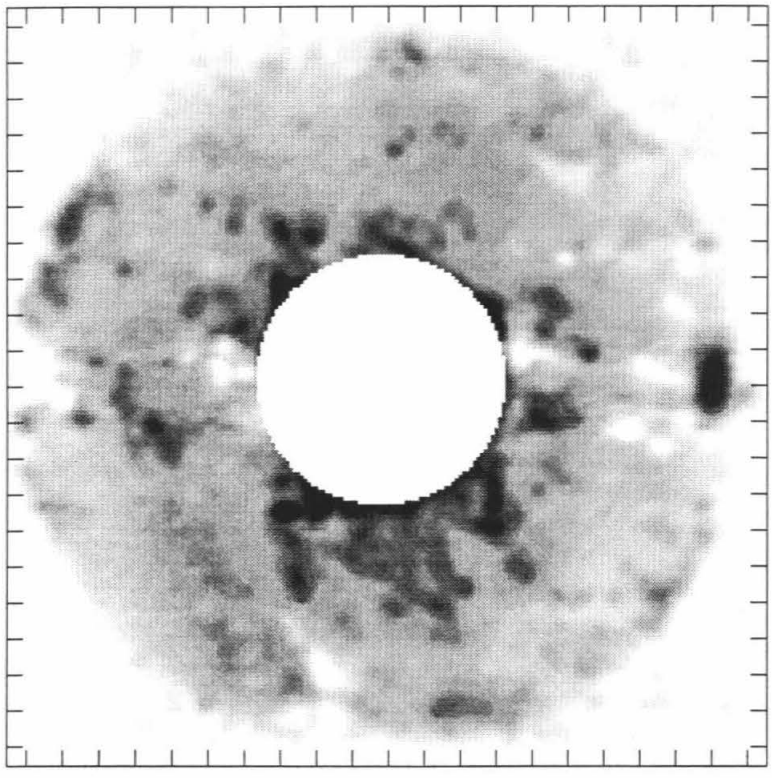

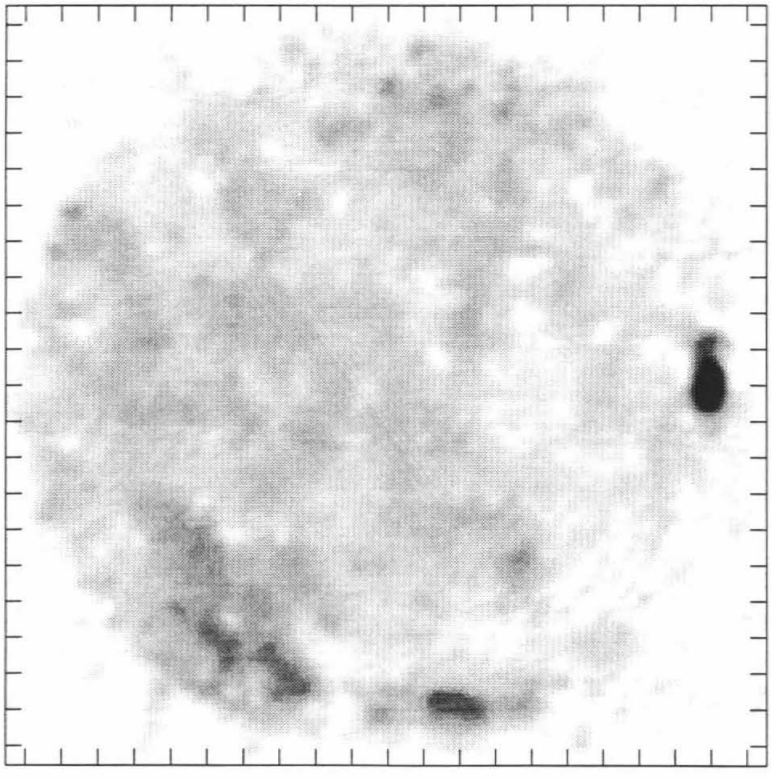

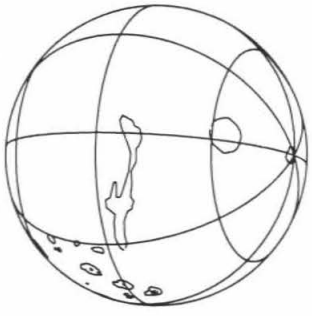

Date: 10/22/88

Snapshot: 5

β_o = 53.7

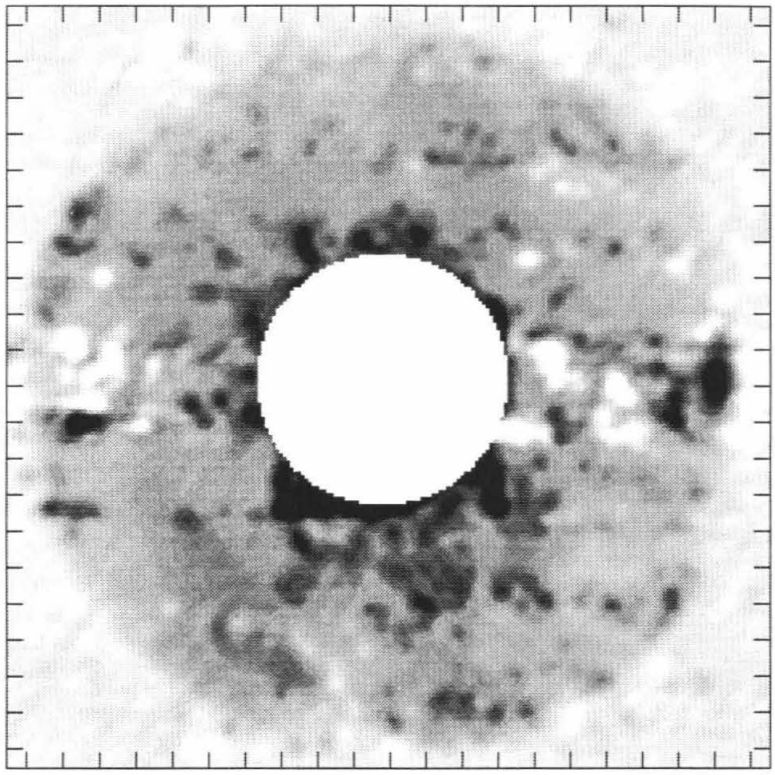

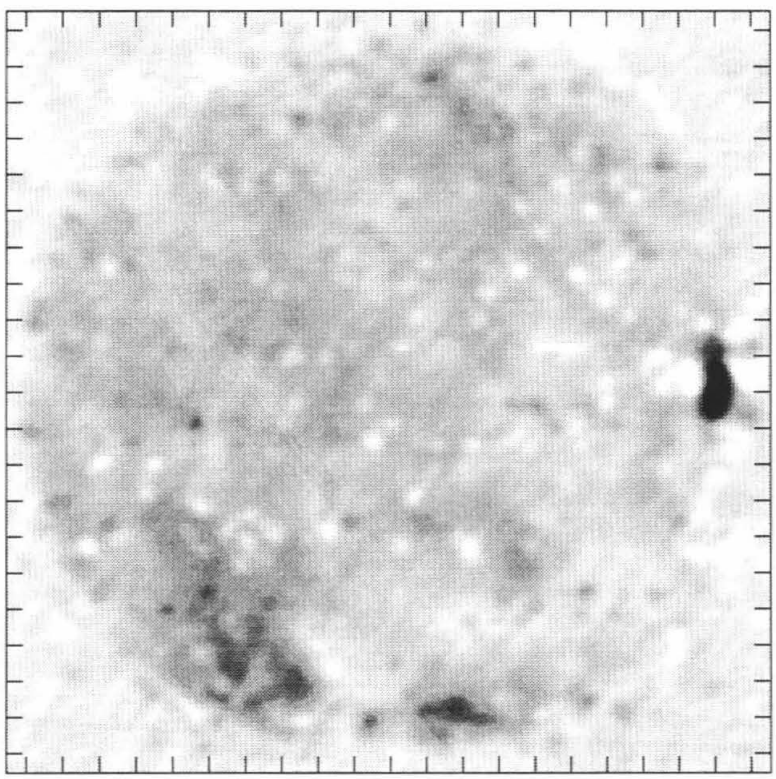

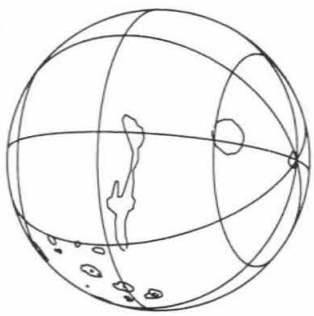

Date: 10/22/88

Snapshot: 6

β_o = 55.9

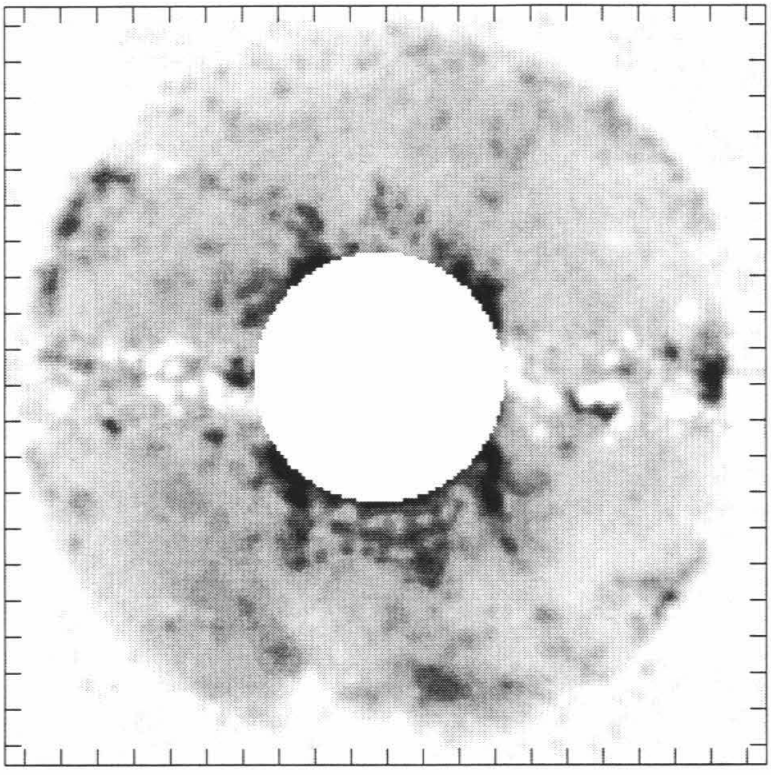

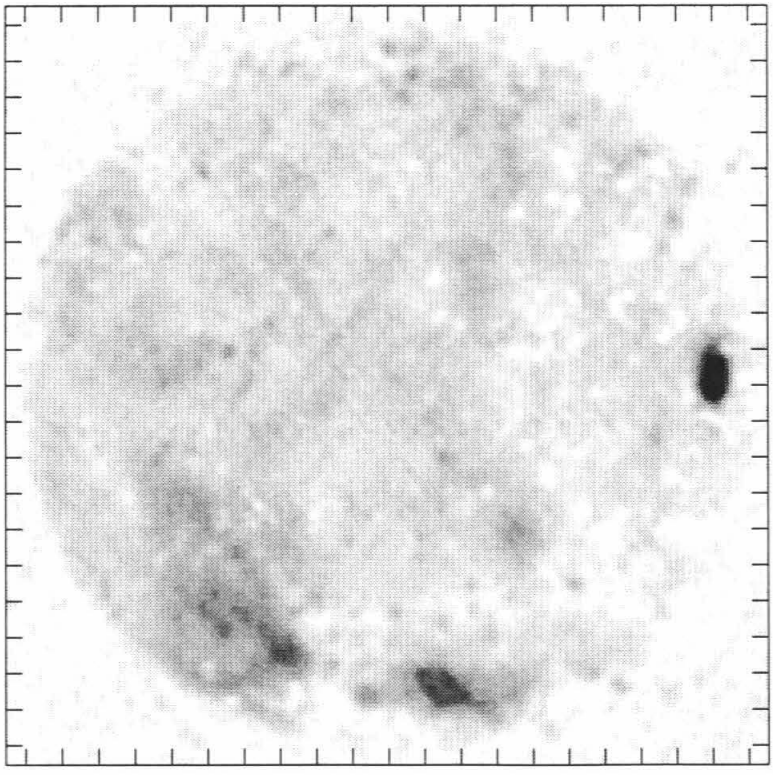

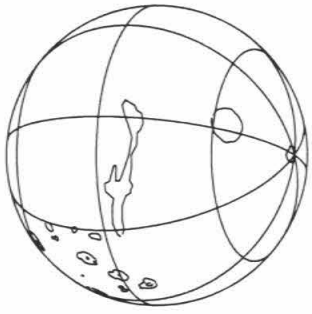

Date: 10/22/88

Snapshot: 7

β_o = 60.2

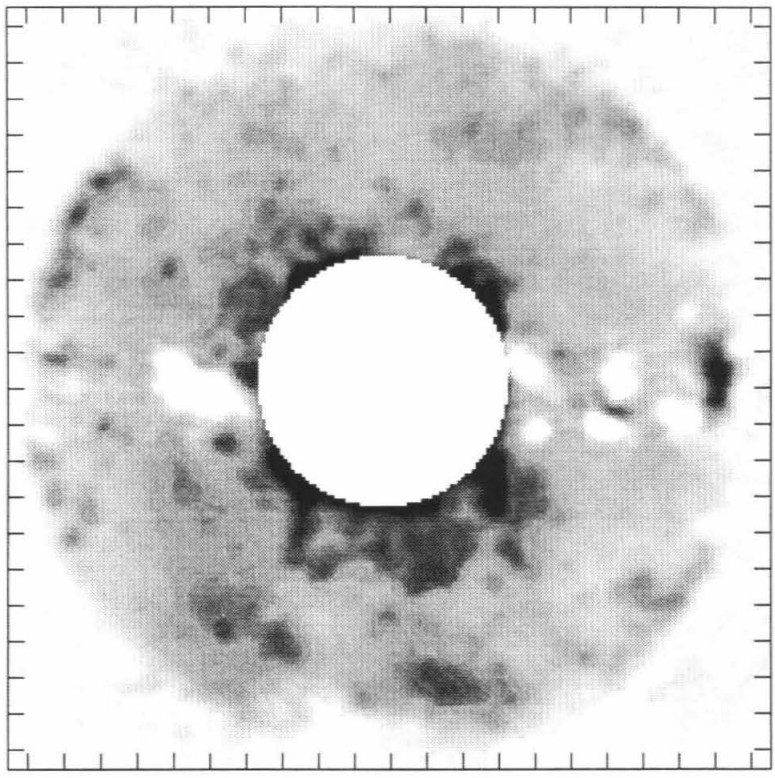

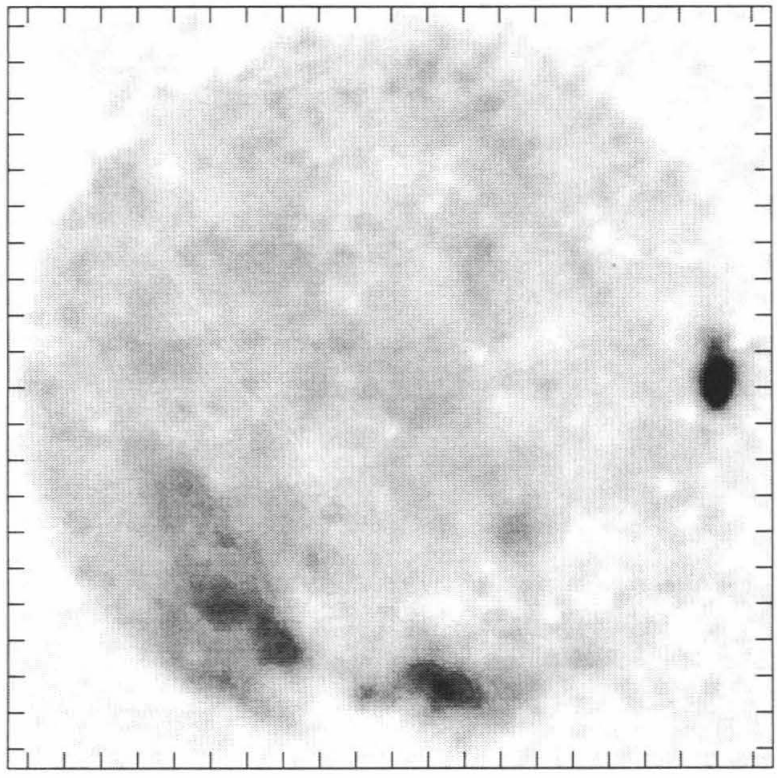

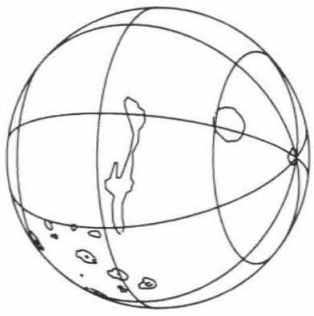

Date: 10/22/88

Snapshot: 8

β_o = 62.2

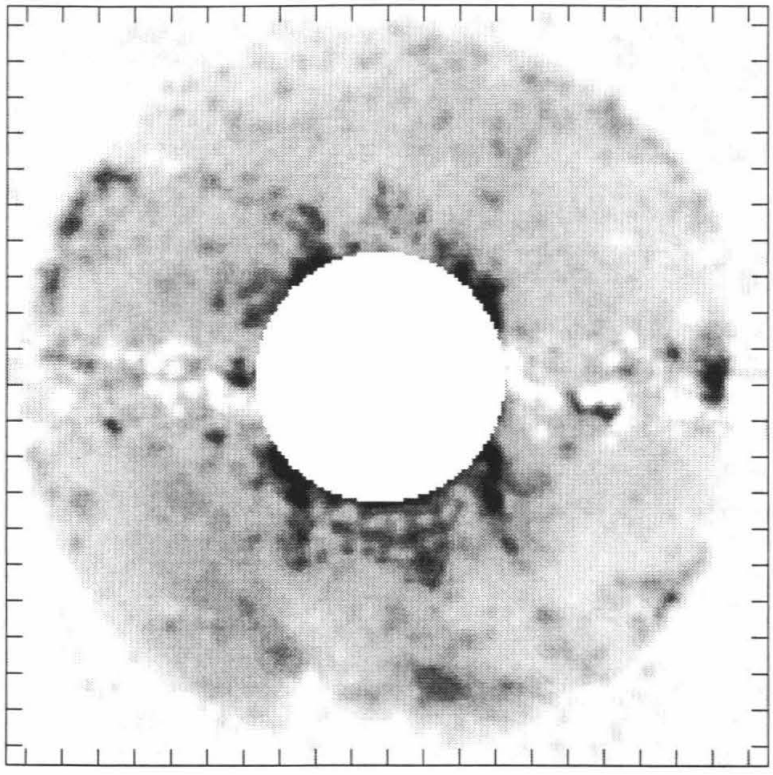

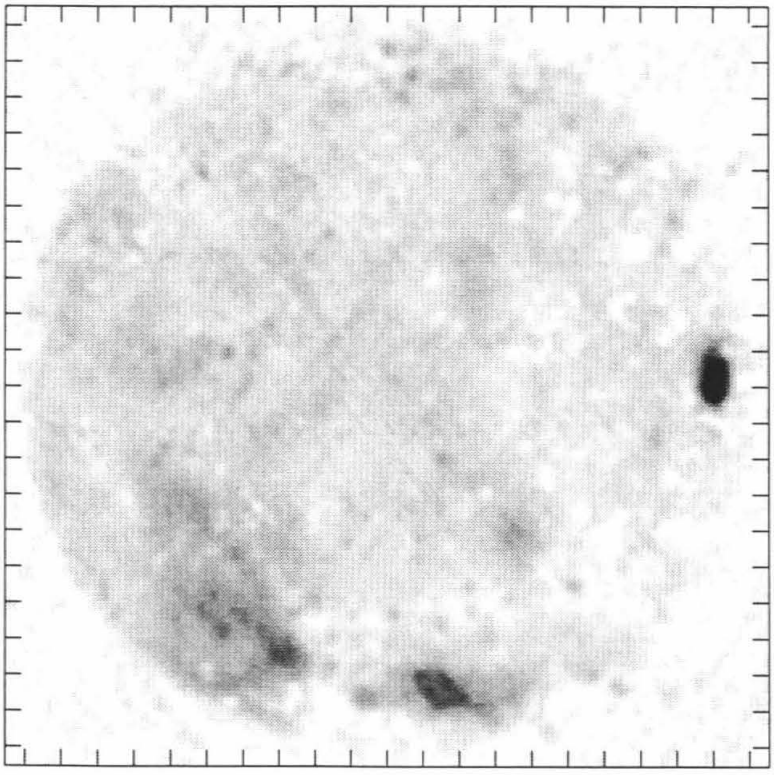

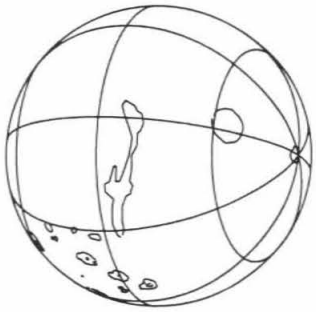

Date: 10/22/88

Snapshot: 7

β_o = 60.2

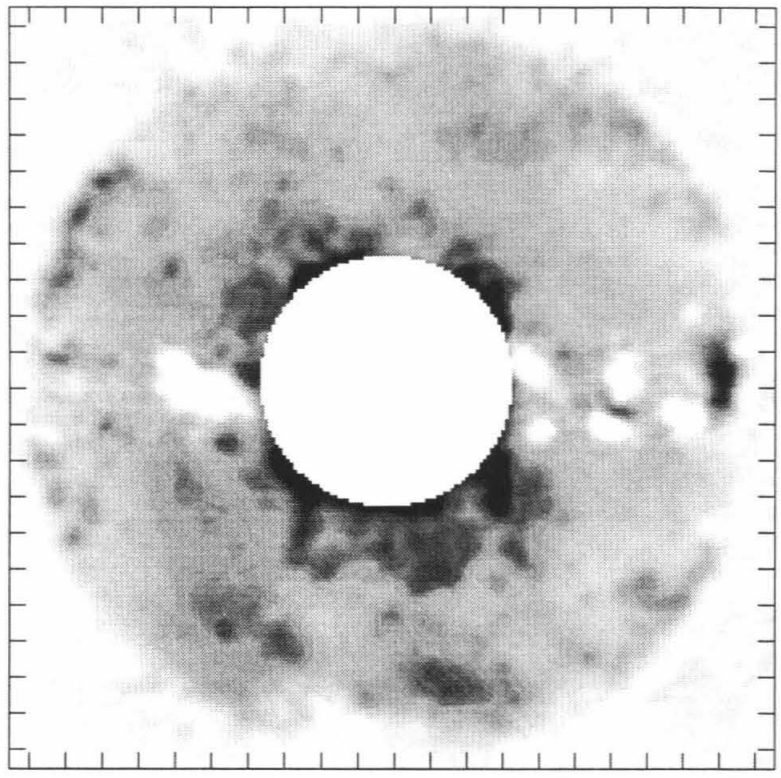

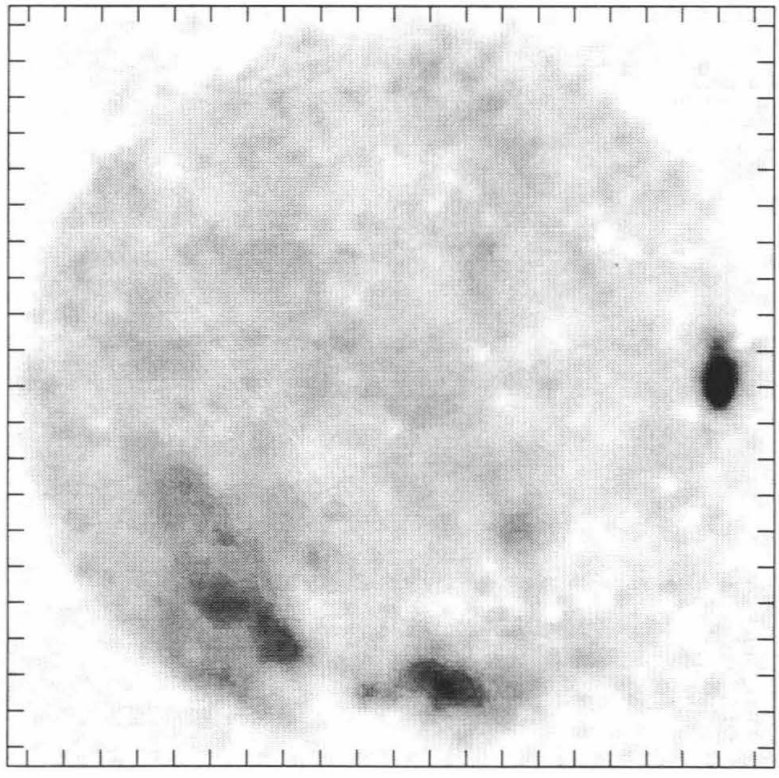

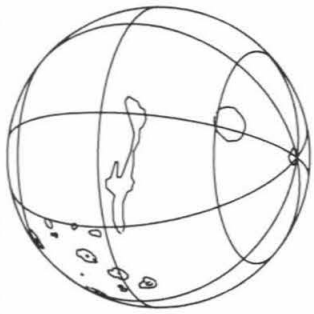

Date: 10/22/88

Snapshot: 8

β_o = 62.2

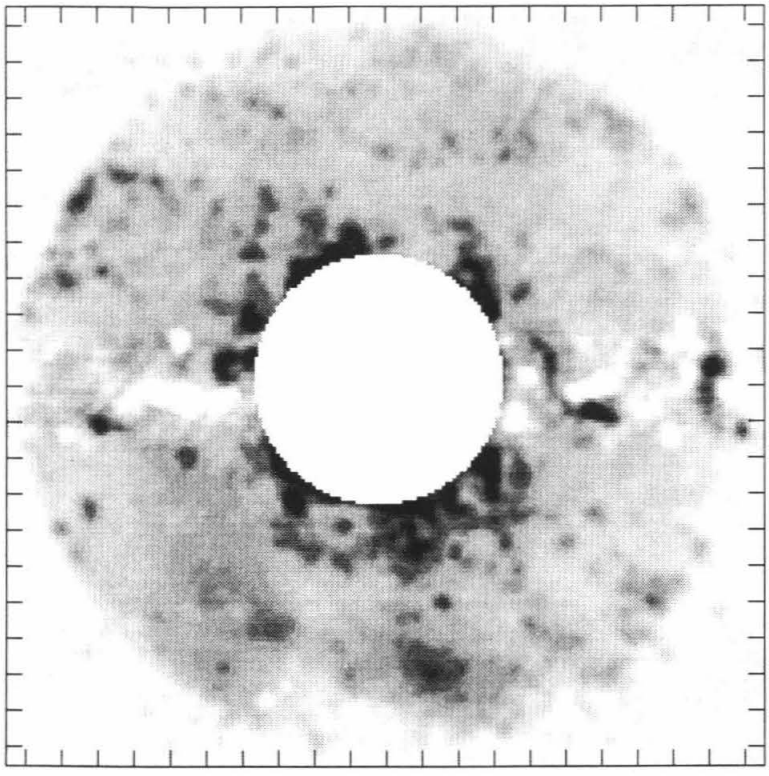

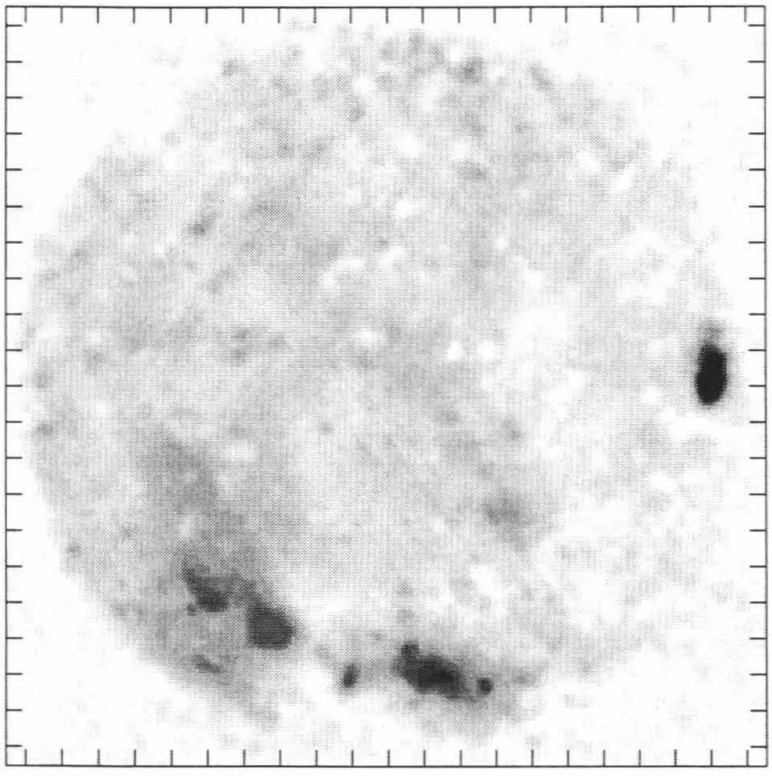

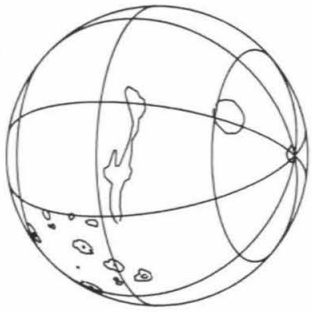

Date: 10/22/88

Snapshot: 9

β_o = 66.1

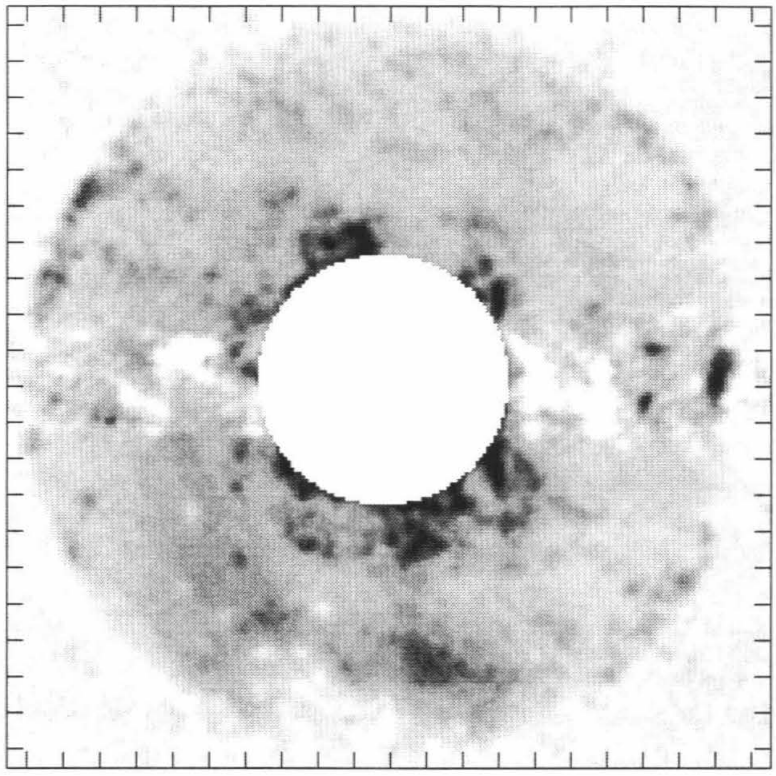

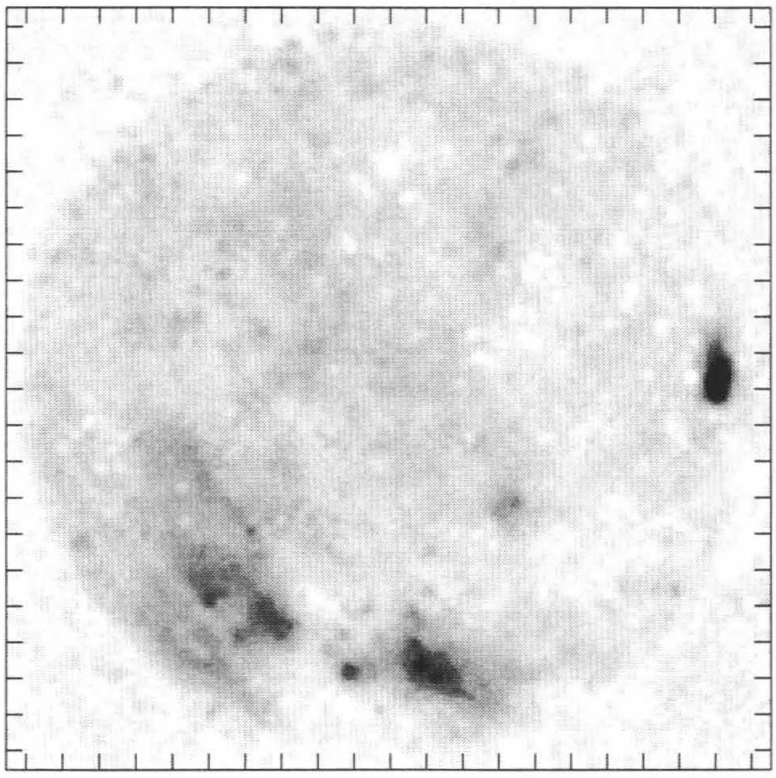

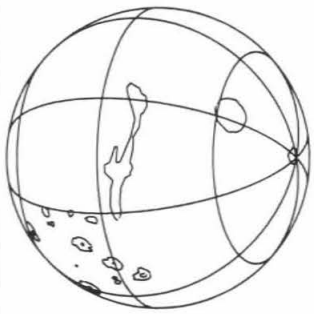

Date: 10/22/88

Snapshot: 10

β_o = 68.2

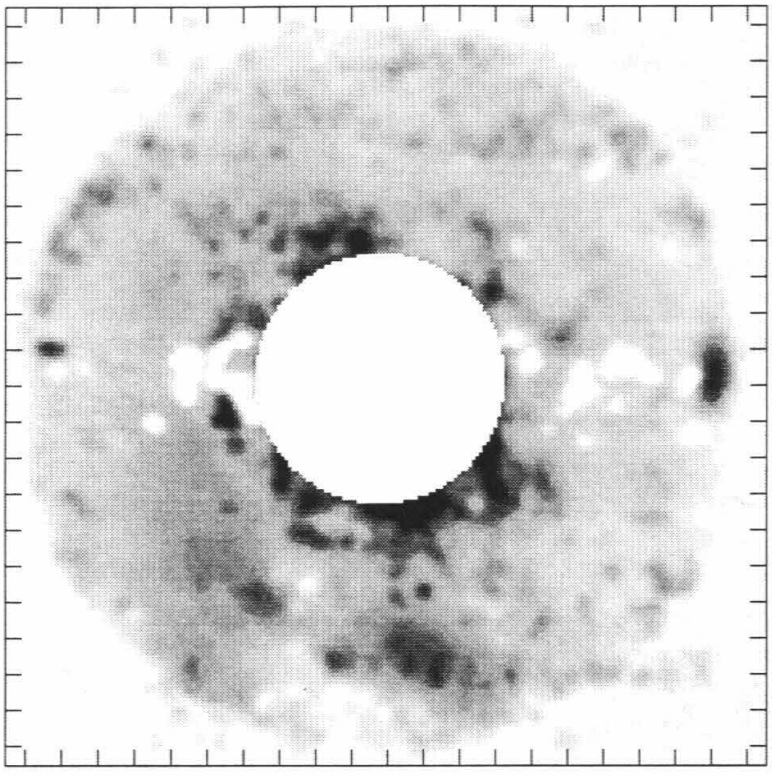

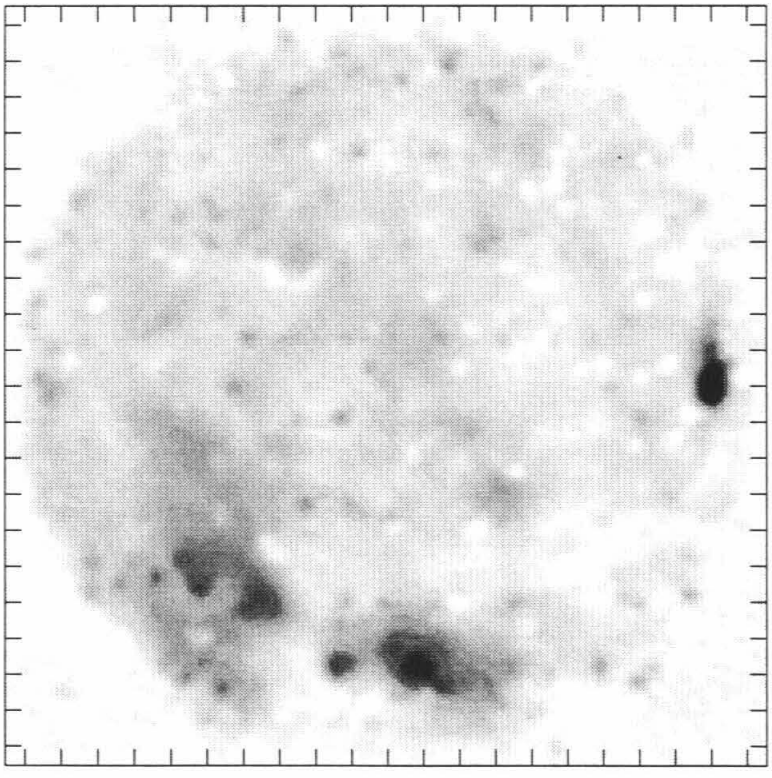

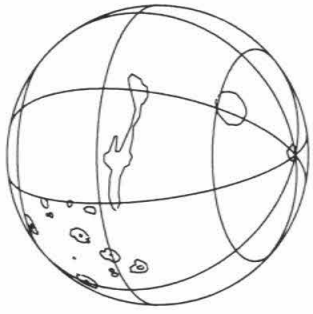

Date: 10/22/88

Snapshot: 11

β_o = 71.4

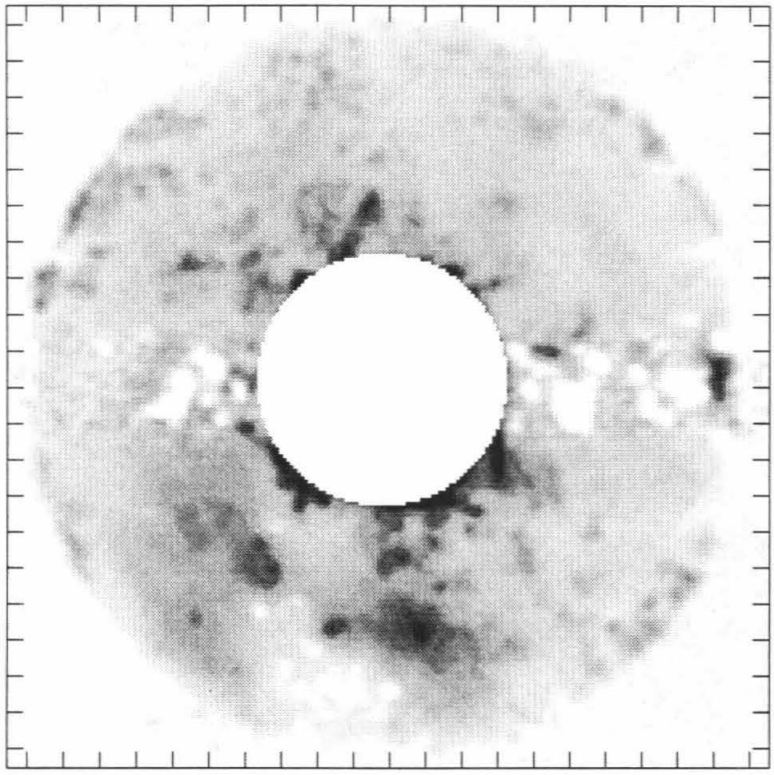

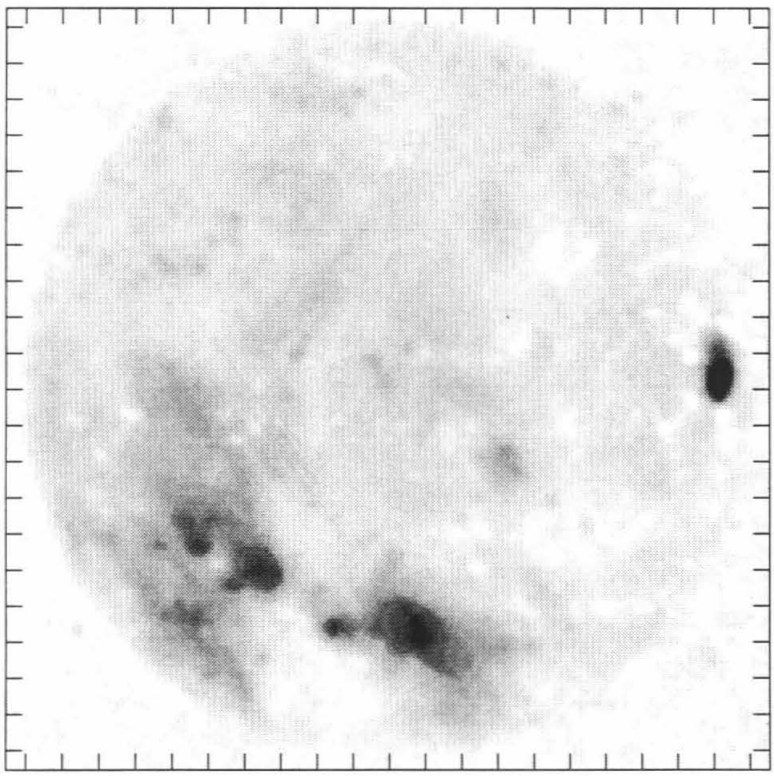

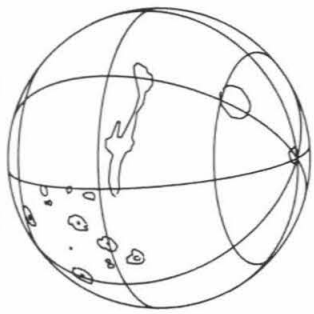

Date: 10/22/88

Snapshot: 12

β_o = 78.2

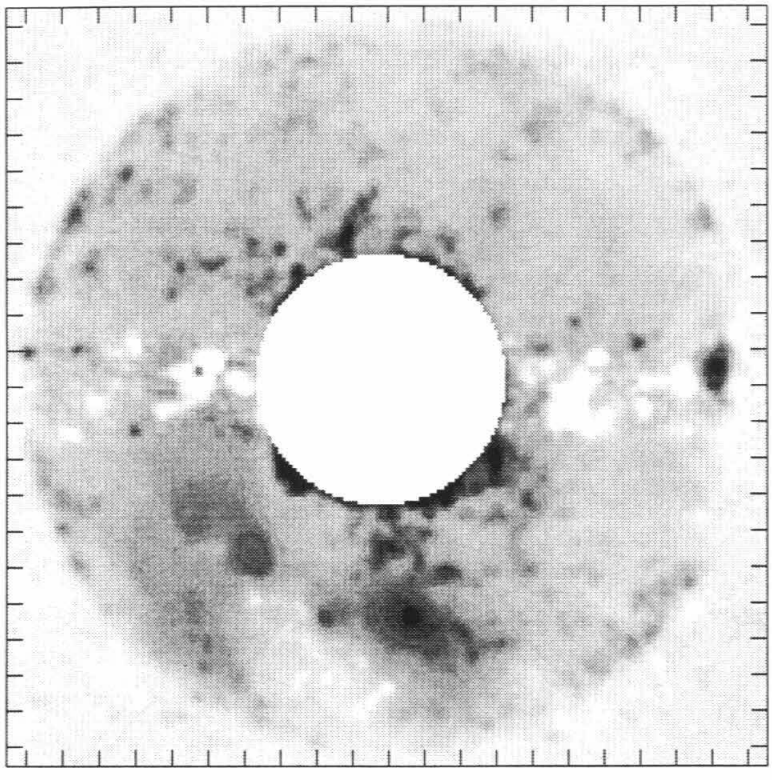

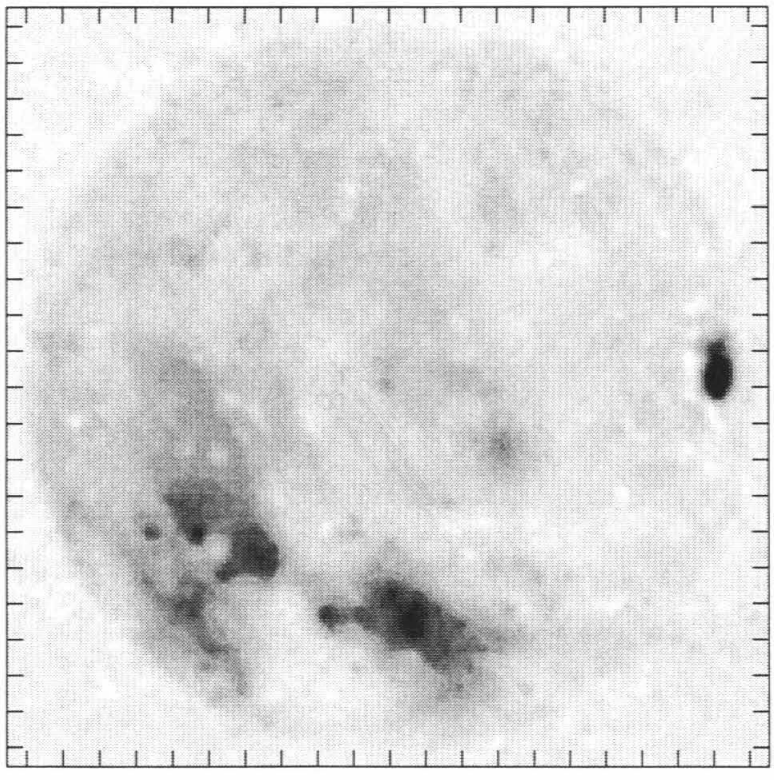

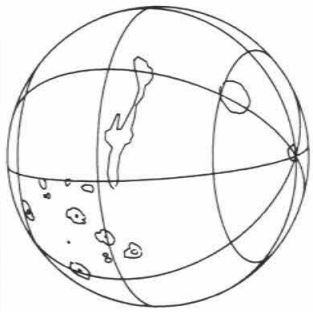

Date: 10/22/88

Snapshot: 13

β_o = 80.4

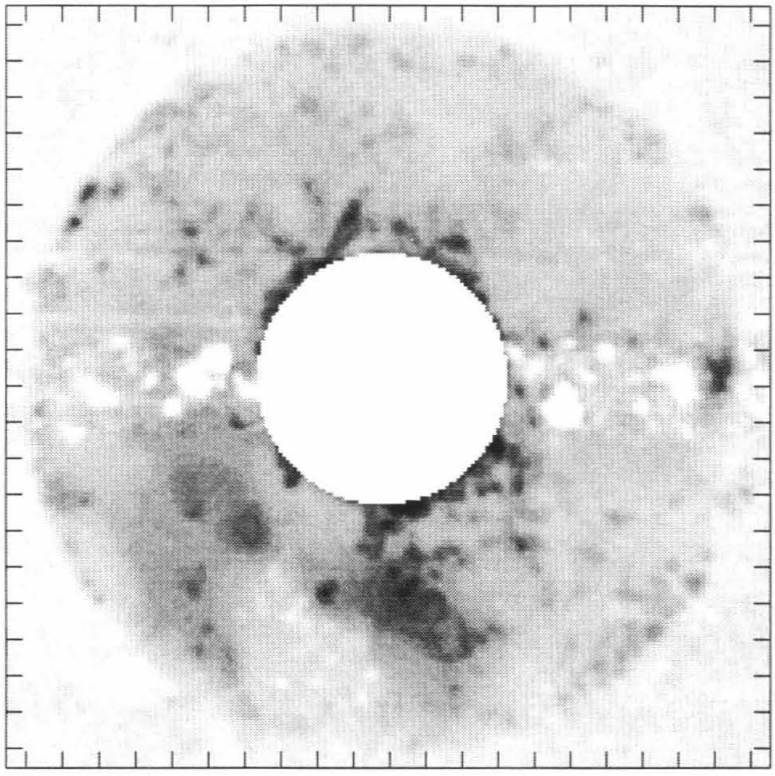

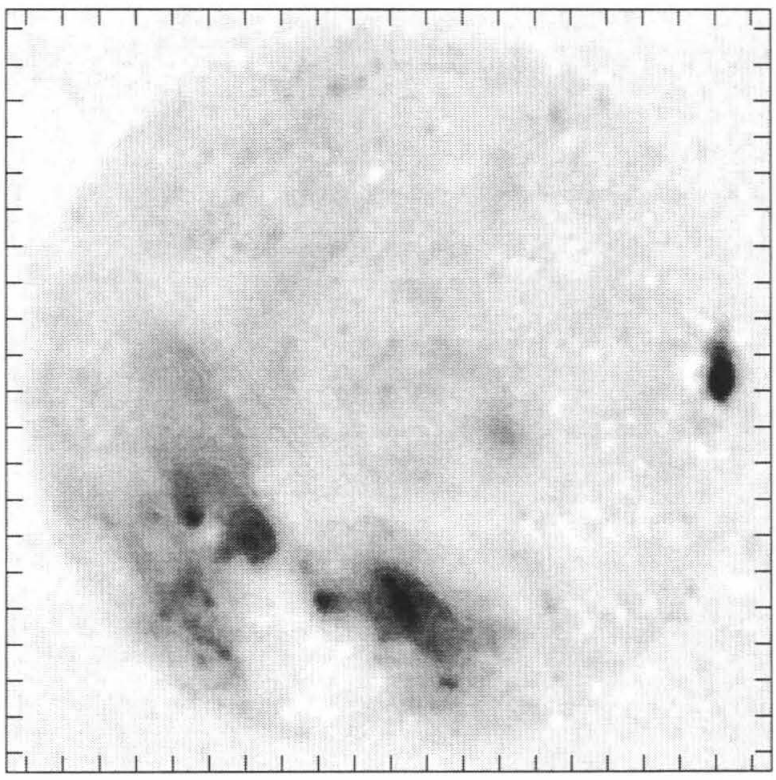

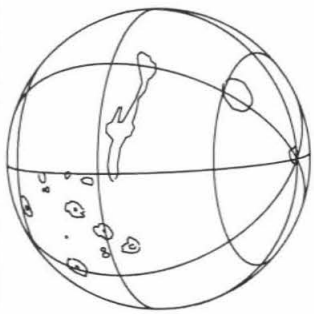

Date: 10/22/88

Snapshot: 14

β_o = 84.3

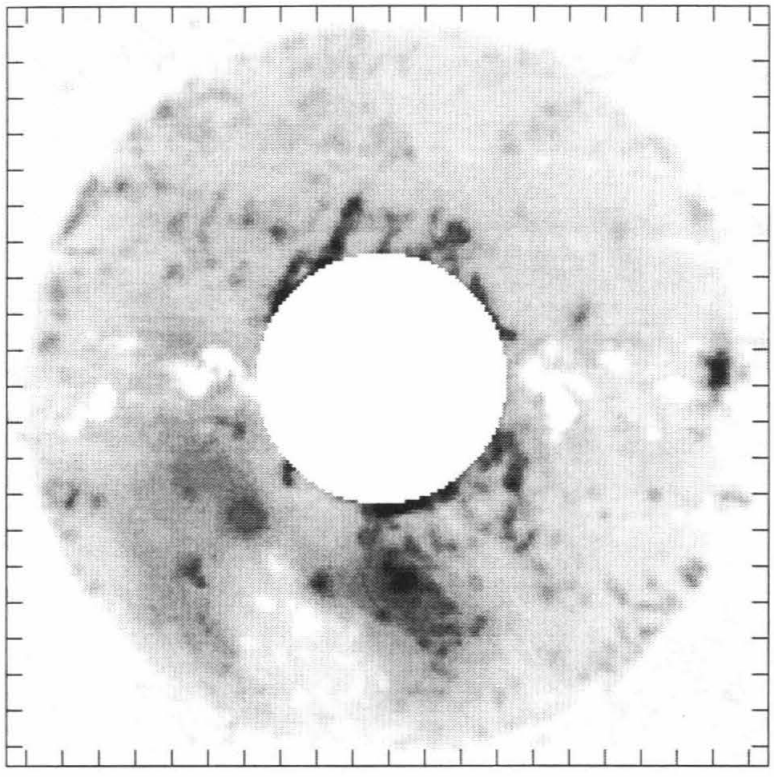

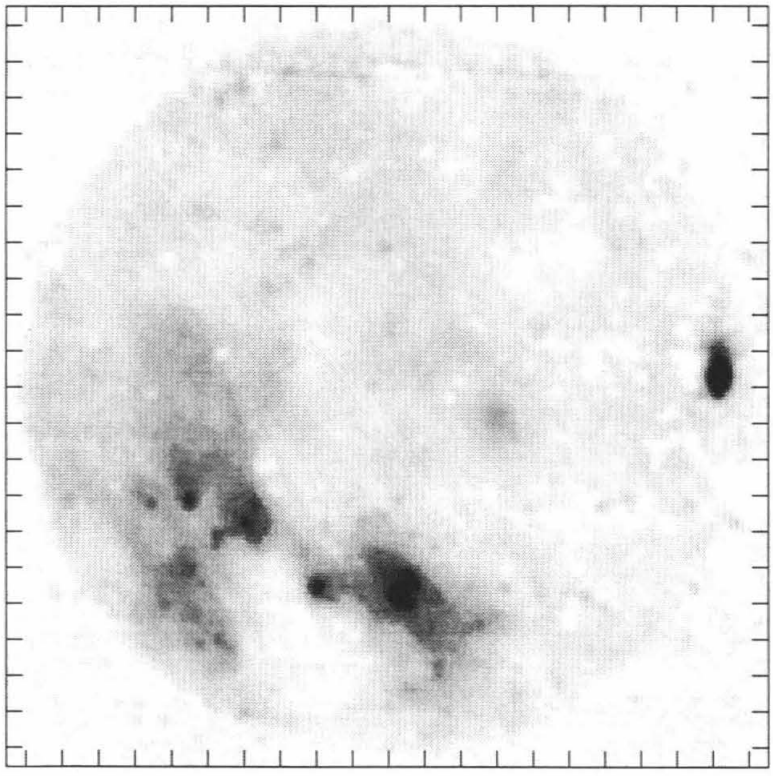

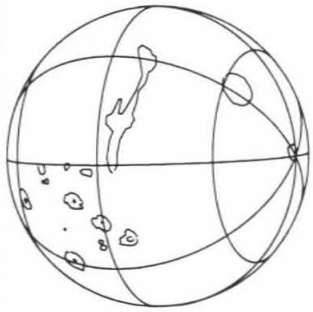

Date: 10/22/88

Snapshot: 15

β_o = 86.5

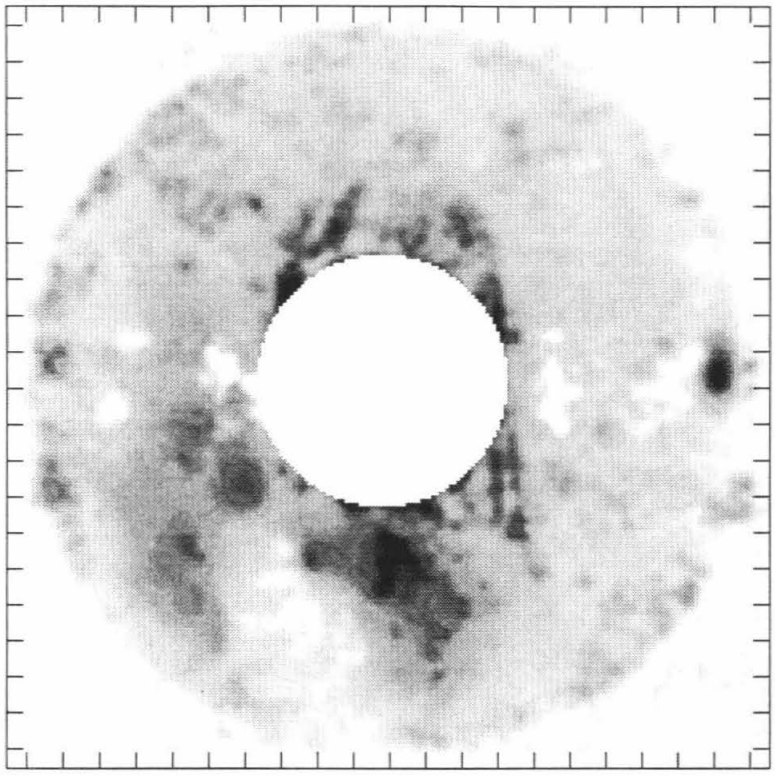

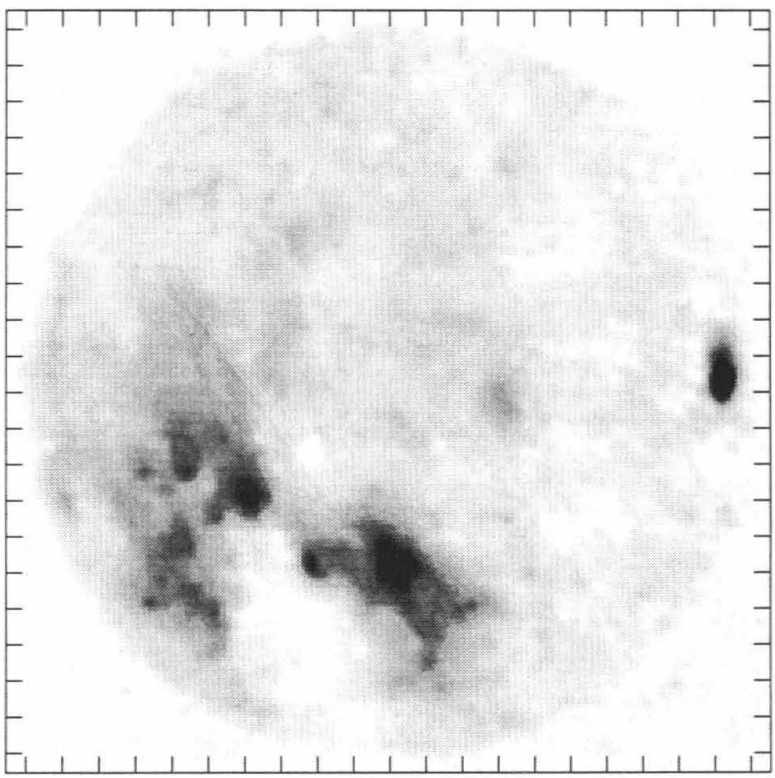

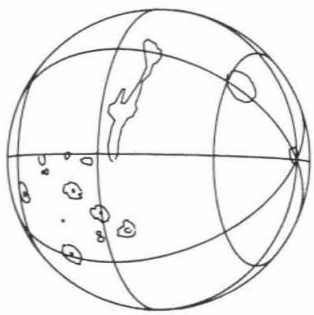

Date: 10/22/88

Snapshot: 16

β_o = 92.2

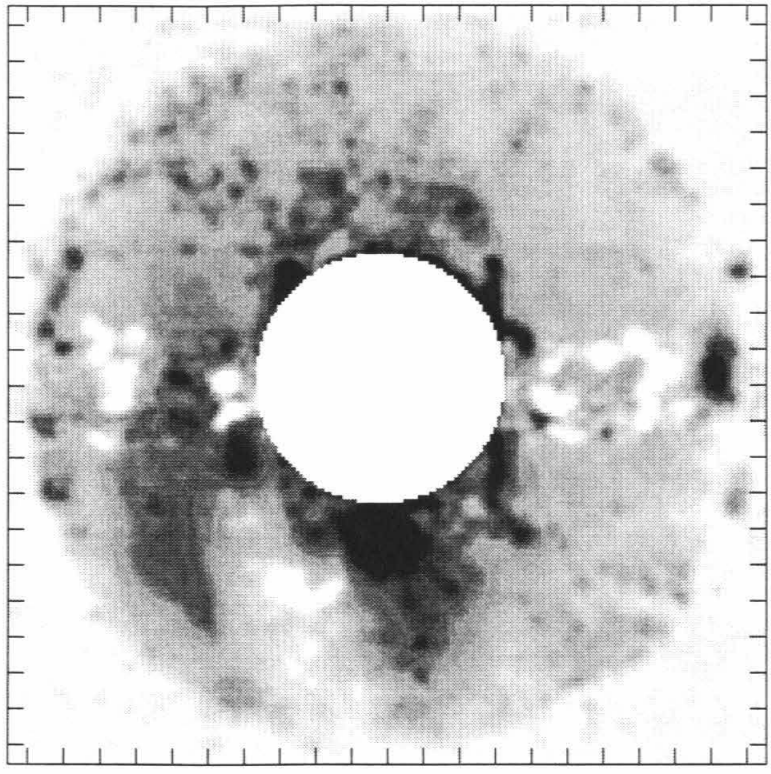

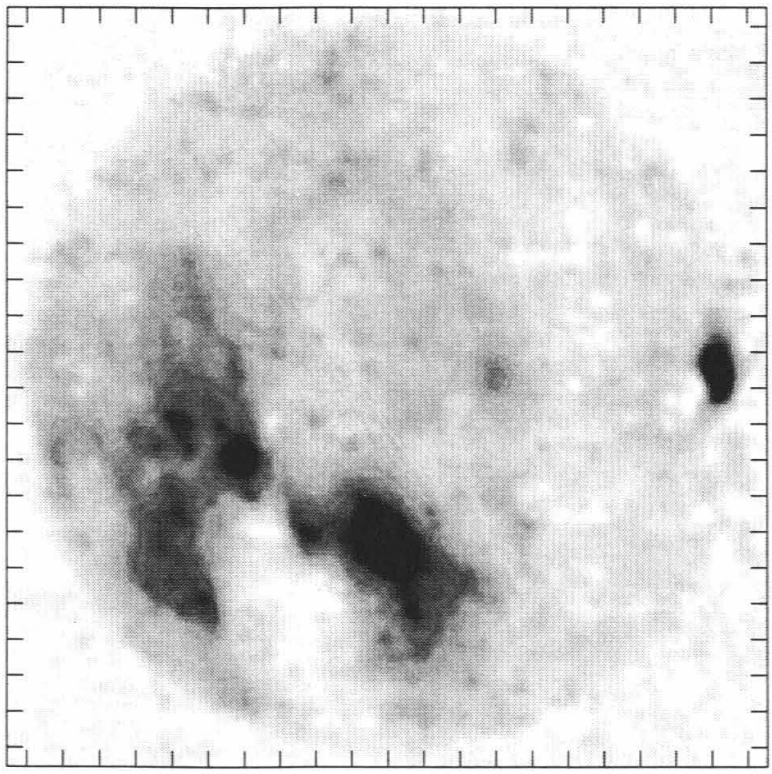

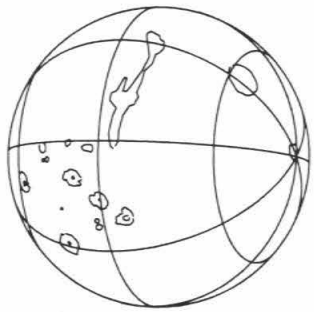

Date: 10/22/88

Snapshot: 17

β_o = 96.2

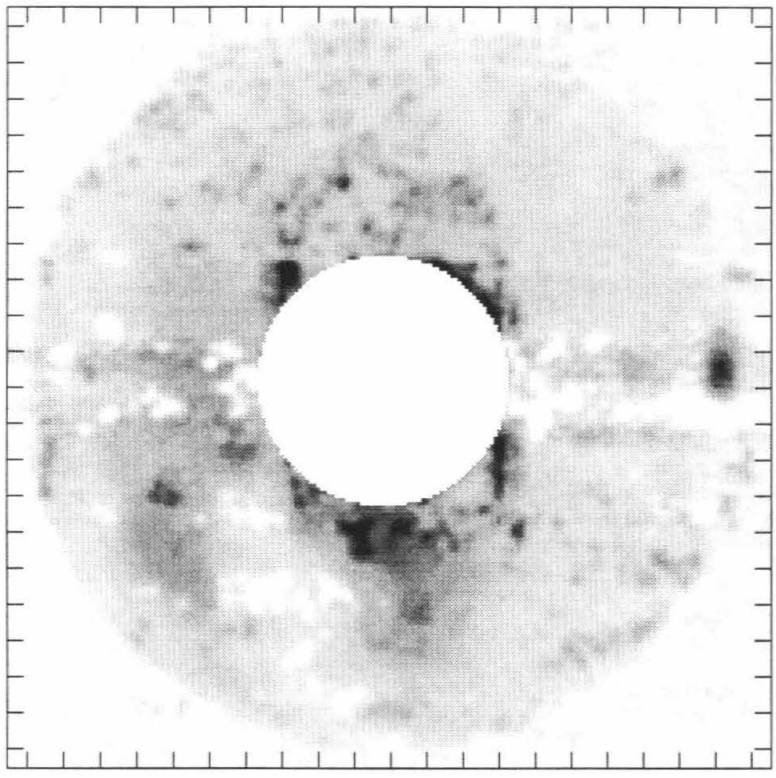

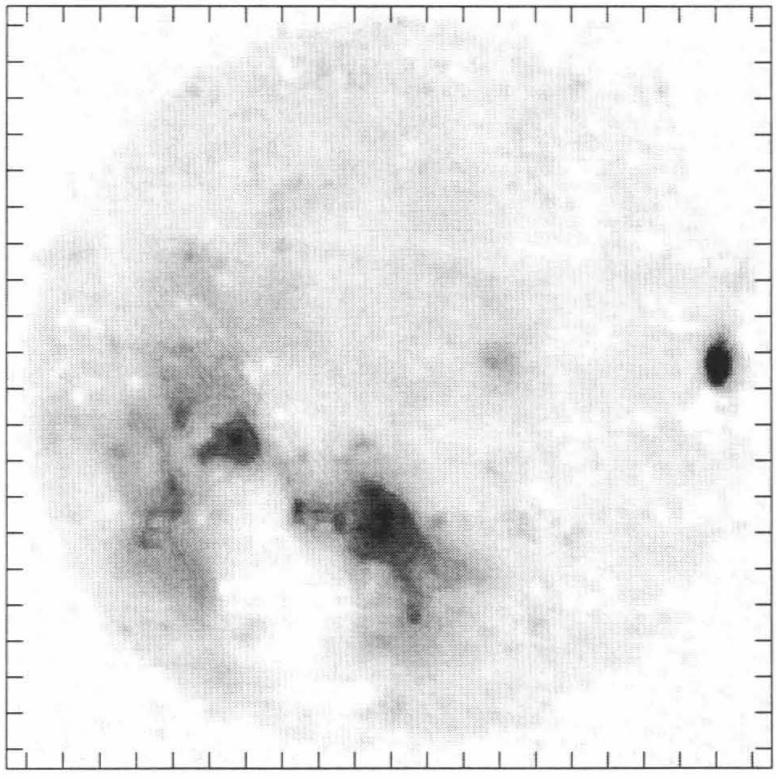

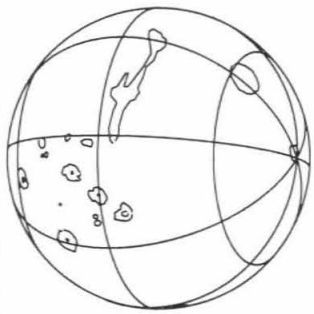

Date: 10/22/88

Snapshot: 18

β_o = 98.6

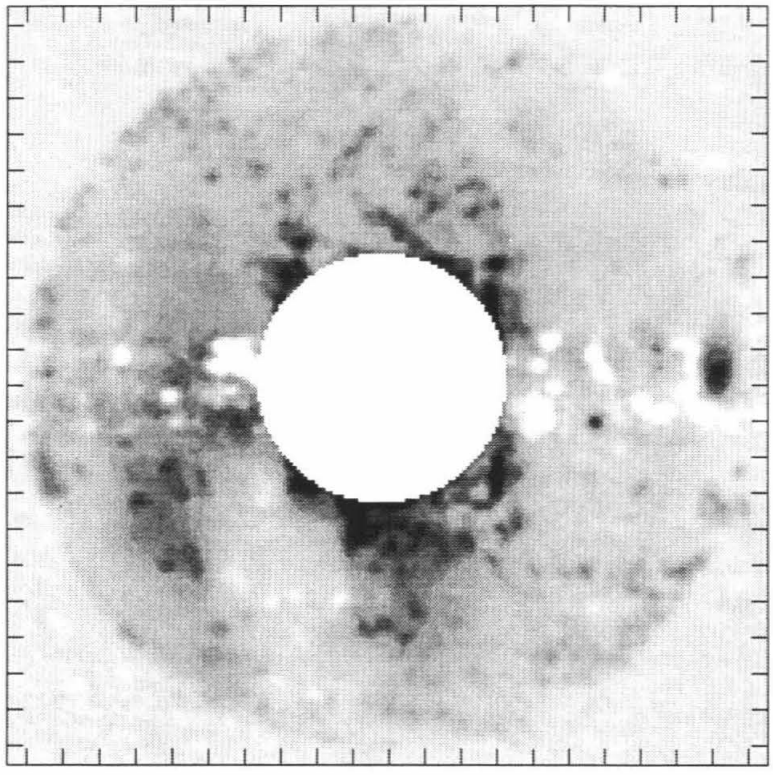

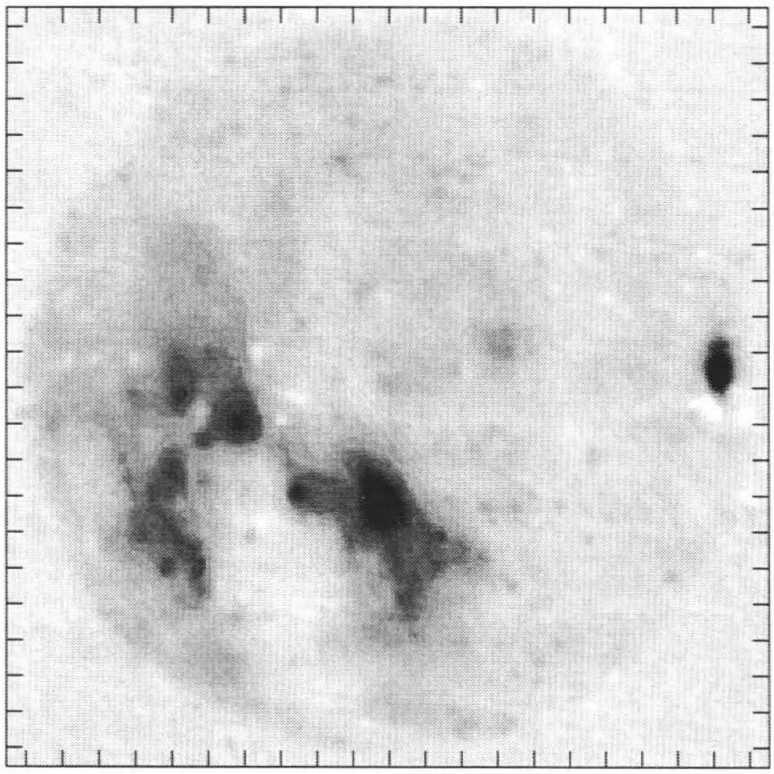

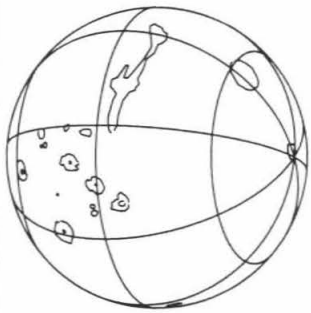

Date: 10/22/88

Snapshot: 19

β_o = 102.3

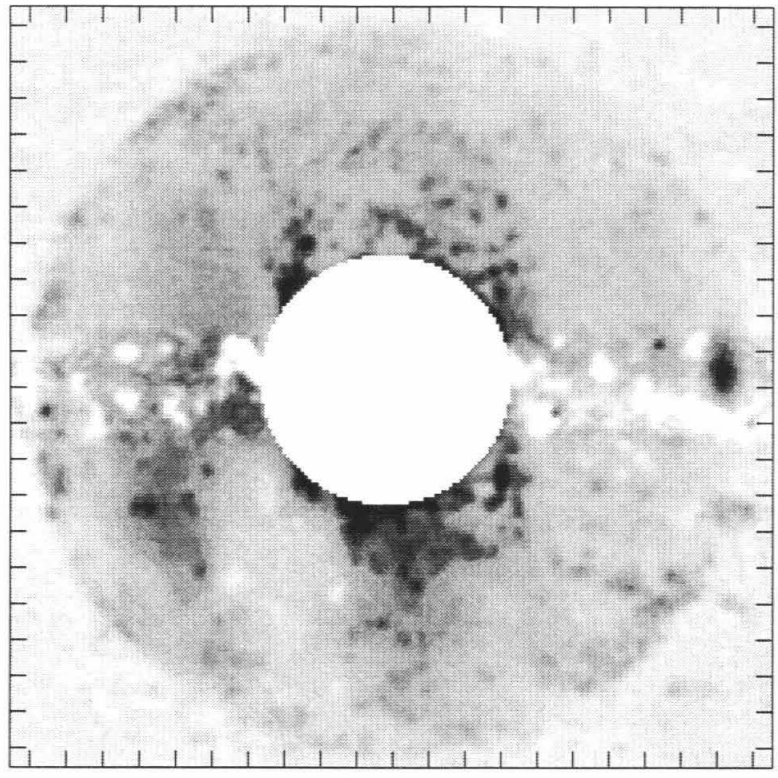

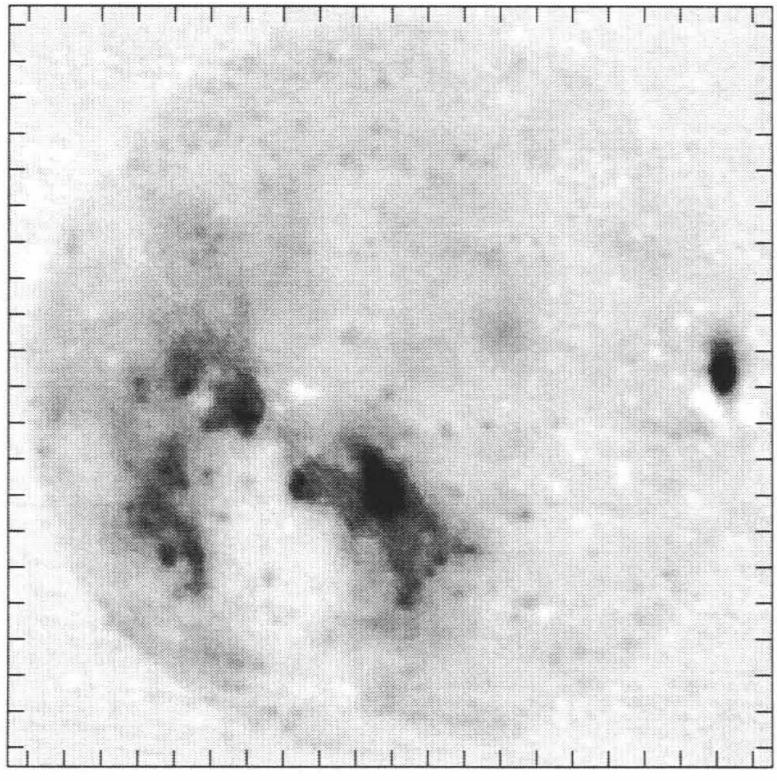

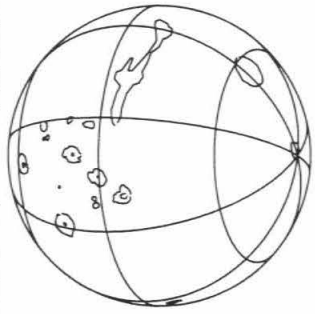

Date: 10/22/88

Snapshot: 20

β_o = 104.6

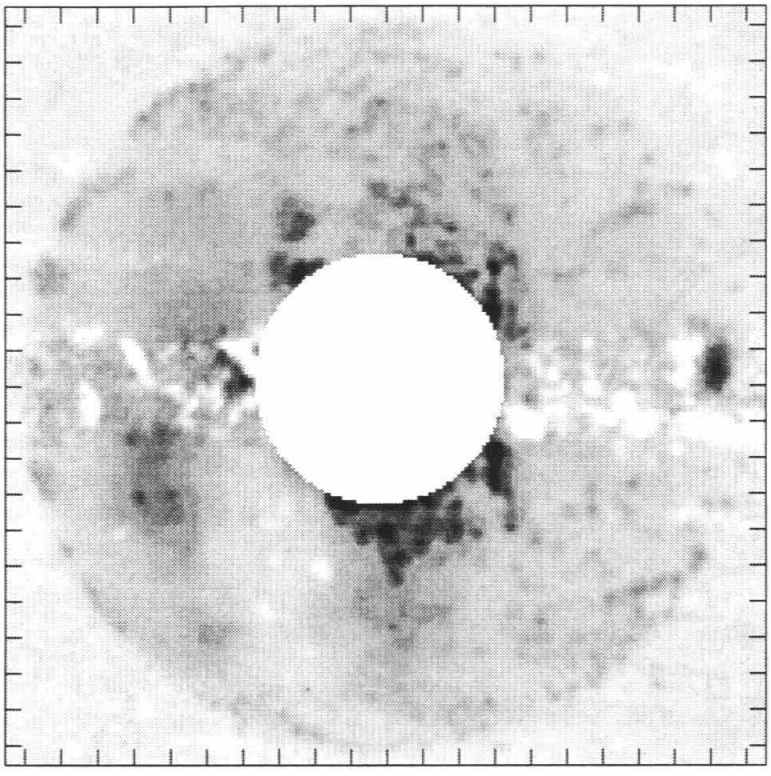

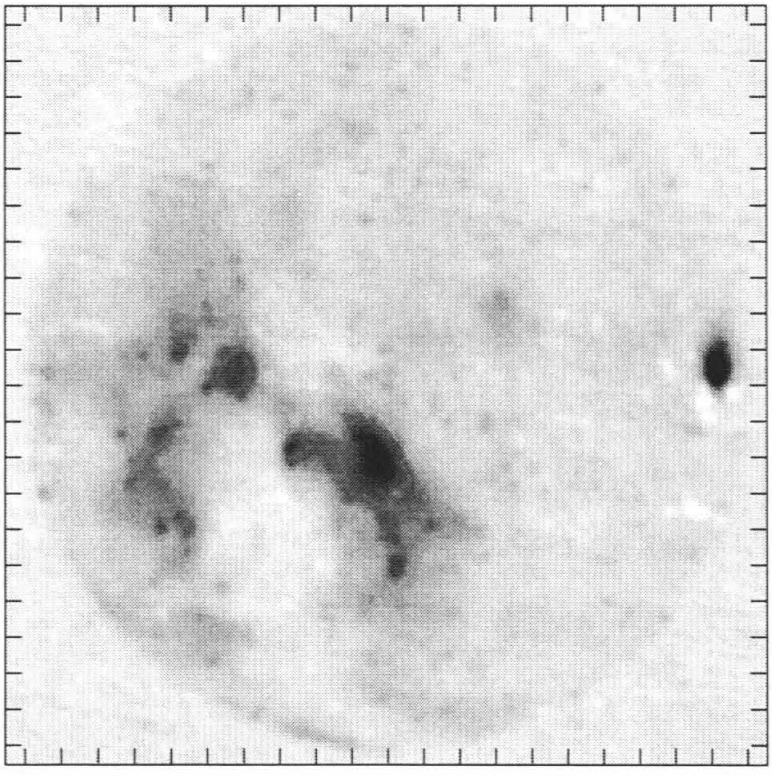

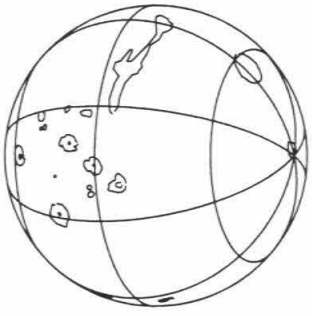

Date: 10/22/88

Snapshot: 21

β_o = 109.3

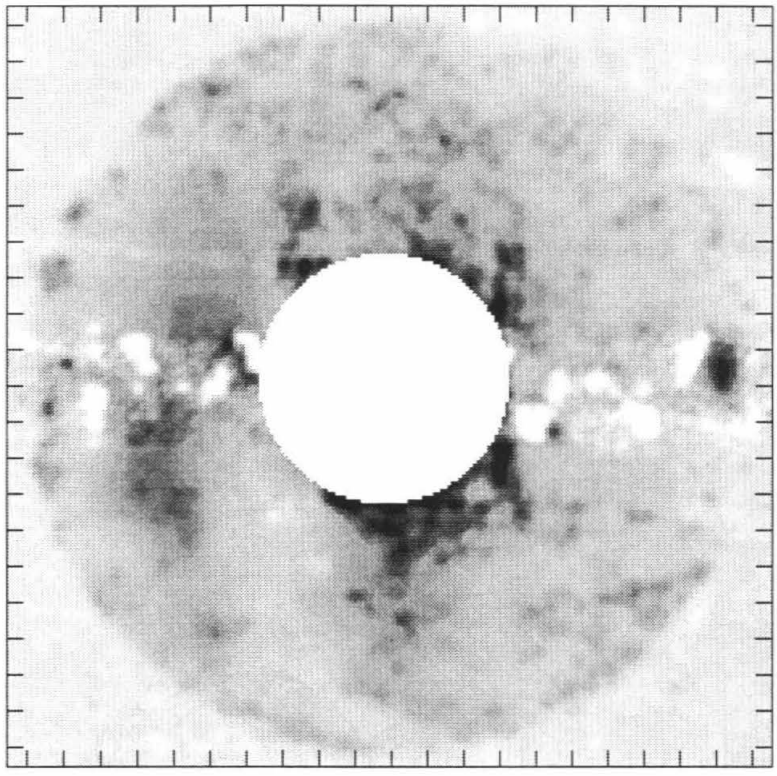

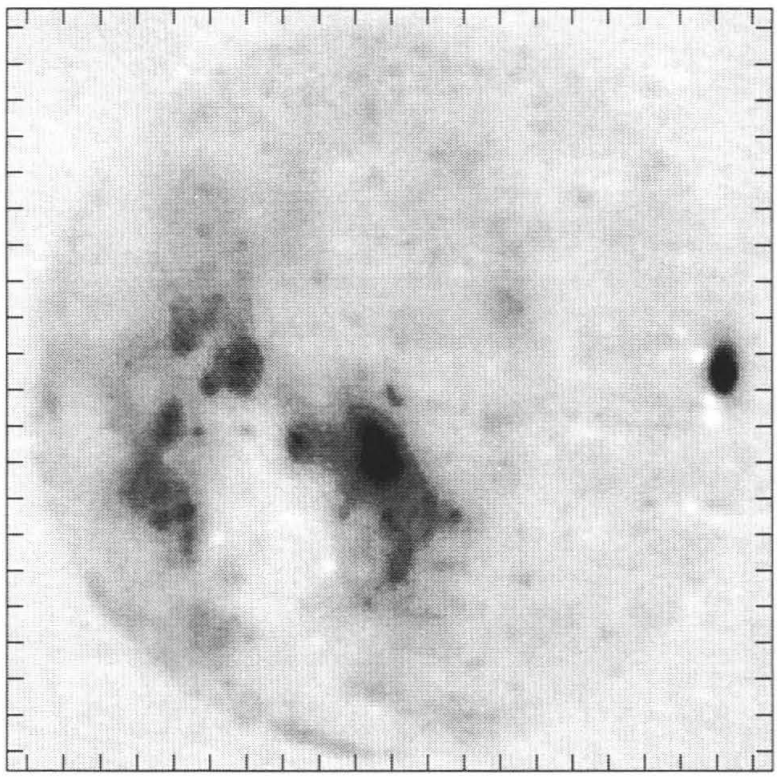

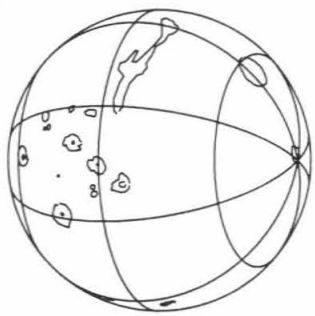

Date: 10/22/88

Snapshot: 22

β_o = 111.1

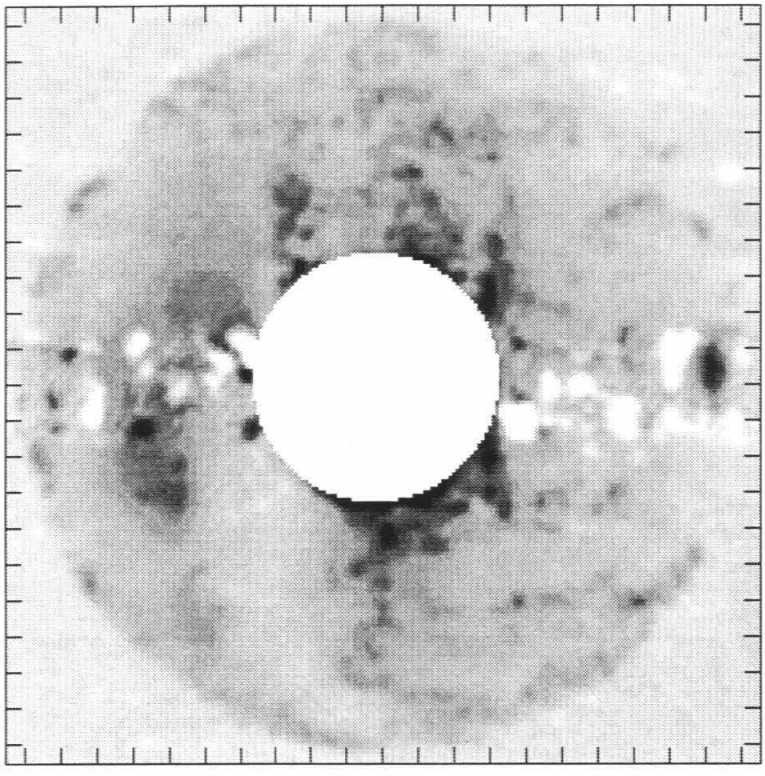

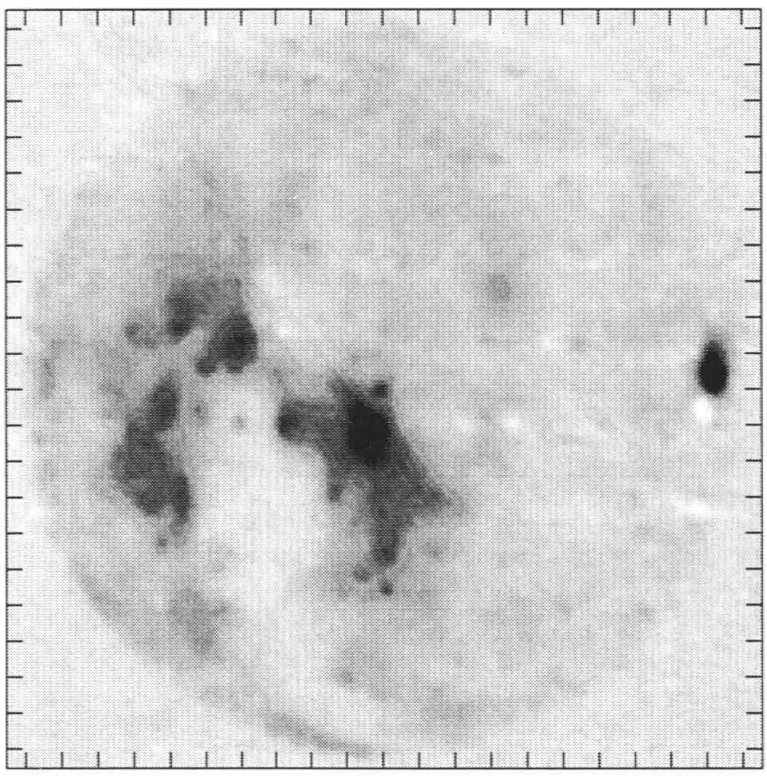

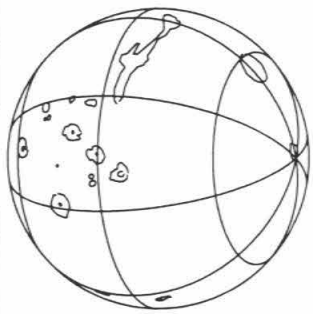

Date: 10/22/88

Snapshot: 23

β_o = 114.5

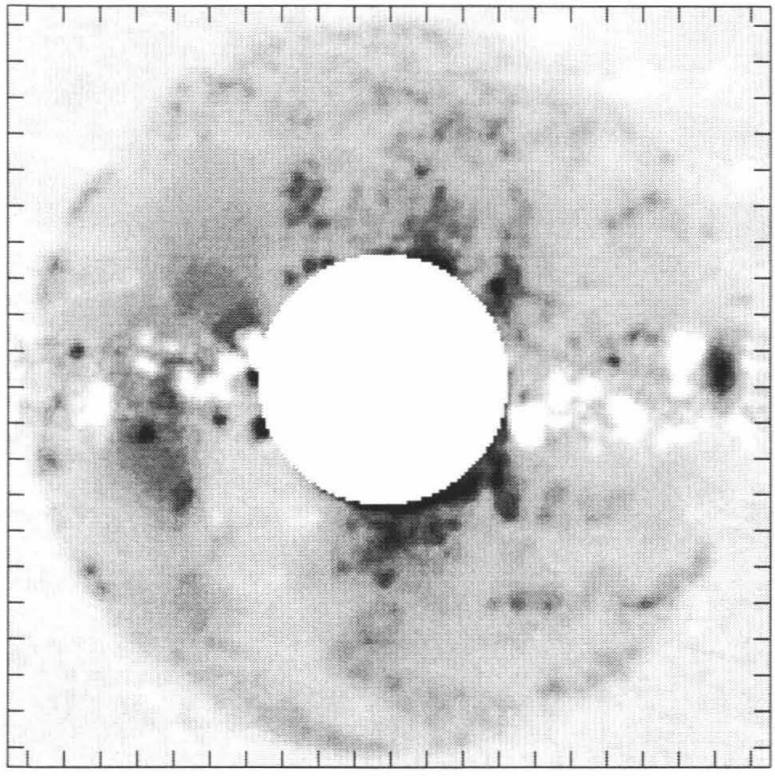

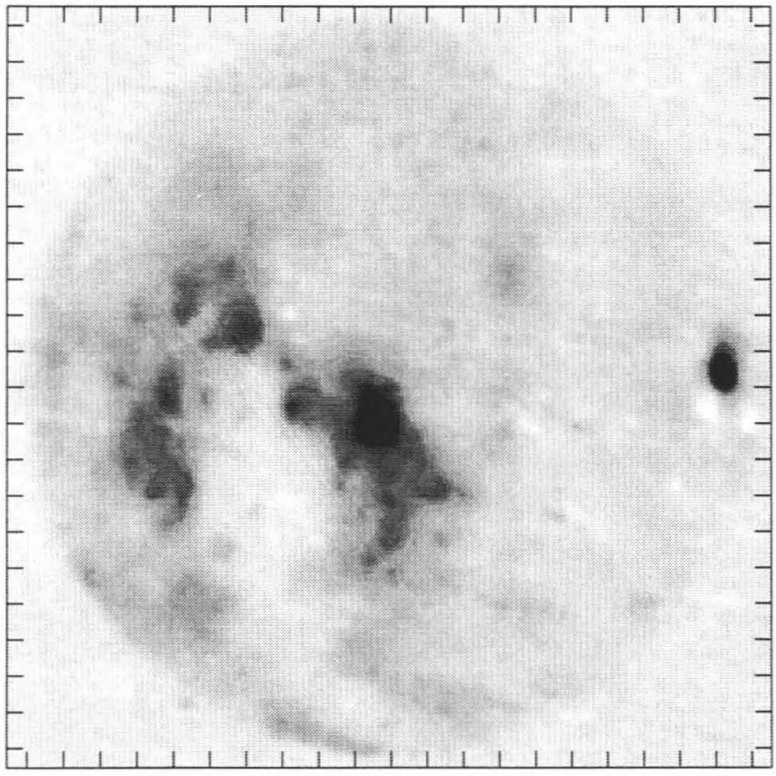

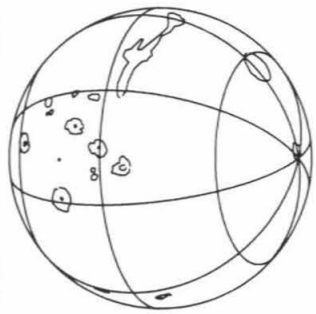

Date: 10/22/88

Snapshot: 24

β_o = 116.8

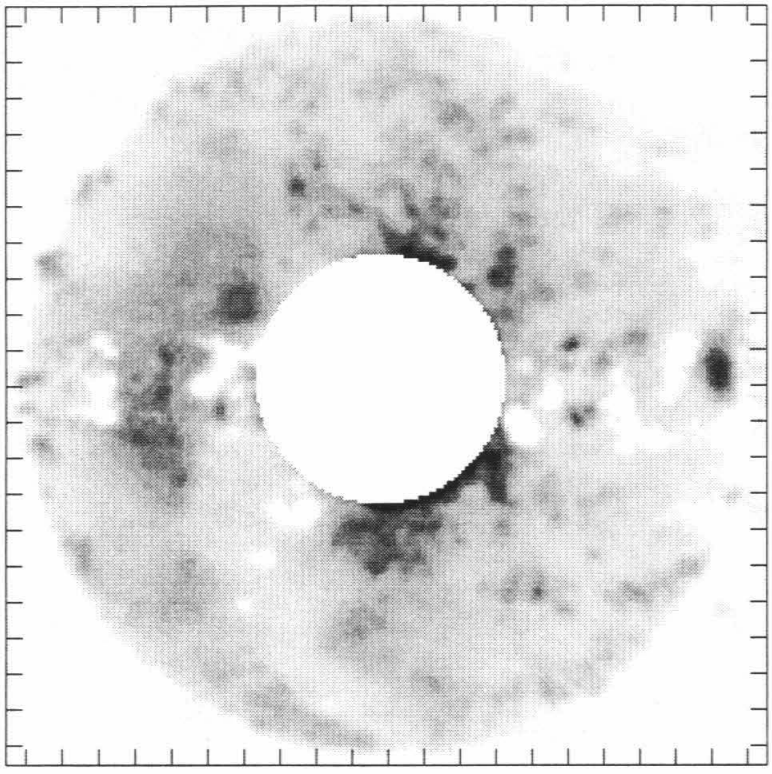

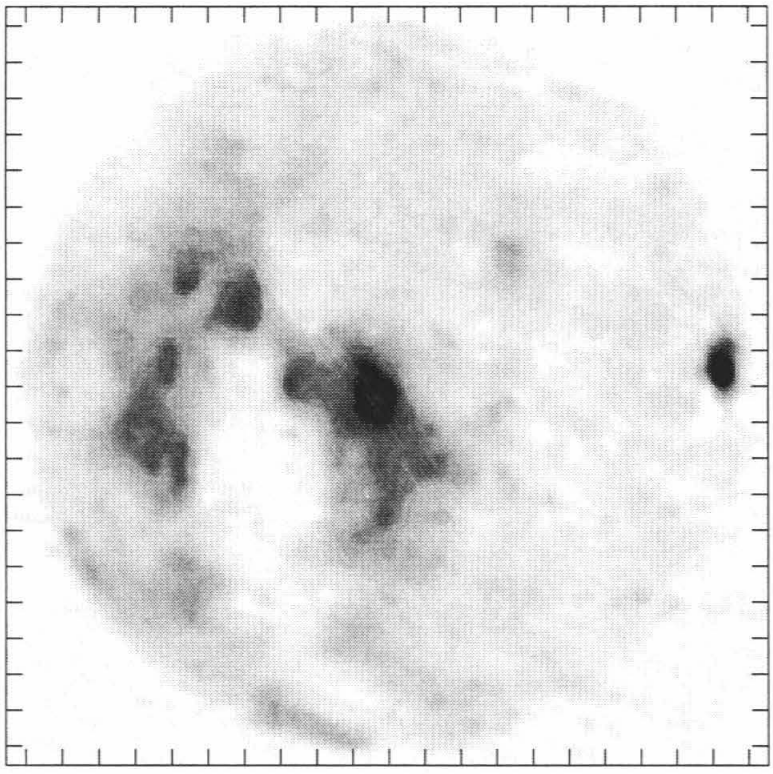

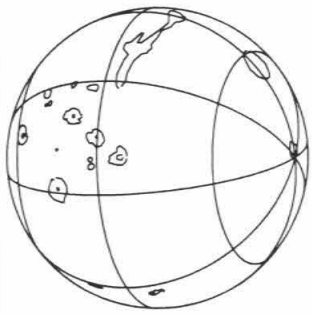

Date: 10/22/88

Snapshot: 25

β_o = 120.6

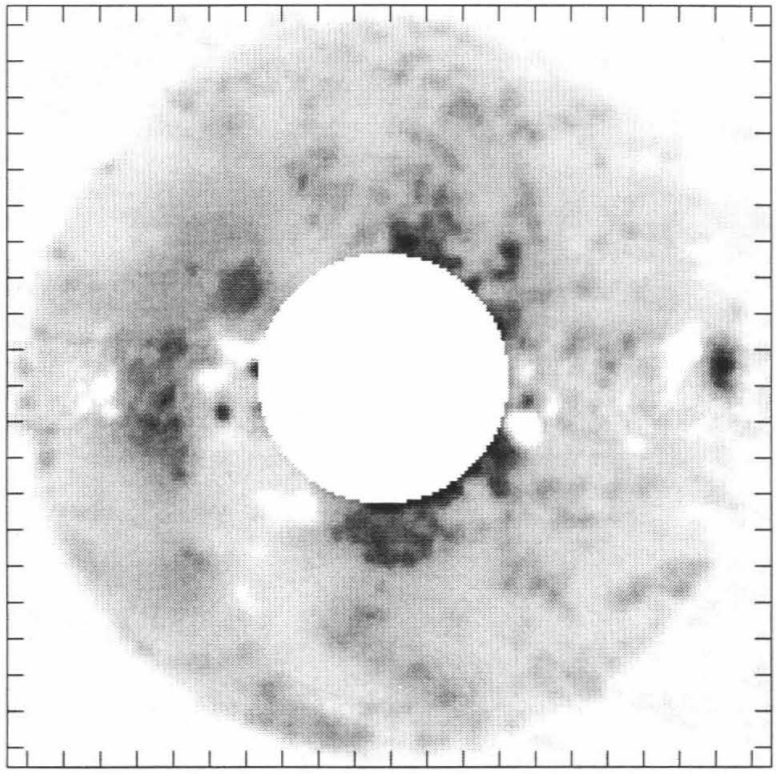

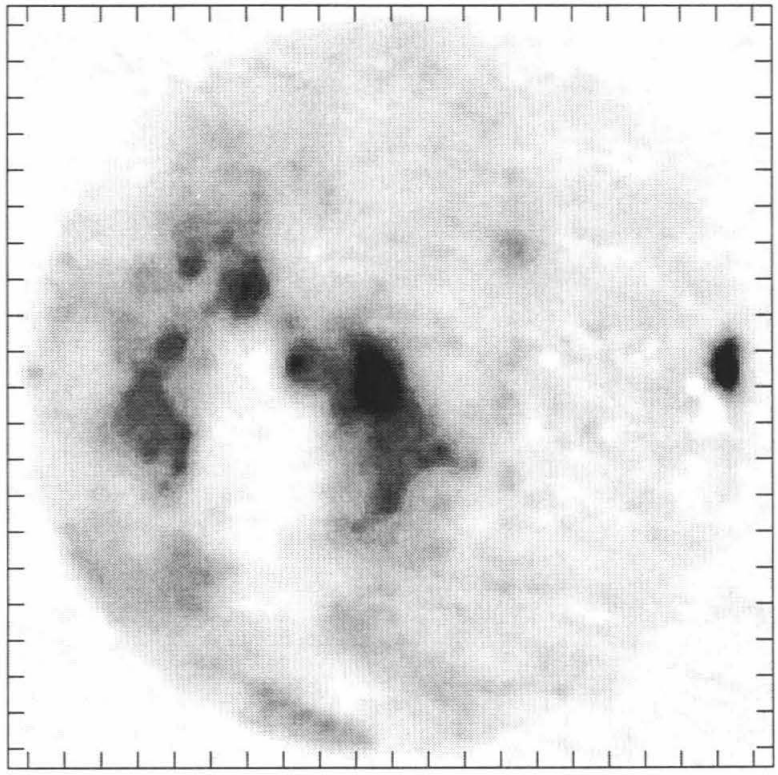

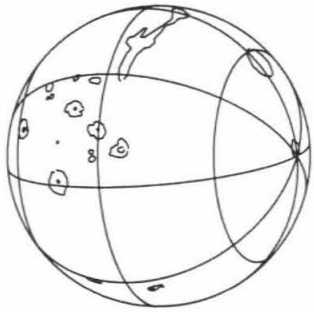

Date: 10/22/88

Snapshot: 26

β_o = 122.9

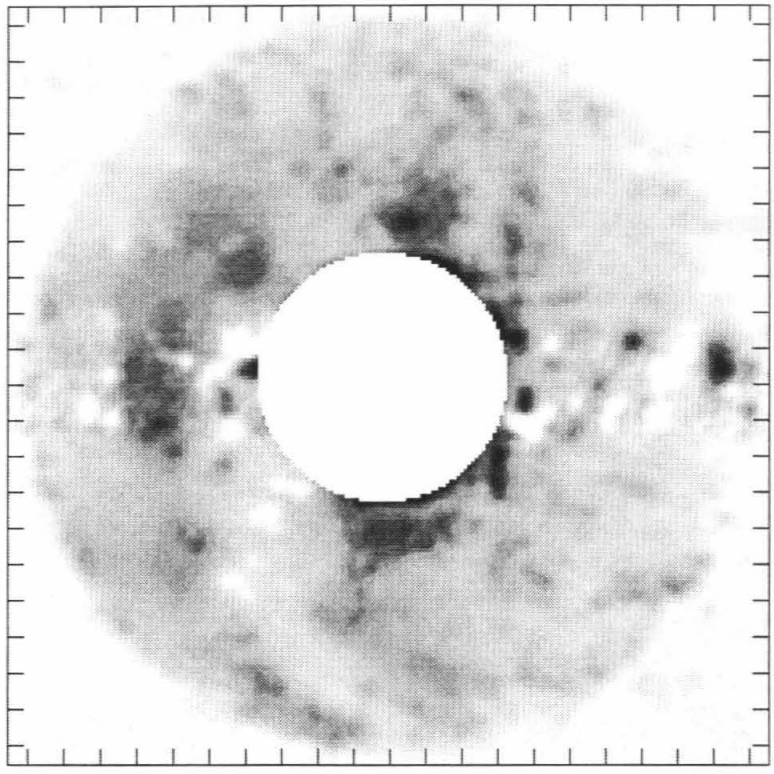

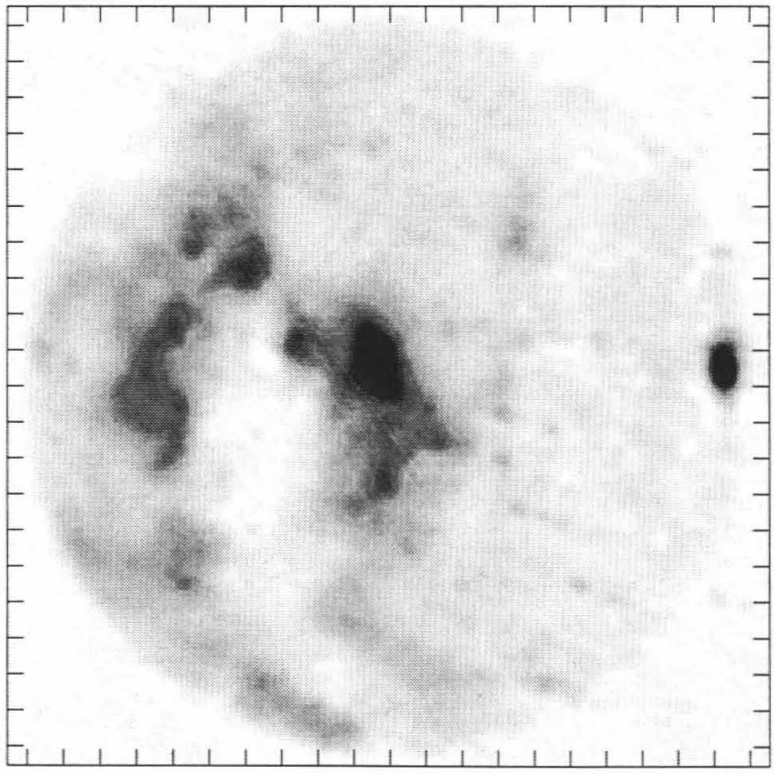

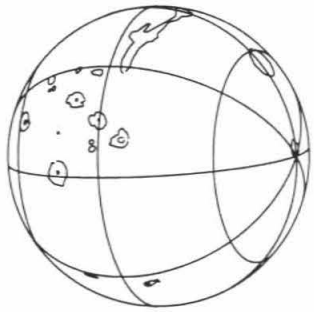

Date: 10/22/88

Snapshot: 27

β_o = 126.7

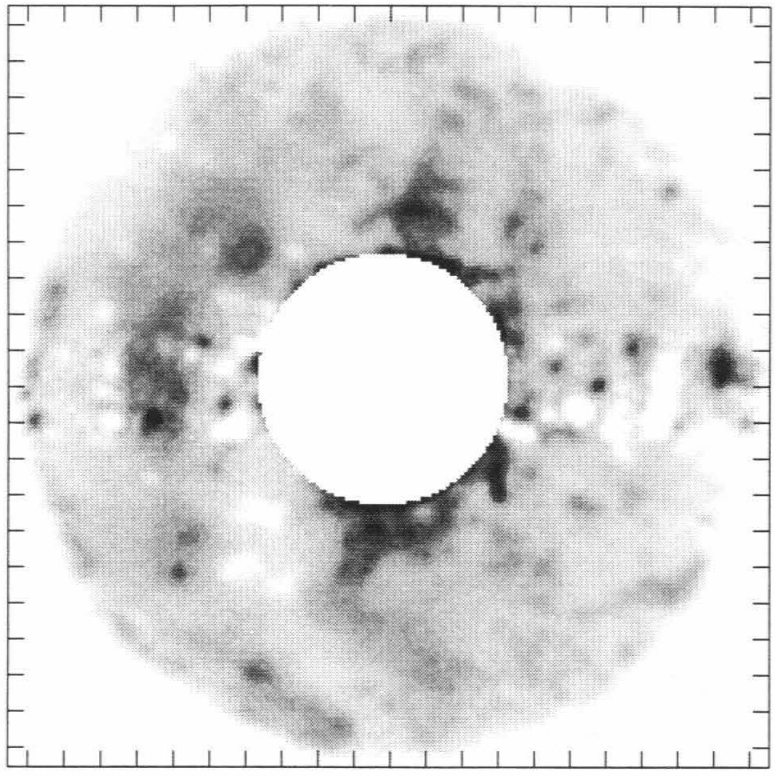

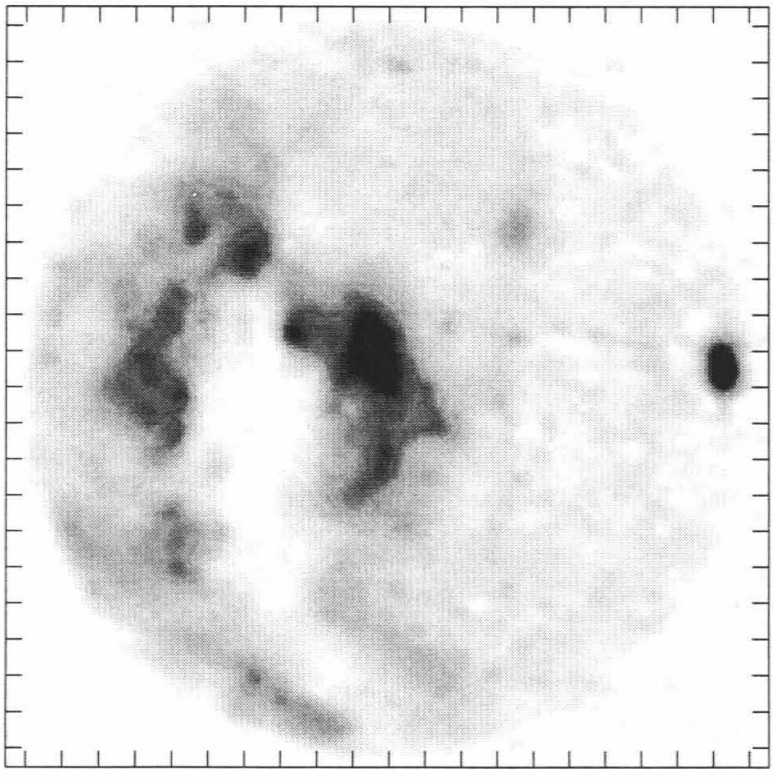

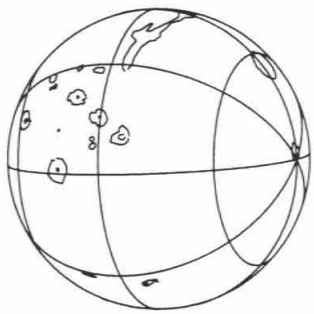

Date: 10/22/88

Snapshot: 28

β_o = 129.0

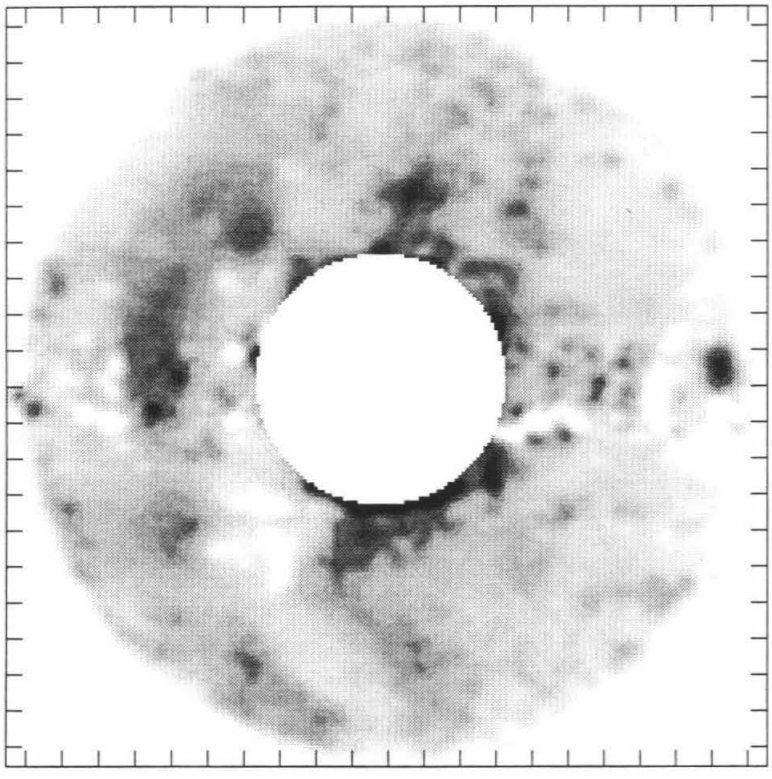

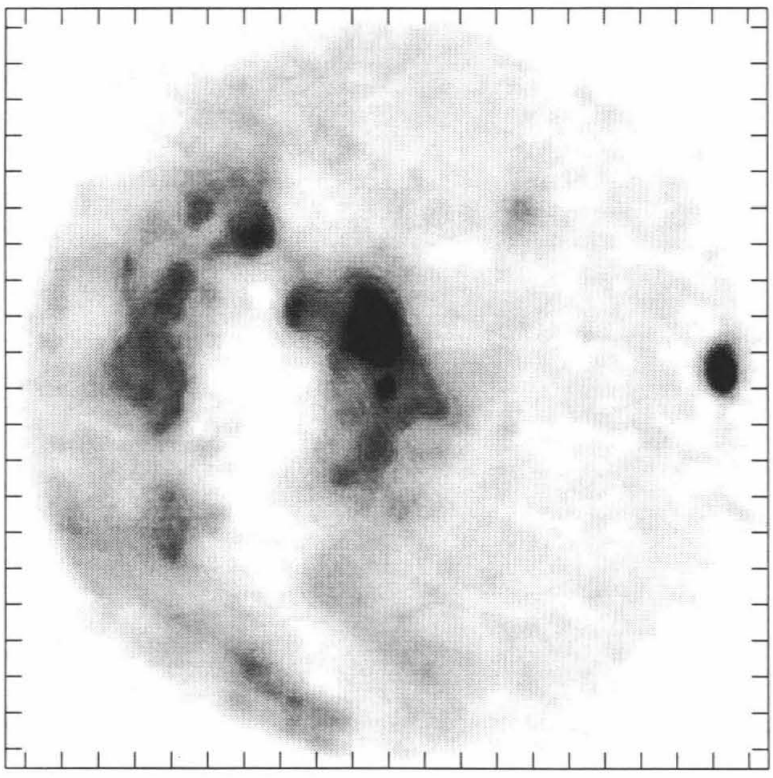

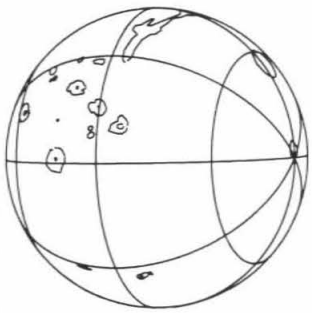

Date: 10/22/88

Snapshot: 29

β_o = 132.8

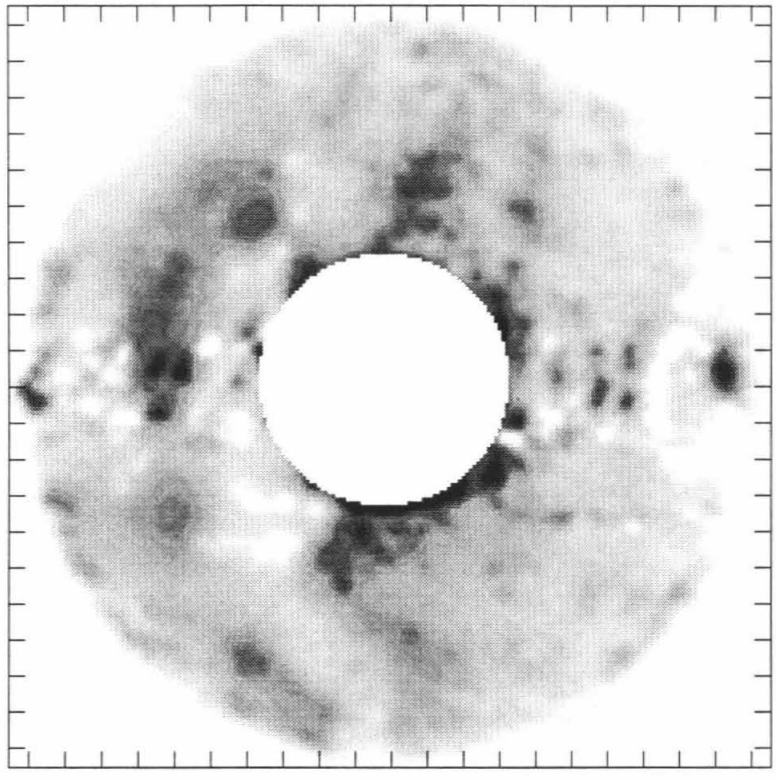

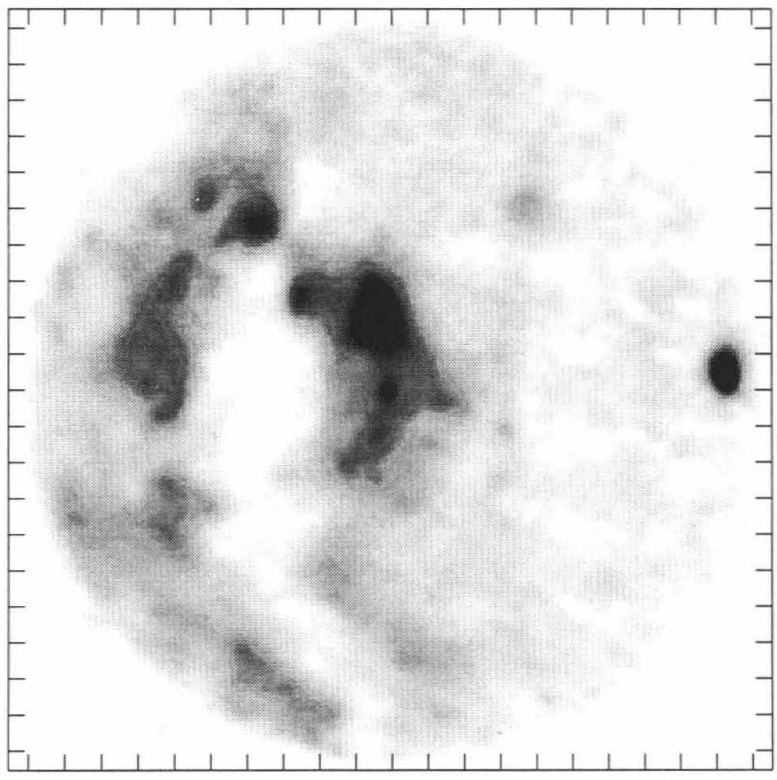

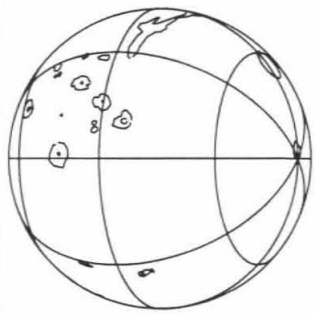

Date: 10/22/88

Snapshot: 30

β_o = 135.1

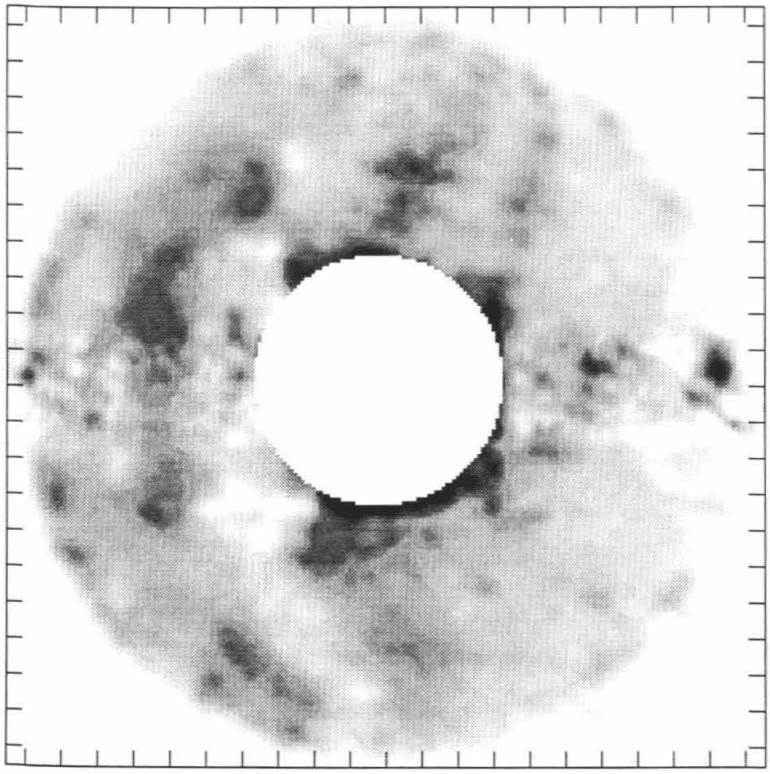

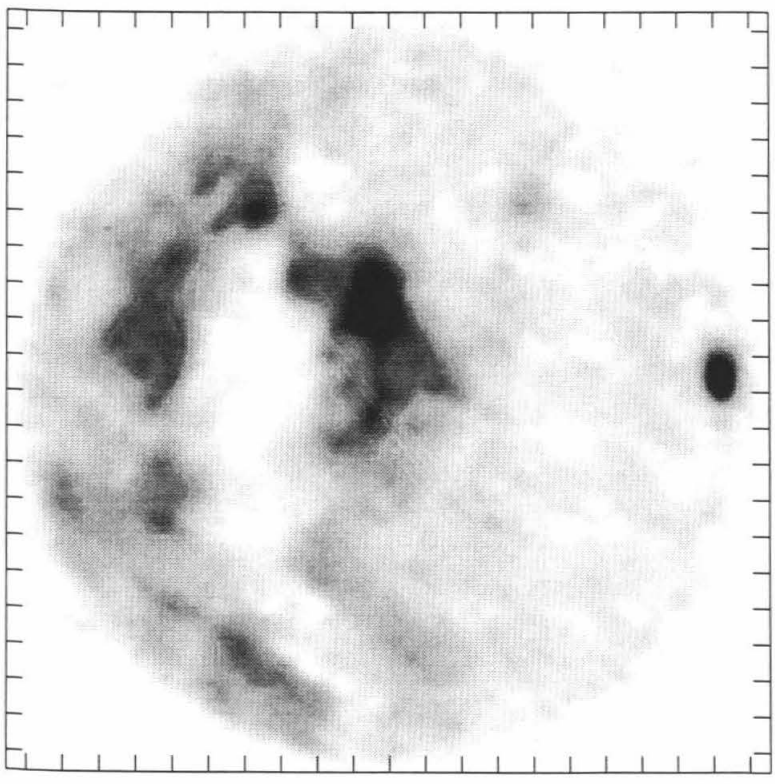

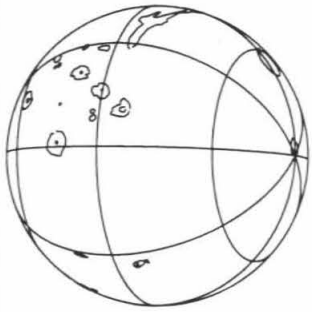

Date: 10/22/88

Snapshot: 31

β_o = 138.9

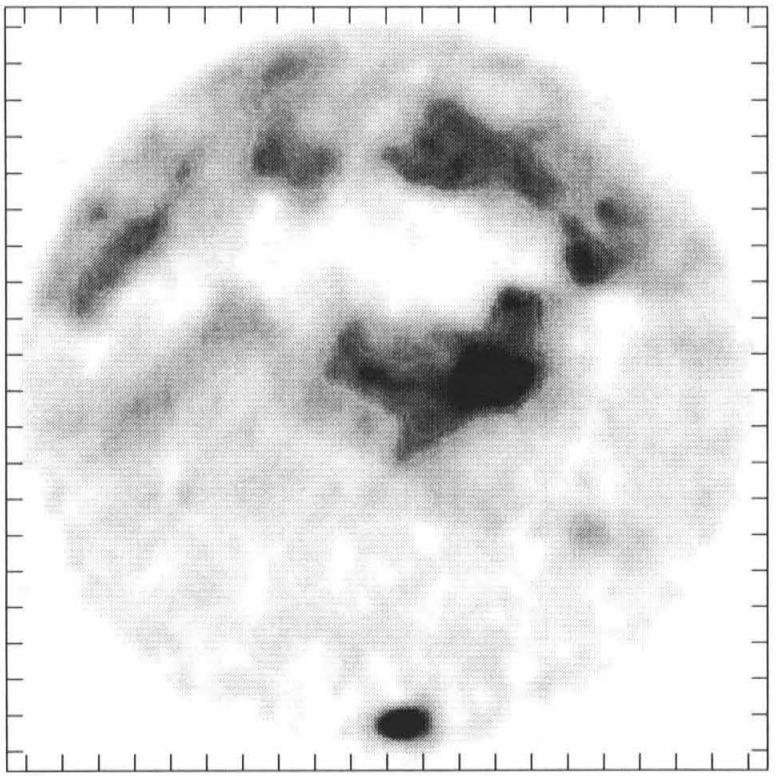

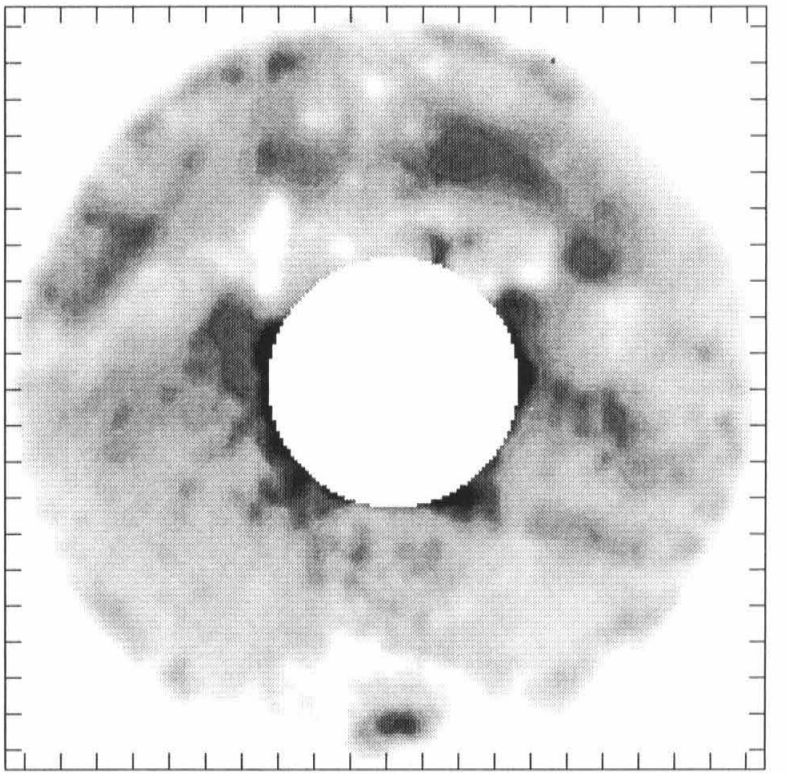

Date: 10/22/88

Snapshot: 32

β_o = 141.2

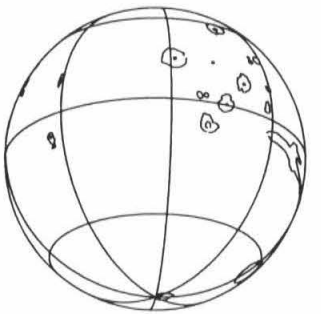

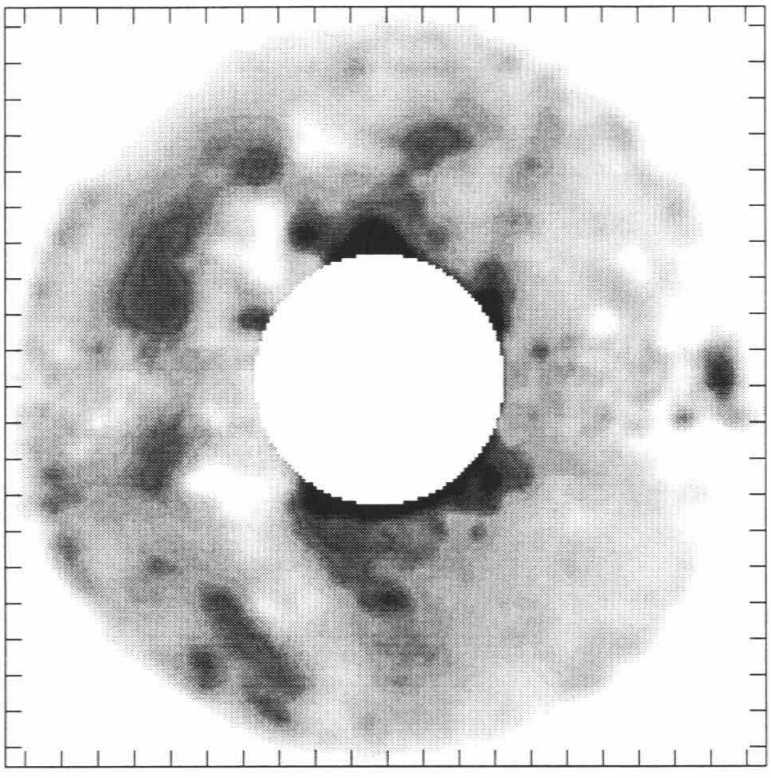

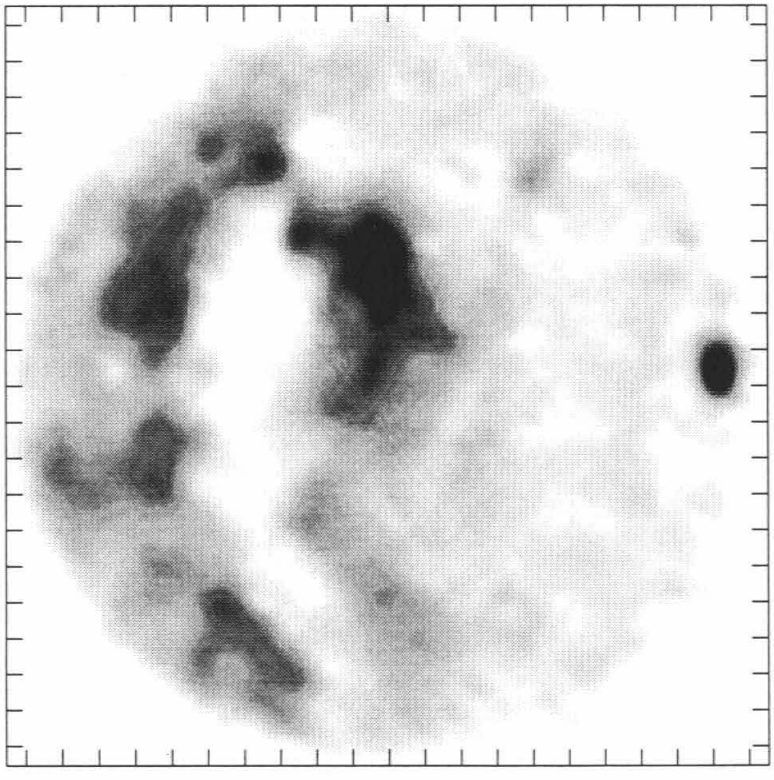

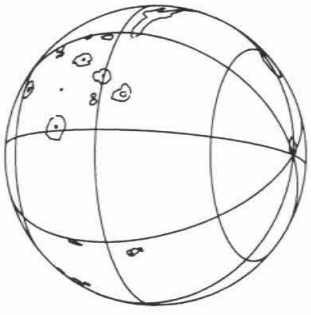

Date: 10/22/88

Snapshot: 33

β_o = 145.0

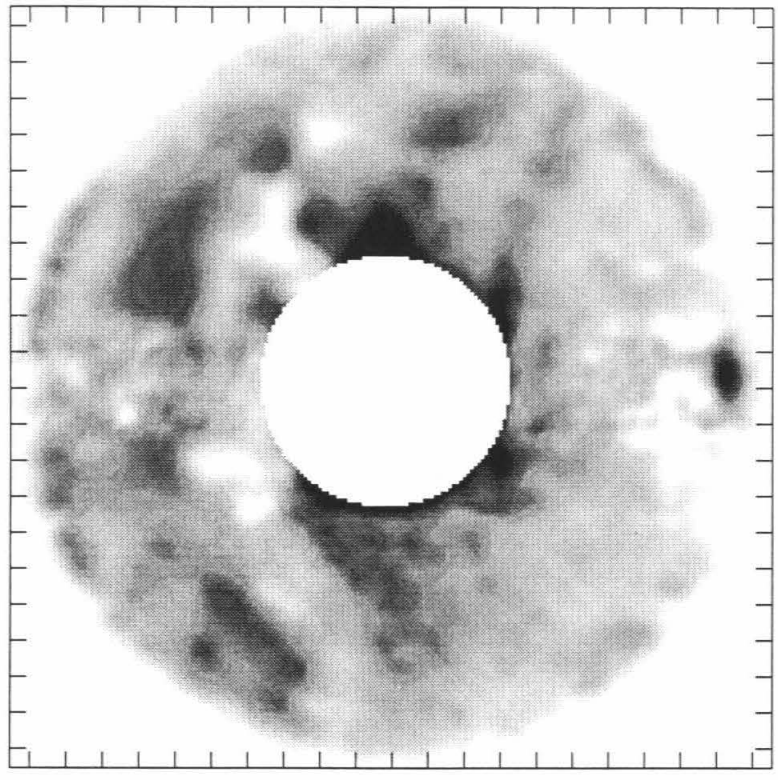

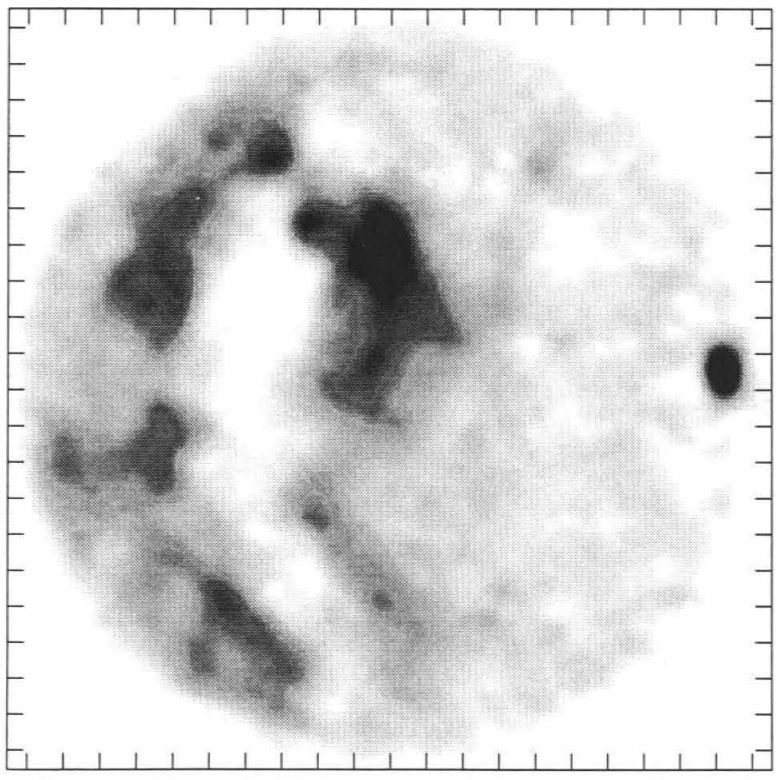

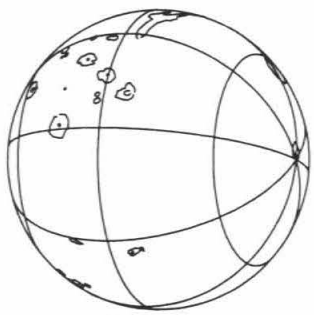

Date: 10/22/88

Snapshot: 34

β_o = 147.2

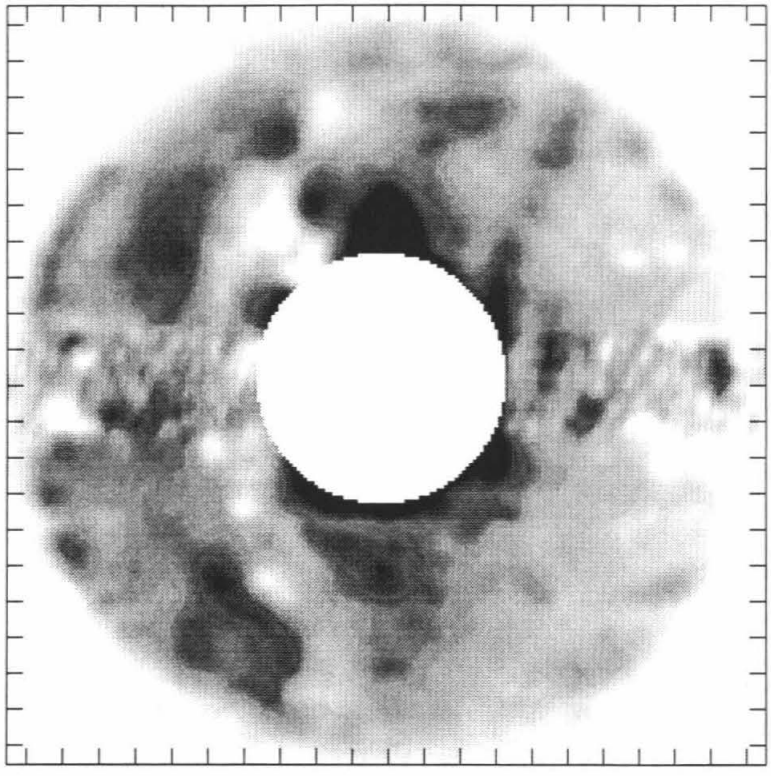

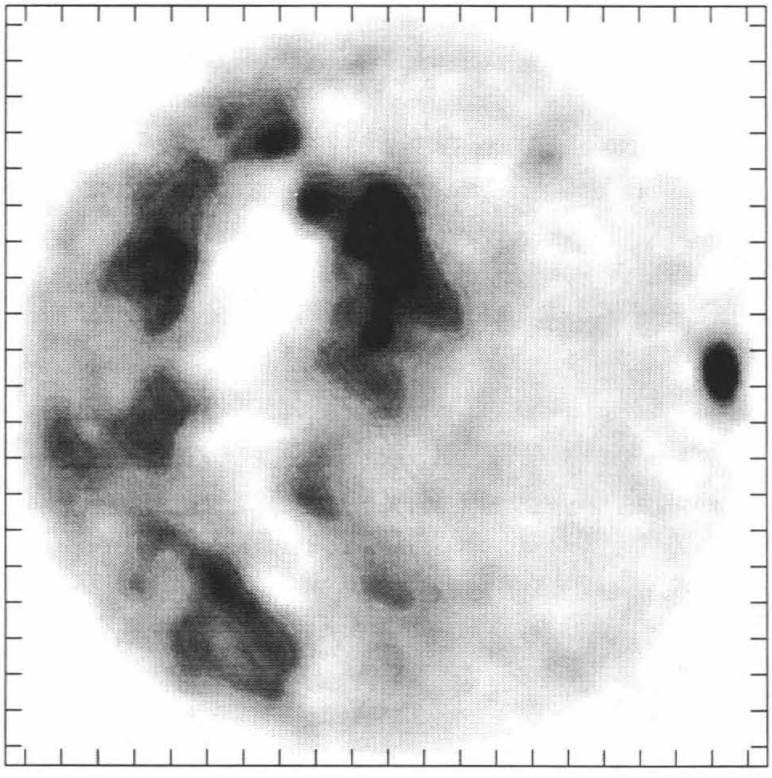

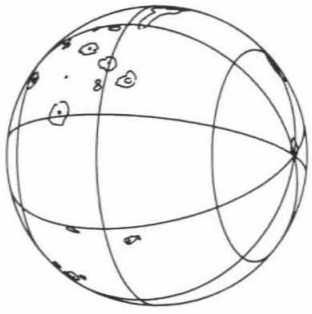

Date: 10/22/88

Snapshot: 35

β_o = 151.1

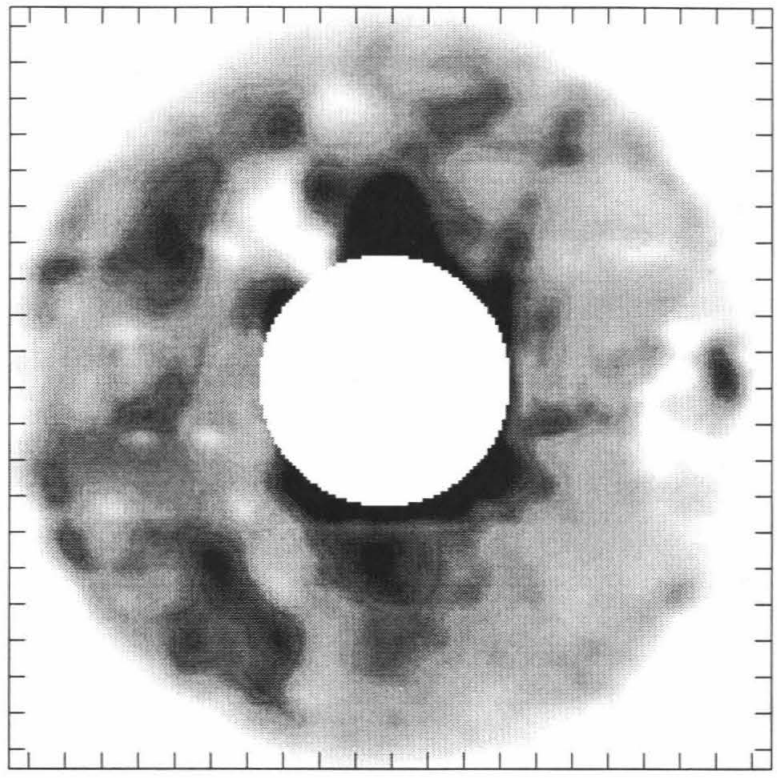

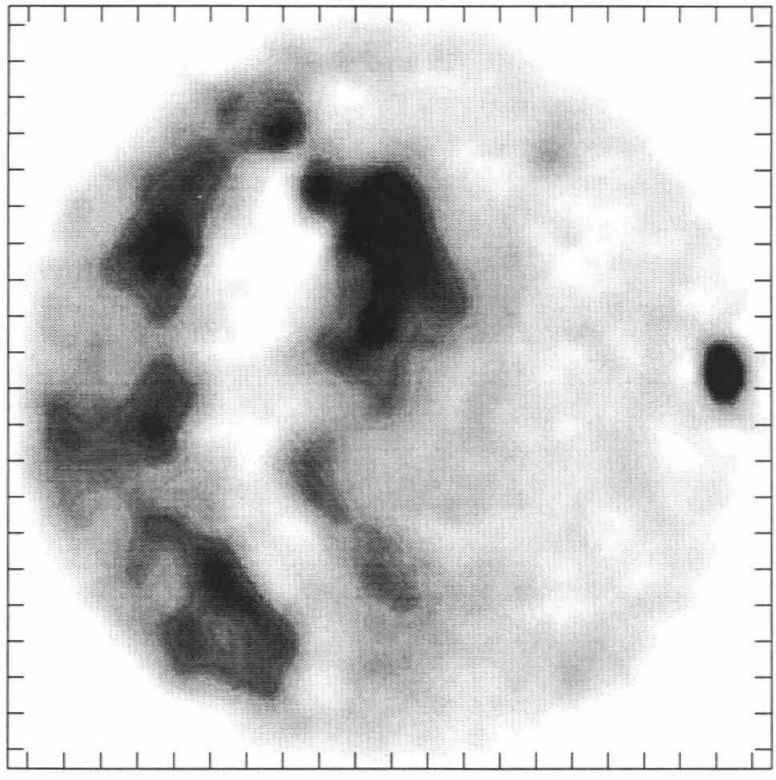

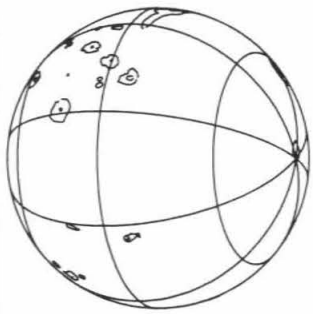

Date: 10/22/88

Snapshot: 36

β_o = 153.3

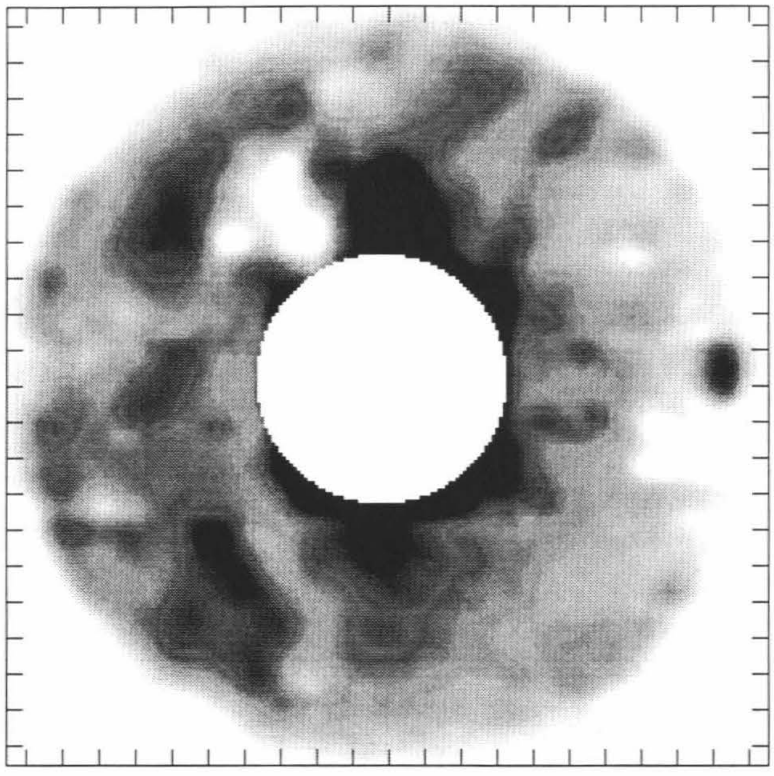

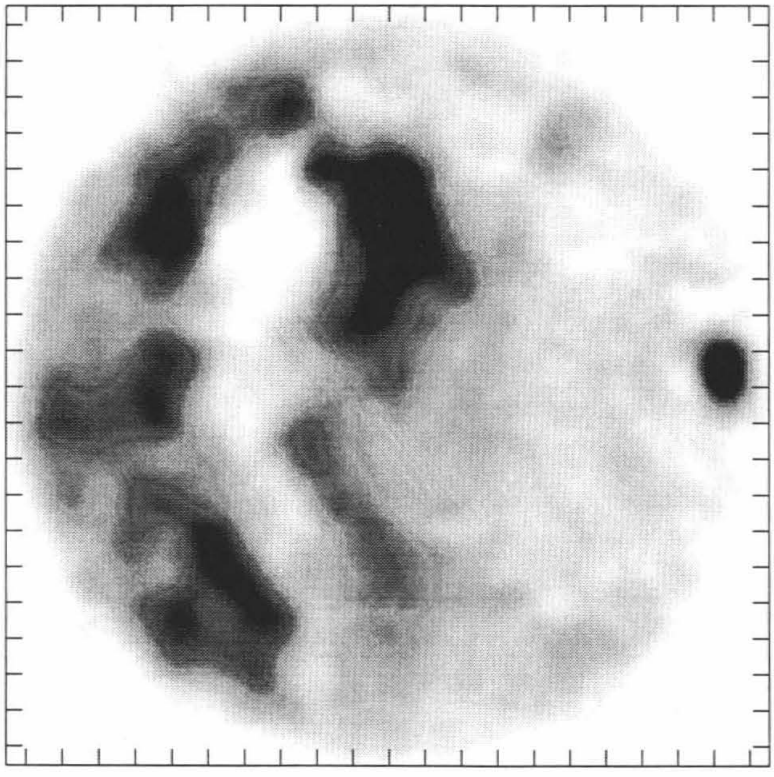

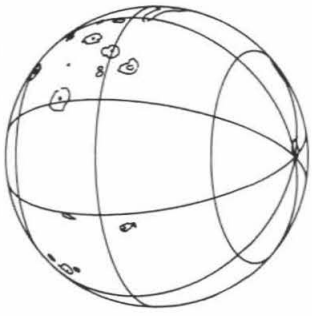

Date: 10/22/88

Snapshot: 37

β_o = 157.2

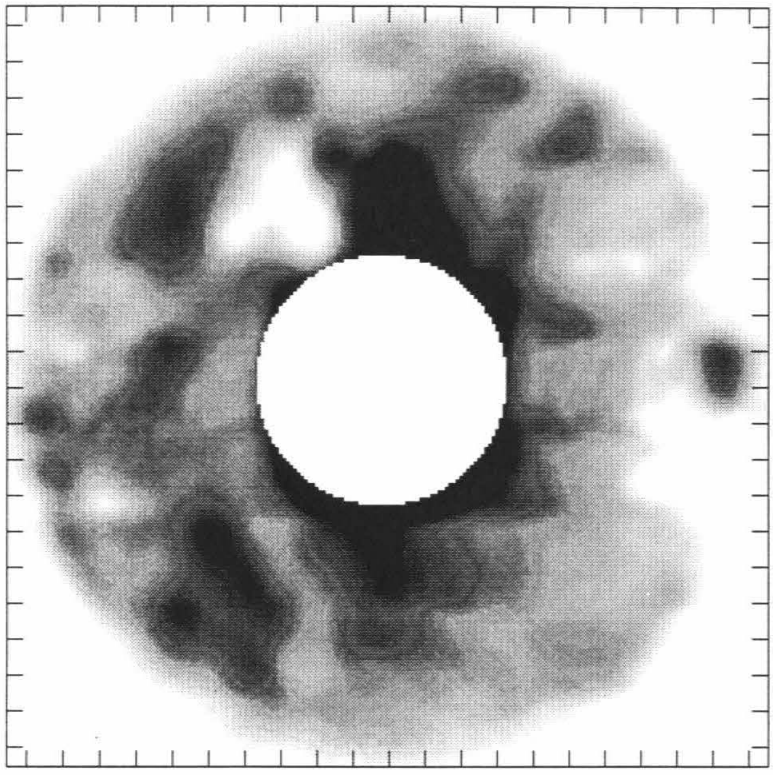

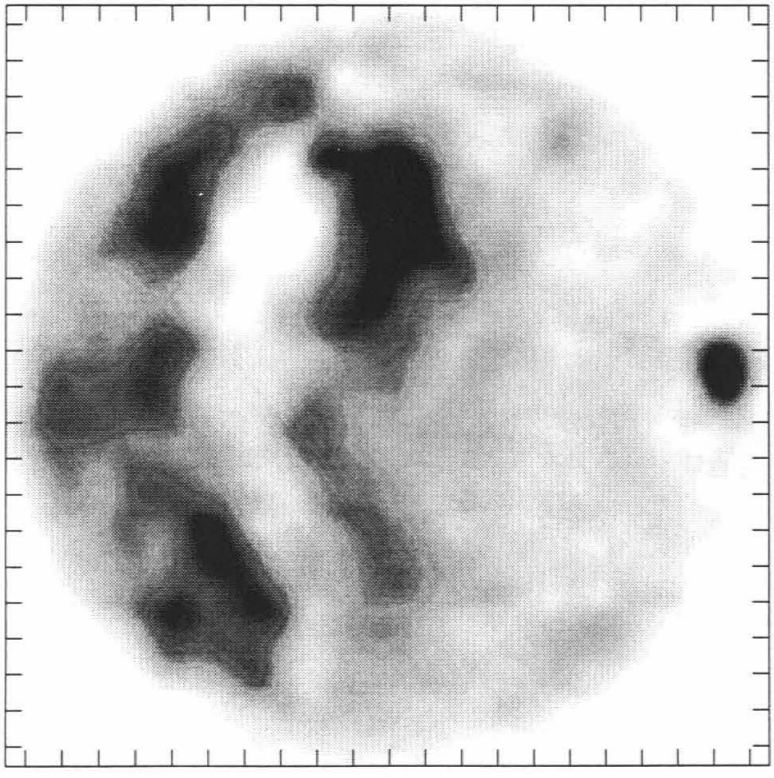

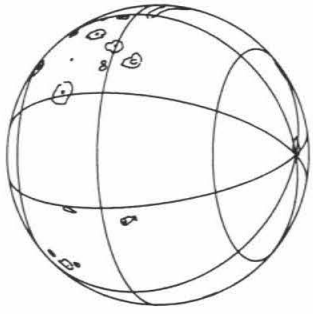

Date: 10/22/88

Snapshot: 38

β_o = 159.4

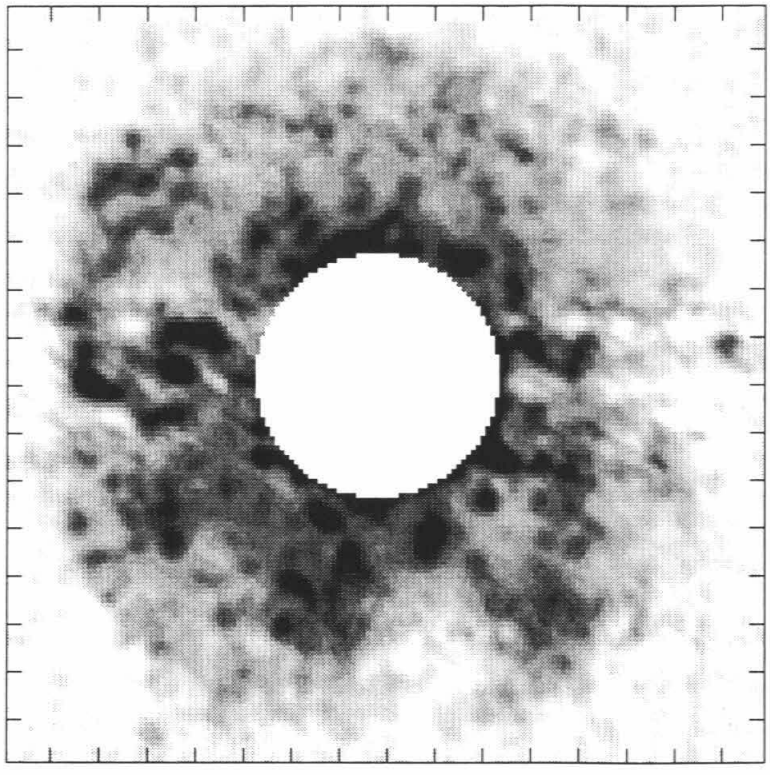

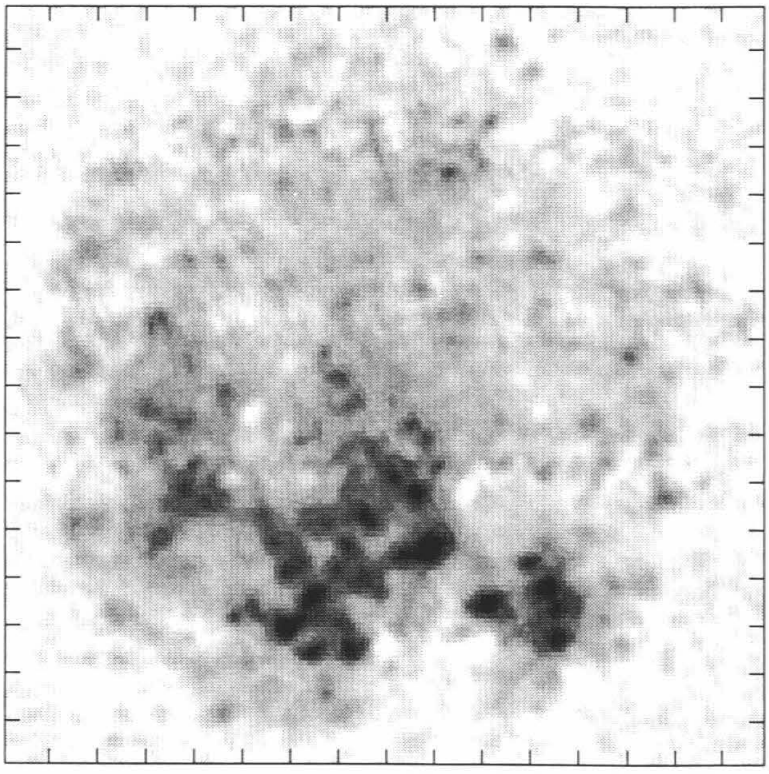

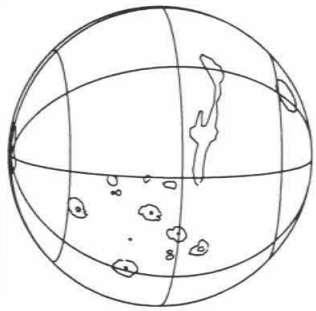

Date: 12/29/92

Snapshot: 1

β_o = 81.6

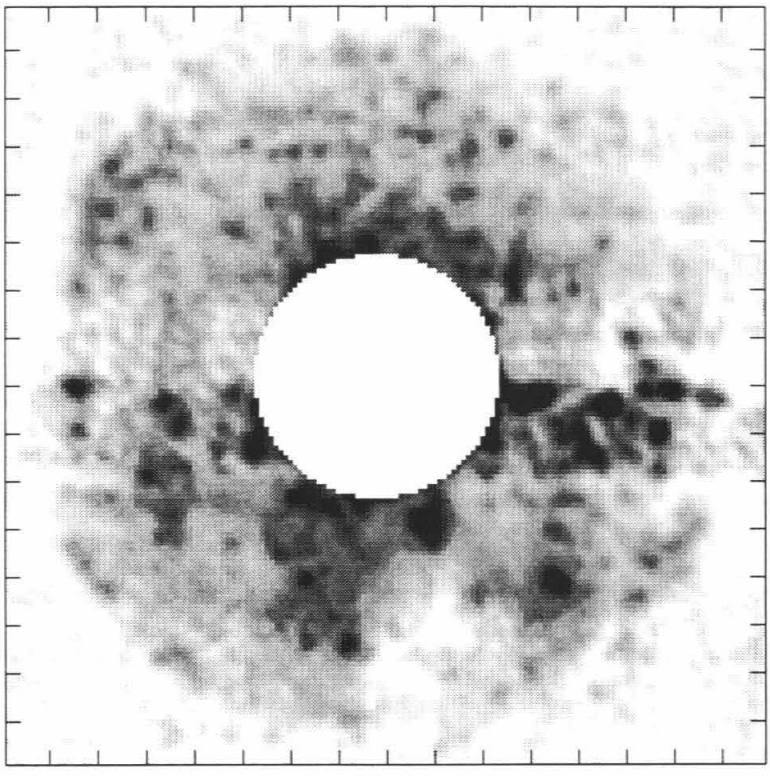

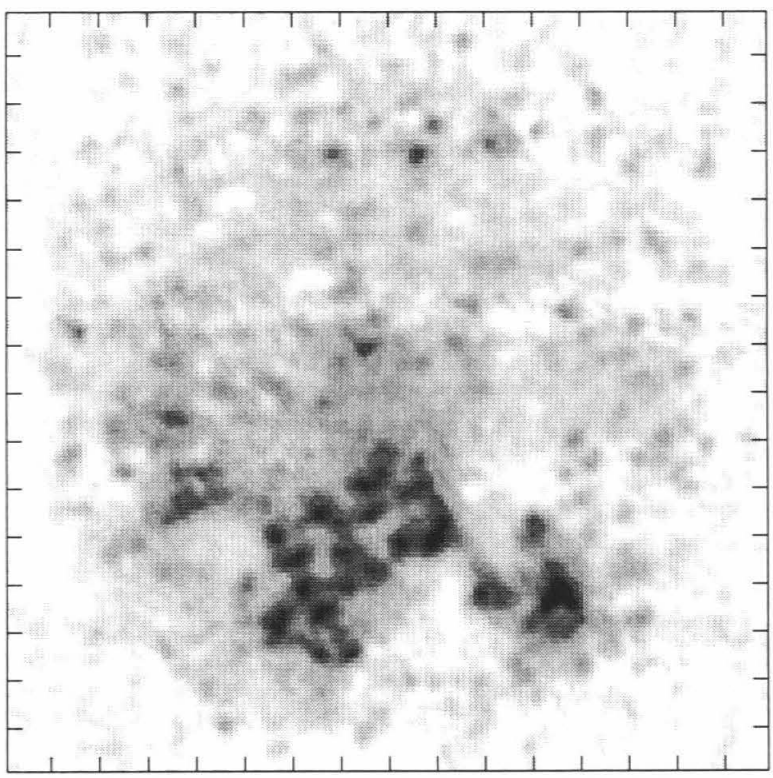

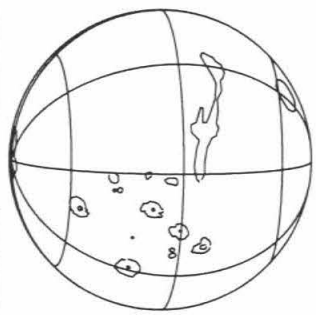

Date: 12/29/92

Snapshot: 2

β_o = 84.4

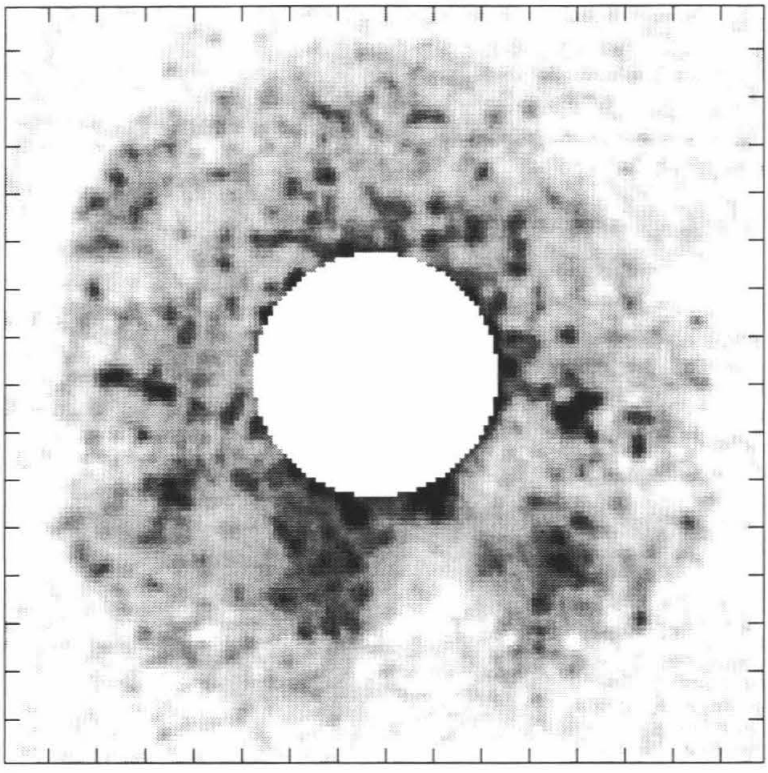

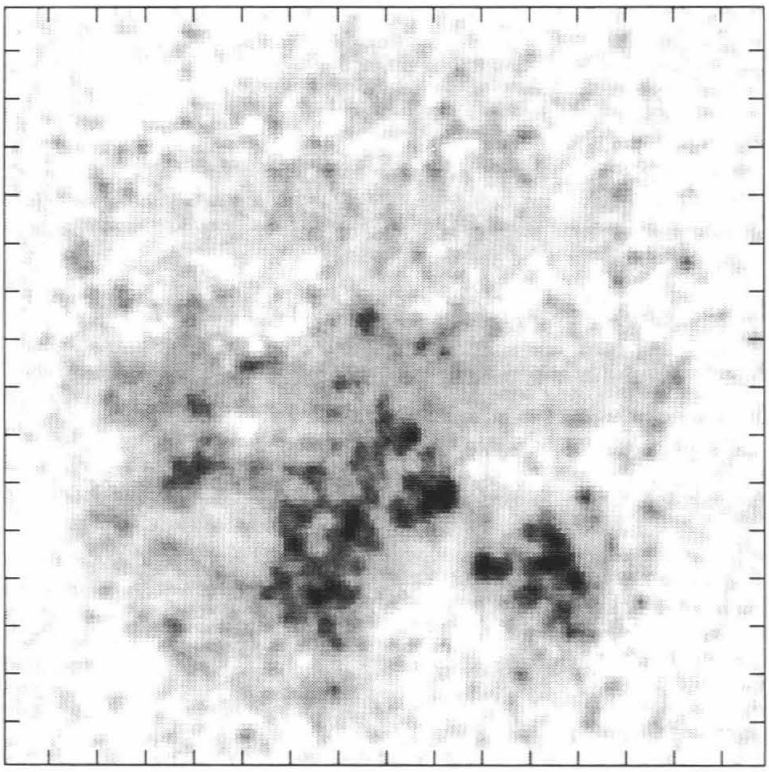

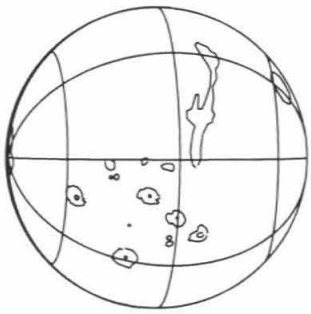

Date: 12/29/92

Snapshot: 3

β_o = 89.1

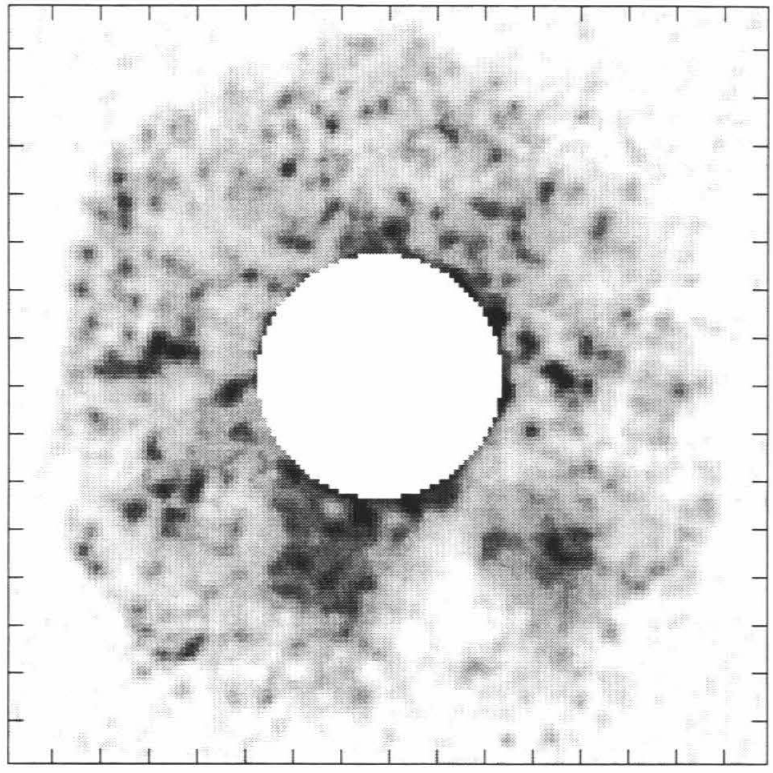

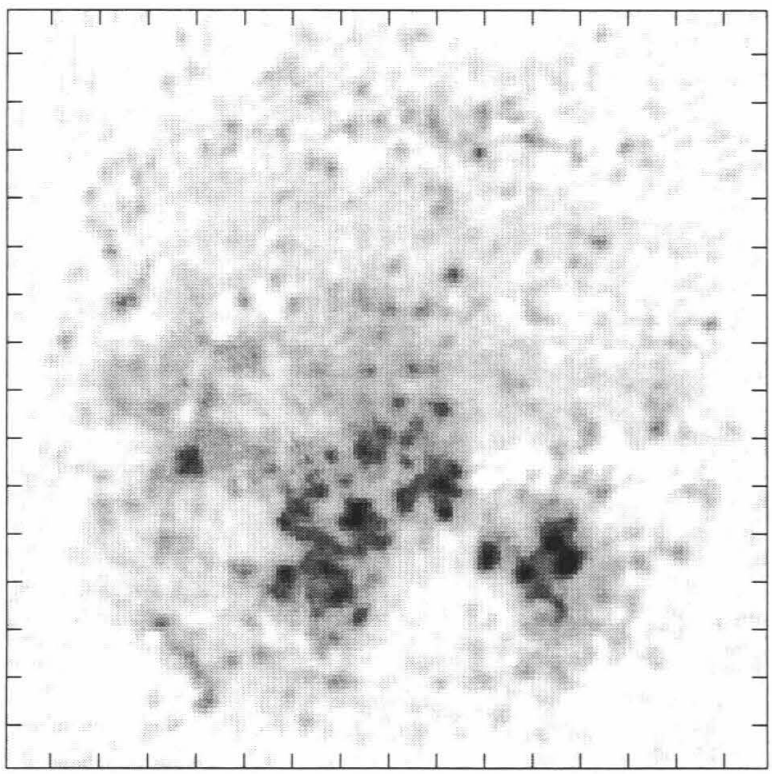

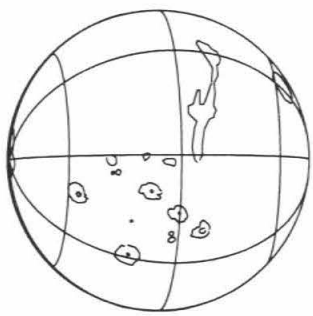

Date: 12/29/92

Snapshot: 4

β_o = 92.0

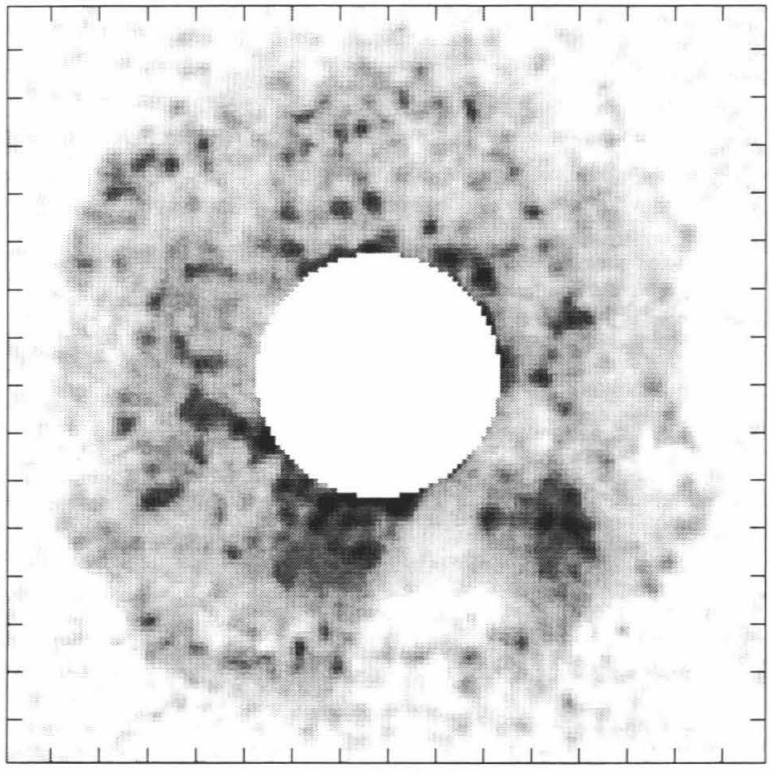

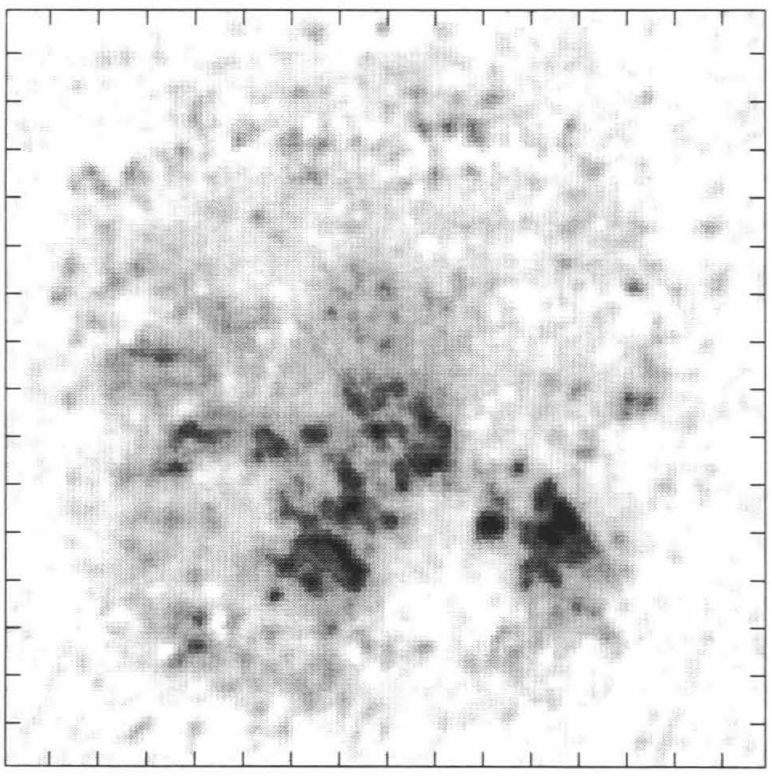

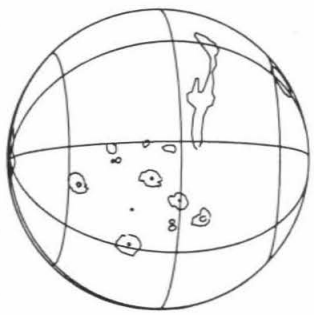

Date: 12/29/92

Snapshot: 5

β_o = 96.7

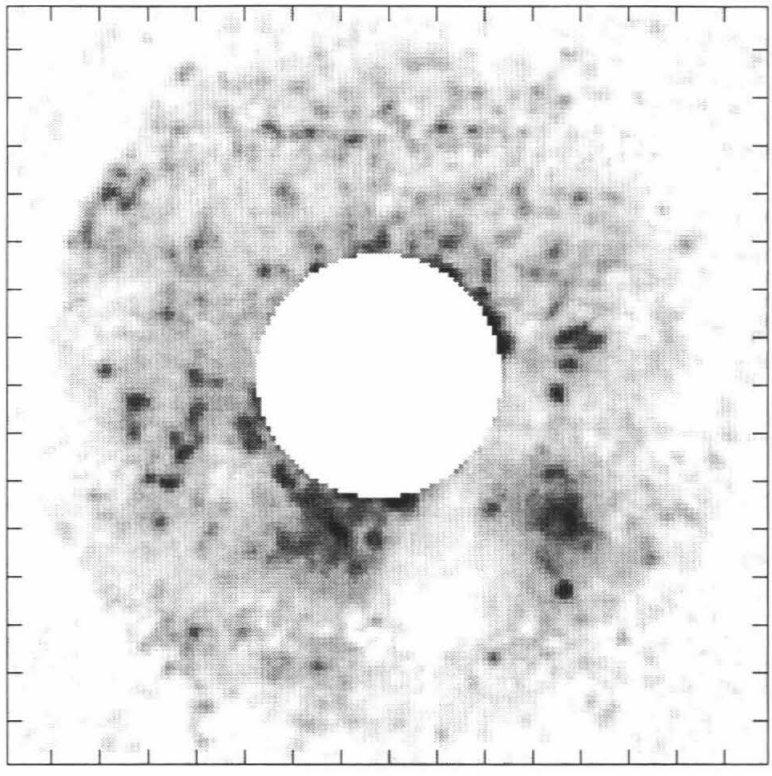

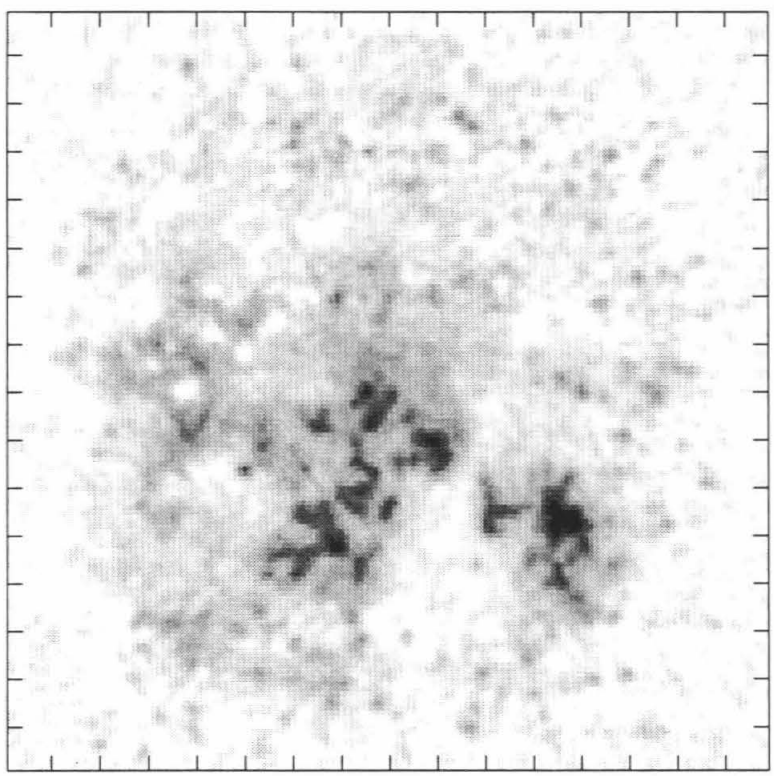

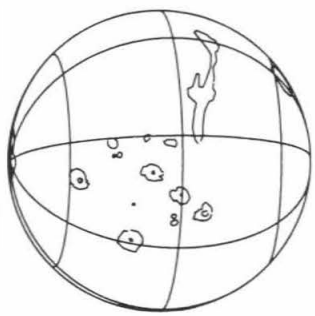

Date: 12/29/92

Snapshot: 6

β_o = 99.6

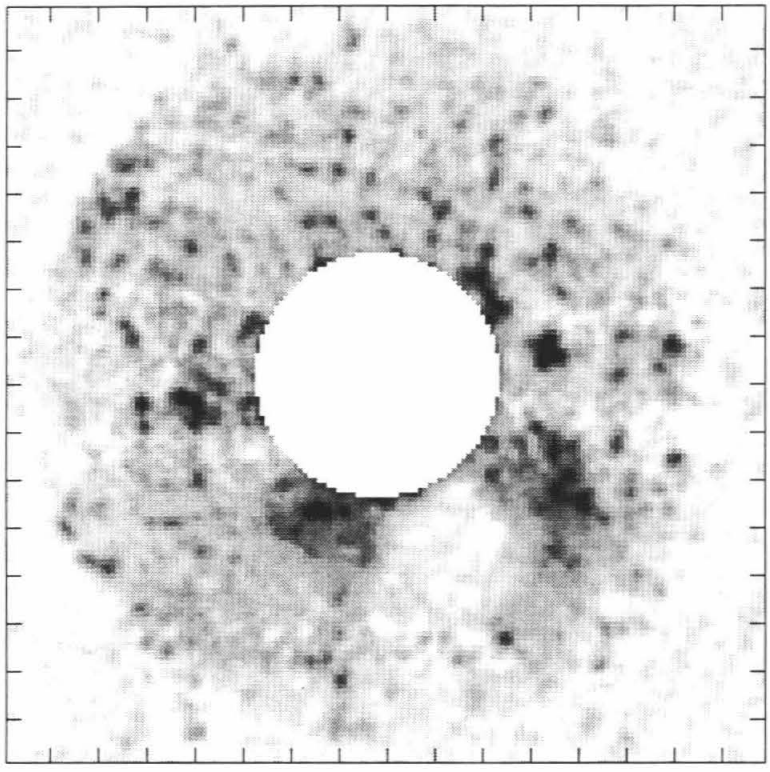

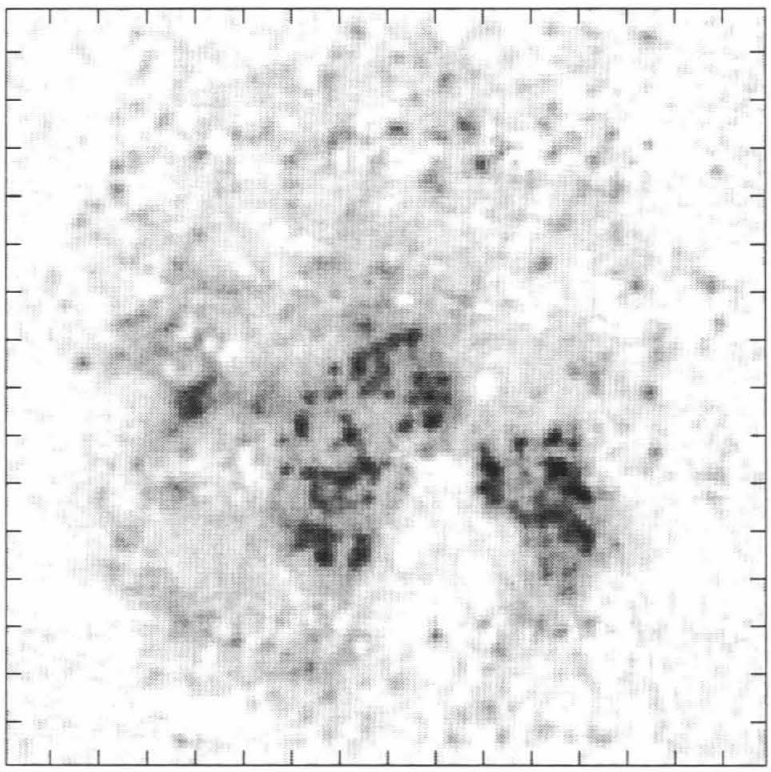

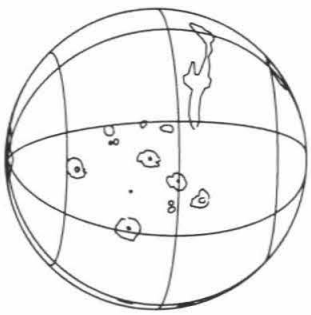

Date: 12/29/92

Snapshot: 7

β_o = 104.4

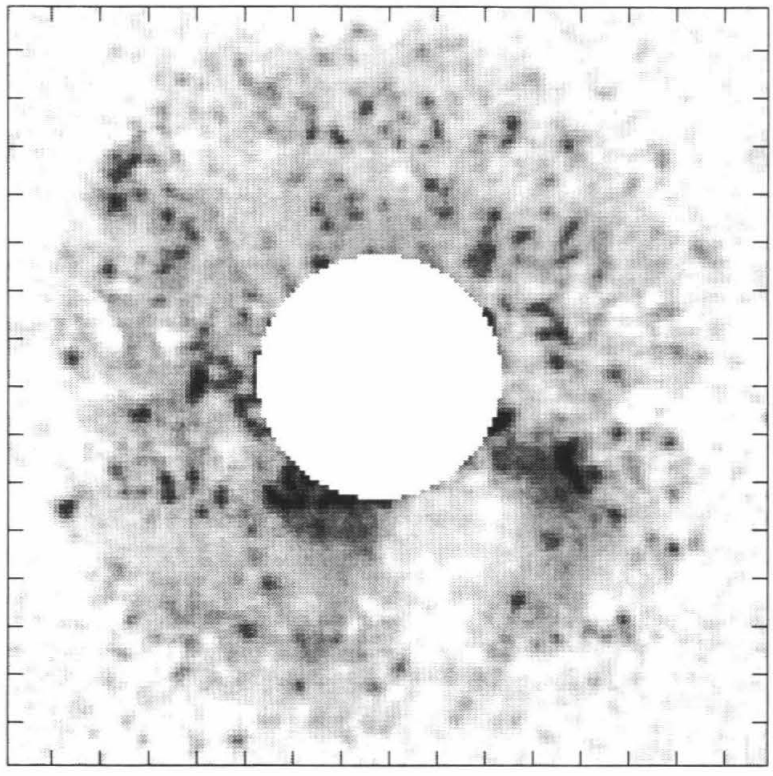

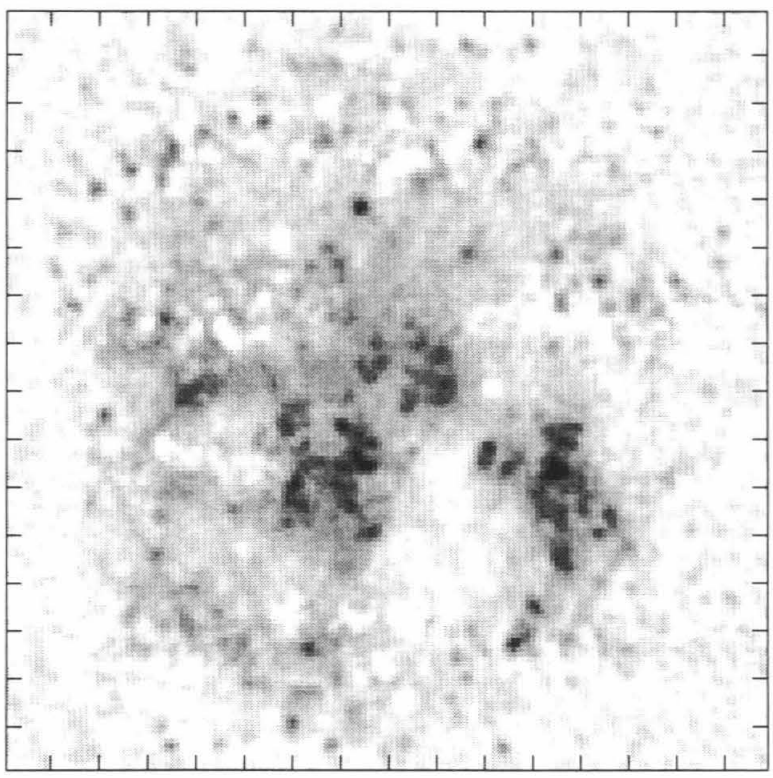

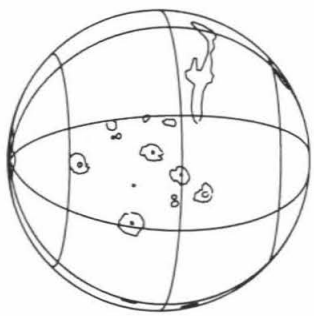

Date: 12/29/92

Snapshot: 8

β_o = 107.2

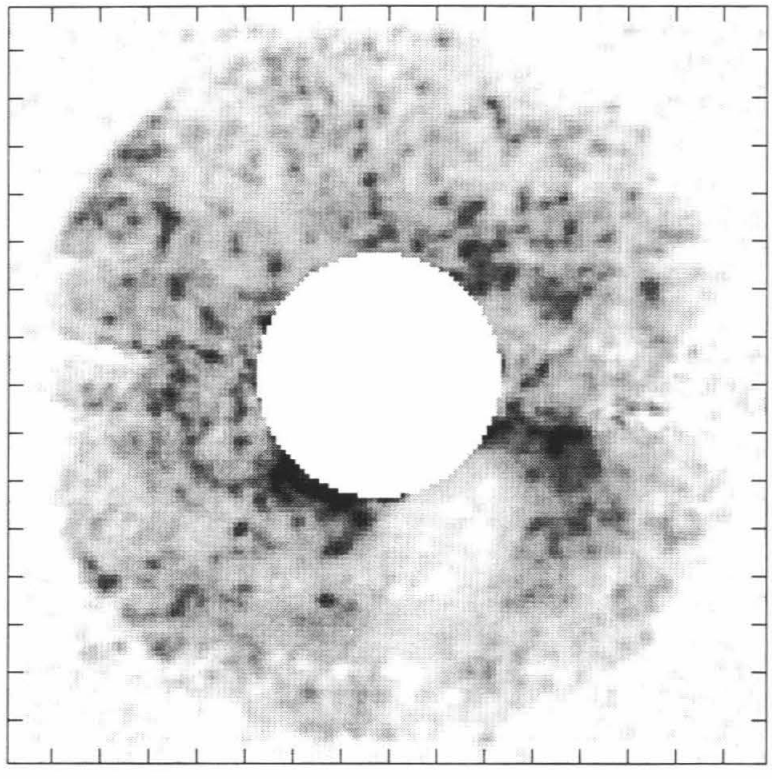

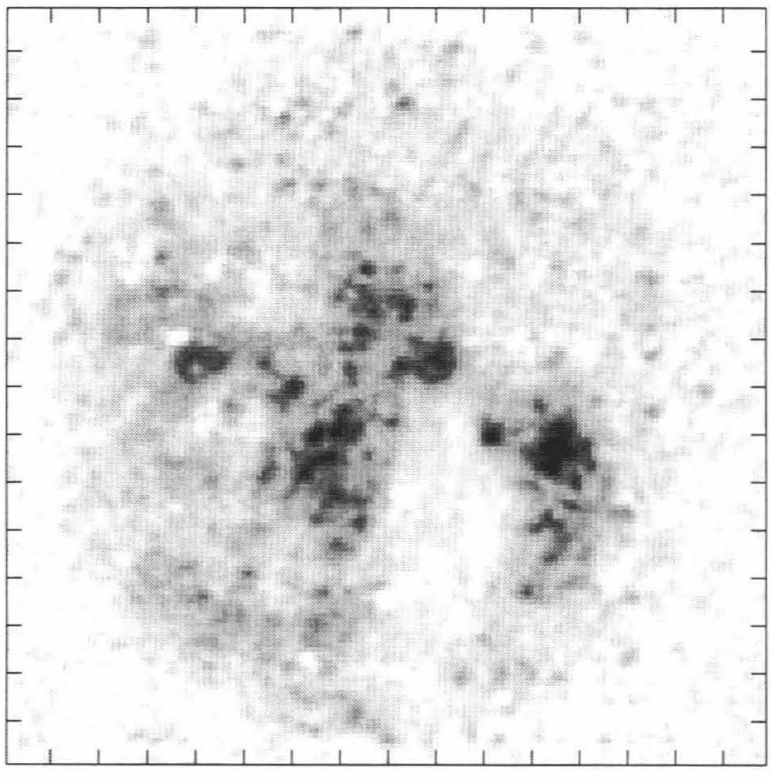

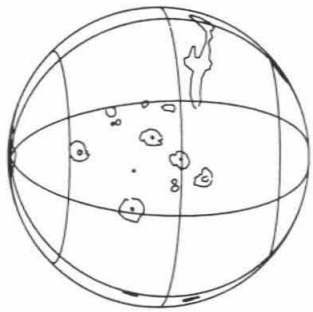

Date: 12/29/92

Snapshot: 9

β_o = 112.1

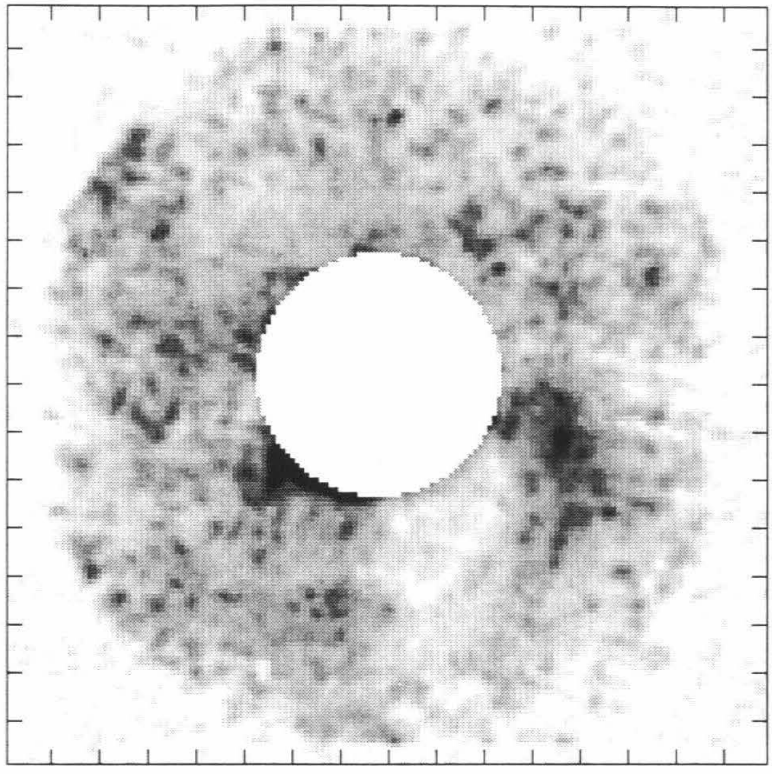

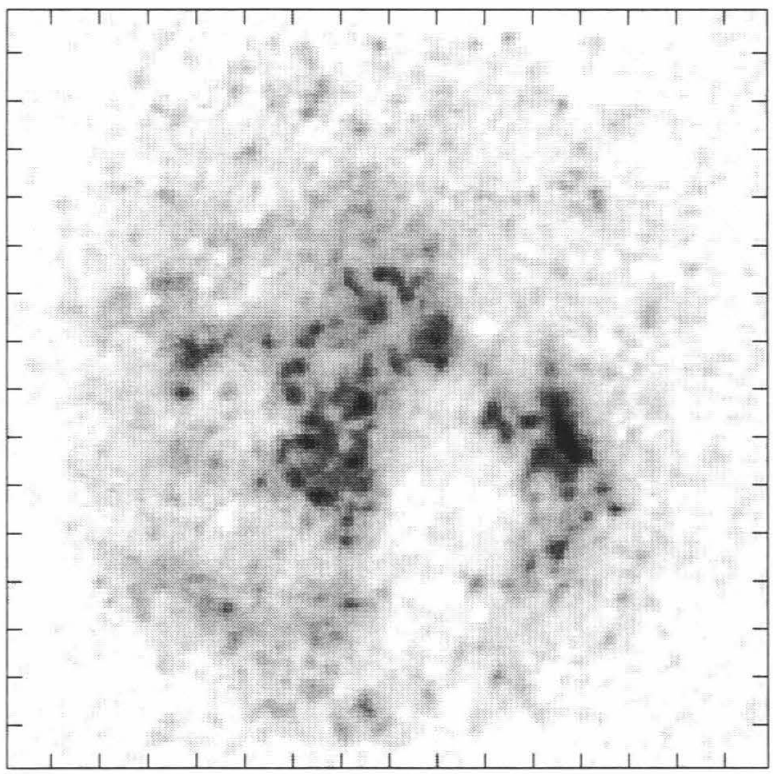

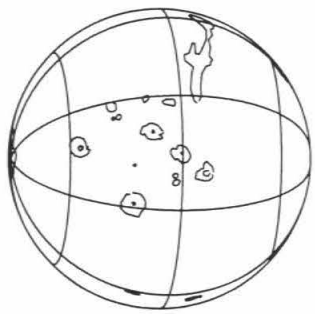

Date: 12/29/92

Snapshot: 10

β_o = 114.9

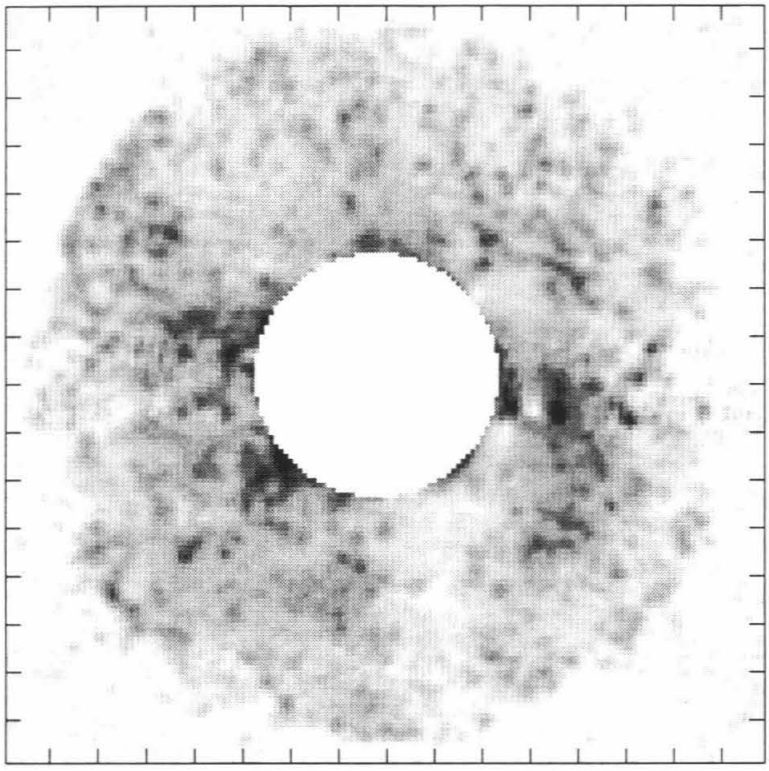

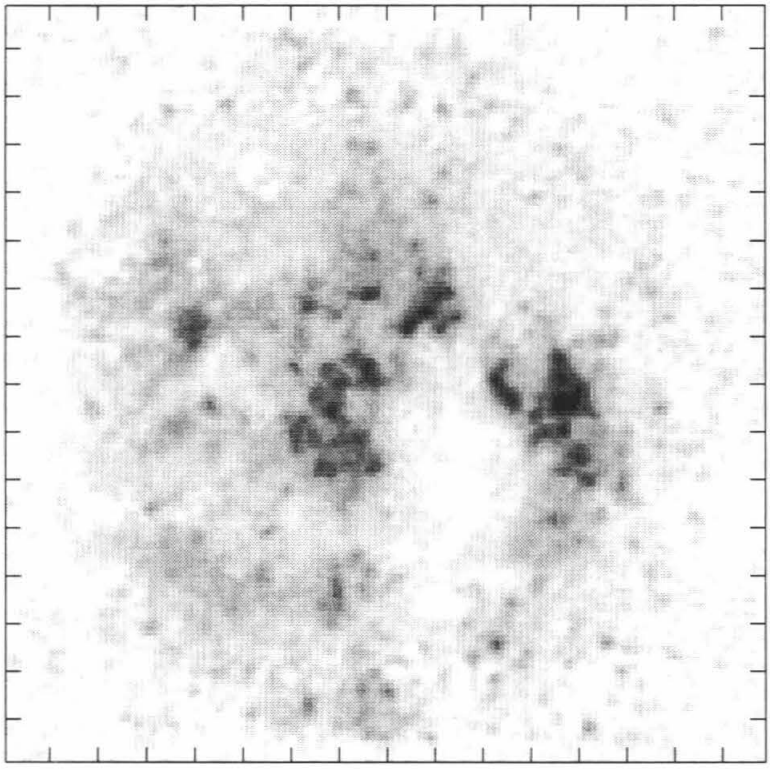

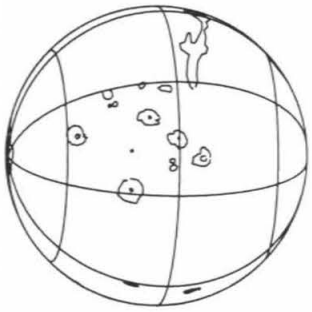

Date: 12/29/92

Snapshot: 11

β_o = 119.6

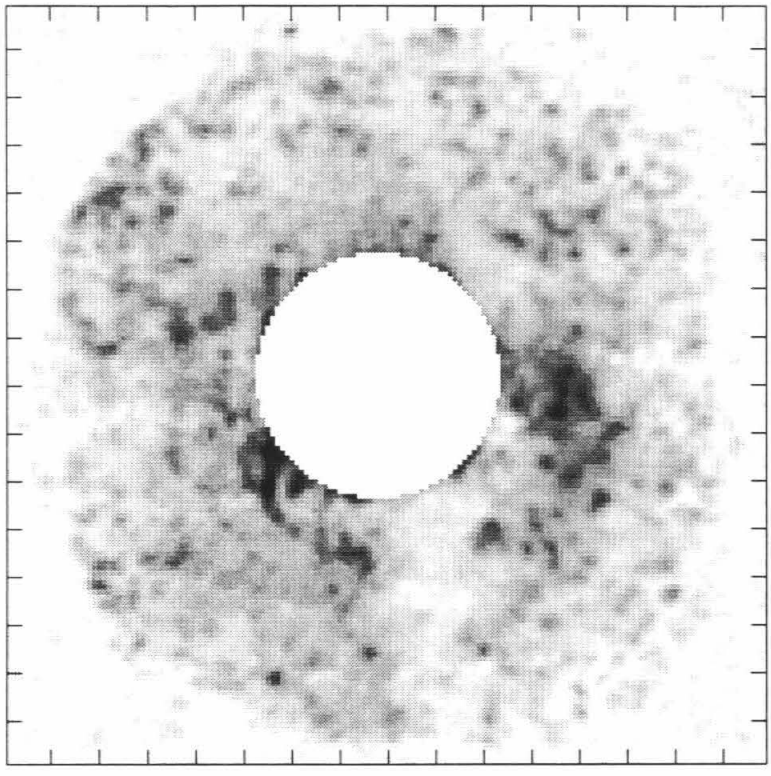

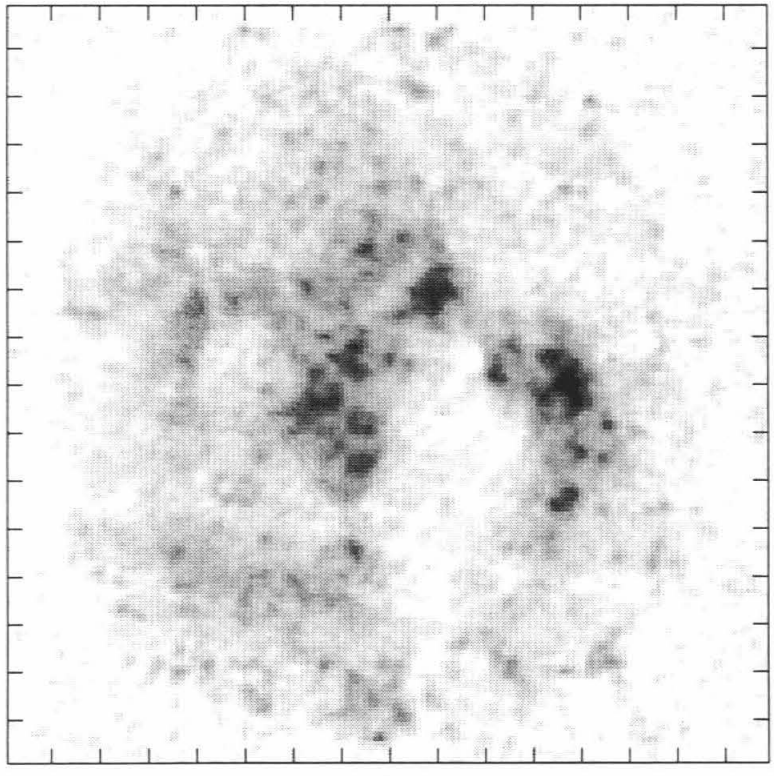

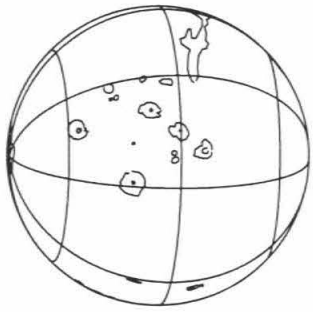

Date: 12/29/92

Snapshot: 12

β_o = 122.4

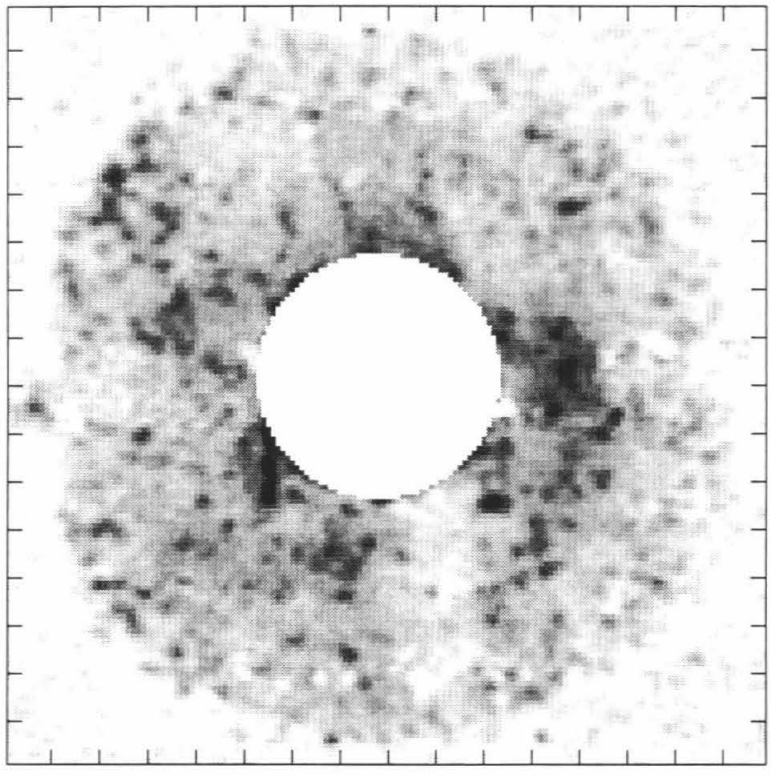

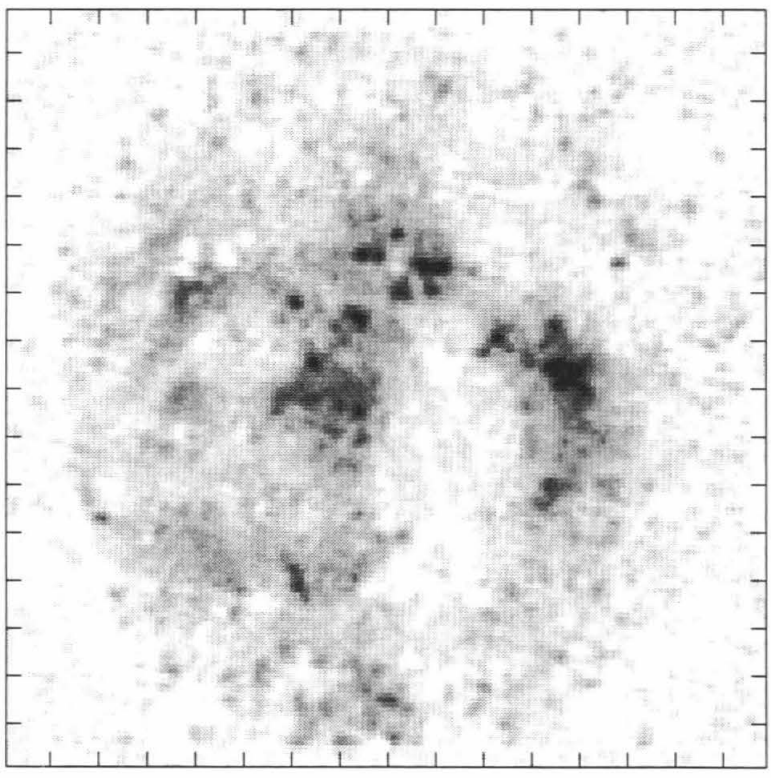

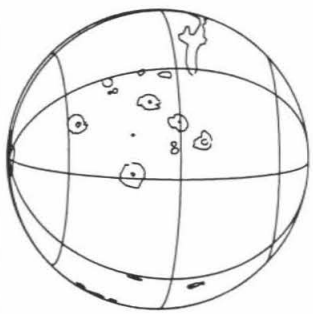

Date: 12/29/92

Snapshot: 13

β_o = 127.1

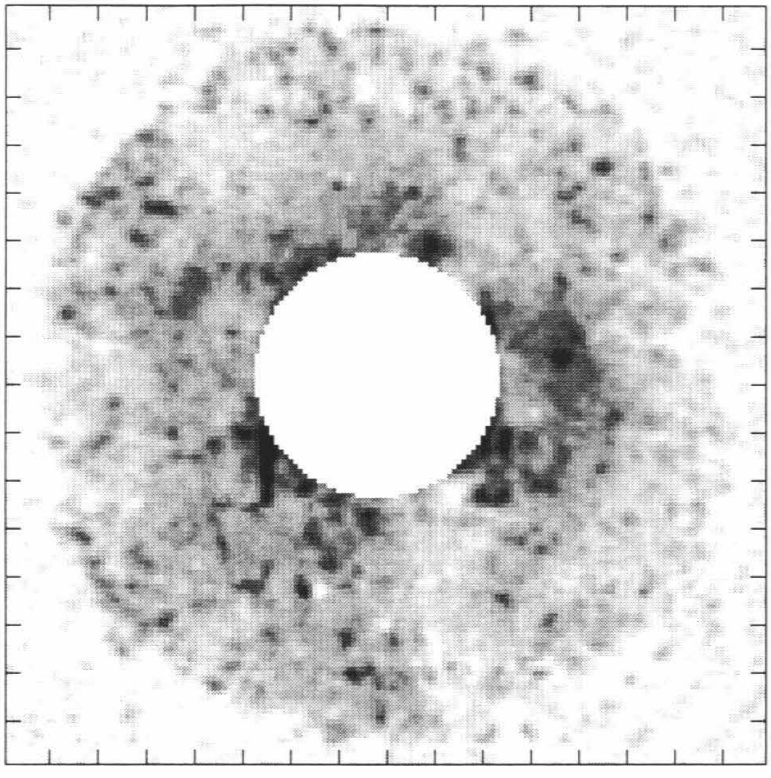

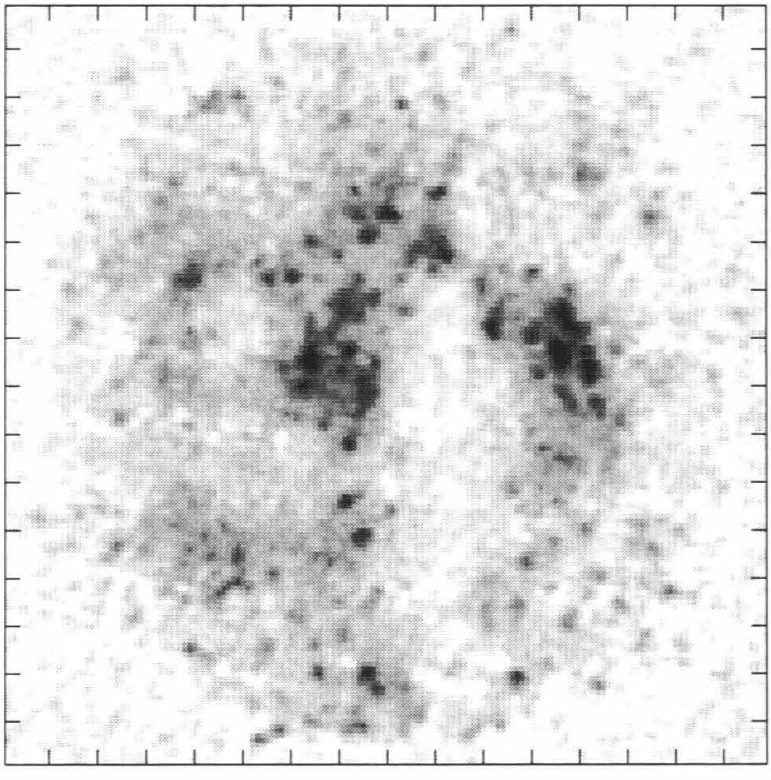

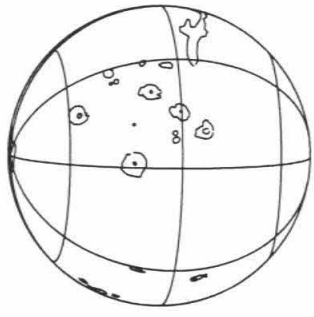

Date: 12/29/92

Snapshot: 14

β_o = 129.9

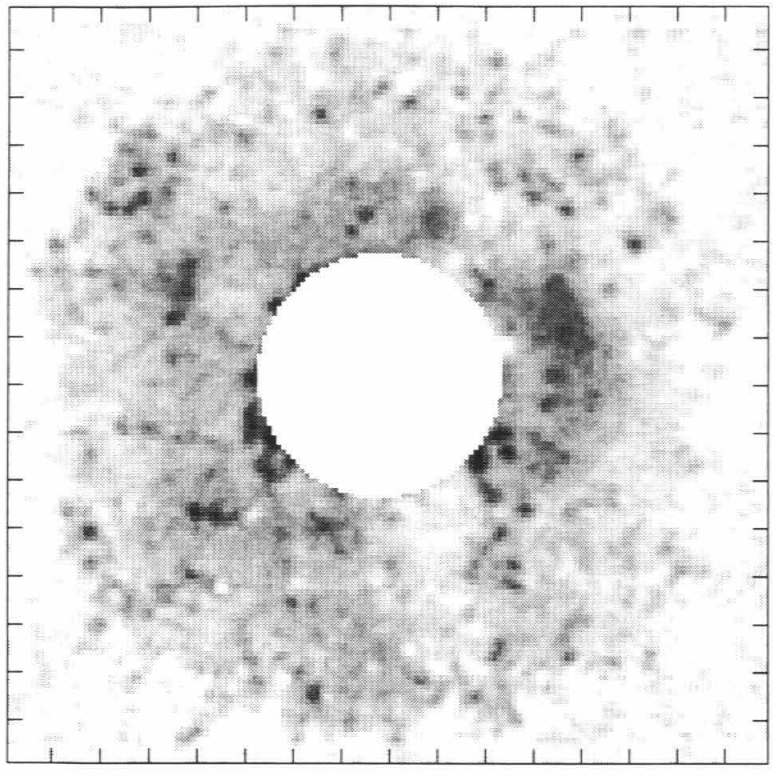

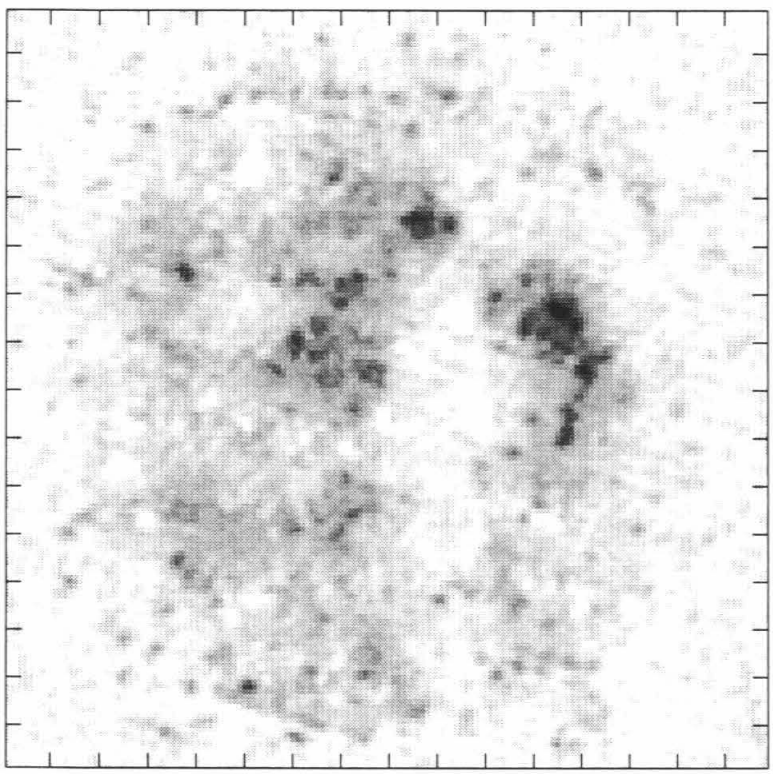

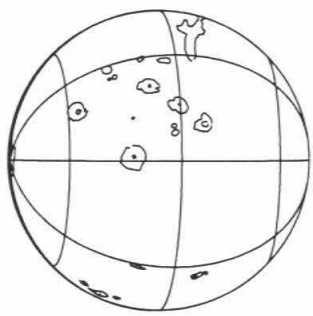

Date: 12/29/92

Snapshot: 15

β_o = 134.6

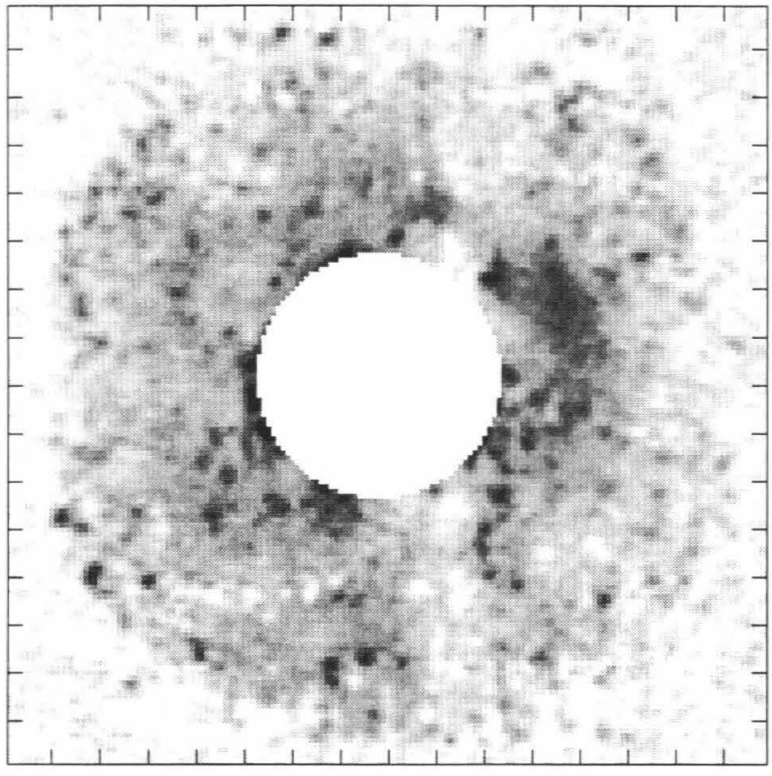

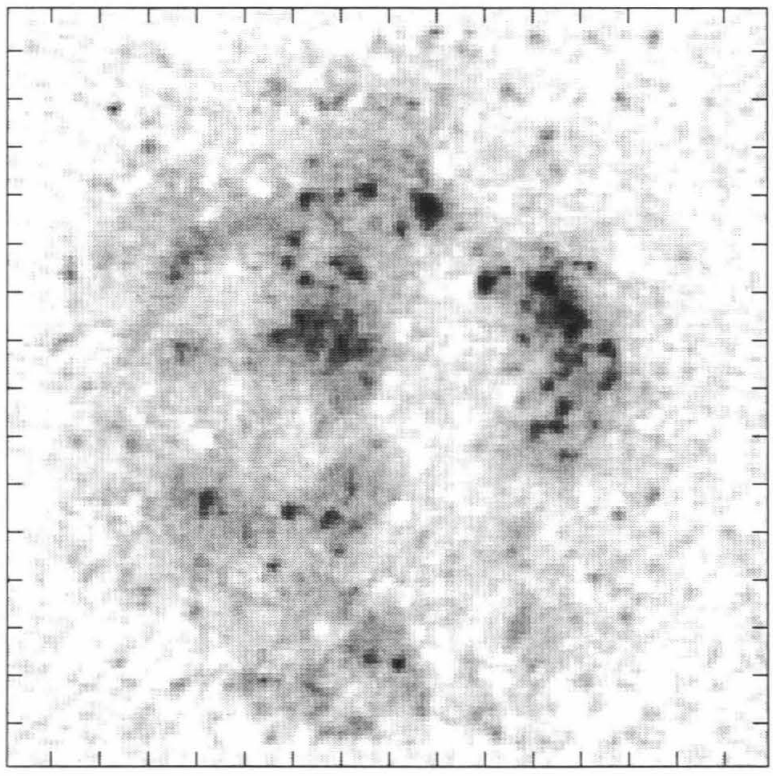

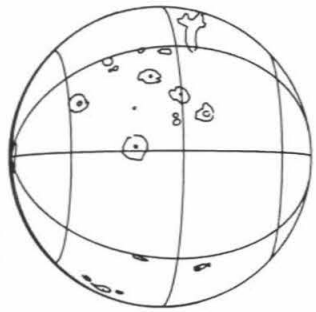

Date: 12/29/92

Snapshot: 16

β_o = 137.4

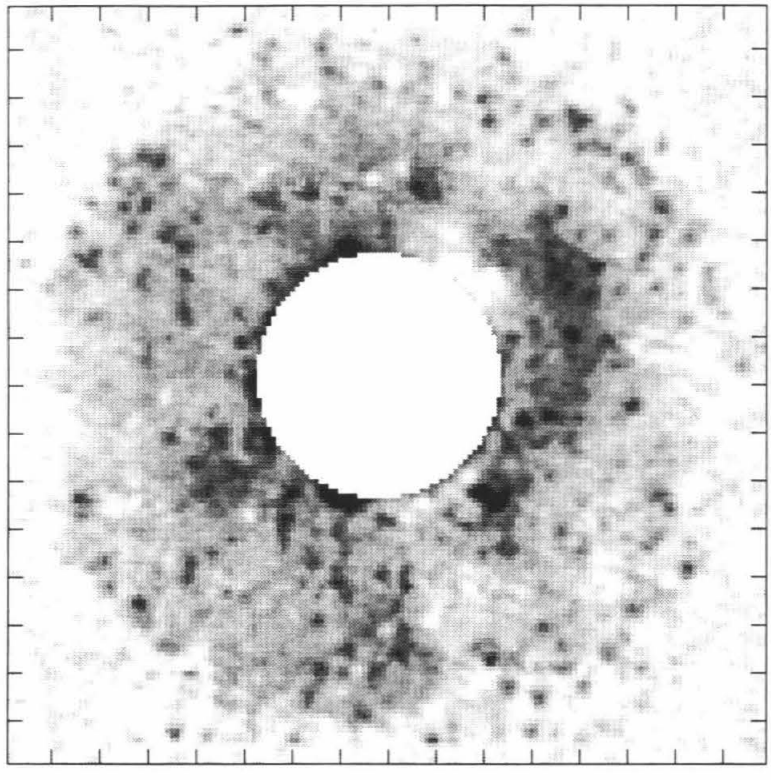

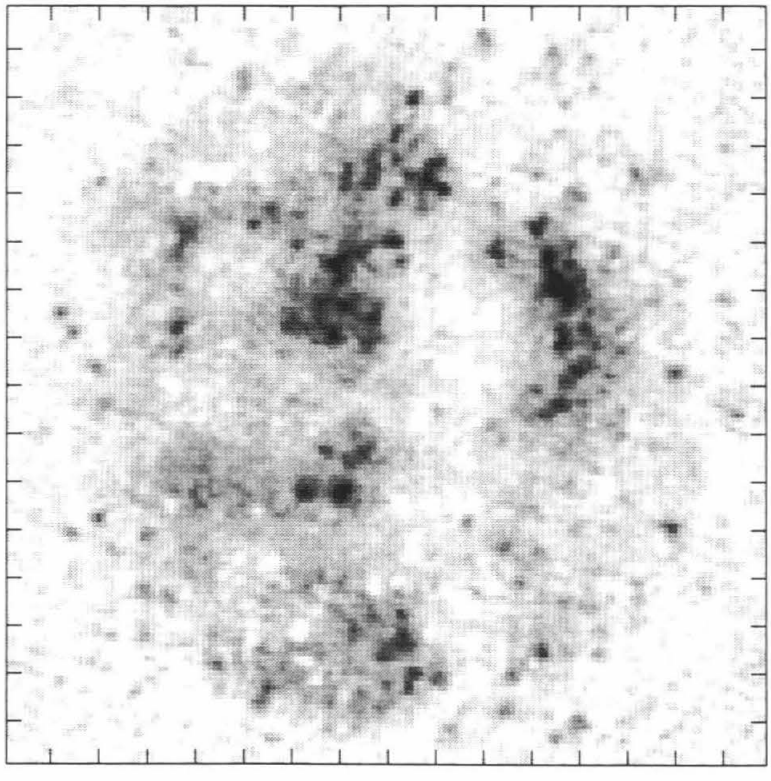

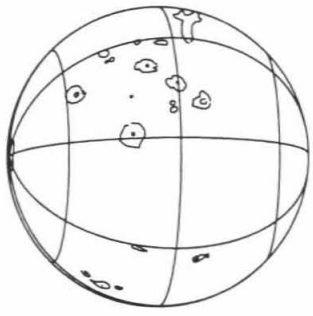

Date: 12/29/92

Snapshot: 17

β_o = 142.3

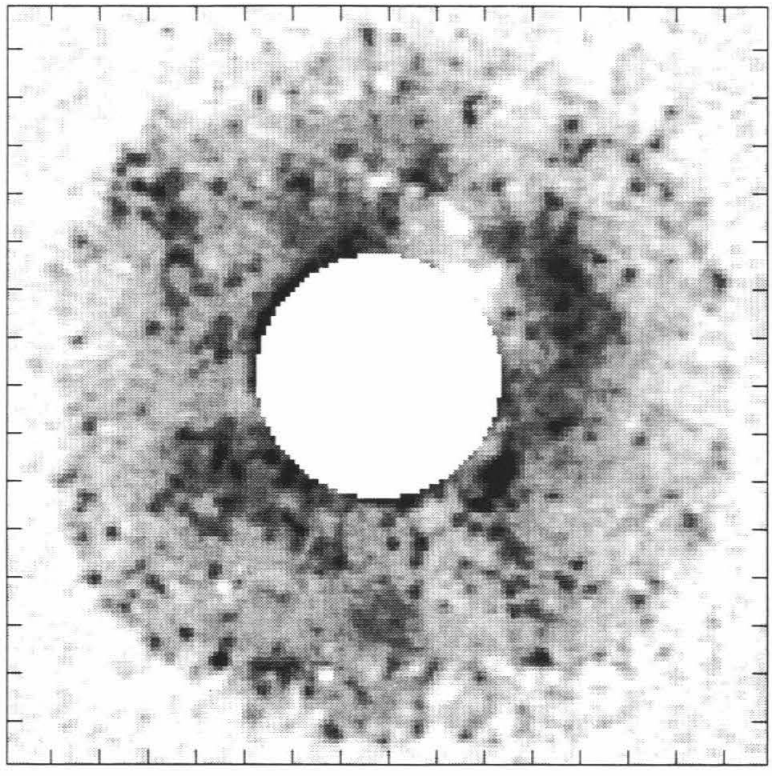

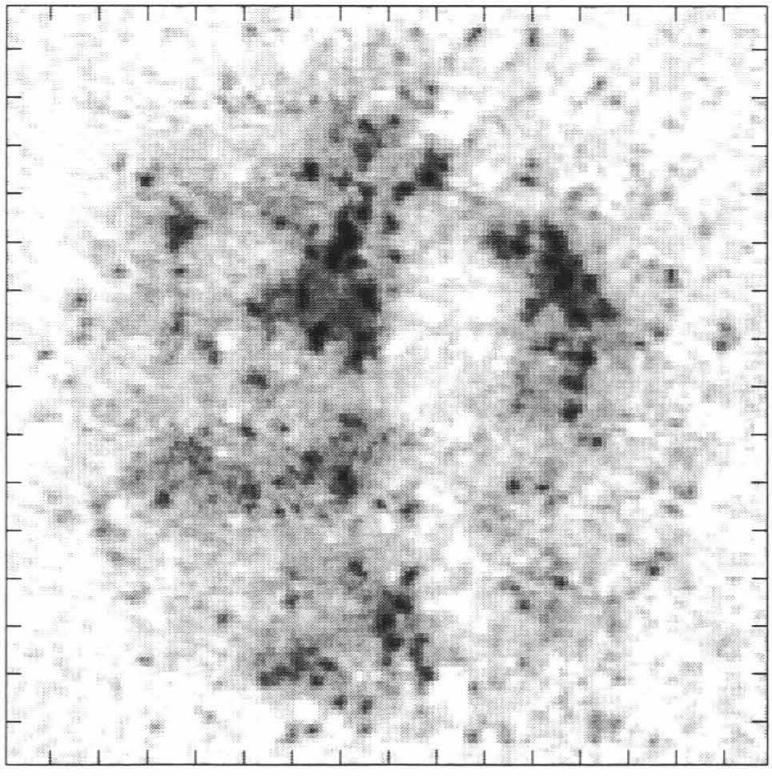

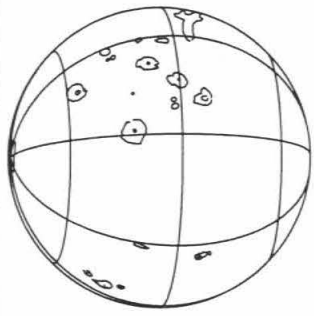

Date: 12/29/92

Snapshot: 18

β_o = 144.1

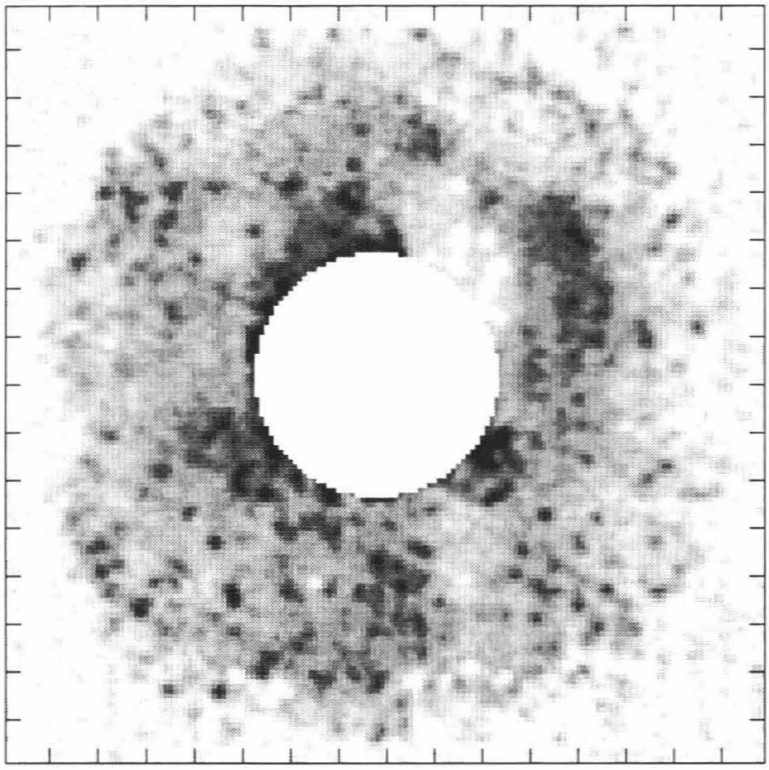

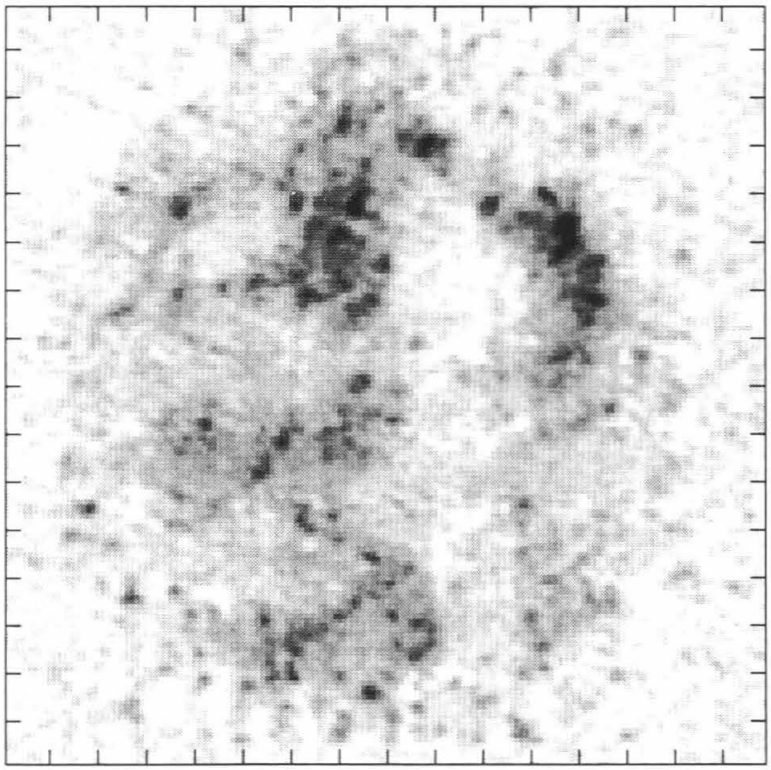

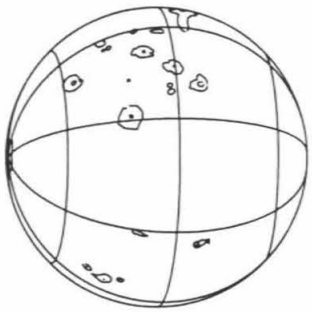

Date: 12/29/92

Snapshot: 19

β_o = 149.9

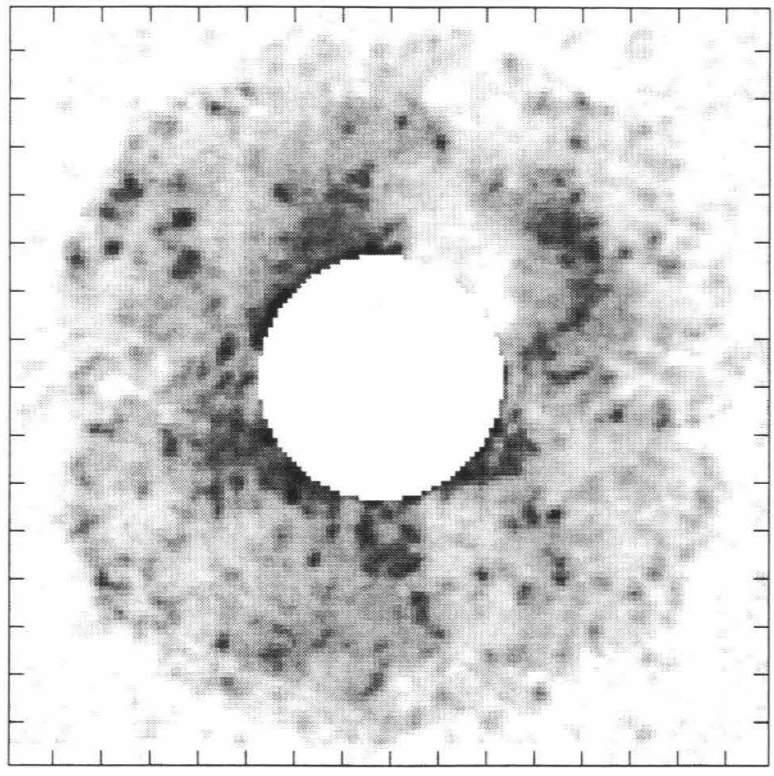

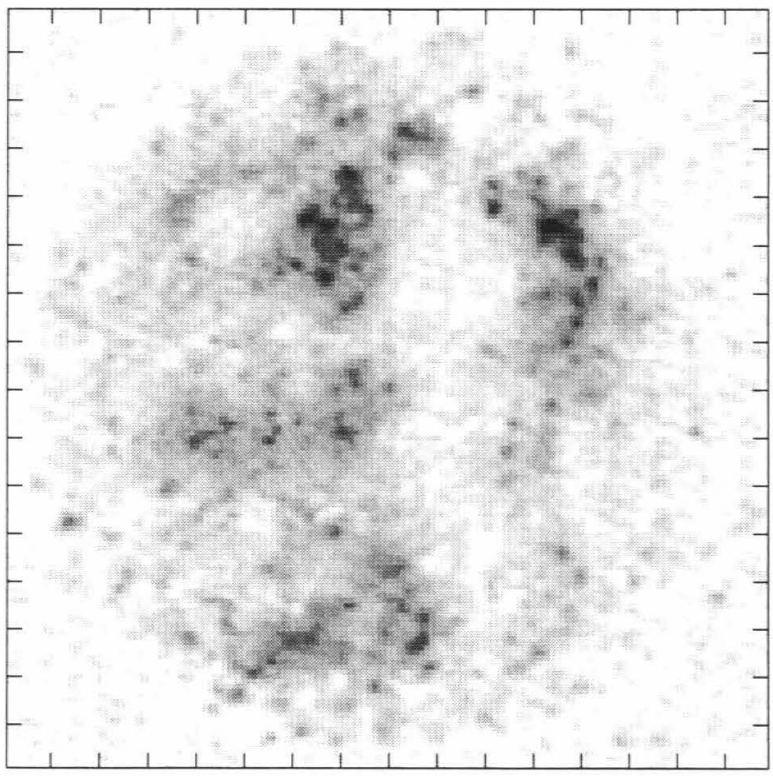

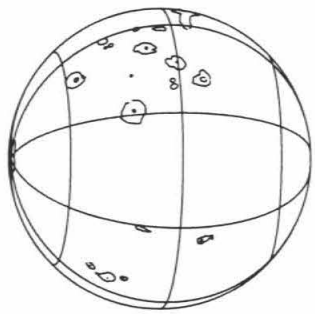

Date: 12/29/92

Snapshot: 20

β_o = 152.7

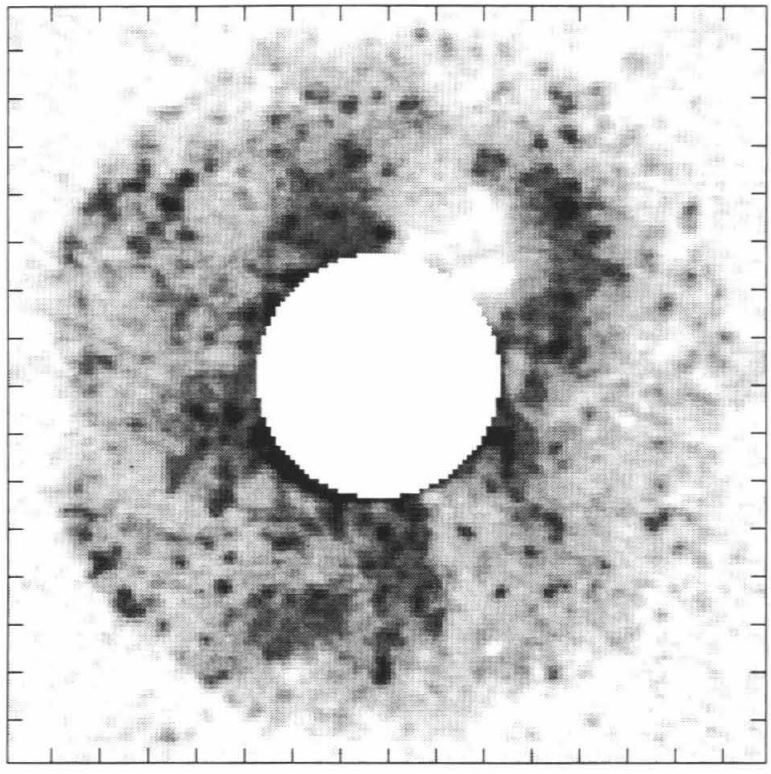

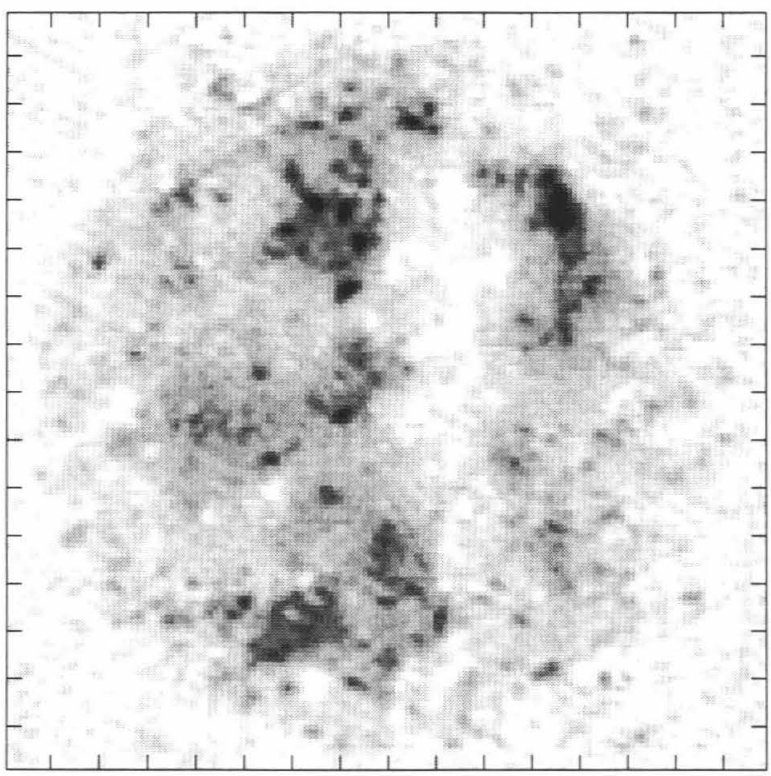

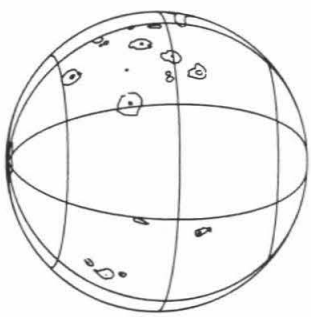

Date: 12/29/92

Snapshot: 21

β_o = 157.3

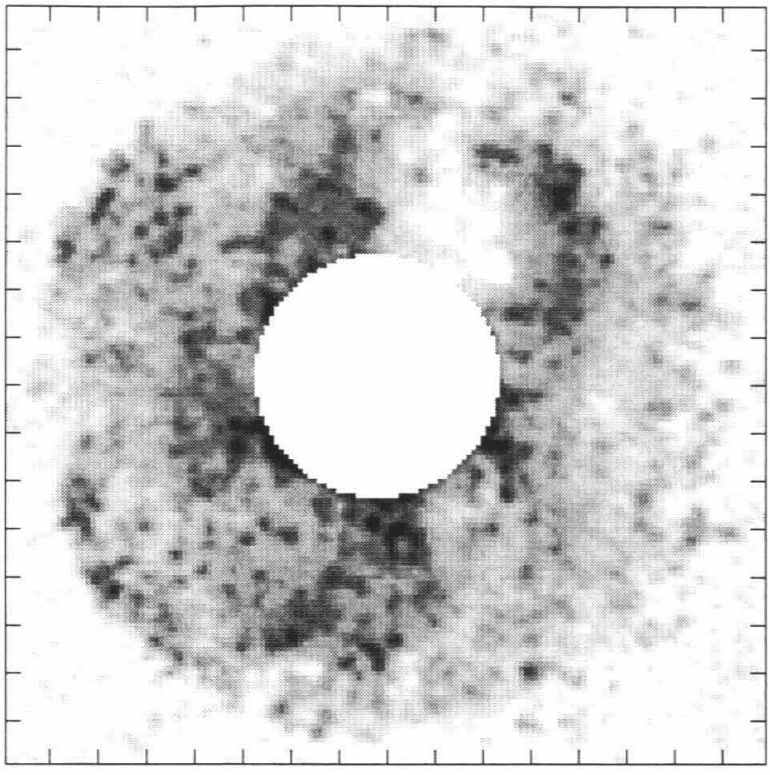

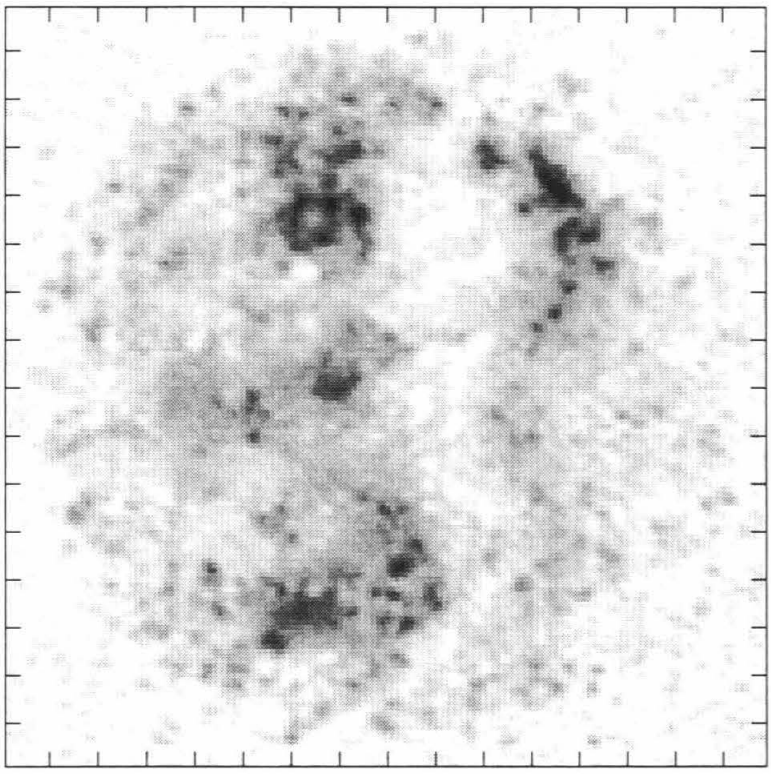

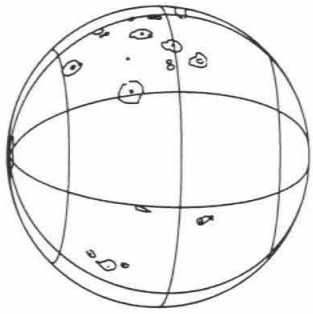

Date: 12/29/92

Snapshot: 22

β_o = 160.2

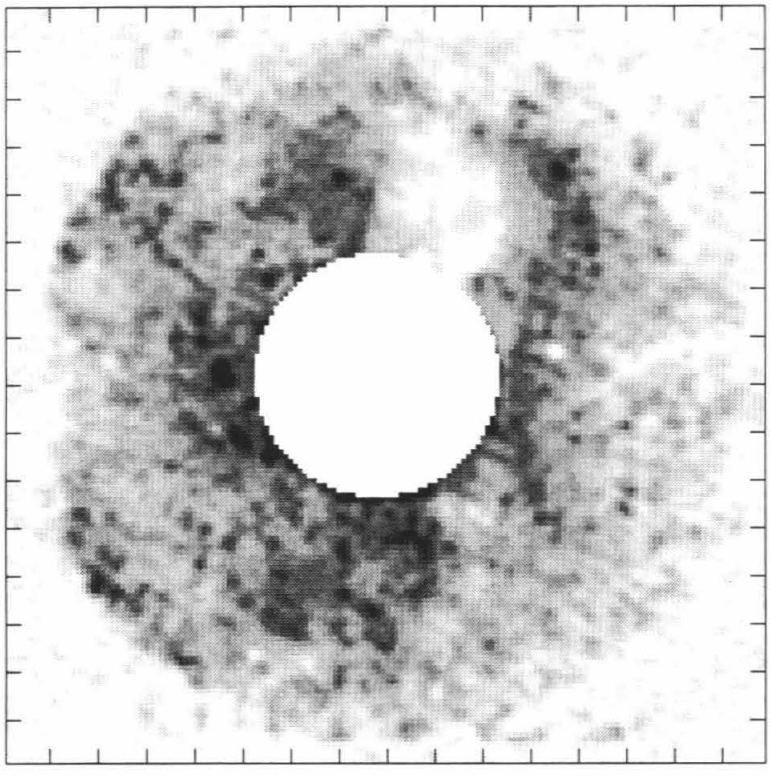

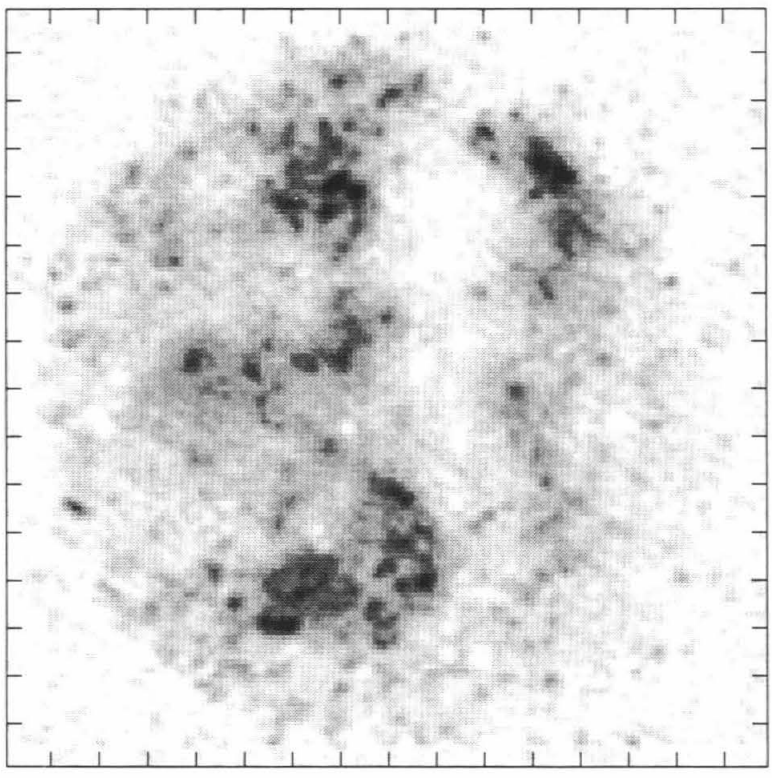

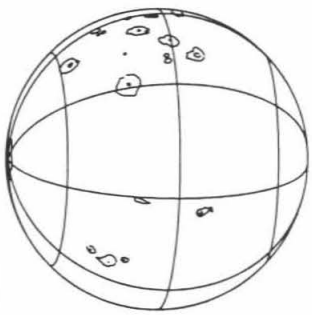

Date: 12/29/92

Snapshot: 23

β_o = 164.8

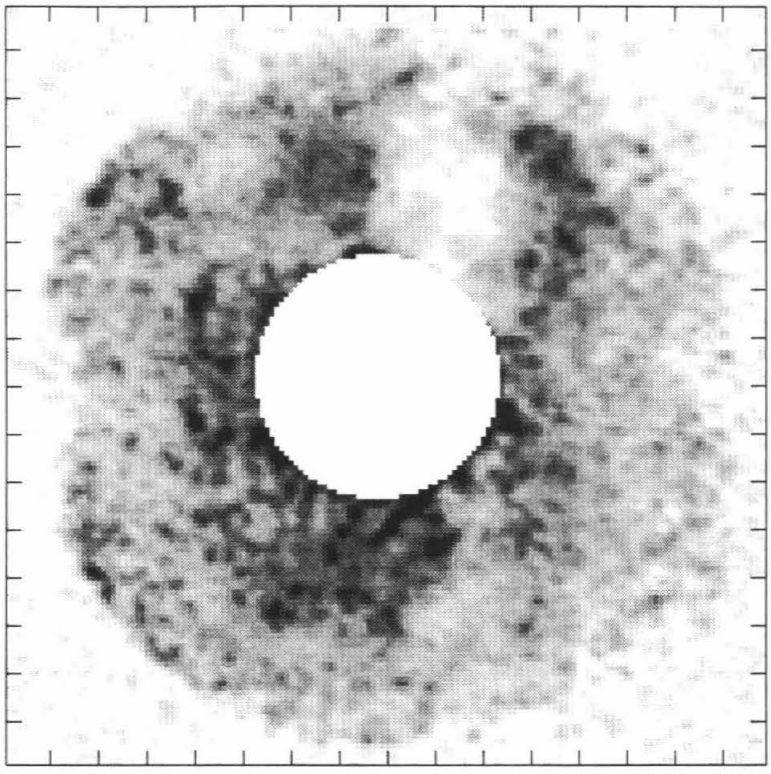

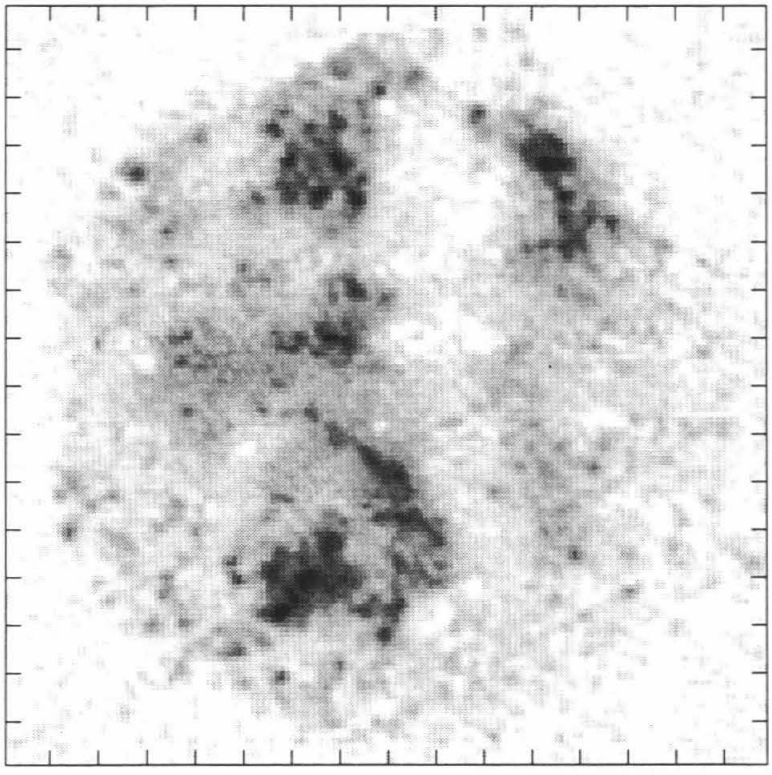

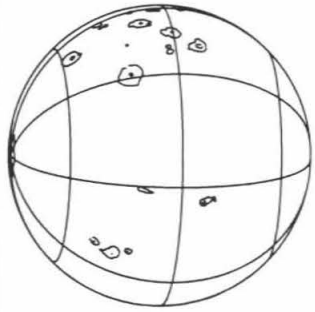

Date: 12/29/92

Snapshot: 24

β_o = 167.6

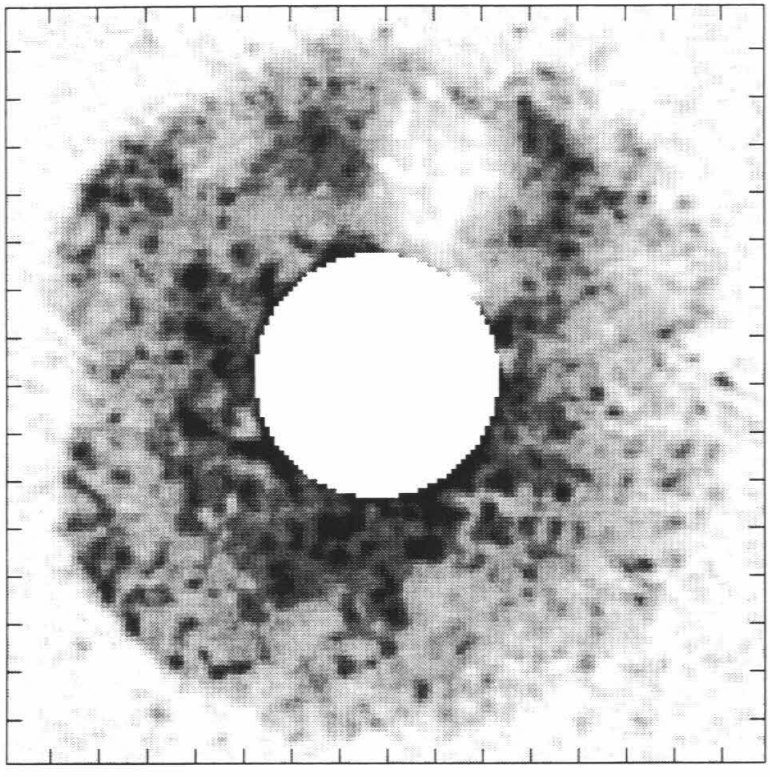

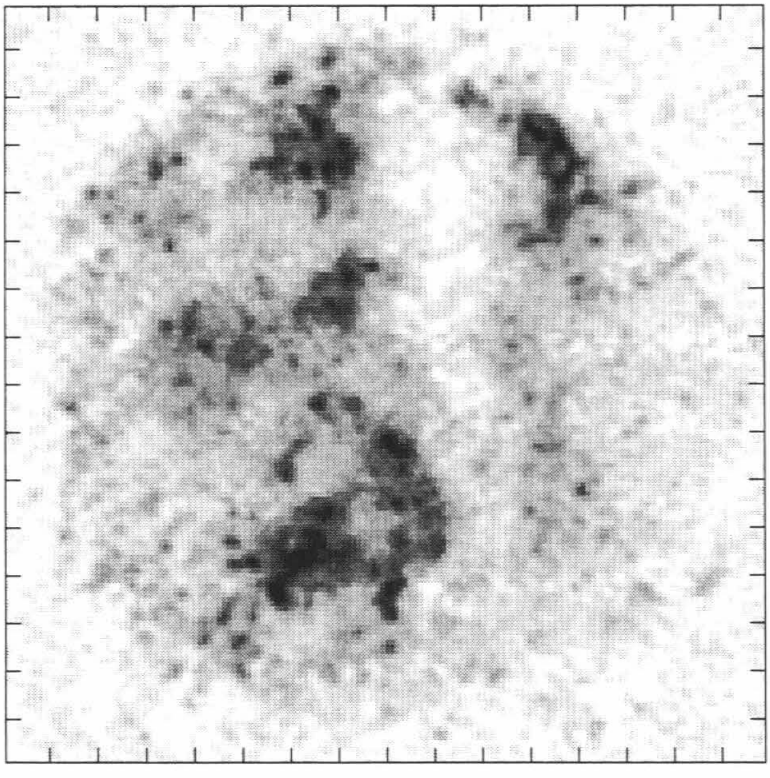

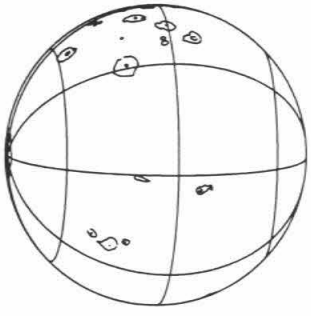

Date: 12/29/92

Snapshot: 25

β_o = 172.2

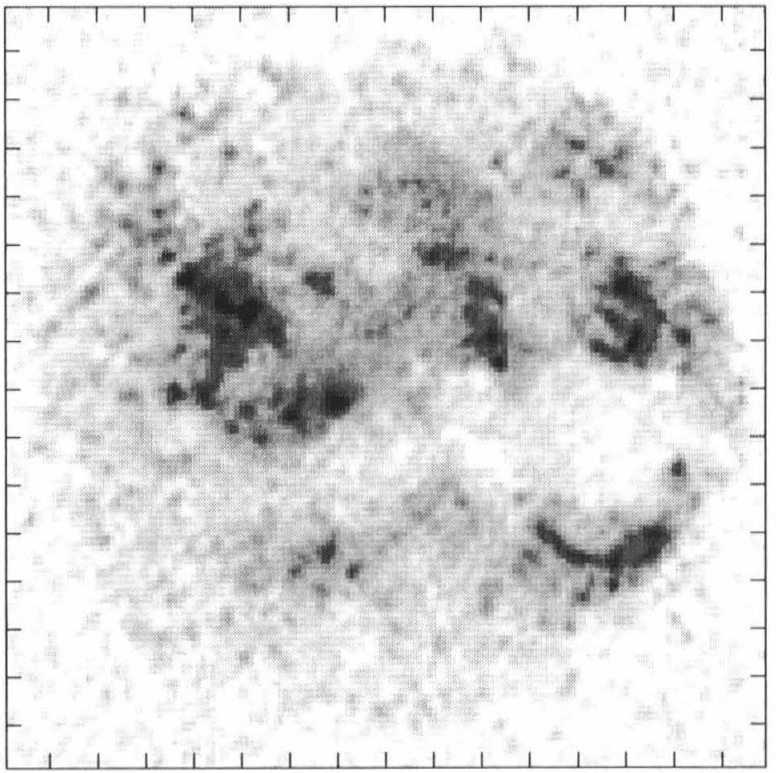

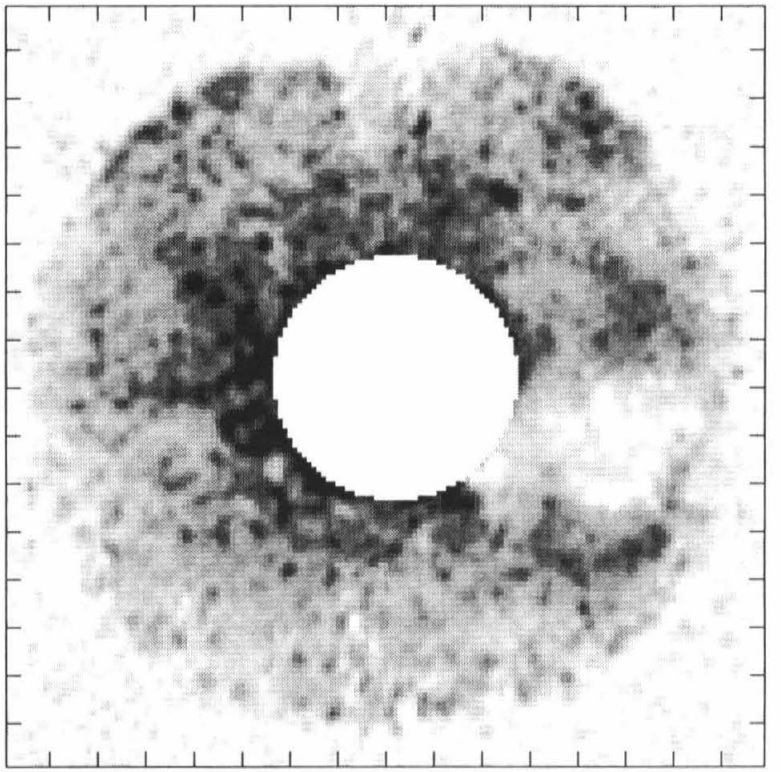

Date: 12/29/92

Snapshot: 26

β_o = 175.1

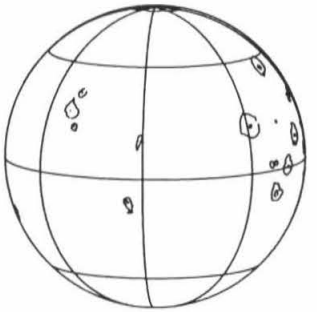

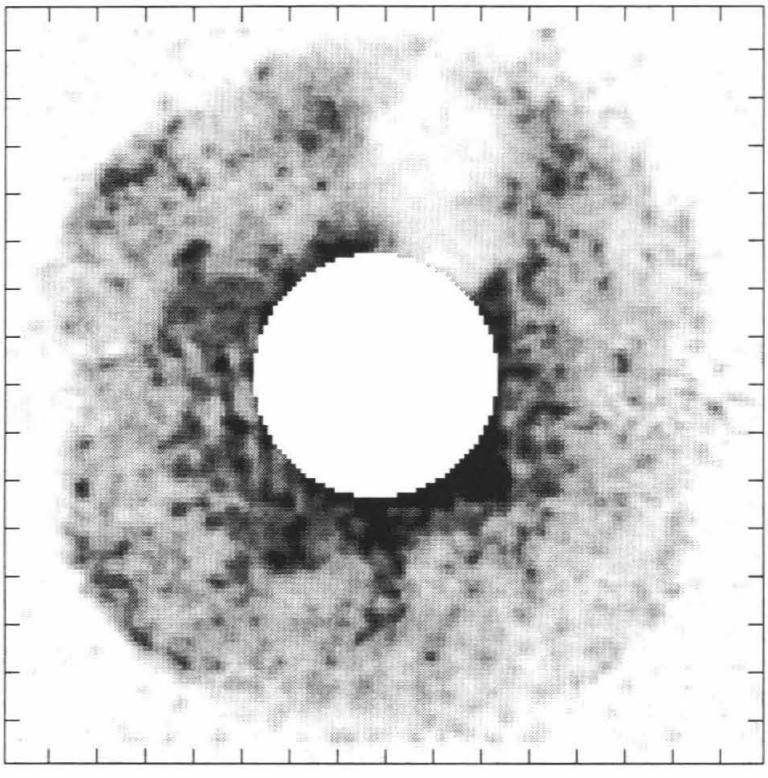

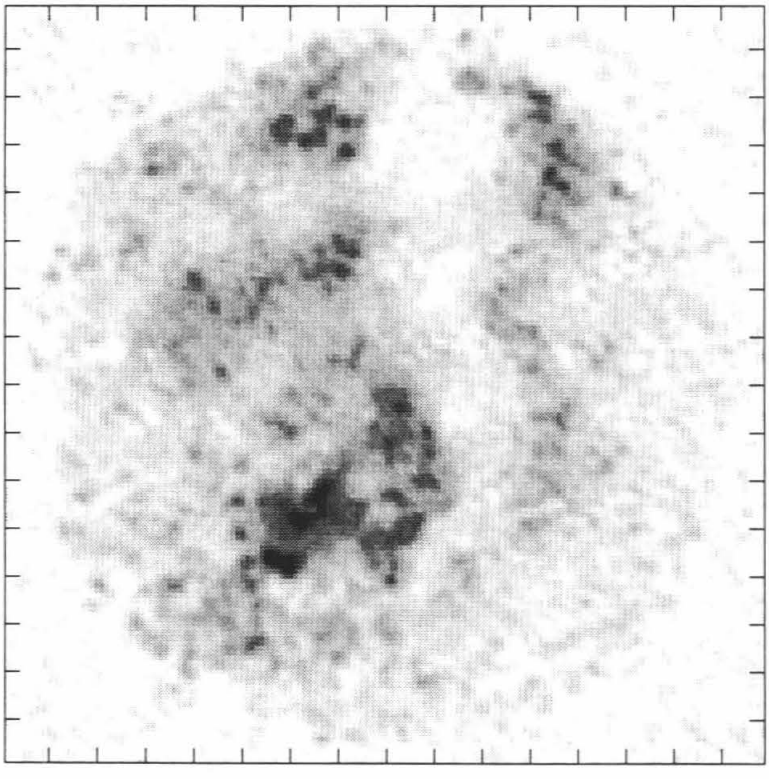

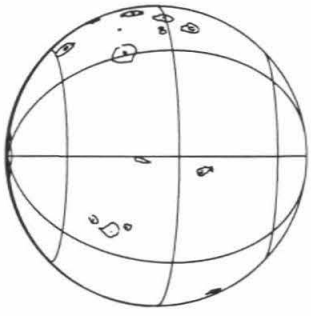

Date: 12/29/92

Snapshot: 27

β_o = 179.8

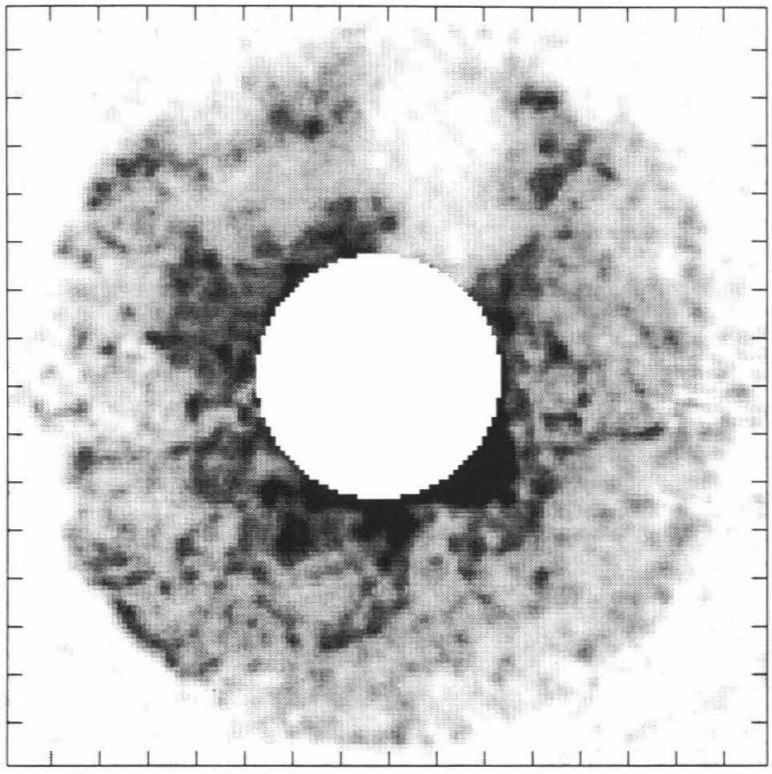

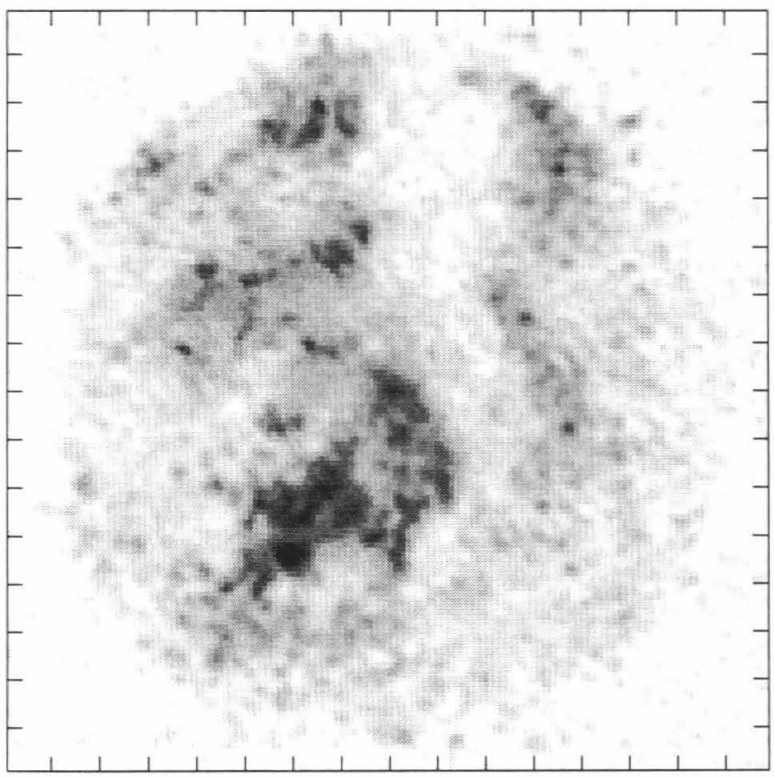

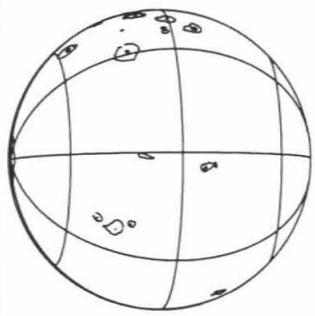

Date: 12/29/92

Snapshot: 28

β_o = 182.7

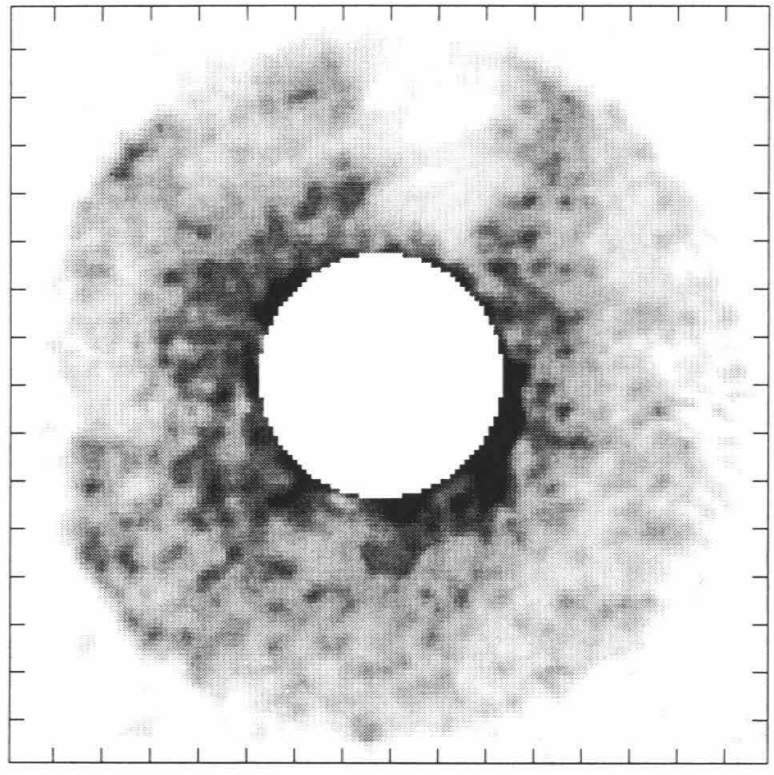

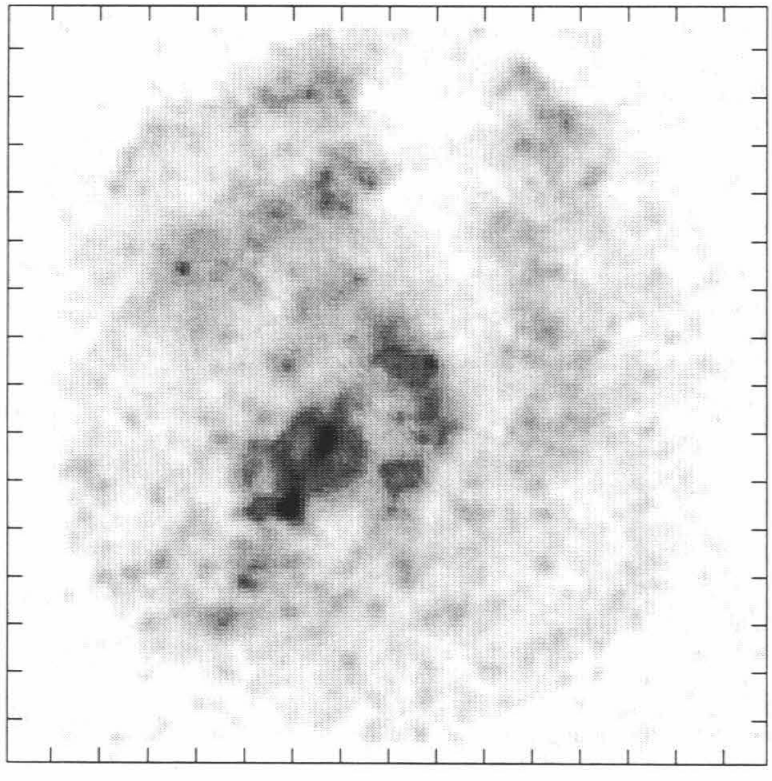

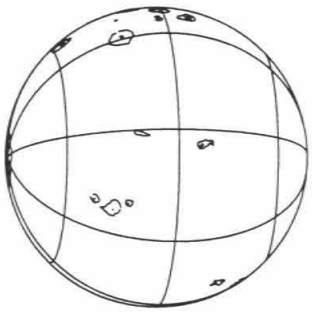

Date: 12/29/92

Snapshot: 29

β_o = 190.8

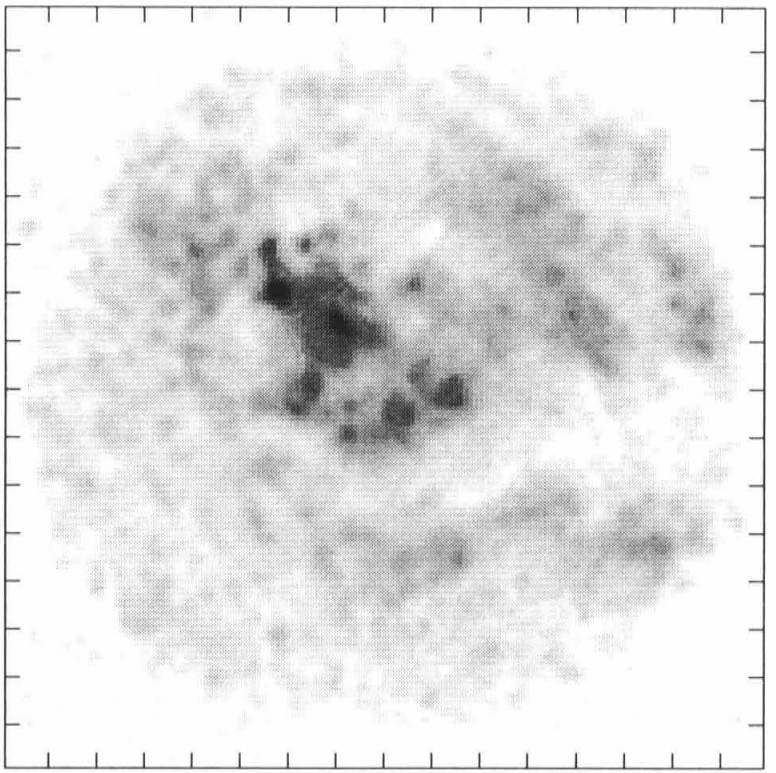

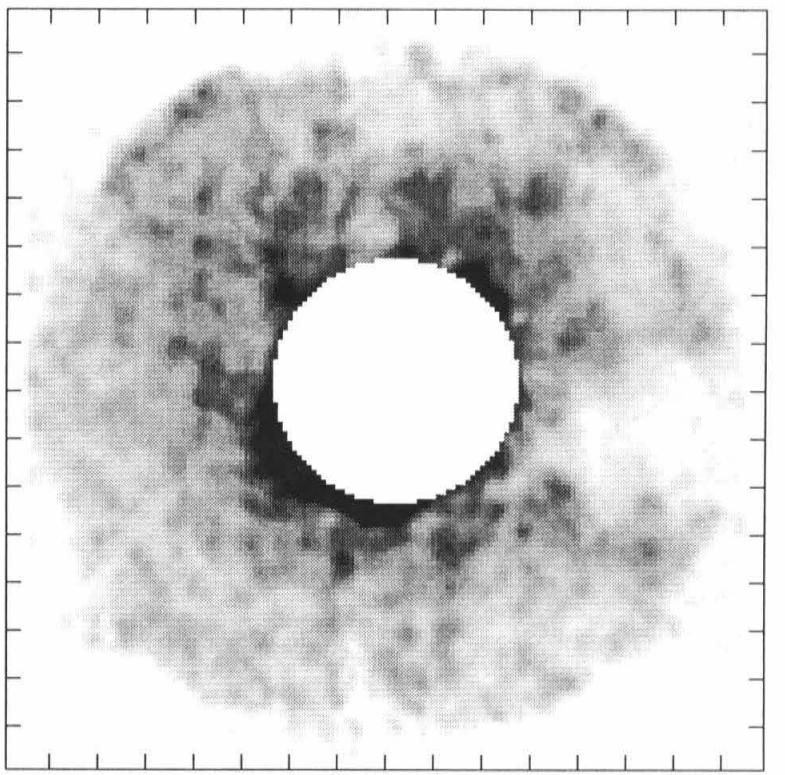

Date: 12/29/92

Snapshot: 30

β_o = 193.6

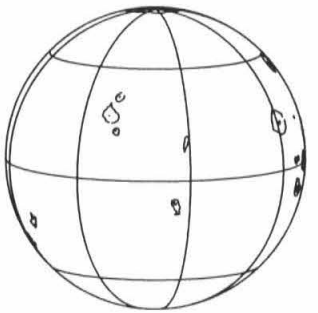

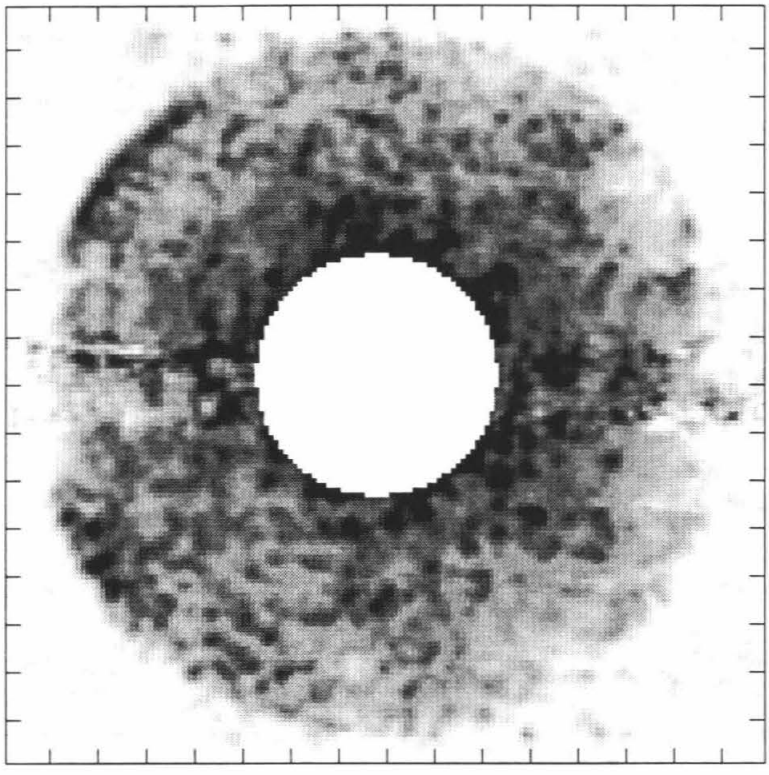

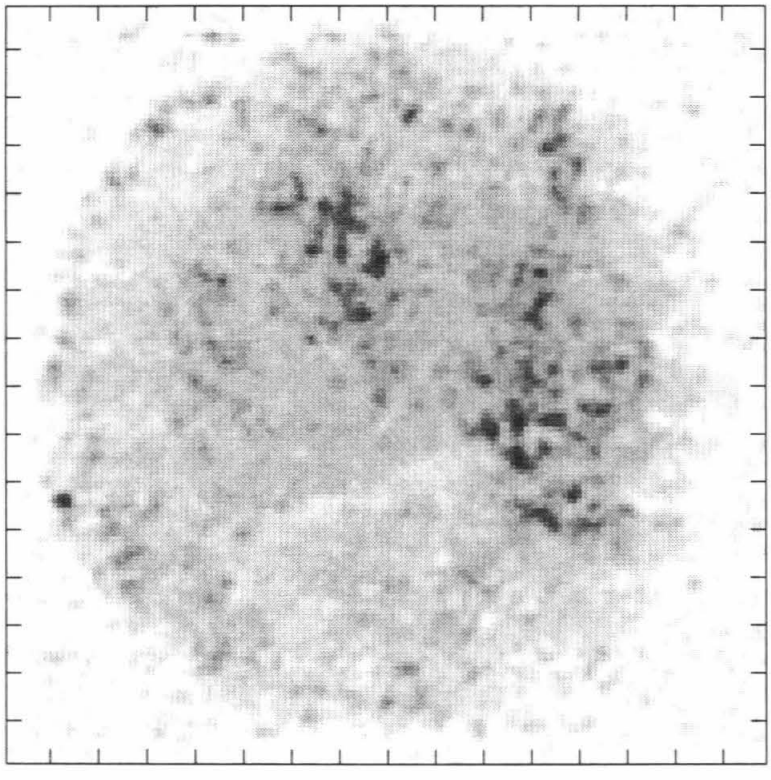

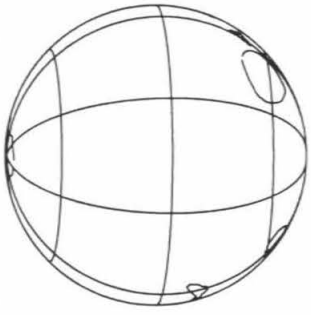

Date: 1/12/93

Snapshot: 1

β_o = 337.3

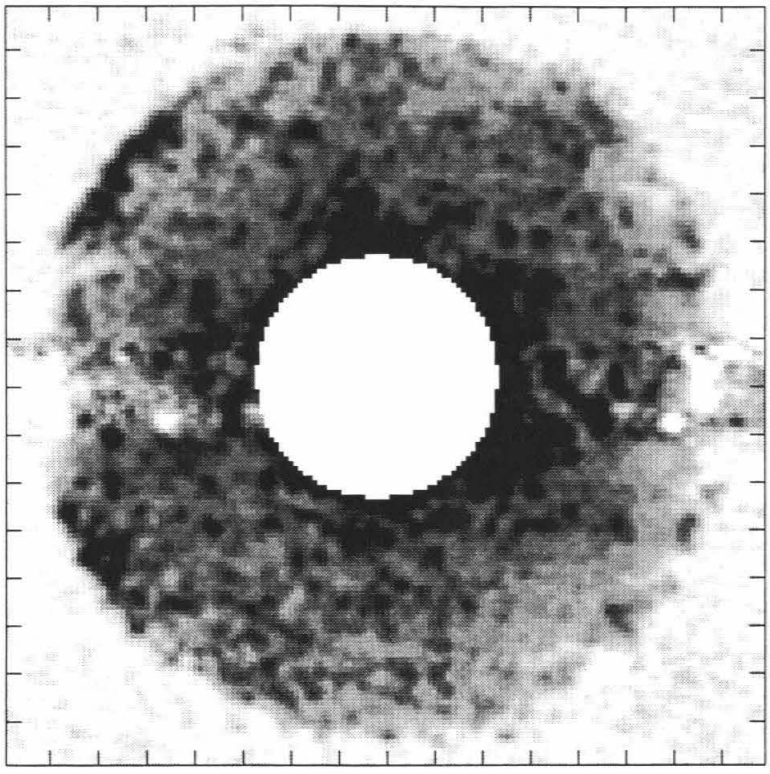

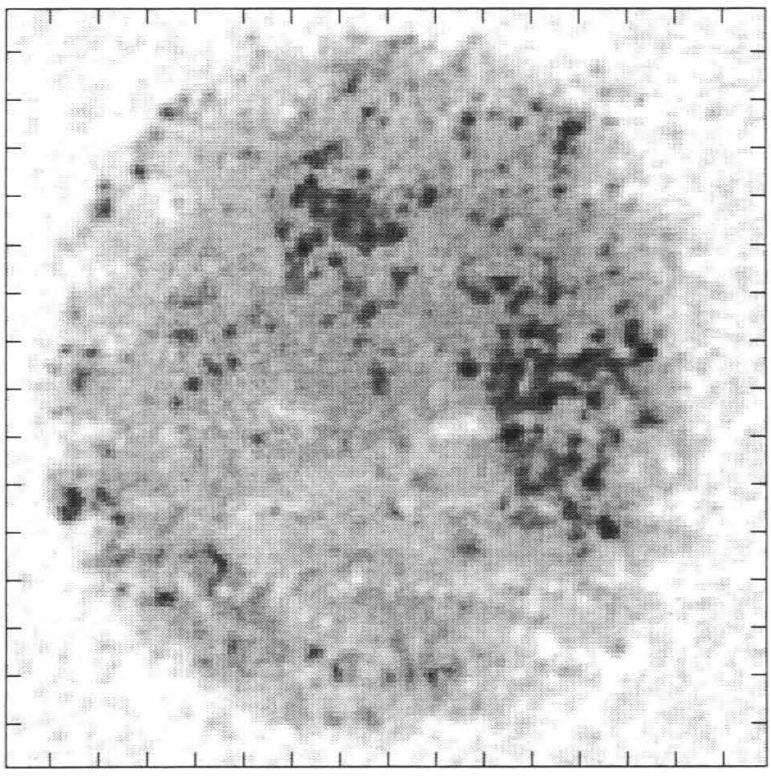

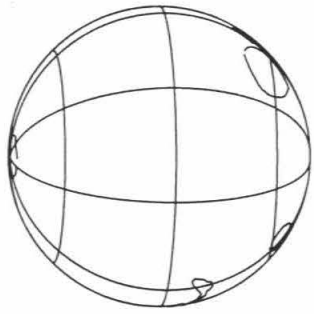

Date: 1/12/93

Snapshot: 2

β_o = 342.2

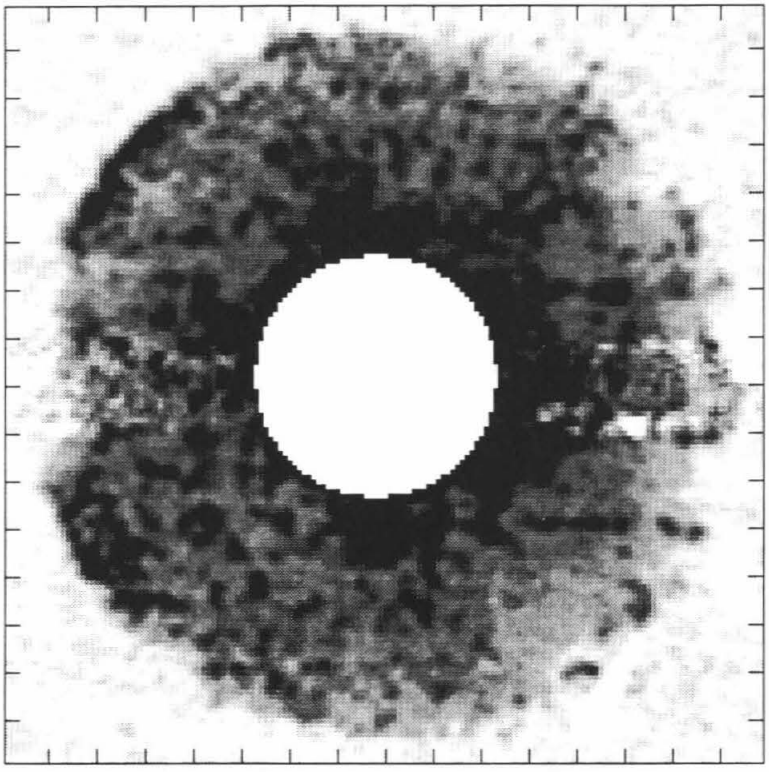

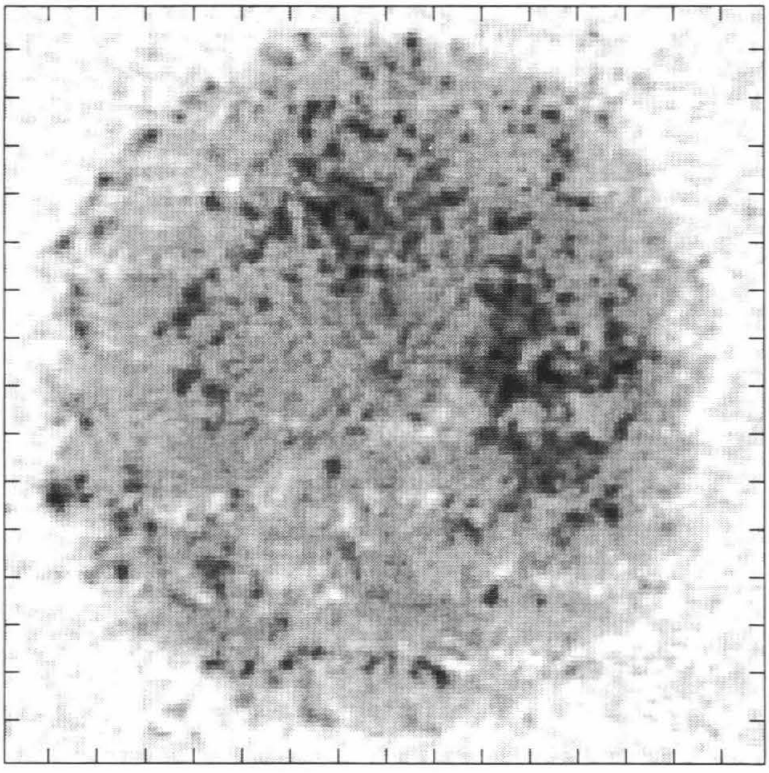

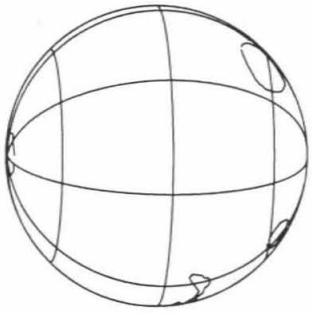

Date: 1/12/93

Snapshot: 3

β_o = 345.0

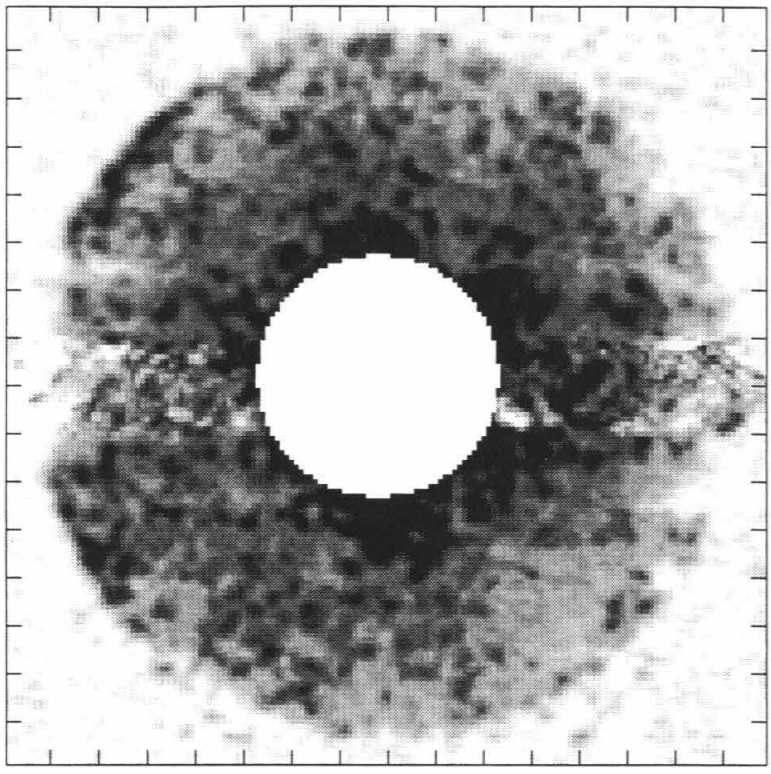

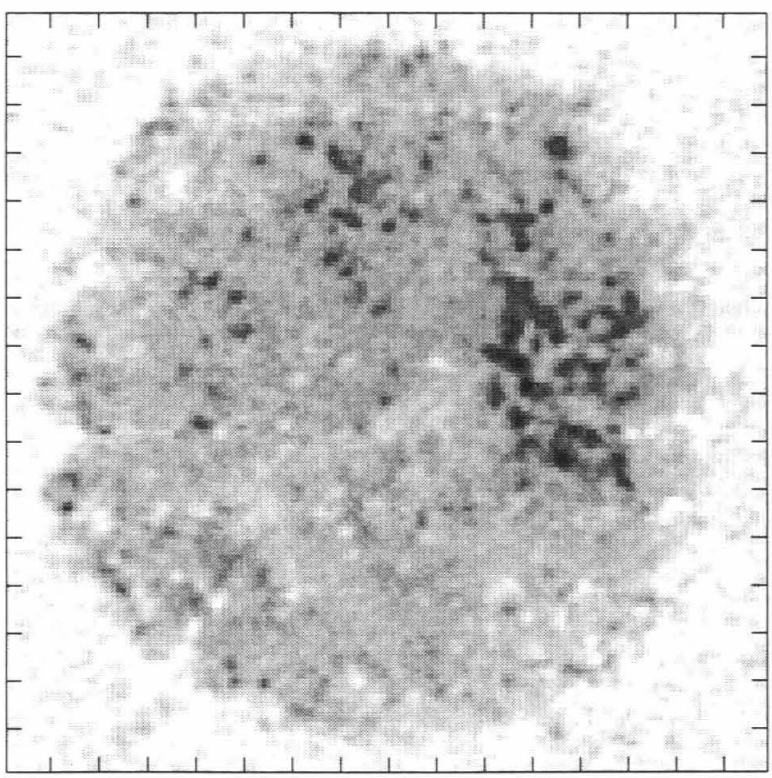

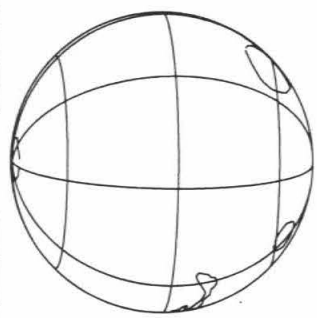

Date: 1/12/93

Snapshot: 4

β_o = 349.8

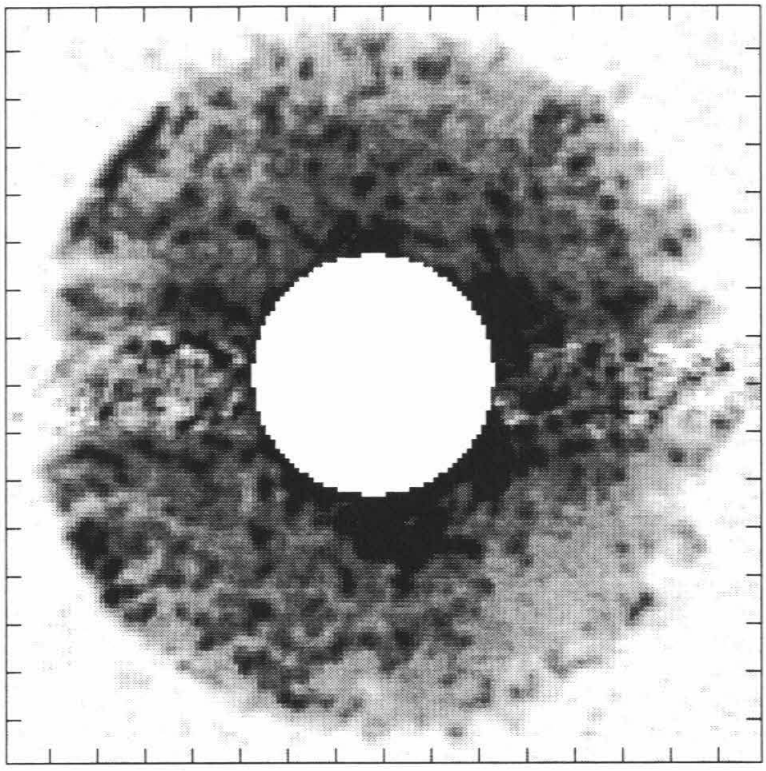

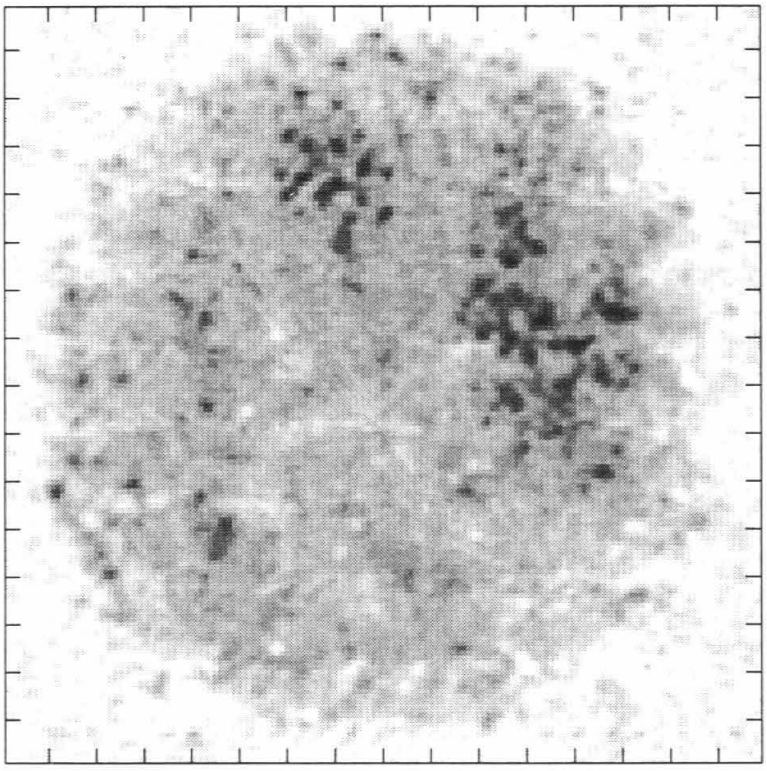

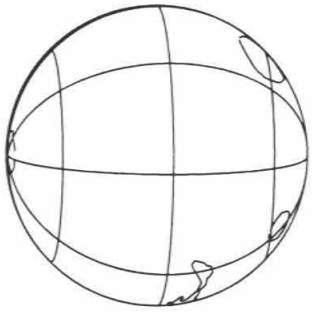

Date: 1/12/93

Snapshot: 5

β_o = 352.6

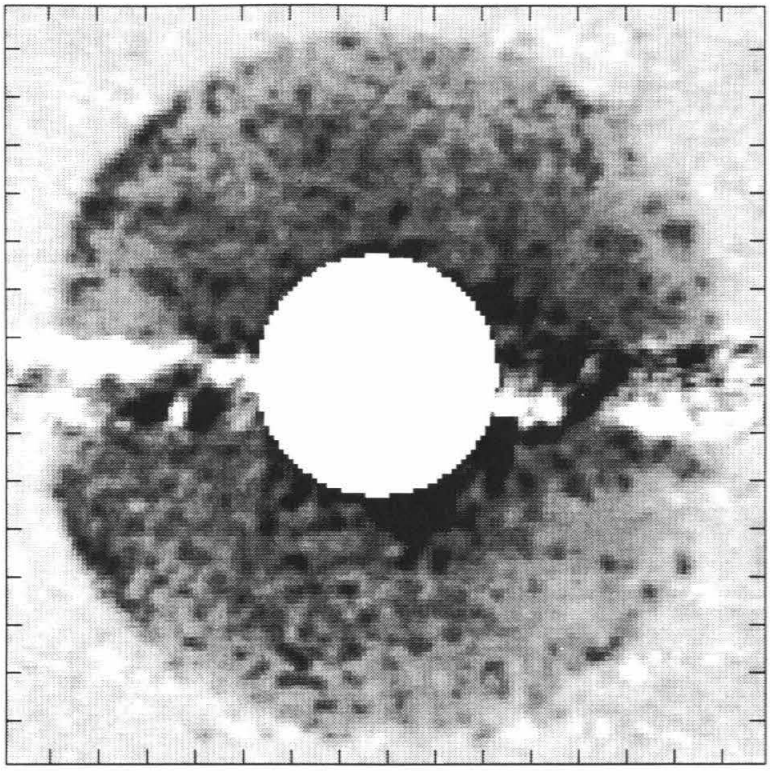

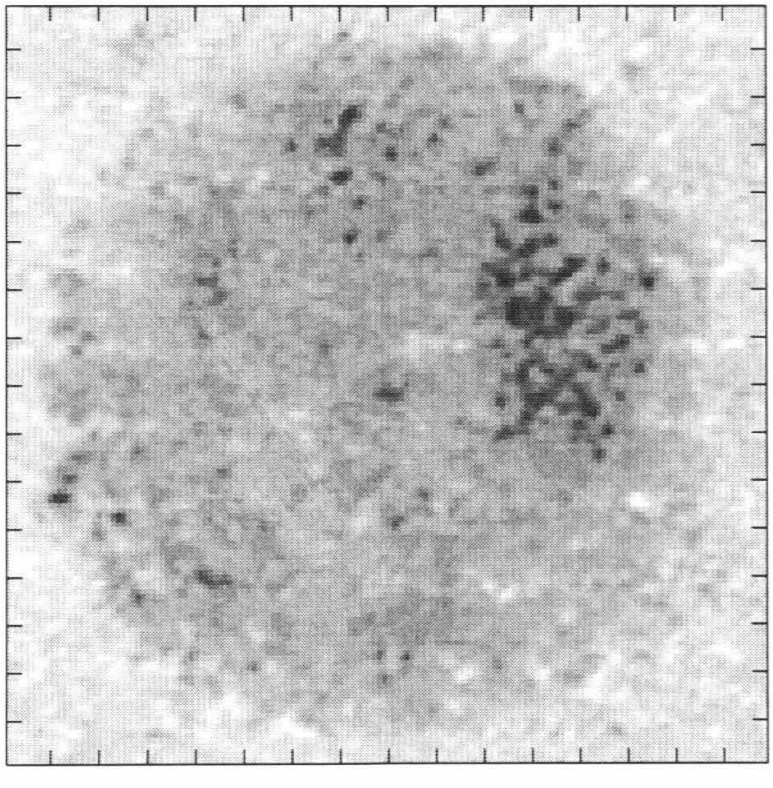

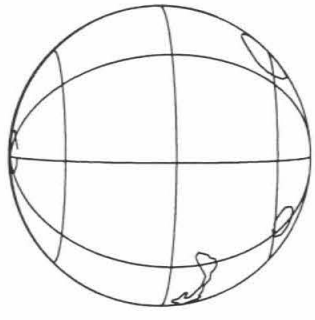

Date: 1/12/93

Snapshot: 6

β_o = 357.3

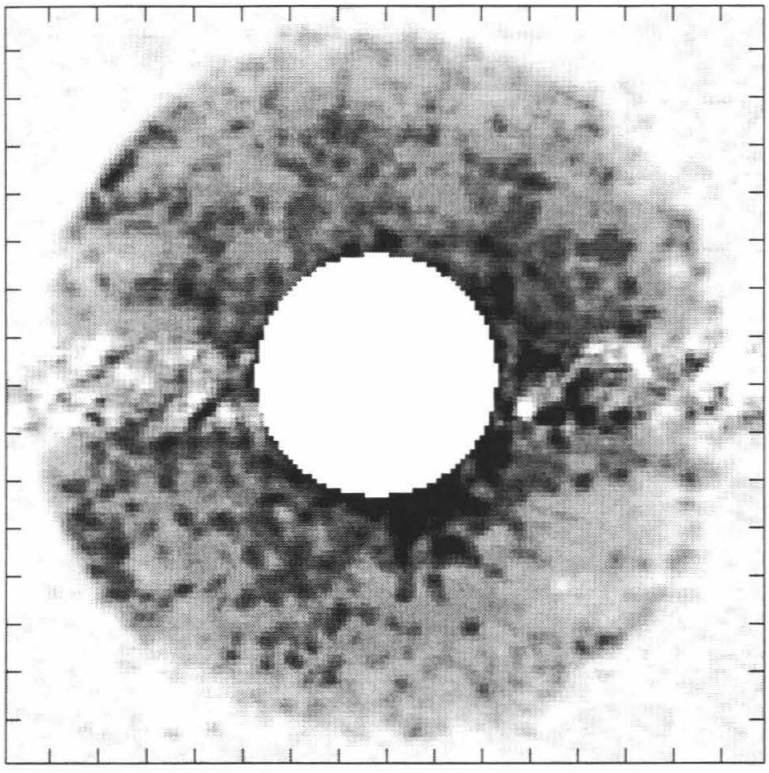

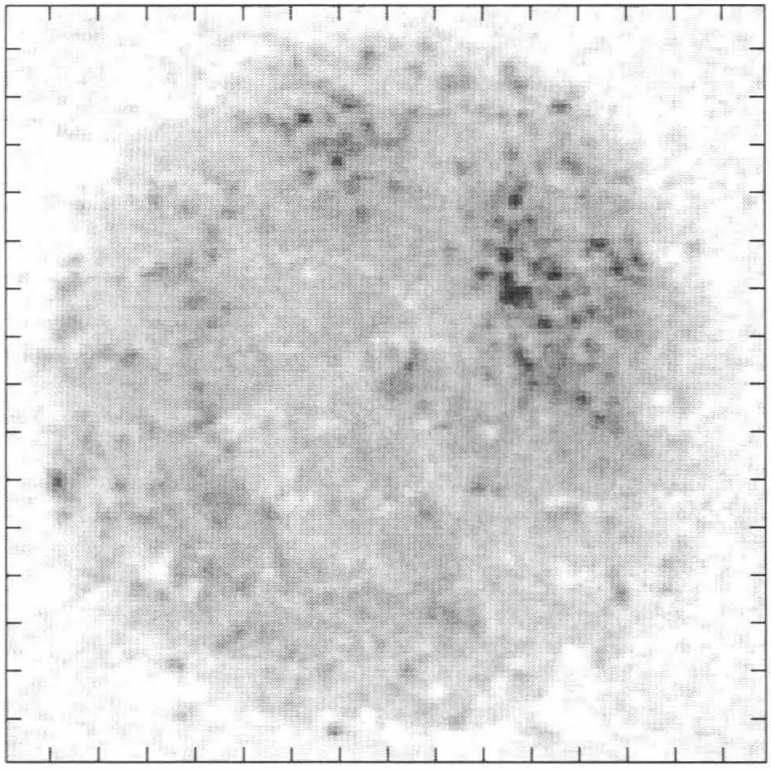

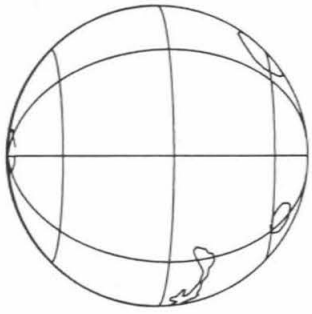

Date: 1/12/93

Snapshot: 7

$\beta_o = 0.1$

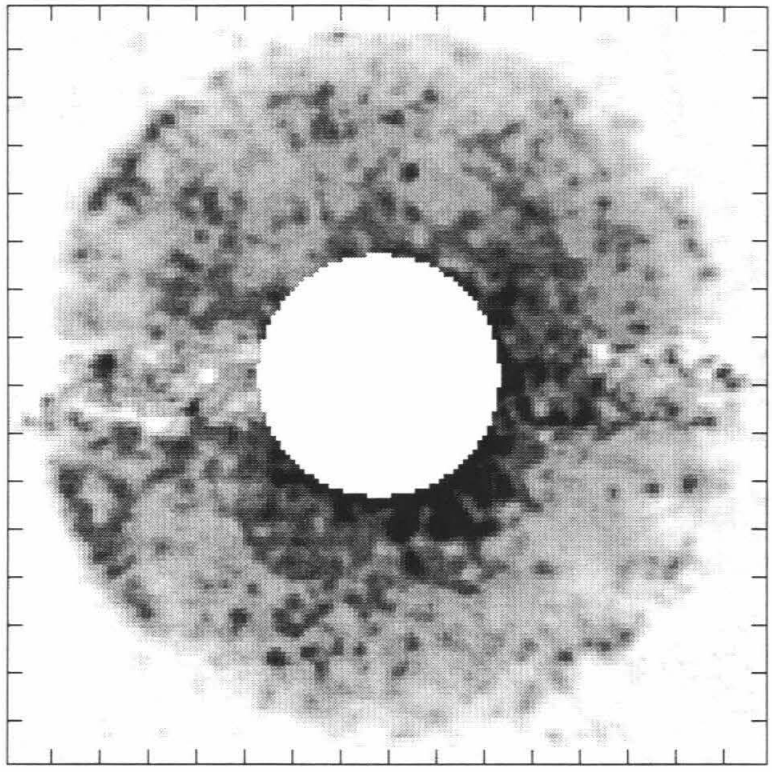

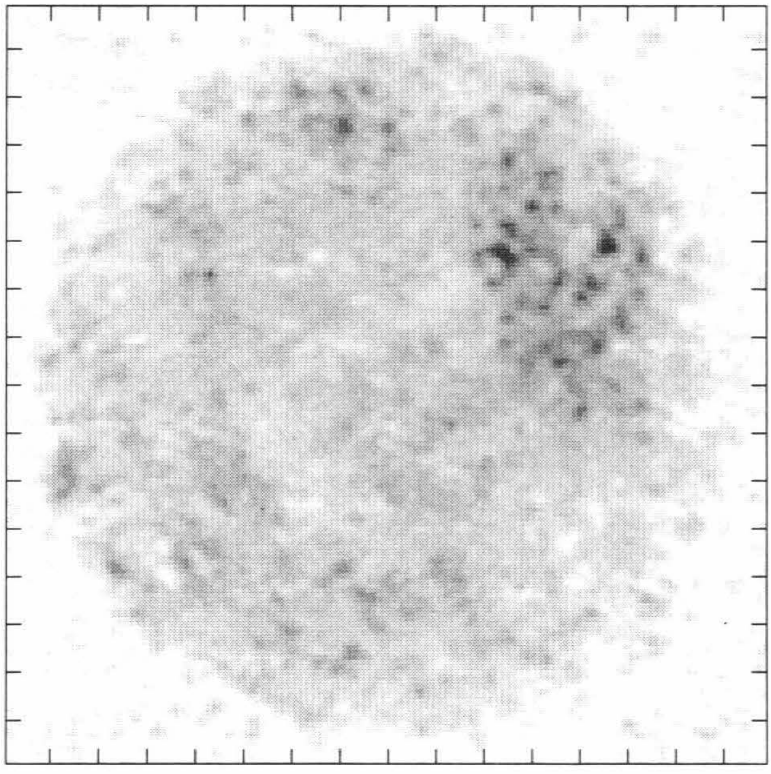

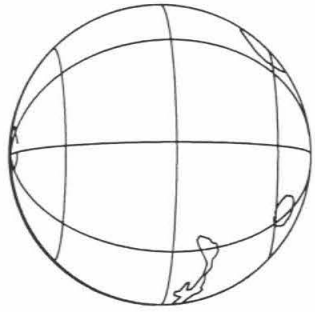

Date: 1/12/93

Snapshot: 8

$\beta_o = 5.0$

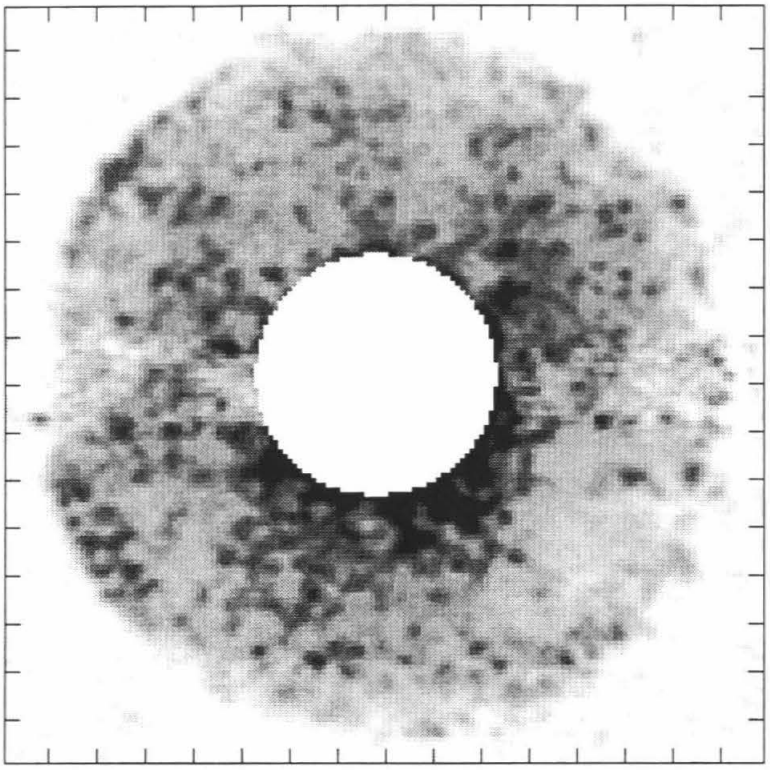

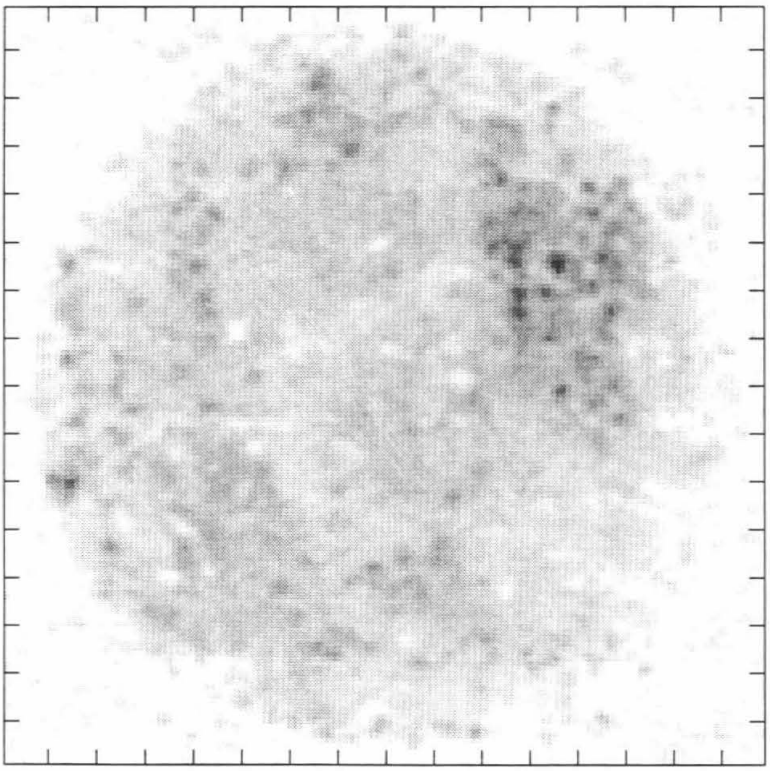

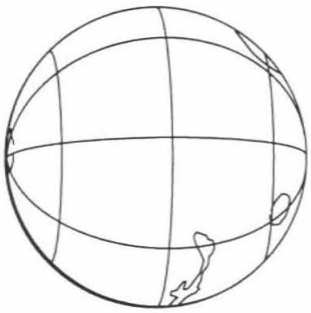

Date: 1/12/93

Snapshot: 9

$\beta_o = 7.6$

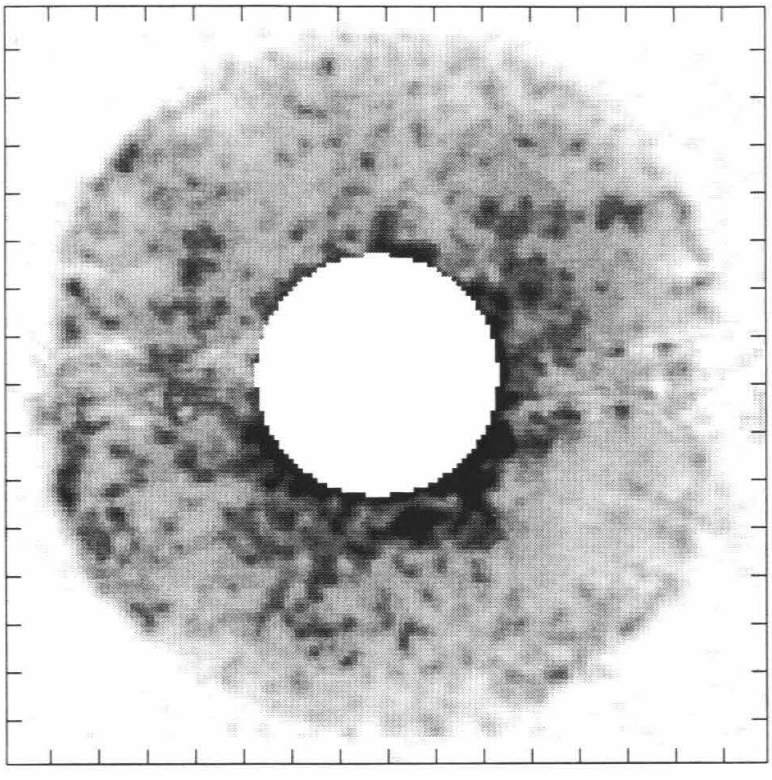

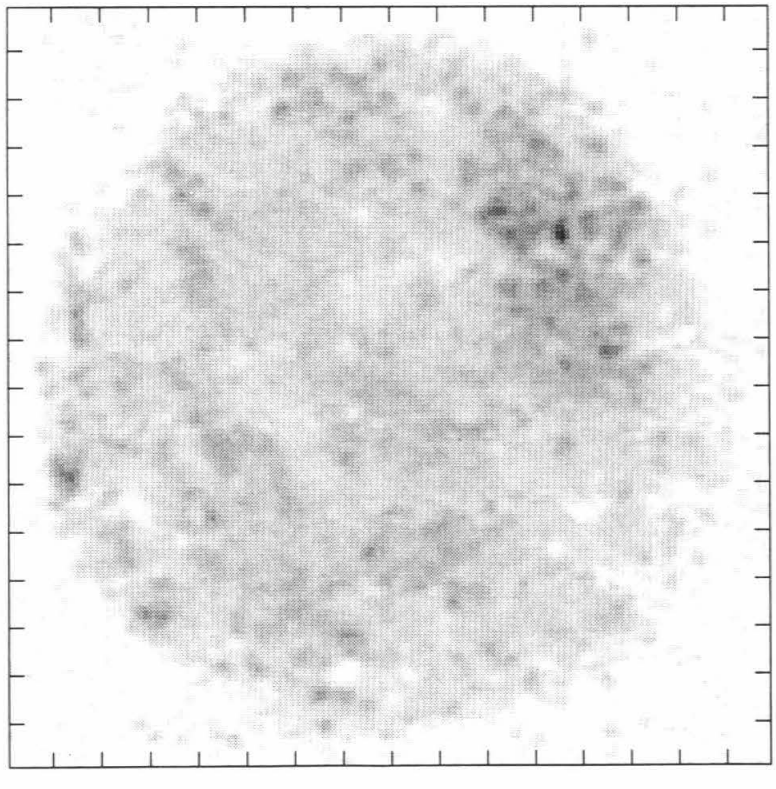

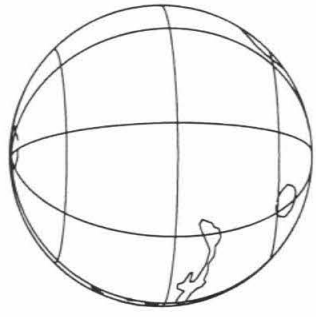

Date: 1/12/93

Snapshot: 10

β_o = 12.5

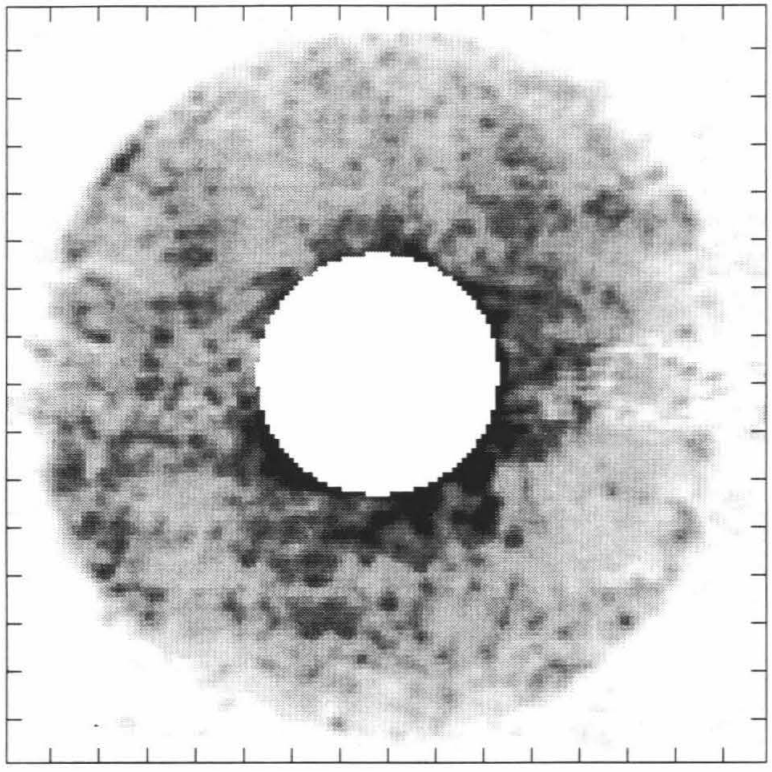

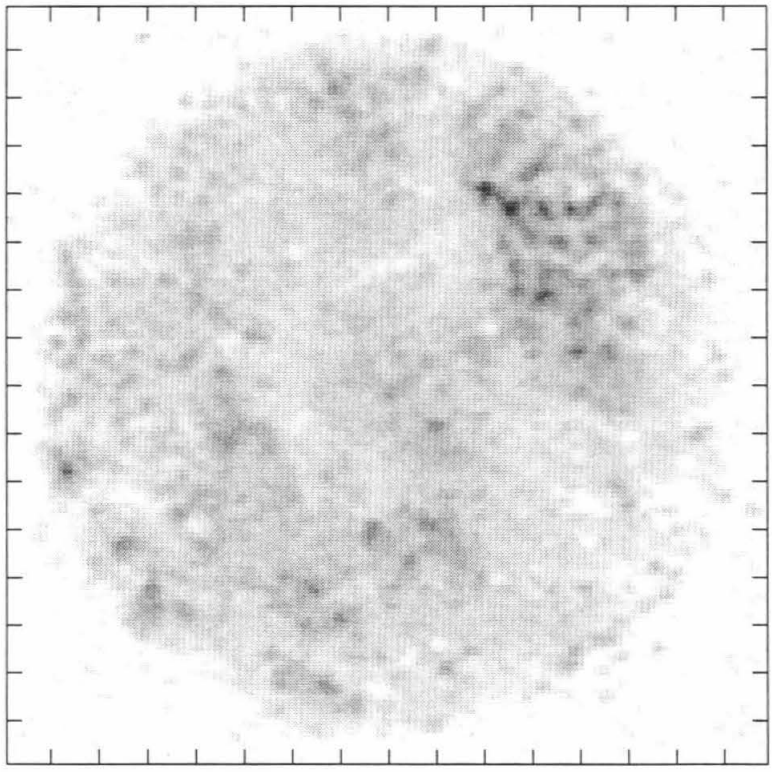

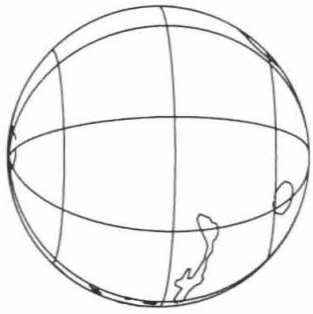

Date: 1/12/93

Snapshot: 11

β_o = 15.2

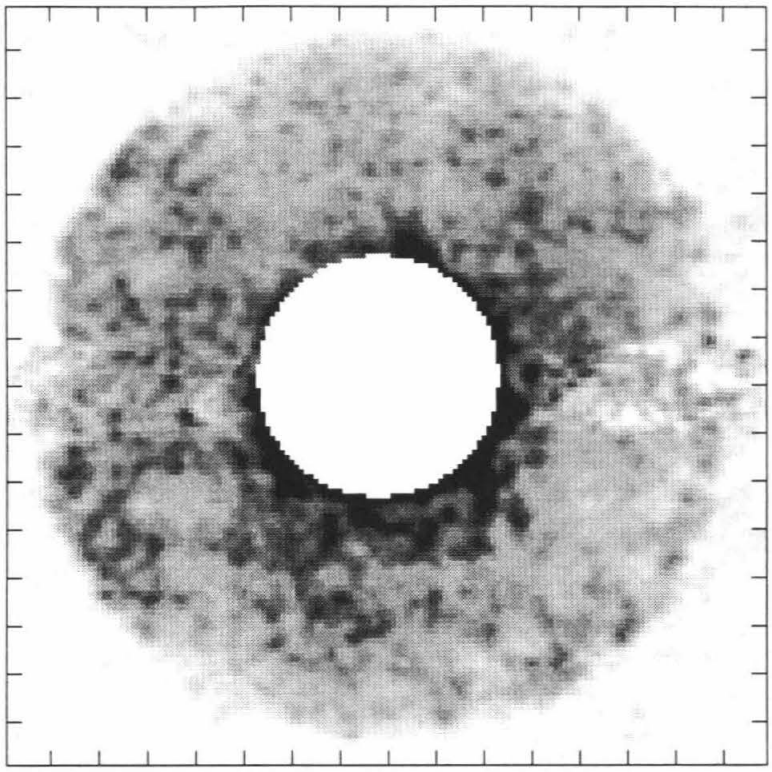

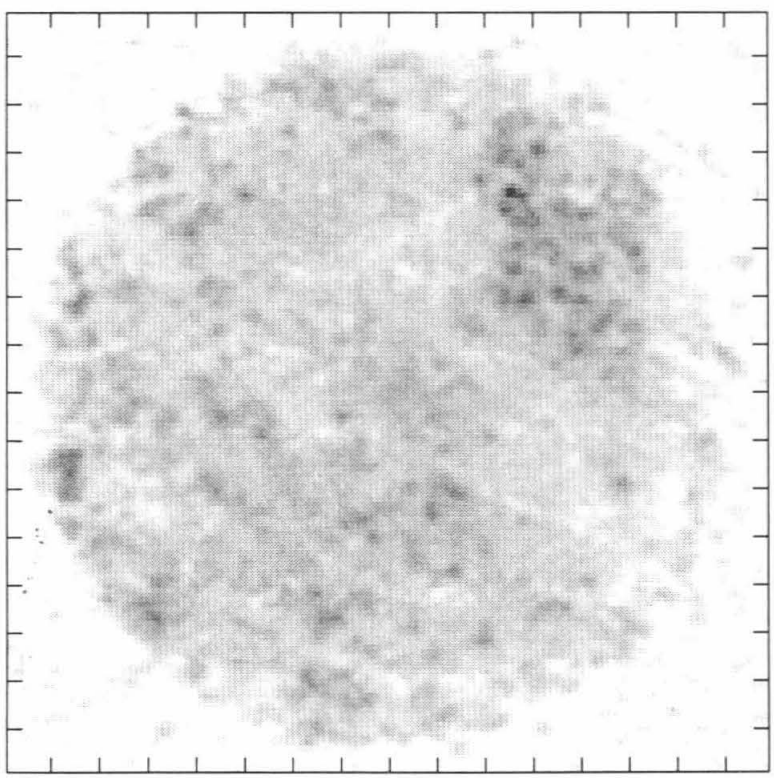

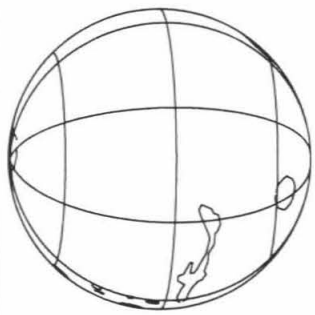

Date: 1/12/93

Snapshot: 12

β_o = 20.0

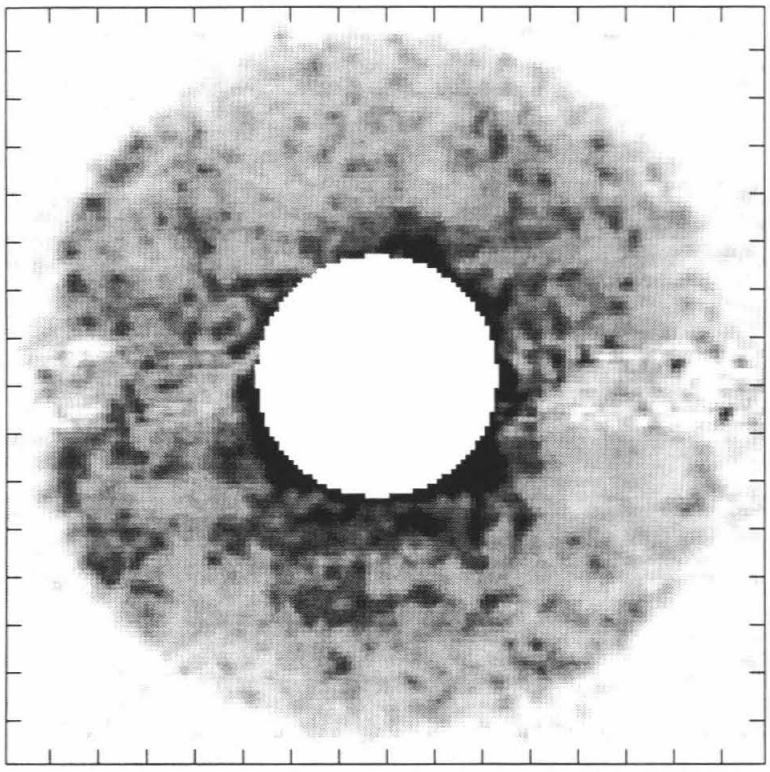

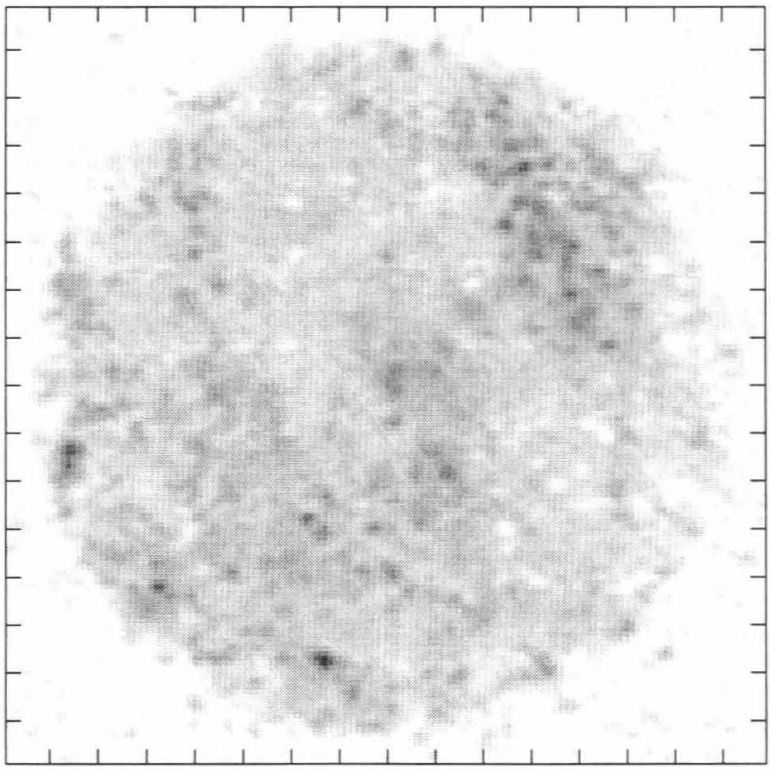

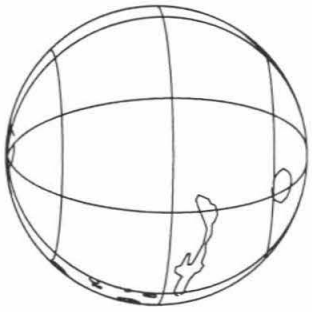

Date: 1/12/93

Snapshot: 13

β_o = 22.6

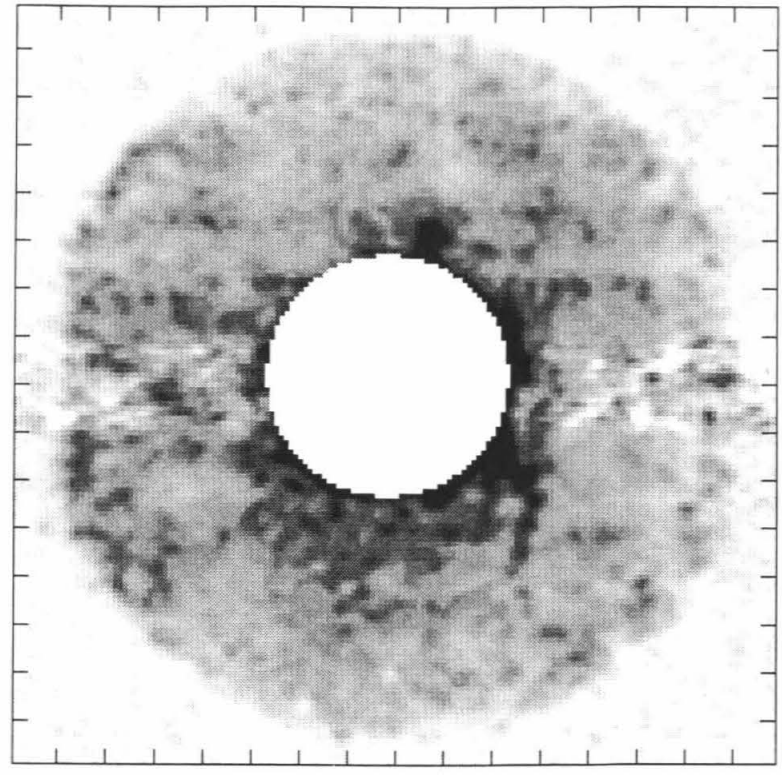

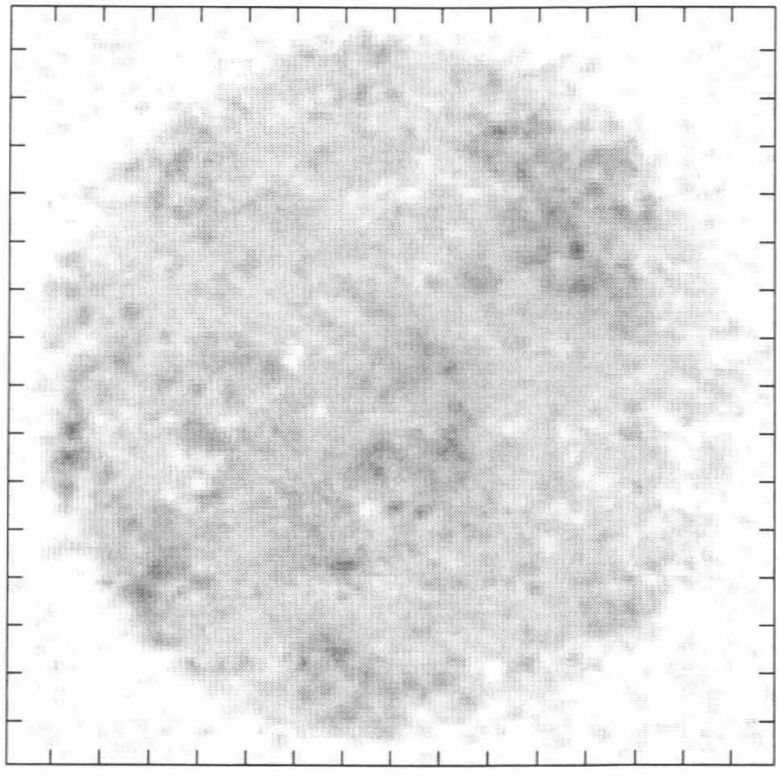

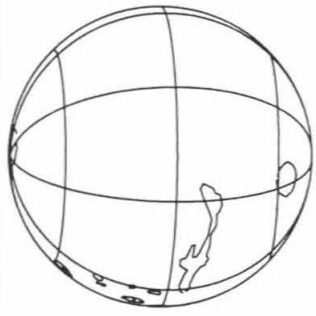

Date: 1/12/93

Snapshot: 14

β_o = 27.4

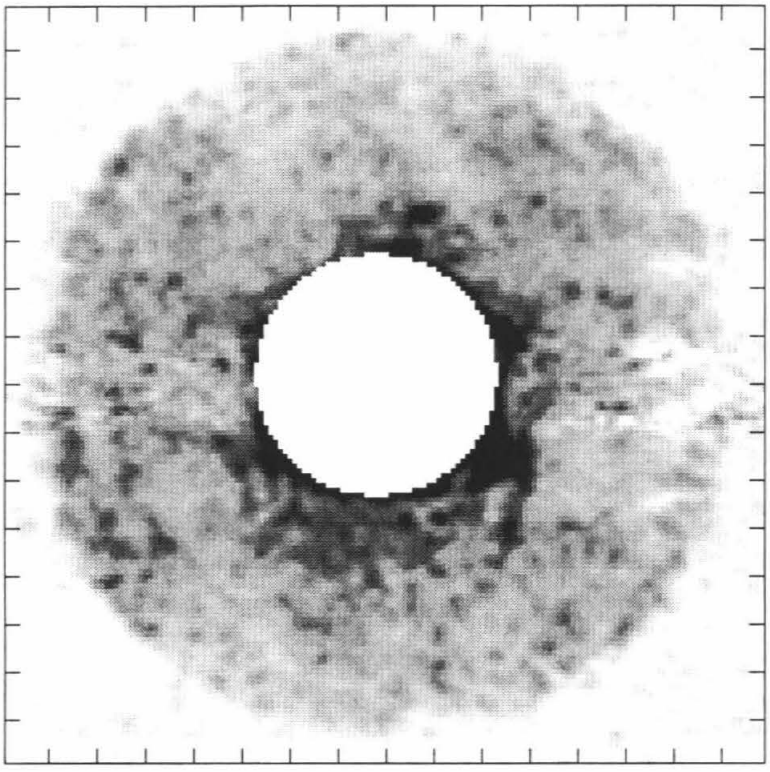

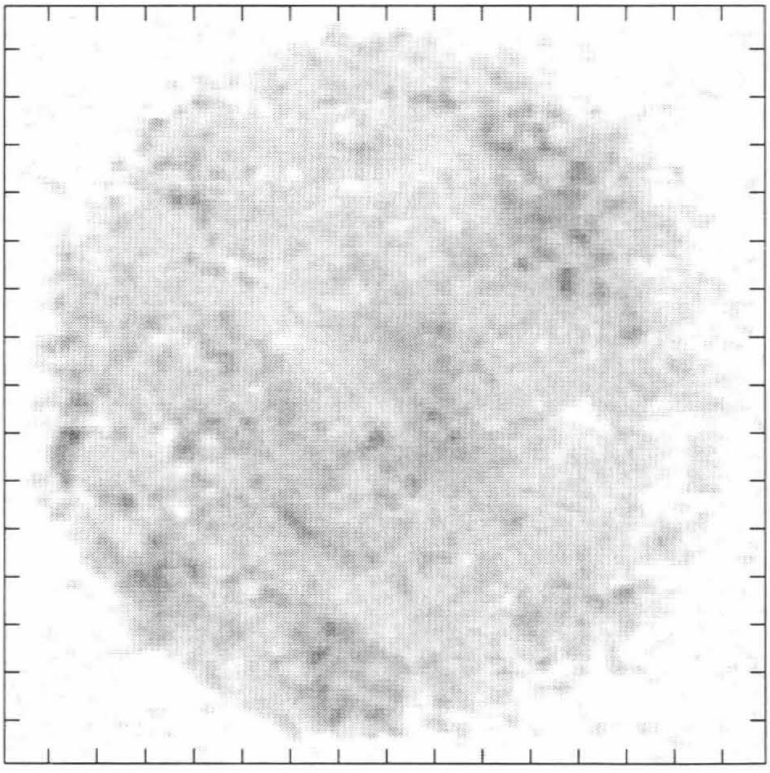

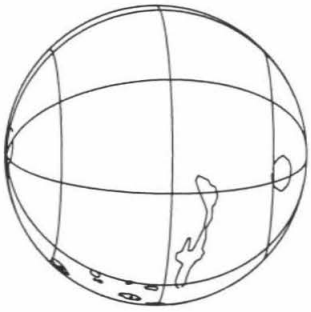

Date: 1/12/93

Snapshot: 15

β_o = 30.2

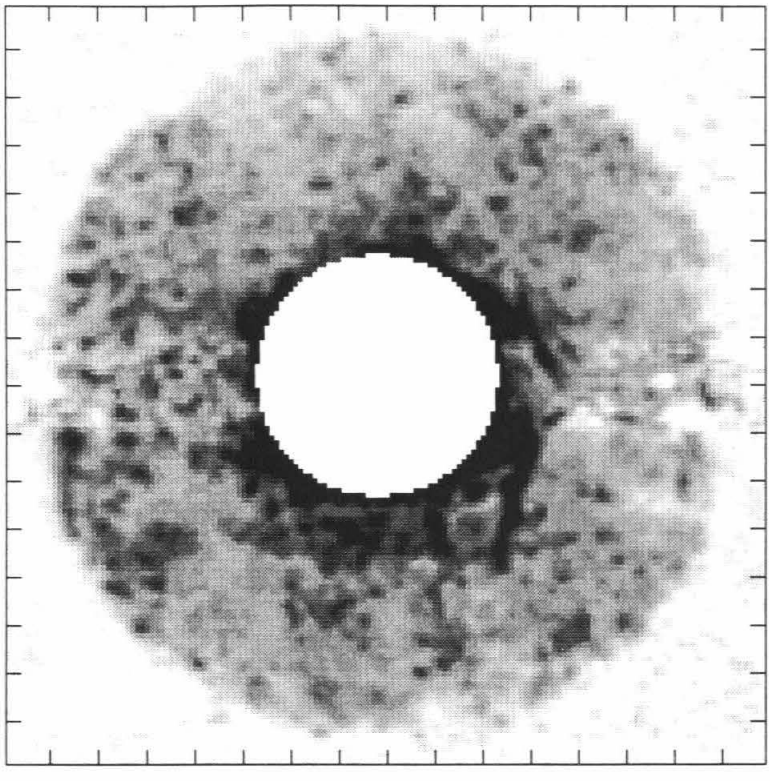

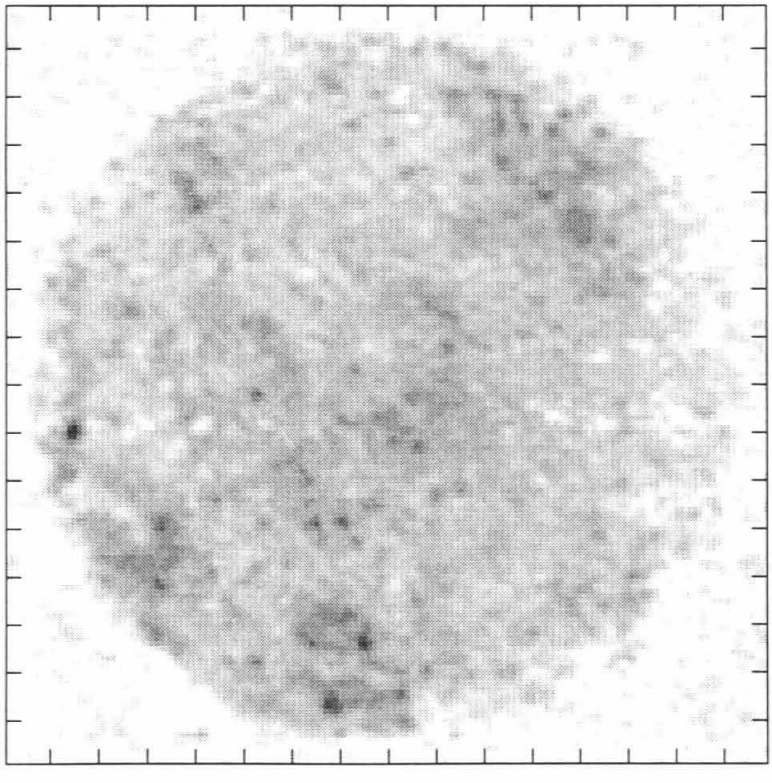

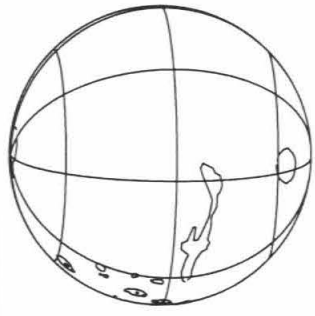

Date: 1/12/93

Snapshot: 16

β_o = 34.9

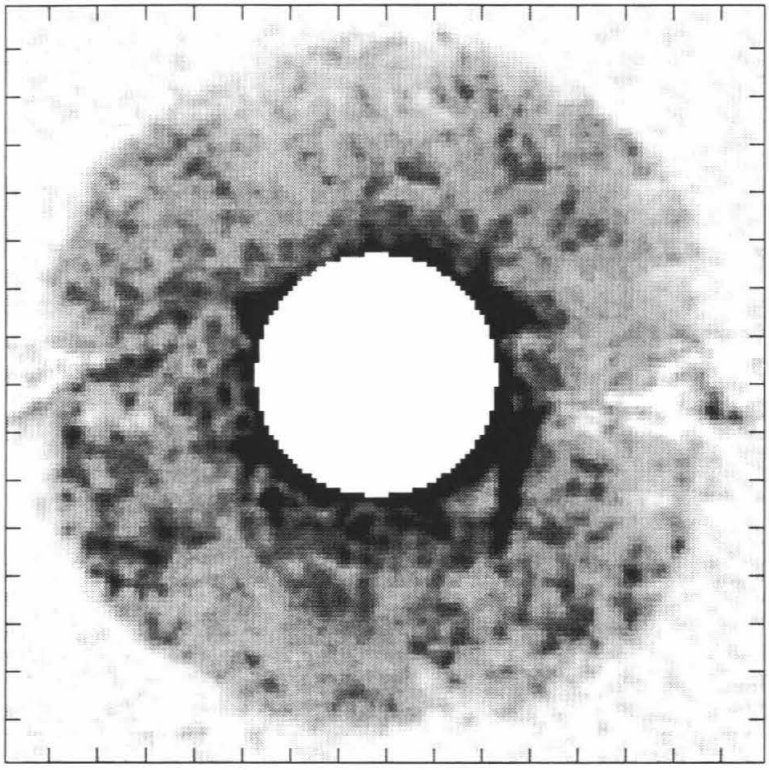

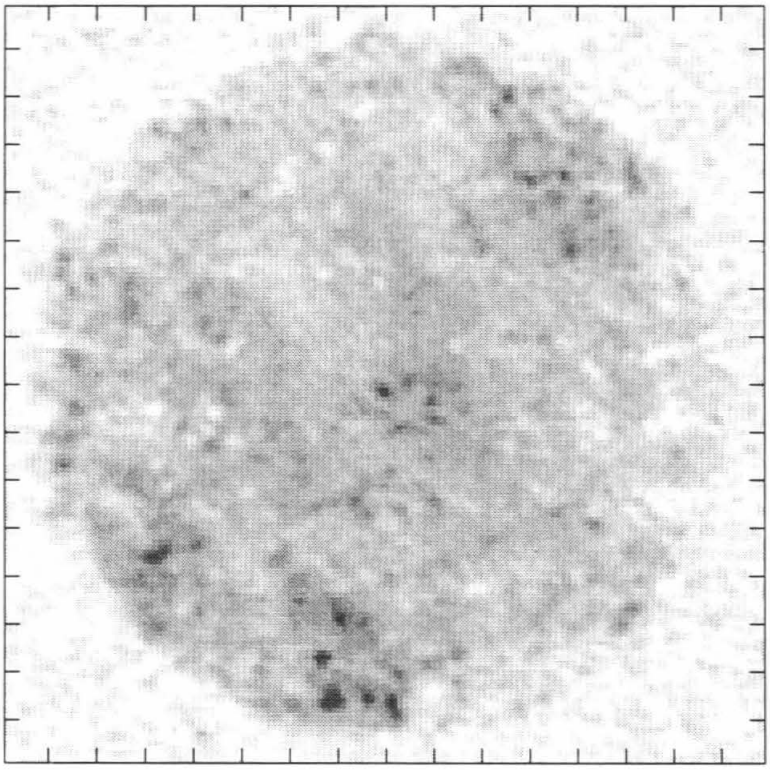

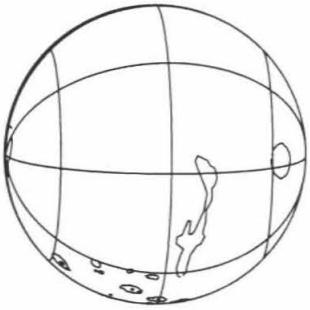

Date: 1/12/93

Snapshot: 17

β_o = 37.7

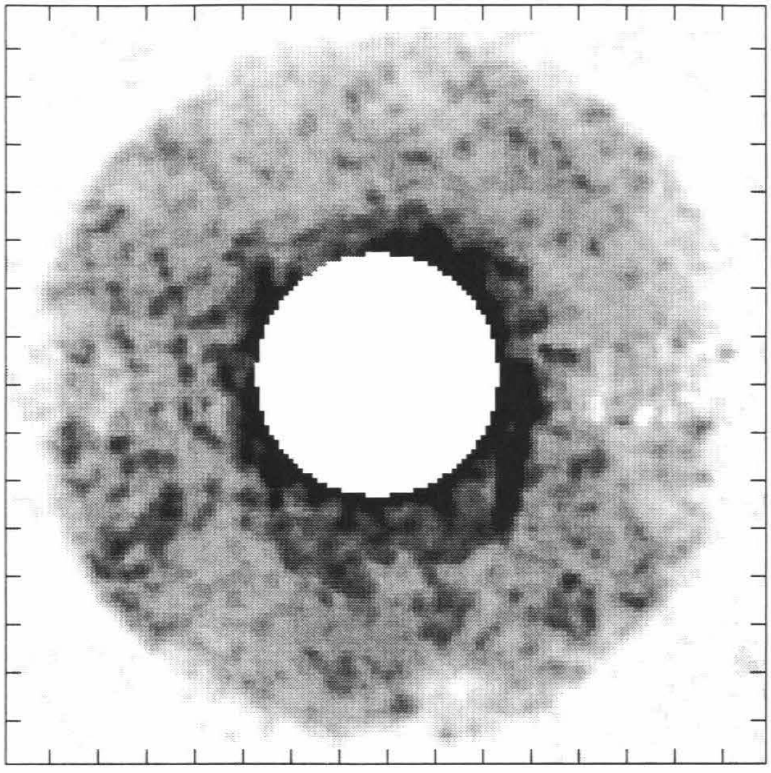

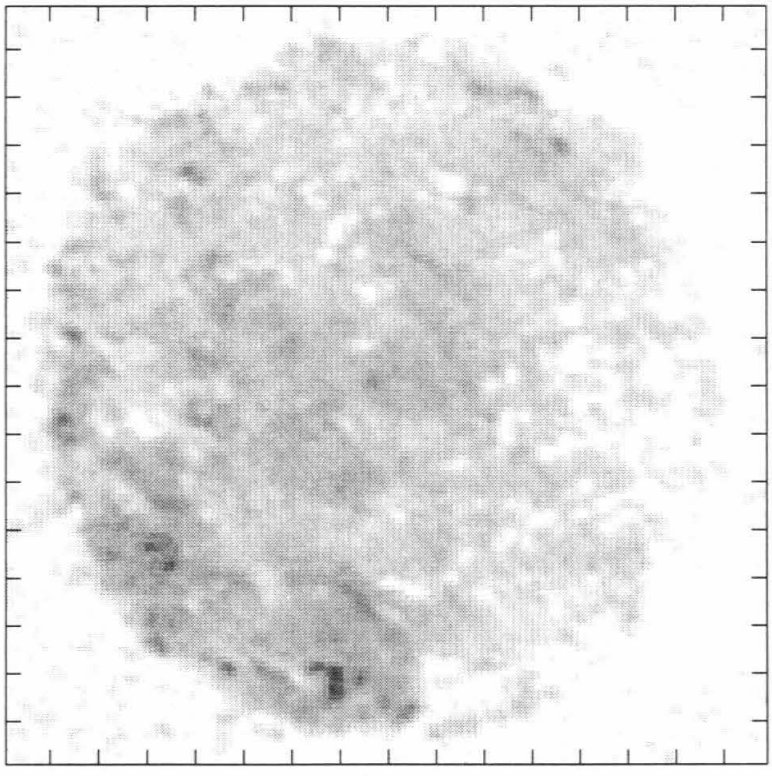

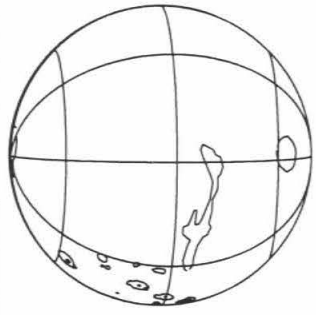

Date: 1/12/93

Snapshot: 18

β_o = 42.4

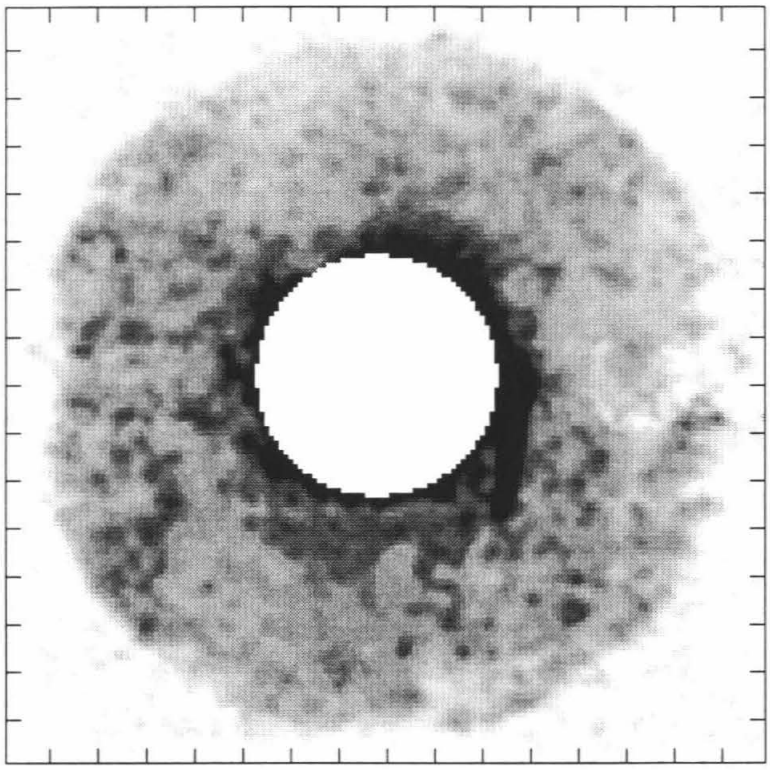

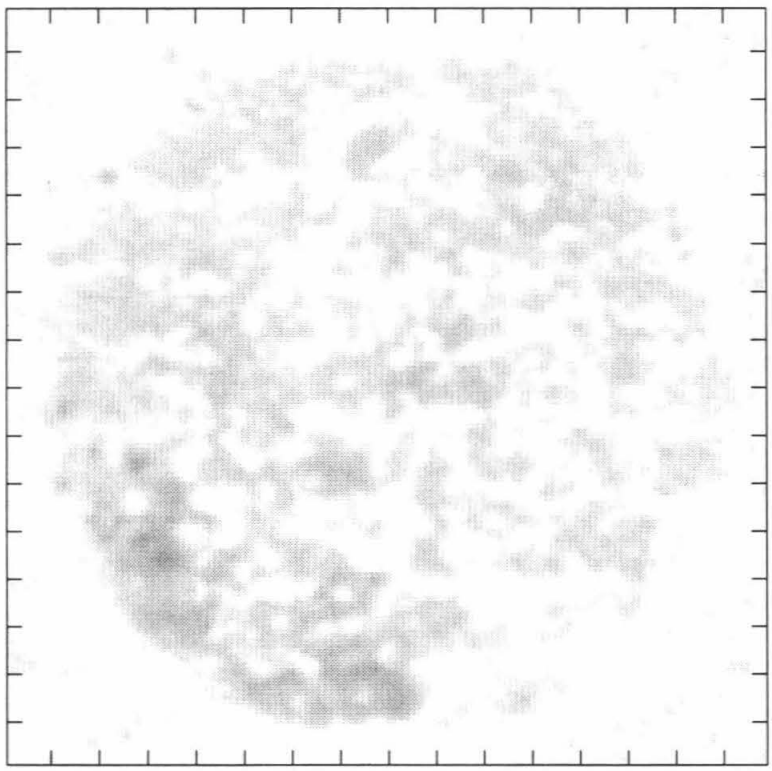

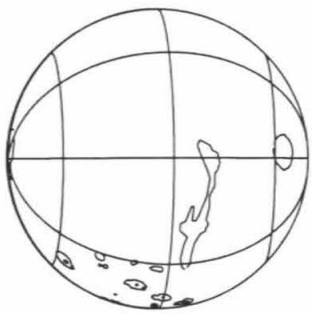

Date: 1/12/93

Snapshot: 19

β_o = 45.3

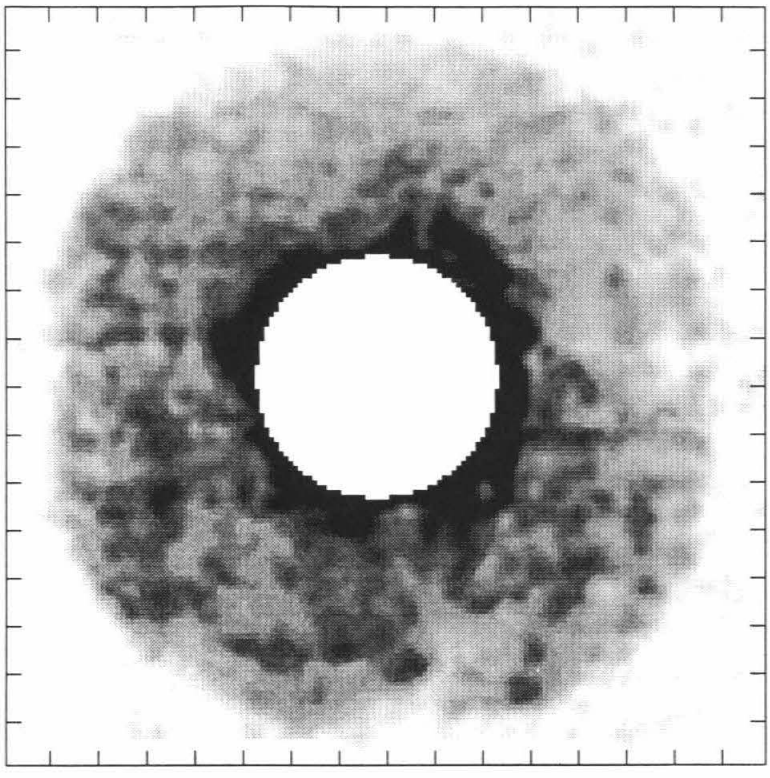

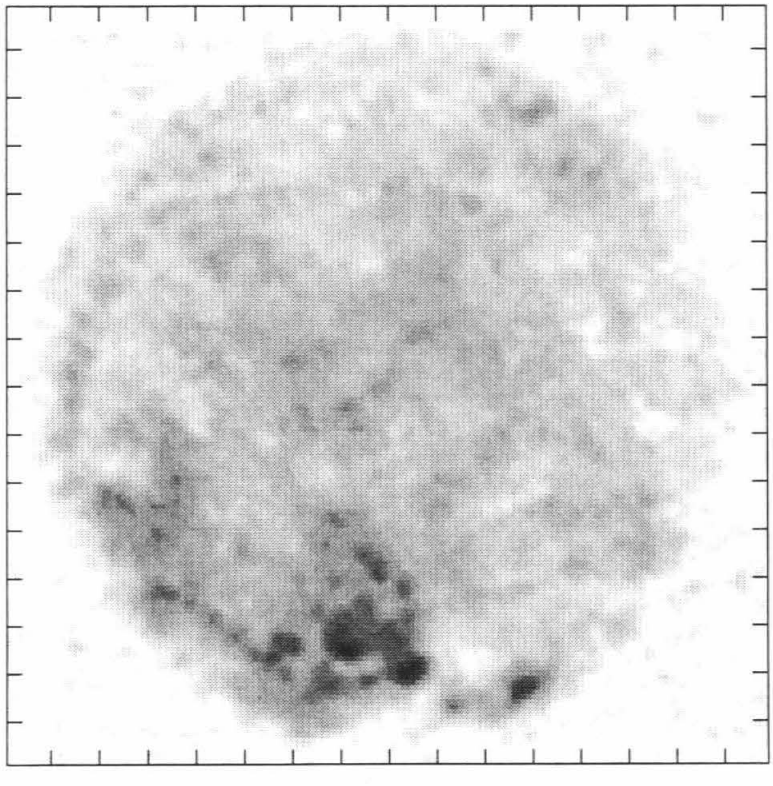

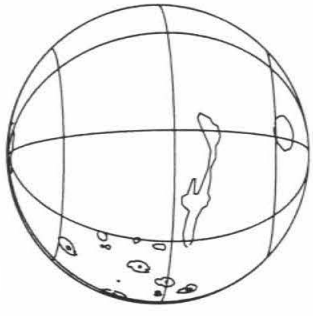

Date: 1/12/93

Snapshot: 20

β_o = 54.3

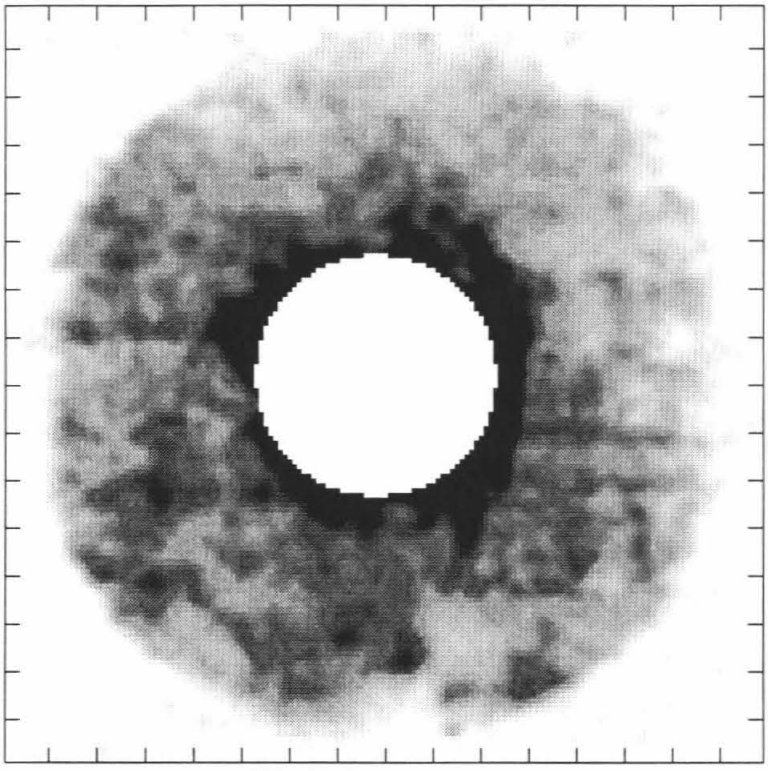

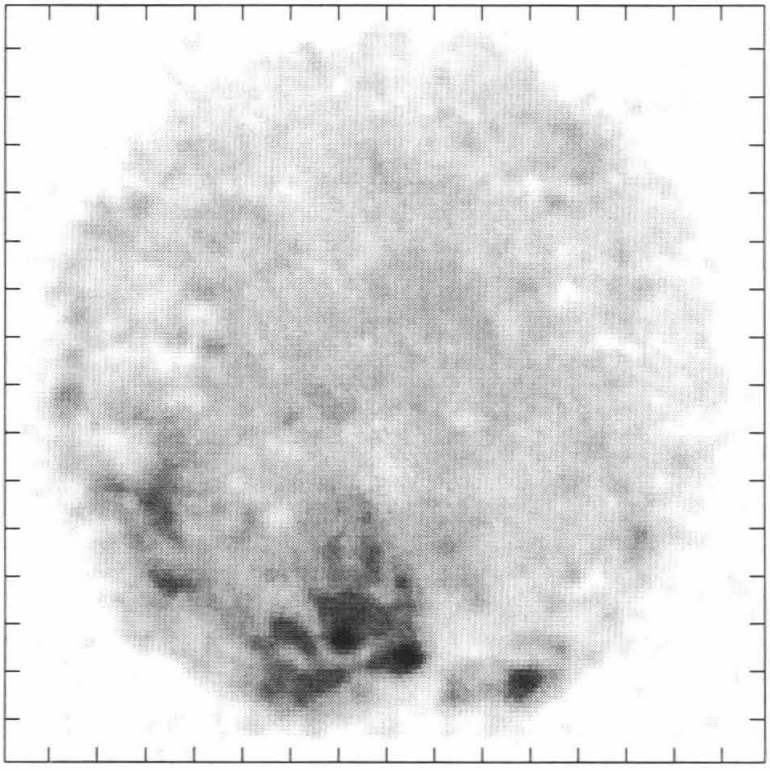

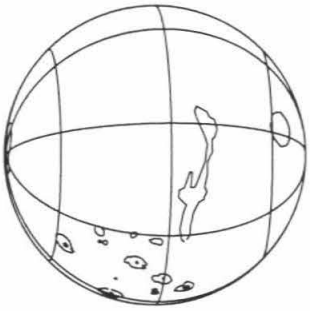

Date: 1/12/93

Snapshot: 21

β_o = 57.2

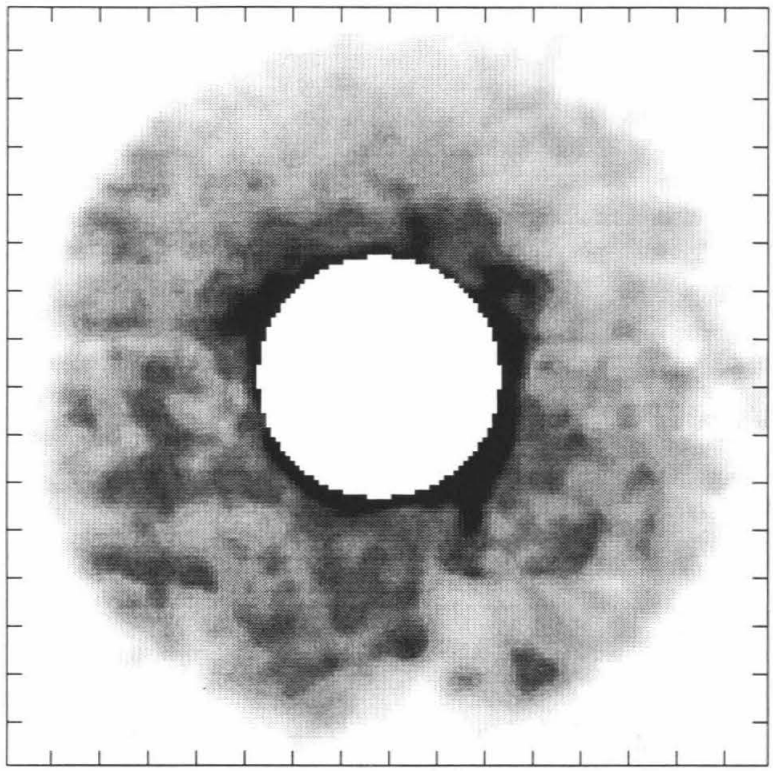

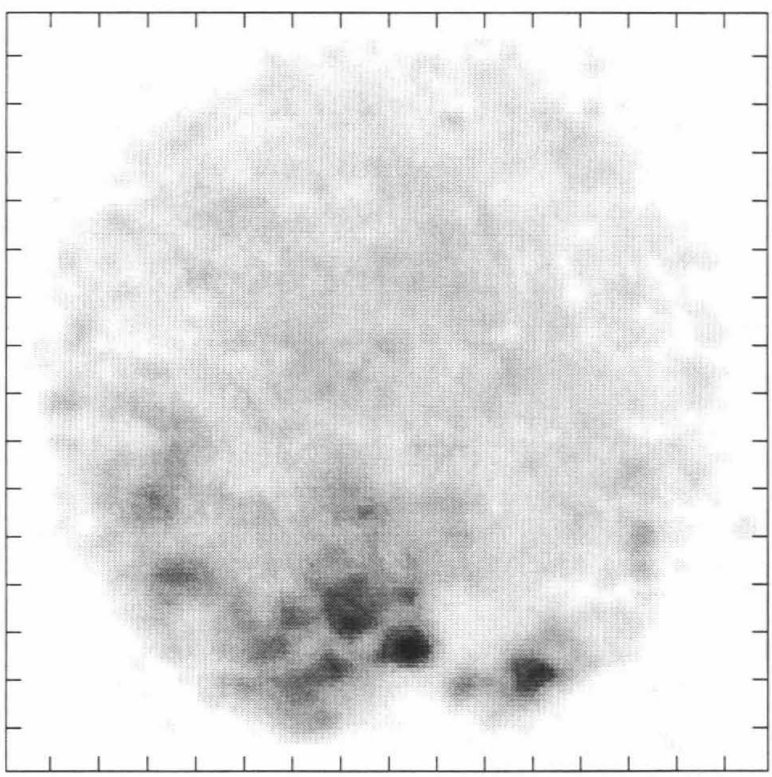

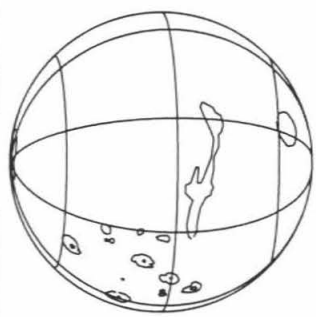

Date: 1/12/93

Snapshot: 22

β_o = 62.0

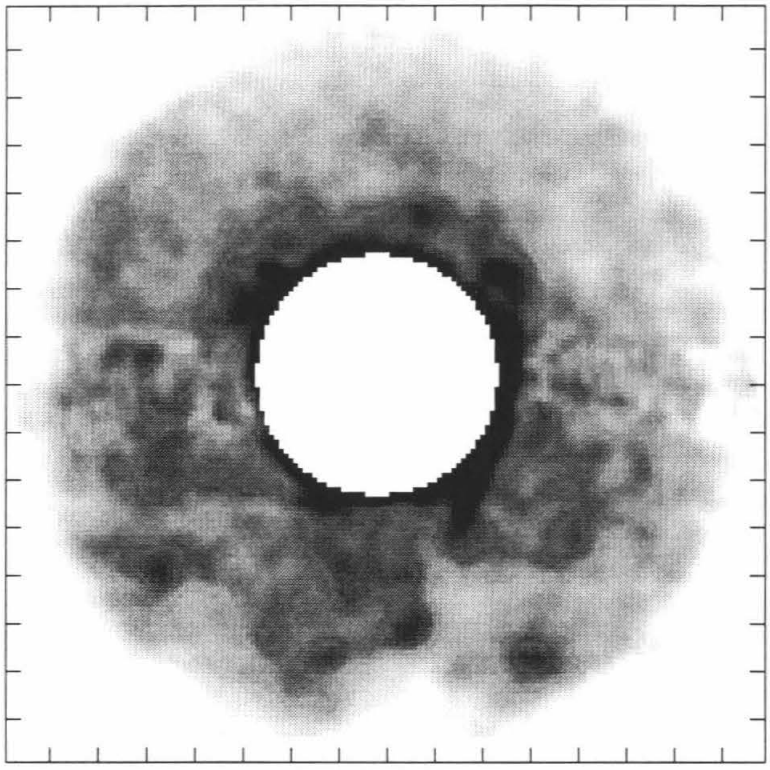

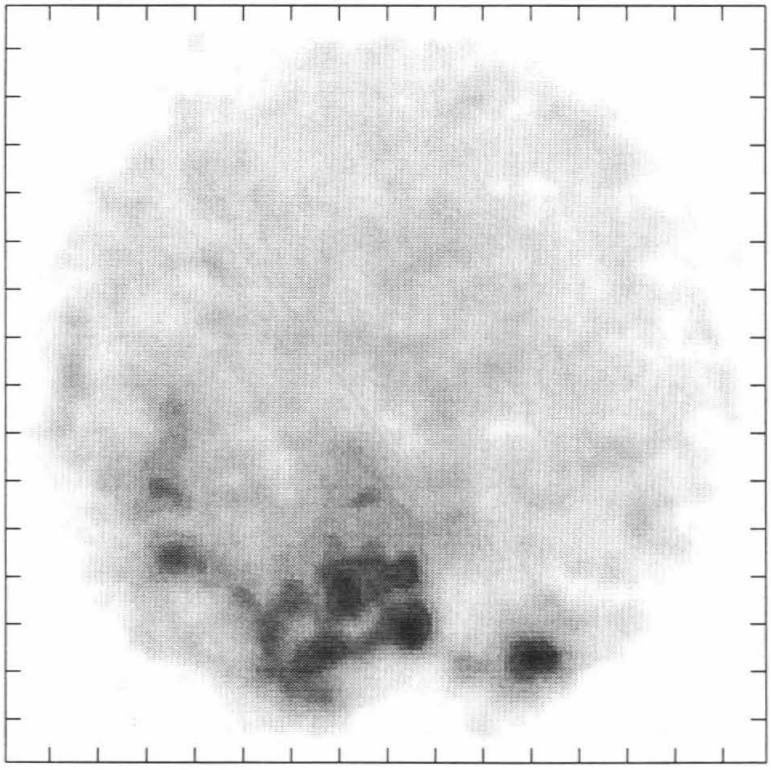

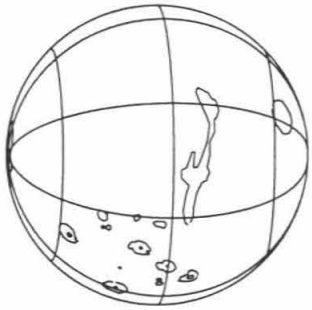

Date: 1/12/93

Snapshot: 23

β_o = 65.1

REFERENCES

Allen, C. W., *Astrophysical Quantities*, Oxford Press, New York, NY, 1964

Allen, M., M. Delitsky, W. Huntress, Y. Yung, W.-H. Ip, R. Schwenn, H. Rosenbauer, E. Shelley, H. Balsiger, and J. Geiss, Evidence for Methane and Ammonia in the Coma of Comet P/Halley, *Astron. Astrophys., 187*, 502–512, 1987

Arnold, J. R., Ice in the Lunar Polar Regions, *J. Geophys. Res., 84*, 5659–5668, 1979

Bar–Nun, A., J. Dror, E. Kochavi, and D. Laufer, Amorphous Water Ice and its Ability to Trap Gases, *Phys. Rev. B, 35*, 2427–2435, 1987

Blom, R. G., L. R. Schenck, and R. E. Alley, What are the Best Radar Wavelengths, Incidence Angles, and Polarizations for Discrimination Among Lava Flows and Sedimentary Rocks? A Statistical Approach, *IEEE Geosci. Remote Sens., 25*, 208–213, 1987

Boyce, J., and D. J. Stevenson, Impact Processes as an Explanation of the Spin Resonance State of Mercury, *Bull. Amer. Astron. Soc., 23*, 1197, 1991

Broadfoot, A. L., D. E. Shemansky, and S. Kumar, Mariner 10: Mercury Atmosphere, *Geophys. Res. Lett., 3*, 577–580, 1976

Brown, G. N., Jr., and W. T. Ziegler, Vapor Pressure and Heats of Vaporization and Sublimation of Liquids and Solids of Interest in Cryogenics Below 1–Atm Pressure, *Advances in Cryogenic Engineering, 25*, 662–670, 1980

Bryson, C. E., III, V. Cazcarra, and L. L. Levenson, Sublimation Rates and Vapor Pressures of H_2O, CO_2, N_2O, and Xe, *J. Chem. Engr. Data, 19*, 107–110, 1974

Butler, B. J., D. O. Muhleman, and M. A. Slade, Mercury: Full–Disk Radar Images and the Detection and Stability of Ice at the North Pole, *J. Geophys. Res., 98*, 15003–15023, 1993

Butler, B. J., D. O. Muhleman, and M. A. Slade, The Polar Regions of Mars: 3.5–cm Radar Images, in preparation, 1994

Campbell, B. A., and D. B. Campbell, Analysis of Volcanic Surface Morphology on Venus From Comparison of Arecibo, Magellan, and Terrestrial Airborne Radar Data, *J. Geophys. Res., 97*, 16293–16314, 1992

Campbell, B. A., R. E. Arvidson, and M. K. Shepard, Radar Polarization Properties of Volcanic and Playa Surfaces: Applications to Terrestrial Remote Sensing and Venus Data Interpretation, *J. Geophys. Res., 98*, 17099–17113, 1993

Campbell, D. B., J. F. Chandler, S. J. Ostro, G. H. Pettengill, and I. I. Shapiro, Galilean Satellites: 1976 Radar Results, *Icarus, 34*, 254–267, 1978

Campbell, M. J., and J. Ulrichs, Electrical Properties of Rocks and Their Significance for Lunar Radar Observations, *J. Geophys. Res., 74*, 5867–5881, 1969

Carpenter, R. L, and R. M. Goldstein, Radar Observations of Mercury, *Science, 142*, 381–382, 1963

Carr, M. H., Volcanism on Mars, *J. Geophys. Res., 78*, 4049–4062, 1973

Carr, M. H., Mars, in *The Geology of the Terrestrial Planets*, NASA SP–469, 1984

Carr, M. H., H. Masursky, and R. S. Saunders, A Generalized Geologic Map of Mars, *Icarus, 78*, 4031–4036, 1973

Carr, M. H., R. Greeley, K. R. Blasius, J. E. Guest, and J. B. Murray, Some Martian Volcanic Features as Viewed From Viking Orbiters, *J. Geophys. Res., 82*, 3985–4015, 1977

Ceplecha, Z., Influx of Interplanetary Bodies onto Earth, *Astron. Astrophys., 263*, 361–366, 1992

Chandrasekhar, S., *Radiative Transfer*, Dover, Mineola, NY, 1960

Chase, S. C., Jr., E. D. Miner, D. Morrison, G. Münch, and G. Neugebauer, Mariner 10 Infrared Radiometer Results: Temperatures and Thermal Properties of the Surface of Mercury, *Icarus, 28*, 565–578, 1976

Christensen, P. R., The Spatial Distribution of Rocks on Mars, *Icarus, 68*, 217–238, 1986

Chyba, C. F., The Cometary Contribution to the Oceans of Primitive Earth, *Nature, 330*, 632–635, 1987

Cintala, M. J., Impact-Induced Thermal Effects in the Lunar and Mercurian Regoliths, *J. Geophys. Res., 97*, 945–973, 1992

Clancy, T., A. Grossman, and D. Muhleman, A Cold, Dry, Cloudy, Dust–free Mars Atmosphere in the 1990's, *Bull. Am. Astron. Soc., 25*, 1060, 1993

Clark, B. G., and J. van Gorkom, Choice of Normalization for Spectral Line Observations, VLA Test Memorandum 131, 1981

Clark, P. E., R. F. Jurgens, T. W. Thompson, L. Robinett, F. Chan, S. Brokl, C. Franck, and E. Stone, Mercury: New Results from Dual Polarization Measurements at X-Band, *Proc. Lunar Plan. Sci. Conf., XVII*, 135–136, 1986

Clark, P. E., M. A. Leake, and R. F. Jurgens, Goldstone Radar Observations of Mercury, in *Mercury*, ed. F. Vilas, C. R. Chapman, and M. S. Matthews, University of Arizona Press, Tucson, AZ, 1988

Cochran, A. L., and D. G. Schleichar, Observational Constraints on the Lifetime of Cometary H_2O, *Icarus, 105*, 235–253, 1993

Cornwell, T., and E. B. Fomalont, Self-Calibration, in *Synthesis Imaging in Radio Astronomy*, ed. R. A. Perley, F. A. Schwab, and A. H. Bridle, Astronomical Society of the Pacific Conference Series, San Francisco, CA, 1989

Crown, D. A., K. H. Price, and R. Greeley, Geologic Evolution of the East Rim of the Hellas Basin, Mars, *Icarus, 100*, 1–25, 1992

Crown, D. A., and R. Greeley, Volcanic Geology of Hadriaca Patera and the Eastern Hellas Region of Mars, *J. Geophys. Res., 98*, 3431–3451, 1993

Cutts, J. A., and R. S. U. Smith, Eolian Deposits and Dunes on Mars, *J. Geophys. Res., 78*, 4139–4154, 1973

Davies, M. E., S. E. Dwornik, D. E. Gault, and R. G. Strom, Atlas of Mercury, NASA SP-423, 1978

Doake, C. S. M., and E. W. Wolff, Flow Law for Ice in Polar Ice Sheets, *Nature, 314*, 255–257, 1985

Downs, G. S., P. E. Reichley, and R. R. Green, Radar Measurements of Martian Topography and Surface Properties: The 1971 and 1973 Oppositions, *Icarus, 18*, 8–21, 1975

Eluszkiewicz, J., On the Microphysical State of the Martian Seasonal Caps, *Icarus, 103*, 43–48, 1993

Epstein, E. E., and B. H. Andrew, Mercury: Thermal Emission at Radio Wavelengths, *Icarus, 62*, 448–457, 1985

Estermann, I., Gases at Low Densities, in *Thermodynamics and Physics of Matter*, Vol. 1, *High Speed Aerodynamics and Jet Propulsion*, ed. F. D. Rossini, Princeton University Press, 1955

Evans, J. V., R. A. Brockelman, J. C. Henry, G. M. Hyde, L. G. Kraft, W. A. Reid, and W. W. Smith, Radio Echo Observations of Venus and Mercury at 23 cm Wavelength, *Astron. J., 70*, 486–501, 1965

Evans, J. V., R. P. Ingalls, L. P. Rainville, and R. R. Silva, Radar Observations of Venus at 3.8-cm Wavelength, *Astron. J., 71*, 902–915, 1966

Evans, J. V., and T. Hagfors, *Radar Astronomy*, McGraw Hill, New York, New York, 1968

Evans, S., Dielectric Properties of Ice and Snow—A Review, *J. Glaciol., 5*, 773–792, 1965

Farmer, C. B., D. W. Davies, and D. D. LaPorte, Mars: Northern Summer Ice Cap–Water Vapor Observations from Viking 2, *Science, 194*, 1339–1341, 1976

Fielding, E. J., W. J. Knox, Jr., and A. L. Bloom, SIR–B Radar Imagery of Volcanic Deposits in the Andes, *IEEE Geosci. Remote Sens., 24*, 582–589, 1986

Francis, P. W., and C. A. Wood, Absence of Silicic Volcanism on Mars: Implications for Crustal Composition and Volatile Abundance, *J. Geophys. Res., 87*, 9881–9889, 1982

Gaddis, L., P. Mouginis-Mark, R. Singer, and V. Kaupp, Geologic Analyses of Shuttle Imaging Radar (SIR-B) Data of Kilauea Volcano, Hawaii, *Geol. Soc. Am. Bull., 101*, 317–332, 1989

Gaddis, L. R., Lava Flow Characterization at Pisgah Volcanic Field, California, With Multiparameter Imaging Radar, *Geol. Soc. Am. Bull., 104*, 695–703, 1992

Gault, D. E., F. Hörz, and J. B. Hartung, Effects of Microcratering on the Lunar Surface, *Proc. Lunar Plan. Sci. Conf., III*, 2713–2734, 1972

Gault, D. E., F. Hörz, D. E. Brownlee, and J. B. Hartung, Mixing of the Lunar Regolith, *Proc. Lunar Plan. Sci. Conf., V*, 2365–2386, 1974

Gibson, E. K. Jr, Production of Simple Molecules on the Surface of Mercury, *Phys. Earth Plan. Interiors, 15*, 303–312, 1977

Glen, J. W., The Creep of Polycrystalline Ice, *Proc. R. Soc. London A, 228*, 519–538

Goldstein, R. M., and W. F. Gillmore, Radar Observations of Mars, *Science, 141*, 1171–1172, 1963

Goldstein, R. M., Venus Characteristics by Earth–Based Radar, *Astron. J., 69*, 12–18, 1964

Goldstein, R. M., Mercury: Surface Features Observed during Radar Studies, *Science, 168*, 467–469, 1970

Goldstein, R. M., Radar Observations of Mercury, *Astron. J., 76*, 1152–1154, 1971

Goldstein, R. M., and R. R. Green, Ganymede: Radar Surface Characteristics, *Science, 207*, 179–180, 1980

Goodstein, B. E., S. T. Suess, and R. J. Walker, Mercury: Magnetospheric Processes and the Atmospheric Supply and Loss Rates, *J. Geophys. Res., 86*, 5485–5499, 1981

Greeley, R., and P. D. Spudis, Volcanism on Mars, *Rev. Geophys. Space Phys., 19*, 13–41, 1981

Greeley, R., Release of Juvenile Water on Mars: Estimated Amounts and Timing Associated with Volcanism, *Science, 236*, 1653–1654, 1987

Greeley, R., and J. E. Guest, Geologic Map of the Eastern Equatorial Region of Mars, *USGS map I–1802–B*, 1987

Greeley, R., and D. A. Crown, Volcanic Geology of Tyrrhena Patera, Mars, *J. Geophys. Res., 95*, 7133–7149, 1990

Hapke, B., Coherent Backscatter and the Radar Characteristics of Outer Planet Satellites, *Icarus, 88*, 407–417, 1990

Hapke, B., and D. Blewitt, Coherent Backscatter Model for the Unusual Radar Reflectivity of Icy Satellites, *Nature, 352*, 46–47, 1991

Harmon, J. K., and S. J. Ostro, Mars: Dual–Polarization Radar Observations with Extended Coverage, *Icarus, 62*, 110–128, 1985

Harmon, J. K., D. B. Campbell, D. L. Bindschadler, J. W. Head, and I. I. Shapiro, Radar Altimetry of Mercury: A Preliminary Analysis, *J. Geophys. Res., 91*, 385–401, 1986

Harmon, J. K., M. P. Sulzer, P. J. Perillat, and J. F. Chandler, Mars Radar Mapping: Strong Backscatter from the Elysium Basin and Outflow Channel, *Icarus, 95*, 153–156, 1992a

Harmon, J. K., M. A. Slade, and R. S. Hudson, Mars Radar Scattering: Arecibo/Goldstone Results at 12.6-cm and 3.5-cm Wavelengths, *Icarus, 98*, 240–253, 1992*b*

Harmon, J. K., and M. A. Slade, Radar Mapping of Mercury: Full–Disk Delay–Doppler Images, *Science, 258*, 640–643, 1992

Harmon, J. K., M. A. Slade, R. A. Velez, A. Crespo, M. J. Dryer, and J. M. Johnson, Radar Mapping of Mercury's Polar Anomalies, *Nature, 369*, 213–215, 1994

Harris, S. A., The Aureole of Olympus Mons, *J. Geophys. Res., 82*, 3099–3107, 1977

Hobbs, P. V., *Ice Physics*, pp. 44–60, Clarendon Press, Oxford, 1974

Högbom, J. A., Aperture Synthesis with a Non-Regular Distribution of Interferometer Baselines, *Astron. Astrophys. Suppl., 15*, 417–426, 1974

Hood, L. L., and G. Schubert, Inhibition of Solar Wind Impingement on Mercury by Planetary Induction Currents, *J. Geophys. Res., 84*, 2641–2647, 1979

Hudson, R. S., and S. J. Ostro, Doppler Radar Imaging of Spherical Planetary

Surfaces, *J. Geophys. Res., 95*, 10947–10963, 1990

Hughes, H. G., F. M. App, and T. R. McGetchin, Global Seismic Effects of Basin-Forming Impacts, *Phys. Earth Planet. Interiors, 15*, 251–263, 1977

Hunten, D. M., T. H. Morgan, and D. E. Shemansky, The Mercury Atmosphere, in *Mercury*, ed. F. Vilas, C. R. Chapman, and M. S. Matthews, University of Arizona Press, Tucson, AZ, 1988

Ingalls, R. P., and L. P. Rainville, Radar Measurements of Mercury: Topography and Scattering Characteristics at 3.8 cm, *Astron. J., 77*, 185–190, 1972

Ingersoll, A. P., T. Svitek, and B. C. Murray, Stability of Polar Frosts in Spherical Bowl-Shaped Craters on the Moon, Mercury, and Mars, *Icarus, 100*, 40–47, 1992

Iwasaki, K., Y. Saito, N. Yoshihiro, T. Akabane, E. Panjaitan, I. Radiman, and S. D. Wiramihardja, Martian South Polar Cap 1988, *J. Geophys. Res., 95*, 14751–14754, 1990

Jakosky, B. M., and R. M. Haberle, The Seasonal Behavior of Water on Mars, in *Mars*, ed. H. H. Kieffer, B. M. Jakosky, C. W. Snyder, and M. S. Matthews, University of Arizona Press, Tucson, AZ, 1992

James, P. B., H. H. Kieffer, and D. A. Paige, The Seasonal Cycle of Carbon Dioxide on Mars, in *Mars*, ed. H. H. Kieffer, B. M. Jakosky, C. W. Snyder, and M. S. Matthews, University of Arizona Press, Tucson, AZ, 1992

James, P. B., R. T. Clancy, S. W. Lee, L. J. Martin, R. B. Singer, E. Smith, R. A. Kahn, and R. P. Zurek, Monitoring Mars with the Hubble Space Telescope: 1990–1991 Observations, accepted for publication in *Icarus*, 1994

Kalos, M. H., and P. A. Whitlock, *Monte Carlo Methods, Volume 1: Basics*, Wiley, New York, NY, 1986

Kharadly, M. M. Z., and W. Jackson, The Properties of Artificial Dielectrics Comprising Arrays of Conducting Elements, *Proc. IEE, 100*, 199–212, 1953

Kieffer, H. H., S. C. Chase Jr., T. Z. Martin, E. D. Miner, and F. D. Palluconi, Martian North Pole Summer Temperatures: Dirty Water Ice, *Science, 194*,

1341–1344, 1976

Kieffer, H. H., Mars South Polar Spring and Summer Temperatures, *J. Geophys. Res., 84*, 8263–8288, 1979

Kieffer, H. H., H_2O Grain Size and the Amount of Dust in Mars' Residual North Polar Cap, *J. Geophys. Res., 95*, 1481–1493, 1990

Kieffer, W. S., and B. C. Murray, The Formation of Mercury's Smooth Plains, *Icarus, 72*, 477–491, 1987

Killen, R. M., A. E. Potter, and T. H. Morgan, Spatial Distribution of Sodium Vapor in the Atmosphere of Mercury, *Icarus, 85*, 145–167, 1990

Killen, R. M., and T. H. Morgan, Maintaining the Na Atmosphere of Mercury, *Icarus, 101*, 293–312, 1993

King, J. S., and J. R. Riehle, A Proposed Origin for the Olympus Mons Escarpment, *Icarus, 23*, 300–317, 1974

Klaasen, K. P., Mercury's Rotation Axis and Period, *Icarus, 28*, 469–478, 1976

Klein, M. J., *The Planet Mercury: Measurements of Variations in the Microwave Disk Temperature*, Ph.D. dissertation, University of Michigan, Ann Arbor, 1968

Klein, M. J., Mercury: Recent Observations at 3.75 cm Wavelength—Summary, *Radio Sci., 5*, 397–400, 1970

Kotel'nikov, V. A., and 8 others, Radar Detection of the Planet Mars in the Soviet Union, *Dokl. Akad. Nauk.*, 151, 811–814, 1963

Kouchi, A., Vapour Pressure of Amorphous H_2O Ice and its Astrophysical Implications, *Nature, 330*, 550–552, 1987

Kouchi, A., J. M. Greenberg, T. Yamamoto, and T. Mukai, Extremely Low Thermal Conductivity of Amorphous Ice: Relevance to Comet Evolution, *Astrophys. J., 388*, L73–L76, 1992

Kumar, S., Mercury's Atmosphere: A Perspective after Mariner 10, *Icarus, 28*, 579–591, 1976

Lanzerotti, L. J., and W. L. Brown, Ice in the Polar Regions of the Moon, *J.*

Geophys. Res., 86, 3949–3950, 1981

Laufer, D., E. Kochavi, and A. Bar-Nun, Structure and Dynamics of Amorphous Water Ice, *Phys. Rev. B, 36*, 9219–9227, 1987

Laul, J. C., J. W. Morgan, R. Ganapathy, and E. Anders, Meteoritic Material in Lunar Samples: Characterization from Trace Elements, *Proc. Lunar Plan. Sci. Conf., II*, 1139–1158, 1971

Ledlow, M. J., J. O. Burns, G. R. Gisler, J.-H. Zhao, M. Zeilik, and D. N. Baker, Subsurface Emissions from Mercury: VLA Radio Observations at 2 and 6 Centimeters, *Astrophys. J., 384*, 640–655, 1992

Lee, S. W., P. C. Thomas, and J. Veverka, Wind Streaks in Tharsis and Elysium: Implications For Sediment Transport by Slope Winds, *J. Geophys. Res., 87*, 10025–10041, 1982

Leighton, R. B., and B. C. Murray, Behavior of Carbon Dioxide and Other Volatiles on Mars, *Science, 153*, 136–144, 1966

Lopes, R., J. E. Guest, K. Hiller, and G. Neukum, Further Evidence for a Mass Movement Origin of the Olympus Mons Aureole, *J. Geophys. Res., 87*, 9917–9928, 1982

Lucchita, B. K., Mars and Earth: Comparison of Cold Climate Features, *Icarus, 45*, 264–303, 1981

Mackay, J. R., Air Temperature, Snow Cover, Creep of Frozen Ground, and the Time of Ice–Wedge Cracking, Western Artic Coast, *Can./ J./ Earth Sci., 30*, 1720–1729, 1993

Marti, J., and K. Mauersberger, A Survey and New Measurements of Ice Vapor Pressure at Temperatures Between 170 and 150 K, *Geophys. Res. Lett., 20*, 363–366, 1993

McCauley, J. F., Mariner 9 Evidence for Wind Erosion in the Equatorial and Mid–Latitude Regions of Mars, *J. Geophys. Res., 78*, 4123–4137, 1973

McCauley, J. F., J. E. Guest, G. G. Schaber, N. J. Trask, and R. Greeley, Stratigraphy of the Caloris Basin, Mercury, *Icarus, 47*, 184–202, 1981

McCollom, T. M., and B. M. Jakosky, Interpretation of Planetary Radar Observations: The Relationship Between Actual and Inferred Slope Distributions, *J. Geophys. Res., 98*, 1173–1184, 1993

Mitchell, D. L., Microwave Imaging of Mercury's Thermal Emission: Observations and Models, Ph.D. Thesis, University of California at Berkeley, 1993

Moore, J. M., and K. S. Edgett, Hellas Planitia, Mars: Site of Net Dust Erosion and Implications for the Nature of Basin Floor Deposits, *Geophys. Res. Lett., 20*, 1599–1602, 1993

Morgan, T. H., A. E. Potter, and H. A. Zook, Impact Driven Supply of Sodium and Potassium to the Atmosphere of Mercury, *Proc. Lunar Plan. Sci. Conf., XVIII*, 663–664, 1987

Morgan, T. H., and D. E. Shemansky, Limits to the Lunar Atmosphere, *J. Geophys. Res., 96*, 1351–1367, 1991

Morris, E. C., Aureole Deposits of the Martian Volcano Olympus Mons, *J. Geophys. Res., 87*, 1164–1178, 1982

Morris, E. C., and S. E. Dwornik, Geologic Map of the Amazonis Quadrangle of Mars, *USGS Map I–1049*, 1980

Mouginis–Mark, P. J., L. Wilson, and M. T. Zuber, The Physical Volcanology of Mars, in *Mars*, ed. H. H. Kieffer, B. M. Jakosky, C. W. Snyder, and M. S. Matthews, University of Arizona Press, Tucson, AZ, 1992

Muhleman, D. O., Radar Scattering from Venus and the Moon, *Astron. J., 69*, 34–41, 1964

Muhleman, D. O., Radar Scattering from Venus and Mercury at 12.5 cm, *Radio Science, 69D*, 1630–1631, 1965

Muhleman, D. O., Planetary Characteristics from Radar Observations, *Space Sci. Rev., 6*, 341–364, 1966

Muhleman, D. O., A. W. Grossman, and R. M. Goldstein, Synthetic Aperture Radar of Saturn's Rings using the VLA as the Receiving Instrument, *Bull. Amer. Astron. Soc., 19*, 882, 1987

Muhleman, D. O., A. W. Grossman, B. J. Butler, and M. A. Slade, Radar Reflectivity of Titan, *Science, 248*, 975–980, 1990

Muhleman, D. O., B. J. Butler, A. W. Grossman, and M. A. Slade, Radar Images of Mars, *Science, 253*, 1508–1513, 1991

Muhleman, D. O., A. W. Grossman, M. A. Slade, and B. J. Butler, Titan's Radar Reflectivity and Rotation, *Bull. Am. Astron. Soc., 25*, 1099, 1993

Murray, B. C., M. J. S. Belton, G. E. Danielson, M. E. Davies, D. E. Gault, B. Hapke, B. O'Leary, R. G. Strom, V. Suomi, and N. Trask, Mercury's Surface: Preliminary Description and Interpretation from Mariner 10 Pictures, *Science, 185*, 169–179, 1974

Ostro, S. J., Radar Properties of Europa, Ganymede, and Callisto, in *Satellites of Jupiter*, ed. D. Morrison, University of Arizona Press, Tucson, AZ, 1982

Ostro, S. J., and E. M. Shoemaker, The Extraordinary Radar Echoes from Europa, Ganymede, and Callisto: A Geological Perspective, *Icarus, 85*, 335–345, 1990

Ostro, S. J., D. B. Campbell, R. A. Simpson, R. S. Hudson, J. F. Chandler, K. D. Rosema, I. I. Shapiro, E. M. Standish, R. Winkler, D. K. Yeomans, R. Velez, and R. M. Goldstein, Europa, Ganymede, and Callisto: New Radar Results from Arecibo and Goldstone, *J. Geophys. Res., 97*, 18227–18244, 1992

Paige, D. A., and A. P. Ingersoll, Annual Heat Balance of Martian Polar Caps: Viking Observations, *Science, 228*, 1160–1168, 1985

Paige, D. A., K. E. Herkenhoff, and B. C. Murray, Mariner 9 Observations of the South Polar Cap of Mars: Evidence for Residual CO_2 Frost, *J. Geophys. Res., 95*, 1319–1335, 1990

Paige, D. A., S. E. Wood, and A. R. Vasavada, The Thermal Stability of Water Ice at the Poles of Mercury, *Science, 258*, 643–646, 1992

Palluconi, F. D., and H. H. Kieffer, Thermal Inertia Mapping of Mars from 60°S to 60°N, *Icarus, 45*, 415–426, 1981

Paterson, W. S. B., *The Physics of Glaciers, 2nd ed.*, Pergamon Press, Oxford, 1981

Peale, S. J., The Rotational Dynamics of Mercury and the State of its Core, in *Mercury*, ed. F. Vilas, C. R. Chapman, and M. S. Matthews, University of Arizona Press, Tucson, AZ, 1988

Plescia, J. B., L. E. Roth, and R. S. Saunders, Tectonic Features of Southeast Tharsis, *Proc. Lunar Plan. Sci., XI*, 891–893, 1980

Plescia, J. B., Recent Flood Lavas in the Elysium Region of Mars, *Icarus, 88*, 465–490, 1990

Poirier, J. P., Rheology of Ices: a Key to the Tectonics of the Ice Moons of Jupiter and Saturn, *Nature, 299*, 683–688, 1982

Pollack, J. B., D. Colburn, R. Kahn, J. Hunter, W. van Camp, C. E. Carlston, and M. R. Wolf, Properties of Aerosols in the Martian Atmosphere, as Inferred From Viking Lander Imaging Data, *J. Geophys. Res., 82*, 4479–4496, 1977

Pollack, J. B., D. S. Colburn, F. M. Flasar, R. Kahn, C. E. Carlston, and D. Pidek, Properties and Effects of Dust Particles Suspended in the Martian Atmosphere, *J. Geophys. Res., 84*, 2929–2945, 1979

Pollack, J. B., R. M. Haberle, J. Schaeffer, and H. Lee, Simulations of the General Circulation of the Martian Atmosphere 1. Polar Processes, *J. Geophys. Res., 95*, 1447–1473, 1990

Potter, A. E., and T. H. Morgan, Evidence for Magnetospheric Effects on the Sodium Atmosphere of Mercury, *Science, 248*, 835–838, 1990

Renka, R. J., Multivariate Interpolation of Large Sets of Scattered Data, ACM Trans. Math. Soft., 14, 139–148, 1988

Rignot, E. J., S. J. Ostro, J. J. van Zyl, and K. C. Jezek, Unusual Radar Echoes from the Greenland Ice Sheet, *Science, 261*, 1710–1713, 1993

Robinson, M. S., P. J. Mouginis–Mark, J. R. Zimbelman, S. S. C. Wu, K. K. Ablin, and A. E. Howington–Kraus, Chronology, Eruption Duration, and Atmospheric Contribution of the Martian Volcano Apollinaris Patera, *Icarus, 104*, 301–323, 1993

Robinson, M. S., and H. Garbeil, Volumes and Depth of Burial of the Lesser Tharsis

Volcanoes, *Proc. Lunar Plan. Sci. Conf., XXV*, 1141–1142, 1994

Rots, A., *A Short Guide for VLA Spectral Line Observers, (Edition 8.0)*, National Radio Astronomy Observatories, 1990

Rudy, D. J., Mars: High Resolution VLA Observations at Wavelengths of 2 and 6cm and Derived Properties, Ph.D. thesis, Calif. Inst. of Tech., 1987

Schultz, P. H., and A. B. Lutz, Polar Wandering of Mars, *Icarus, 73*, 91–141, 1988

Scott, D. H., and M. H. Carr, Geologic Map of Mars, *USGS Map I–1083*, 1978

Scott, D. H., G. G. Schaber, K. L. Tanaka, K. C. Horstman, and A. L. Dial, Jr., Map series showing lava flow fronts in the Tharsis region of Mars, *USGS Maps I–1266 to 1280*, 1981

Scott, D. H., and K. L. Tanaka, Ignimbrites of Amazonis Planitia Region of Mars, *J. Geophys. Res., 87*, 1179–1190, 1982

Scott, D. H., and K. L. Tanaka, Geologic Map of the Western Equatorial Region of Mars, *USGS map I–1802–A*, 1986

Scott, D. H., and M. G. Chapman, Mars Elysium Basin: Geologic/Volumetric Analyses of a Young Lake and Exobiologic Implications, *Proc. Lunar Plan. Sci., 21*, 669–677, 1991

Shapiro, I. I., Theory of Radar Determination of Planetary Rotations, *Astron. J., 72*, 1309–1323, 1967

Simpson, R. A., G. L. Tyler, and B. J. Lipa, Mars Surface Properties Observed by Earth–Based Radar at 70–, 12.5–, and 3.8–cm Wavelengths, *Icarus, 32*, 147–167, 1977

Simpson, R. A., G. L. Tyler, and D. B. Campbell, Arecibo Radar Observations of Martian Surface Characteristics Near the Equator, *Icarus, 33*, 102–115, 1978*a*

Simpson, R. A., G. L. Tyler, and D. B. Campbell, Arecibo Radar Observations of Mars Surface Characteristics in the Northern Hemisphere, *Icarus, 36*, 153–173, 1978*b*

Simpson, R. A., B. C. Fair, and H. T. Howard, Microwave Properties of Solid CO_2,

J. Geophys. Res., 85, 5481–5484, 1980

Simpson, R. A., and G. L. Tyler, Viking Bistatic Radar Experiment: Summary of First–Order Results Emphasizing North Polar Data, *Icarus, 46*, 361–389, 1981

Slade, M. A., B. J. Butler, and D. O. Muhleman, Mercury Radar Imaging: Evidence for Polar Ice, *Science, 258*, 635–640, 1992

Snyder, J. P., Map Projections—A Working Manual, USGS Professional Paper 1395, 1987

Soter, S. L., and J. Ulrichs, Rotation and Heating of the Planet Mercury, *Nature, 214*, 1315–1316, 1967

Sprague, A. L., R. W. H. Kozlowski, and D. M. Hunten, Caloris Basin: An Enhanced Source for Potassium in Mercury's Atmosphere, *Science, 249*, 1140–1142, 1990

Sprague, A. L., Mercury's Atmospheric Bright Spots and Potassium Variations: A Possible Cause, *J. Geophys. Res., 97*, 18257–18264, 1992

Tanaka, K. L., and M. G. Chapman, The Relation of Catastrophic Flooding of Mangala Valles, Mars, to Faulting of Memnonia Fossae and Tharsis Volcanism, *J. Geophys. Res., 95*, 14315–14323, 1990

Thomas, G. E., Mercury: Does Its Atmosphere Contain Water?, *Science, 183*, 1197–1198, 1974

Thomas, P., and J. Veverka, Seasonal and Secular Variation of Wind Streaks on Mars: An Analysis of Mariner 9 and Viking Data, *J. Geophys. Res., 84*, 8131–8146, 1979

Thompson, A. R., J. M. Moran, and G. W. Swenson, Jr., *Interferometry and Synthesis in Radio Astronomy*, Krieger Publishing Co., Malabar, Fl., 1991

Thompson, T. W., Atlas of Lunar Radar Maps at 70-cm Wavelength, *The Moon, 10*, 51–85, 1974

Thompson, T. W., and H. J. Moore, A Model for Depolarized Radar Echoes from Mars, *Proc. Lunar Plan. Sci. 19*, 409–422, 1989

Thompson, T. W., T. C. O'Brien, R. F. Jurgens, M. A. Slade, and H. J. Moore, Mars Quasi–Specular Echoes: Preliminary Results at 3.5–cm Wavelength, *Proc. Lunar Plan. Sci. Conf., XXIII*, 1431–1432, 1992

Tryka, K. A., D. O. Muhleman, B. Butler, G. Berge, M. Slade and A. Grossman, Correlation of Multiple Reflections from the Venus Surface with Topography, *Proc. Lunar Plan. Sci. Conf., XXII*, 1417–1418, 1991

Tryka, K. A., and D. O. Muhleman, Reflection and Emission Properties on Venus: Alpha Regio, *J. Geophys. Res., 97*, 13379–13394, 1992

van Langevelde, H. J., and W. D. Cotton, Visibility Based Continuum Subtraction, in *Radio Interferometry: Theory, Techniques, and Applications*, ed. T. J. Cornwell and R. A. Perley, Astronomical Society of the Pacific Conference Series, San Francisco, CA, 1991

Veverka, J., P. Thomas, and R. Greeley, A Study of Variable Features on Mars During the Viking Primary Mission, *J. Geophys. Res., 82*, 4167–4187, 1977

Wang, R. T., and H. C. van de Hulst, Rainbows: Mie Computations and the Airy Approximation, *Appl. Opt., 30*, 106–117, 1991

Ward, A. W., Yardangs on Mars: Evidence of Recent Wind Erosion, *J. Geophys. Res., 84*, 81147–8166, 1979

Warren, S. G., Optical Constants of Ice from the Ultraviolet to the Microwave, *Appl. Opt., 23*, 1206–1225, 1984

Warren, S. G., Optical Constants of Carbon Dioxide Ice, *Appl. Opt., 25*, 2650–2674, 1986

Watkins, J. S., and R. L. Kovach, Seismic Investigation of the Lunar Regolith, *Proc. Lunar Plan. Sci. Conf., IV*, 2561–2574, 1973

Watson, K., B. C. Murray, and H. Brown, The Behavior of Volatiles on the Lunar Surface, *J. Geophys. Res., 66*, 3033–3045, 1961

Watts, A. W., R. Greeley, and H. J. Melosh, The Formation of Terrains Antipodal to Major Impacts, *Icarus, 93*, 159–168, 1991

Weertman, J., Creep of Ice, in *Physics and Chemistry of Ice*, ed. E. Whalley, S. J.

Jones, and L. W. Gold, University of Toronto Press, Toronto, 1973

Weertman, J., Creep Deformation of Ice, *Ann. Rev. Earth Planet. Sci., 11*, 215–240, 1983

Yamamoto, T., Formation History and Environment of Cometary Nuclei, in *Ices in the Solar System*, ed. J. Klinger, D. Benest, A. Dollfus, and R. Smoluchowski, D. Reidel Publishing Company, Dordrecht, Holland, 1985

Zimbelman, J. R., and K. S. Edgett, The Tharsis Montes, Mars: Comparison of Volcanic and Modified Landforms, *Proc. Lunar Plan. Soc., 22*, 31–44, 1992

Zisk, S. H., G. H. Pettengill, and G. W. Catuna, High-Resolution Radar Maps of the Lunar Surface at 3.8-cm Wavelength, *The Moon, 10*, 17–50, 1974

Zohar, S., and R. M. Goldstein, Surface Features on Mercury, *Astron. J., 79*, 85–91, 1974

Zook, H. A., The State of Meteoritic Material on the Moon, *Proc. Lunar Plan. Sci. Conf., VI*, 1653–1672, 1975